

Dissertation

Studies for the Commissioning of the CERN CMS Silicon Strip Tracker

ausgeführt zum Zwecke der Erlangung des akademischen Grades eines Doktors
der technischen Wissenschaften unter der Leitung von

Univ.Doz. Univ.Prof. Dr. Dipl.-Ing. Christian W. Fabjan
Atominstitut der Österreichischen Universitäten (E141)

eingereicht an der



TECHNISCHE UNIVERSITÄT WIEN
FAKULTÄT FÜR TECHNISCHE PHYSIK

eingereicht von: Dipl.-Ing. Christoph Bloch
Matrikelnummer: 9625803
geboren am 10. April 1976
Franz-Josefs Kai 43, A-1010 Wien

Diese Arbeit wurde unterstützt vom Österreichischen Bundesministerium für Bildung,
Wissenschaft und Kultur.

Genf, am 17. Dezember 2007

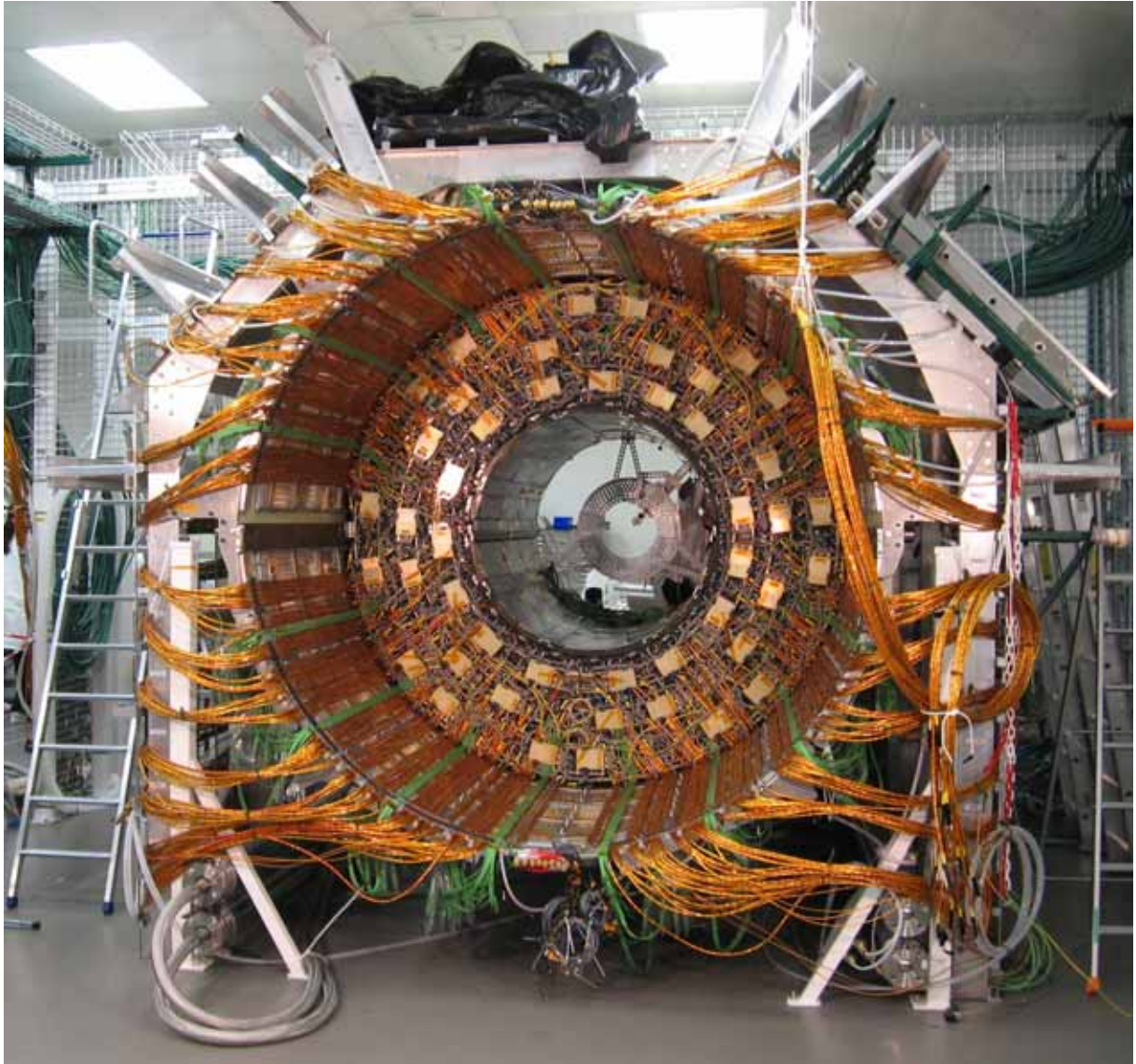


FIGURE 1: *The CMS Tracker "Outer Barrel" inside the Tracker Support Tube. Picture taken inside the Tracker Integration Facility just after the completion of the Outer Barrel construction and commissioning.*

Zusammenfassung

Der Large Hadron Collider (LHC) am CERN wird 2008 in Betrieb genommen, womit Proton-Proton Kollisionen in einem nie zuvor erreichten Energiebereich möglich werden. Eines der Hauptexperimente ist der Compact Muon Solenoid (CMS), ein Vielzweck-Detektor, der optimiert wurde für die Suche nach dem Higgs Boson und supersymmetrischen Teilchen. Für solche Entdeckungen ist der CMS-Detektor auf ein hochpräzises Spurenerkennungssystem angewiesen. Dieses Spurenerkennungssystem besteht aus einem Pixeldetektor und dem größten jemals gebauten Silizium-Streifen-Detektor. Um einen derart komplexen Detektor wie den CMS Silizium-Streifen-Detektor erfolgreich betreiben und sein gesamtes Potential ausschöpfen zu können, müssen die instrumentalen Eigenschaften so genau wie möglich bestimmt und die zugehörige Rekonstruktionssoftware mit physikalischen Daten getestet werden. Eine Reihe von Parametern des Arbeitsverhaltens müssen untersucht werden, um den Detektor erfolgreich in Betrieb zu nehmen. Einige dieser Eigenschaften sind relevant für den gesamten Spurendetektor, während andere spezifisch für das Tracker Outer Barrel (TOB) sind:

- Die Zeitentwicklung der Signale der Ausleselektronik muss genau gemessen werden und korrekt simuliert werden, da sie kritische Parameter, wie die Okkupanz und das Datenvolumen, beeinflussen.

- Eine eventuelle Kopplung der Auslesekanäle, muss bestimmt werden, da sie zur Clustergröße beiträgt, und somit Einfluss auf die Ortsauflösung und die Okkupanz hat.

- Die Subkomponenten des TOB, "Rods", bestehen hauptsächlich aus Kohlefaser-Elementen, an die Aluminiumeinsätze geklebt werden, die einen effizienten Wärmeaustausch zwischen den Siliziumdetektoren und dem dünnen Kühlrohr aus einer Kupfer-Nickel-Legierung gewährleisten. Die unterschiedlichen Wärmeausdehnungskoeffizienten dieser Materialien können jedoch zu thermischen Spannungen in der Struktur führen, wenn diese auf die Arbeitstemperatur des Spurendetektor (-10°C) heruntergekühlt wird. Eine genaue Untersuchung dieser Effekte und der geometrischen Präzision der Rods, sind wichtige Informationen für die Spurenrekonstruktion bei CMS.

Diese und weitere Punkte werden in der vorliegenden Arbeit untersucht. Dafür wurde ein großer Testaufbau, der für die Aufzeichnung von Spuren kosmischer Myonen ausgelegt ist, mehrere Monate lang betrieben. Es wurden Daten sowohl bei Raumtemperatur als auch bei der nominellen Arbeitstemperatur des CMS Spurendetektor von -10°C aufgezeichnet. Diese Daten wurden benutzt, um die Rekonstruktions- und Alignierungsalgorithmen für den Spurendetektor zu testen; ferner um die mechanische Präzision der Rods und das Verhalten bei verschiedenen Temperaturen zu studieren.

Abstract

In 2008 the Large Hardon Collider (LHC) at CERN will start producing proton-proton collisions of unprecedented energy. One of its main experiments is the Compact Muon Solenoid (CMS), a general purpose detector, optimized for the search of the Higgs boson and super symmetric particles. The discovery potential of the CMS detector relies on a high precision tracking system, made of a pixel detector and the largest silicon strip Tracker ever built.

In order to operate successfully a device as complex as the CMS silicon strip Tracker, and to fully exploit its potential, the properties of the hardware need to be characterized as precisely as possible, and the reconstruction software needs to be commissioned with physics signals. A number of issues were identified and studied to commission the detector, some of which concern the entire Tracker, while some are specific to the Tracker Outer Barrel (TOB):

- the time evolution of the signals in the readout electronics need to be precisely measured and correctly simulated, as it affects the expected occupancy and the data volume, critical issues in high-luminosity running;

- the electronics coupling between neighbouring channels affects the cluster size and hence the hit resolution, the tracking precision, the occupancy and the data volume;

- the mechanical structure of the Rods (the sub-assemblies of the TOB) is mostly made of carbon fiber elements; aluminum inserts glued to the carbon fiber frame provide efficient cooling contacts between the silicon detectors and the thin cooling pipe, made of a copper-nickel alloy; the different thermal expansion coefficients of the various components induce stresses on the structure when this is cooled down to the operating temperature, possibly causing small deformations; a detailed characterization of the geometrical precision of the rods and of its possible evolution with temperature is a valuable input for track reconstruction in CMS.

These and other issues were studied in this thesis. For this purpose, a large scale test setup, designed to study the detector performance by tracking cosmic muons, was operated over several months. A dedicated trigger system was set up, to select tracks synchronous with the fast readout electronics, and to be able to perform a precise measurement of the time evolution of the front-end signals. Data collected at room temperature and at the Tracker operating temperature of -10°C were used to test reconstruction and alignment algorithms for the Tracker, as well as to perform a detailed qualification of the geometry and the functionality of the structures at different temperatures.

Acknowledgements

The work presented in the following would not have been possible without the help and contributions of many people: First and foremost I would like to deeply thank my supervisors Christian Fabjan and Duccio Abbaneo without whom my research would not have been possible. I am especially grateful to Christian Fabjan, who supported my application to work at CERN, thus enabling me to do research in this stimulating international environment and for guiding me through my thesis.

I want to express my gratitude towards Duccio Abbaneo for his ongoing support throughout the course of this project. His profound knowledge of the CMS Tracker and capability of analyzing and solving problems inspired me and profited my work tremendously.

Many thanks to Anne-Sylvie Giolo Nicollerat, for setting up the reconstruction geometry for the Cosmic Rack and her contribution to the analysis. I also want to thank her for always keeping her positive attitude, even when things did not work as expected (which they sometimes tend to do during a thesis).

I am grateful for Alexander Dierlamms detailed introduction to the Cosmic Rack DAQ, his insights on silicon detectors, our many fruitful discussions, and for being brave enough to read early versions of this thesis (Alex if you should read this I owe you a bottle of wine!).

I want to thank Michael Eppard who always helped in installing and acquiring components, needed for the operation of the Cosmic Rack (including coffee), and the fun it was working with him.

Many thanks to the following colleagues of mine for their various help and support, namely: The DAQ team Laurent Mirabito, Frederic Drouhin, Jonathan Fulcher, and Osman Zorba for the support with the Cosmic Rack DAQ. Erkki Anttila and Antti Onnela, for their excellent work in designing and building the Cosmic Rack mechanics. Gero Flucke for the introduction and the support to the "Millepede" algorithm. Tapio Lampen for the introduction to the "HIP" algorithm. Wolfgang Adam for his precise statements on the interiors of tracking, invaluable input for the debugging of the track reconstruction with the Cosmic Rack. Martin Weber and Ivan Reid for the introduction to "ORCA". Richard Brauer for his excellent analysis package "AC1Analysis" that eased up the analysis of noise. Marvin Johnson for lifting some mysteries of the world of electronics noise. Imtiaz Ahmed and Mohsin Abbas for their help in debugging the Cosmic Rack hardware. Guido Magazzu and Slawomir Tkaczyk for their help in debugging the tracker power supplies. Mark Raymond for letting me participate on his vast knowledge of the front-end electronics. James Lamb and Kristen Eppard for proof reading parts of my thesis. Andromachi Tsirou and Piero Giorgio Verdini for designing and installing the Cosmic Rack interlock system. Frank Hartman and Guido Dirkes for many interesting discussions on silicon strip sensors.

I also want to thank Julia Trummer and Fadmar Osmic, who hosted me during my early days at CERN and provided me with a smooth start.

Last but not least I am most grateful for the support I received from my family and friends.

Contents

1	Introduction	1
	Introduction	1
1.1	The Large Hadron Collider	2
1.2	Physics Objectives of the LHC	3
1.3	The CMS Experiment	7
2	Silicon Strip Detectors	11
2.1	Interaction with Matter and Charge Generation	11
2.2	Properties of Intrinsic Semiconductors	14
2.3	PN-Junction Semiconductor Detectors	15
2.4	Silicon Strip Sensor Design	17
2.5	Readout and Mechanism of the Charge Collection	17
2.6	Radiation Damage	24
2.7	Summary	25
3	The CMS Tracker	27
3.1	The CMS Pixel Detector	28
3.2	The CMS Silicon Strip Tracker	28
3.3	Design Choices of the Strip Sensors	31
3.4	Summary	38
4	CMS Readout Electronics	39
4.1	System Overview	39
4.2	Radiation Hardness	40
4.3	Front-End Electronics	41
4.4	Front-End Readout Chip APV25	42
4.5	Optical Link System	45
4.6	Control Architecture	47
4.7	Front End Driver	48
5	The Cosmic Rack - A Large Scale Test Setup for the CMS Tracker	51
5.1	Cosmic Rack Mechanics	54
5.2	Services and Grounding Scheme	54
5.3	Data Acquisition System	56
5.4	Cosmic Trigger System	58
5.5	Filtering Low Momentum Particles	60
5.6	Summary	60

6	Studies of the Noise and Grounding Scheme	61
6.1	Introduction	61
6.2	Expected Noise Performance	61
6.3	Common Mode Noise	64
6.4	Measured Noise Performance	66
6.5	Noise Correlations	73
6.6	Summary	80
7	Tracking Cosmic Particles	81
7.1	Cosmic Radiation	81
7.2	Tracking Cosmics	84
7.3	Cluster Properties	89
7.4	Summary	93
8	Detector Response	95
8.1	Reconstruction of the Pulse Shape	95
8.2	Cluster Analysis	98
8.3	Measurements of the Electronics Crosstalk	102
8.4	Time Evolution of the Coupling	106
8.5	Summary	116
9	The CMS Tracker Alignment Strategy	117
9.1	Introduction	117
9.2	Survey	117
9.3	Laser Alignment System	118
9.4	Track Based Alignment	119
9.5	Alignment Algorithms for Track based alignment	122
10	Alignment by Tracking Cosmic Particles	127
10.1	Introduction	127
10.2	Measurement Setup	127
10.3	Alignment with the Millepede Algorithm	128
10.4	Test of the Alignment Procedure with a Simulation	132
10.5	Alignment of the Cosmic Rack	140
10.6	Geometrical Precision of TOB Rods	150
10.7	Summary	157
11	Conclusions	159
11.1	Results	159
11.2	Outlook and open Issues	160
A	Charge Sensitive Amplifier	161
A.1	Charge Amplification	161
A.2	Equivalent Noise Charge	163
B	Noise in Deconvolution Mode	165

Chapter 1

Introduction

Particle physics addresses one of the oldest questions of mankind: what are the constituents of matter, what are their properties and the fundamental interactions that govern them.

The current knowledge of particle physics is summarized by the Standard Model (SM), a quantum field theory that unifies the strong and the electroweak interactions. In the SM the fundamental constituents of matter are described by 12 fermions: 6 quarks and 6 leptons, and all forces (except gravity) are described by the exchange of 12 gauge bosons (shown in Figure 1.1).

FERMIONS			matter constituents spin = 1/2, 3/2, 5/2, ...		
Leptons spin = 1/2			Quarks spin = 1/2		
Flavor	Mass GeV/c ²	Electric charge	Flavor	Approx. Mass GeV/c ²	Electric charge
ν_e electron neutrino	$<1 \cdot 10^{-8}$	0	u up	0.003	2/3
e electron	0.000511	-1	d down	0.006	-1/3
ν_μ muon neutrino	<0.0002	0	c charm	1.3	2/3
μ muon	0.106	-1	s strange	0.1	-1/3
ν_τ tau neutrino	<0.02	0	t top	175	2/3
τ tau	1.7771	-1	b bottom	4.3	-1/3

BOSONS			force carriers spin = 0, 1, 2, ...		
Unified Electroweak spin = 1			Strong (color) spin = 1		
Name	Mass GeV/c ²	Electric charge	Name	Mass GeV/c ²	Electric charge
γ photon	0	0	g gluon	0	0
W⁻	80.4	-1			
W⁺	80.4	+1			
Z⁰	91.187	0			

FIGURE 1.1: *Fundamental particles of the standard model: the constituents of matter (left), and the gauge bosons (right) [1].*

The SM is a theory with great predictive power, able to predict yet unobserved particles and allowing quantitative calculations of fundamental physics processes. SM predictions are as of today in nearly perfect agreement with experimental observations and precision measurements.

A major limitation of the SM, in its initial form, was that all particles (including quarks and leptons) were expected to be massless. To overcome this limitation, the Higgs mechanism was introduced. The theory developed by Peter Higgs (Brout and Englert 1964) [2] describes particle masses arising from an interaction with the Higgs boson, postulated as a spin zero boson with unknown mass. The discovery of the Higgs boson¹ is the missing key in the verification of the SM.

A major step in the study of the validity of the SM at the TeV energy scale (including the possible discovery of the Higgs boson) is expected from the analysis of the data provided by the Large Hadron Collider that will start operation in 2008.

¹Several extensions of the SM predict the existence of more than one Higgs boson.

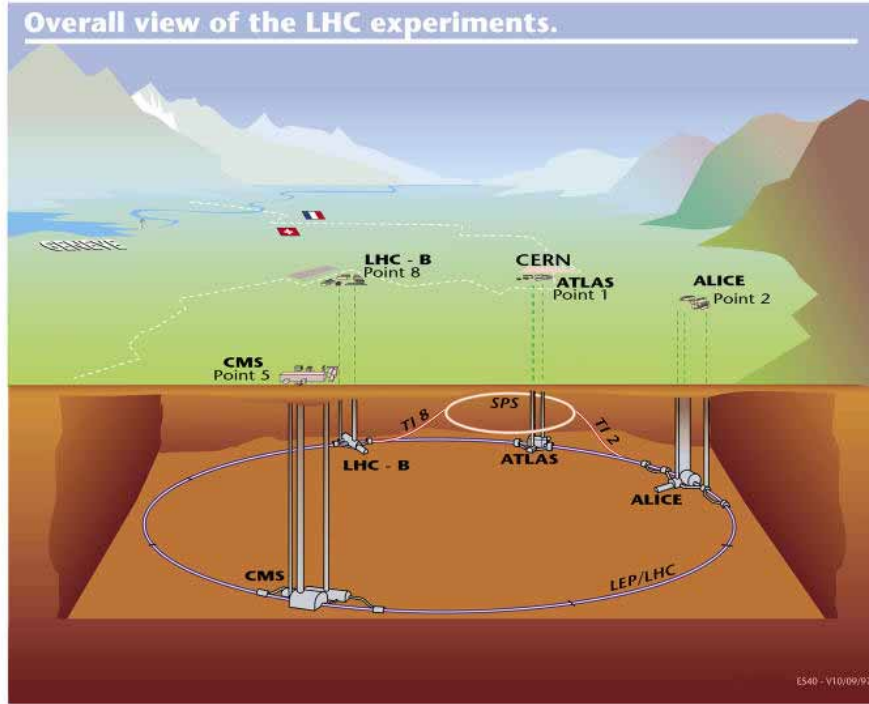


FIGURE 1.2: Schematic view of the LHC and its experiments [3].

1.1 The Large Hadron Collider

The Large Hadron Collider (LHC), illustrated in Figure 1.2, is a huge proton-proton collider of almost 27 km circumference. The LHC is built at CERN² in the tunnel of the former Large Electron Positron (LEP) collider. LEP reached a maximum center of mass energy \sqrt{s} of 209 GeV, limited by synchrotron radiation. The energy loss per turn ΔE_{turn} due to synchrotron radiation is given by:

$$\Delta E_{turn} \approx -\frac{4\pi e^2}{3R} \left(\frac{pc}{mc^2}\right)^4 \quad (1.1)$$

where R is the radius, m the particles mass and p its momentum. The synchrotron radiation scales with m^{-4} , thus by colliding heavier particles such limitation can be overcome.

The LHC accelerates protons in two counter rotating beams up to energies of 7 TeV (\sqrt{s} of 14 TeV), and is expected to reach a high luminosity of $\mathcal{L} \approx 10^{34} \text{ cm}^{-2} \text{ s}^{-1}$.

The design of the LHC is versatile enough, to allow also for the collisions of heavy ions such as fully stripped $^{208}\text{Pb}^{82+}$, reaching center of mass energies of about $\sqrt{s_{n,n}}$ of 5.5 TeV per nucleon ($\sqrt{s_{tot}} \approx 1150 \text{ TeV}$) at a reduced luminosity of $\mathcal{L} \approx 10^{27} \text{ cm}^{-2} \text{ s}^{-1}$.

The limitation in center of mass energy at the LHC is not given by synchrotron radiation, but by the magnetic field that is required to keep the protons in the ring ($p(\text{TeV}) = 0.3 \cdot B(T) \cdot R(\text{km})$). The LHC uses superconductive dipole magnets for the beam guidance that provide a field of about 8.3 T, which is the limit of currently available technologies. The temperature of these dipoles is kept below 2 K by a liquid helium cooling system³. The machine parameters for proton-proton operation are summarized in Table 1.1.

²The Conseil Européen pour la Recherche Nucléaire is the world largest particle physics laboratory. CERN is located at Swiss-France border and was founded in 1954. Today it has 20 member states.

³This makes the LHC the largest cryogenic system world wide.

Momentum at collision	7 TeV
Momentum at injection	450 GeV
Dipole field at 7 TeV	8.33 T
Radius of curvature	2812 m
Circumference	26658 m
Design luminosity	$10^{34} \text{ cm}^{-2} \text{ s}^{-1}$
Number of bunches	2808
Particles per bunch	$1.15 \cdot 10^{11}$
Collision rate	40.08 MHz
DC beam current	0.58 A
Stored energy per beam	362 MJ

TABLE 1.1: *Some of the LHC design parameters [4].*

1.2 Physics Objectives of the LHC

The LHC is opening up an unprecedented energy range, and with its high luminosity it will be a factory for many particles. It should however be noticed that not the full center of mass energy of 14 TeV is available in single collisions, as the colliding particles have an internal structure and the momentum is shared between the components. Furthermore the transferred energy depends on the impact parameter, varying in each single collision. The cross sections for physics processes are shown in Figure 1.3, as well as the expected event rates at the LHC for nominal luminosity. These high generation rates provide a rich physics program to study. At the four interaction points (where the counter rotating beams are brought to collision) five experiments have been set up (Figure 1.2):

- ATLAS (A Large Toroidal AparatuS) [6]
- CMS (Compact Muon Solenoid) [7, 8]
- ALICE (A Large Ion Collider Experiment) [9]
- LHCb (Large Hadron Collider beauty) [10]
- TOTEM (TOTal and Elastic Measurement) [11].

ATLAS and CMS are general purpose experiments, designed for the same physics program. This redundancy increases not only the accumulated cross sections in the combined research, but more importantly - since both experiments are realized in complementary technologies, provides a natural way of checking the findings of each experiment. ALICE, LHCb and TOTEM are specialized experiments.

An (non-exhaustive) overview of the physics program at LHC is given below, while the CMS experiment is described in the following section.

1.2.1 SM Higgs Physics

The mass of the Higgs boson is a free parameter in the SM; for a given mass, however the cross sections for the production and the branching ratios for the decay can be derived. Furthermore with the results from past experiments, the expected mass of the Higgs boson m_H can be restricted to the range: $114.4 \text{ GeV}/c^2 < m_H < 241 \text{ GeV}/c^2$, where the lower limit follows from direct search in the LEP experiments, while the upper limit follows from global fits to electroweak data [12].

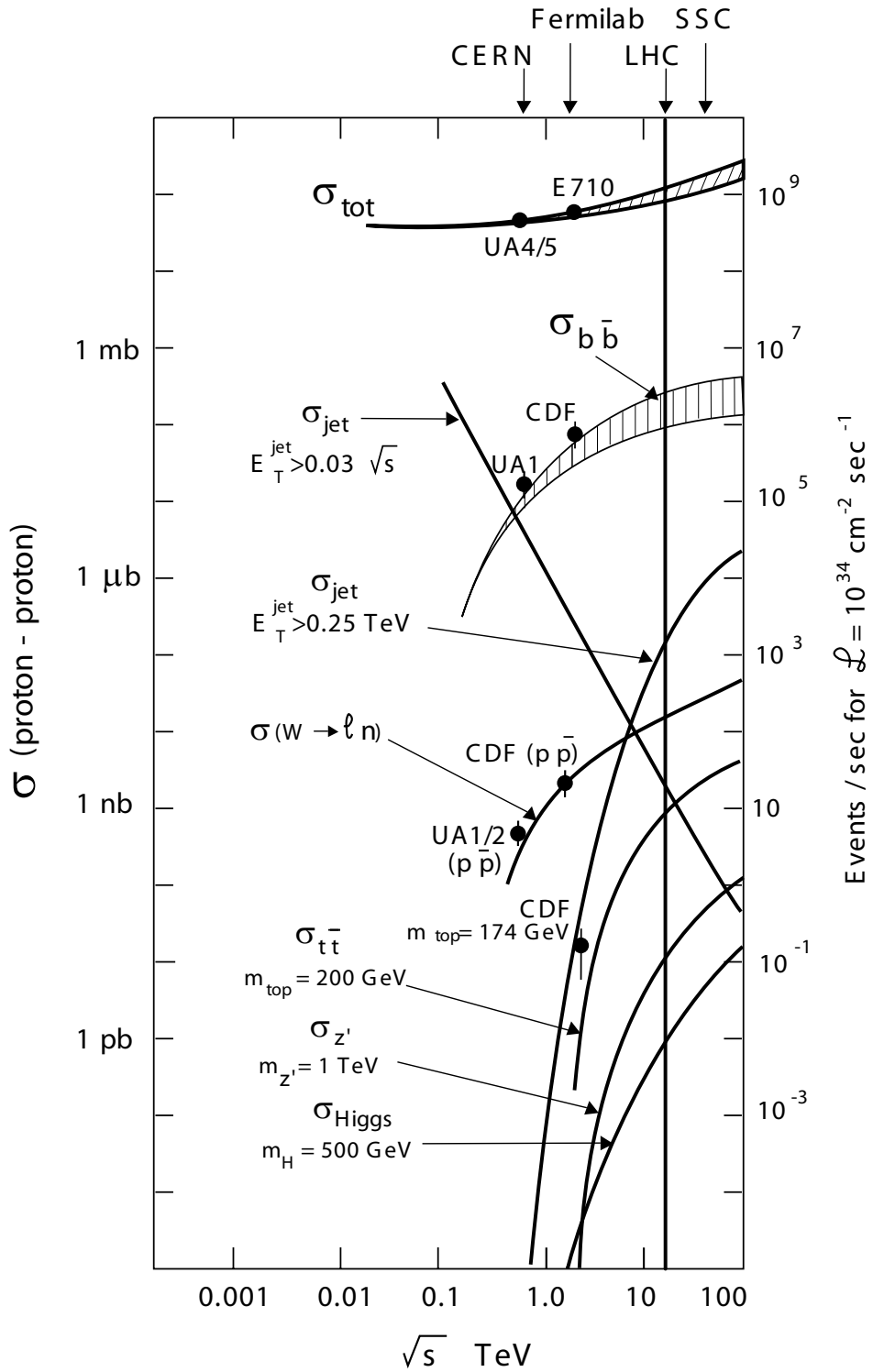


FIGURE 1.3: Cross sections for proton proton collisions, and expected event rates at the LHC for nominal luminosity, as a function of the center of mass energy [5].

Estimates for possible production channels in proton-proton collisions and their cross sections at the LHC energy are shown in Figure 1.4. The dominant process is gluon gluon fusion, with cross sections ranging from 0.1 pb to 100 pb.

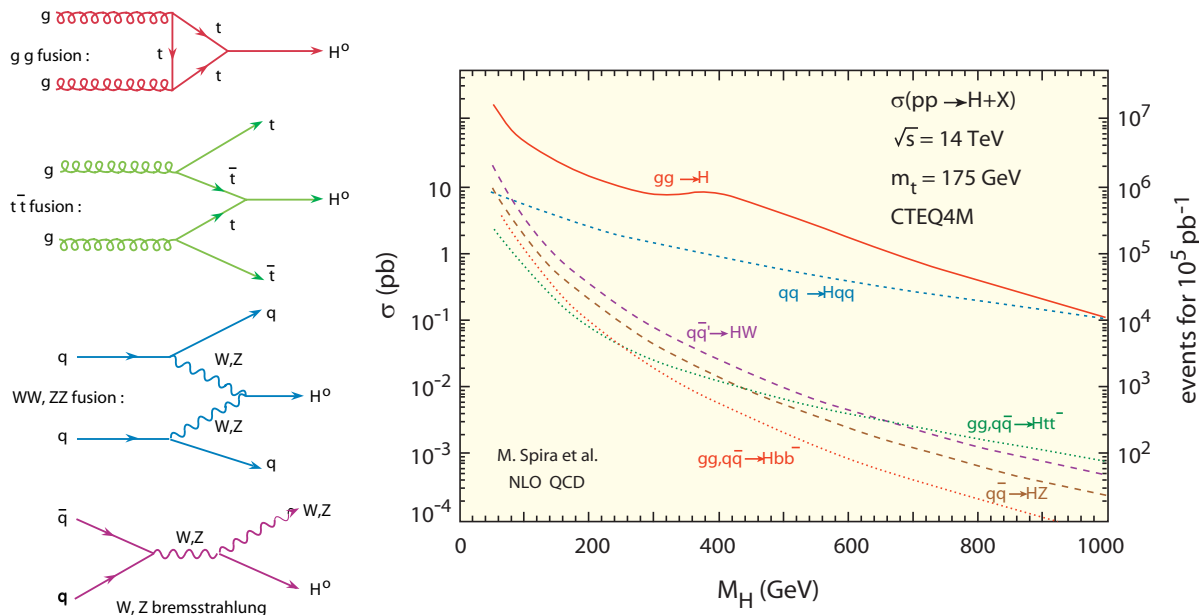


FIGURE 1.4: Production channels for the SM Higgs (left), and their cross sections as a function of the Higgs mass (right) at the LHC [13]. The number of events is shown for an accumulated luminosity of 100 fb^{-1} , that corresponds to 1 year of LHC operation, with one third of the time at nominal luminosity.

The branching ratios for the decay of the Higgs are illustrated in Figure 1.5; the relative rates of the different channels strongly depend on the mass of the Higgs. The ATLAS and the CMS experiments have been designed to allow for a discovery of the Higgs in the range of $100 \text{ GeV}/c^2 < m_H < 1 \text{ TeV}/c^2$, where - following a common convention in particle physics - for an unambiguous discovery a significance better than 5σ is required, here $\sigma = \frac{S}{\sqrt{B}}$, S and B are the number of signal and background events, respectively. The most suitable channels for the discovery are not necessarily those with the largest branching ratios, as the possibility to distinguish the signal from the background plays a key role. In fact for the search at the LHC the channels with fully hadronic final states are very difficult to use, because of the overwhelming QCD background (see the production cross sections shown in Figure 1.3). The preferred discovery channels for the (SM)⁴ Higgs at the LHC for different mass regions are briefly discussed below.

Light Higgs ($m_H < 120 \text{ GeV}/c^2$)

For a light Higgs boson the decay channel with the highest branching ratio is:

$$H \rightarrow b\bar{b} \quad (1.2)$$

Due to the purely hadronic final state, this channel cannot be used inclusively, as it is impossible to achieve sufficient rejection of the large QCD background. However if the Higgs boson is produced together with a $t\bar{t}$ pair, the final state can be disentangled from the background searching for a high energetic lepton from the top quark decay.

For a slightly heavier Higgs, the branching ratios for the decay into two photons becomes the most relevant:

$$H \rightarrow \gamma\gamma \quad (1.3)$$

⁴In the Super Symmetry extension of the SM, production and decay channels have different rates.

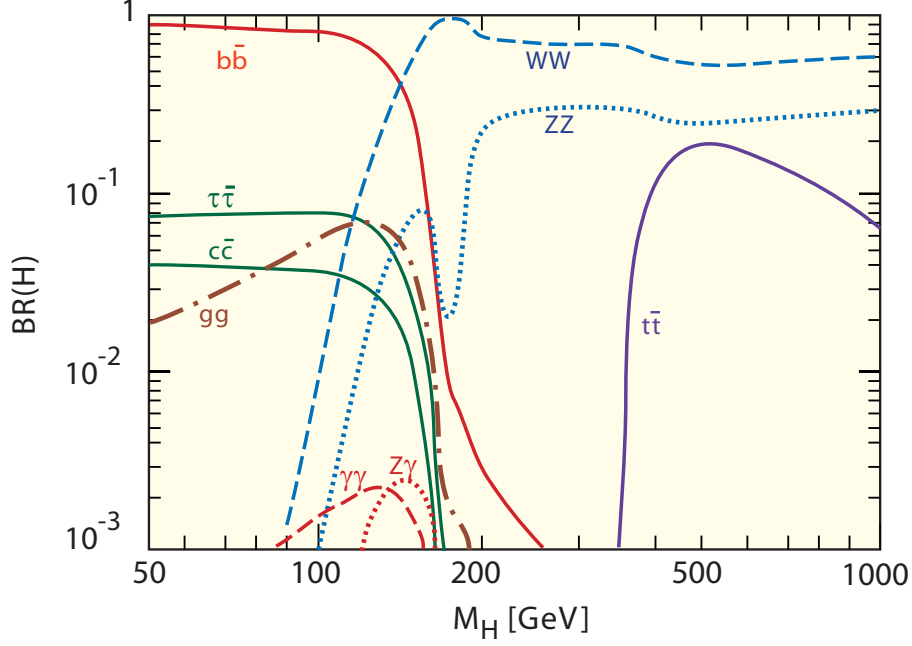


FIGURE 1.5: Branching ratios for the Higgs decay channels in the SM [13].

Despite the low branching ratio, this channel is promising in the discovery due to a good detectable signature and controlled background. For the detection, however an electromagnetic calorimeter with excellent energy resolution and angular resolution is required.

Intermediate Higgs: ($120 \text{ GeV}/c^2 < m_H < 2m_Z$)

$$H \rightarrow ZZ^* \rightarrow l^+l^- l^+l^- \quad (1.4)$$

This channel gives a good signature, however at around $160 \text{ GeV}/c^2$ the channel for the decay of the Higgs in WW opens up and the branching ratios for the decay into ZZ^* almost vanish. Therefore the process:

$$H \rightarrow WW \rightarrow l\nu l\nu \quad (1.5)$$

has also to be used. Precise measurements of the mass peak however are difficult due to the escaping neutrinos. Both channels require a good lepton identification, and the decay into neutrinos requires a good hermeticity for the detection of the missing (transverse) energy.

Heavy Higgs: ($2m_Z < m_H < 700 \text{ GeV}/c^2$)

$$H \rightarrow ZZ \rightarrow l^+l^- l^+l^- \quad (1.6)$$

This is also known as the "gold plated channel" as the four leptons give a clear signature for the detection and the background is low.

Very Heavy Higgs: ($700 \text{ GeV}/c^2 < m_H < 1000 \text{ GeV}/c^2$)

For a very heavy Higgs particle the following channels can also be considered for the detection:

$$H \rightarrow ZZ \rightarrow l^+l^- \nu\bar{\nu} \quad (1.7)$$

$$H \rightarrow WW \rightarrow l\nu \text{ jet jet} \quad (1.8)$$

Efficient reconstruction of jets is mandatory for this discovery channel.

1.2.2 Super Symmetry

The Super SYmmetry (SUSY) theory is addressing shortcomings of the SM in explaining the nature of dark matter (that according to cosmology makes up for most of the matter in our universe), and may allow to incorporate gravity in the model of interactions. SUSY is an extension of the SM, postulating for each fermion a partner boson, and vice versa. Currently no SUSY particles have been discovered, as it is assumed that even the lightest SUSY particle is too heavy to be discovered at current experiments. With the energies available at the LHC machine, however at least the lightest SUSY particles should be discovered.

1.2.3 Heavy Ion Physics

The LHC will not only collide proton beams; about one month per year will be used for heavy ion experiments, colliding beams of heavy nuclei such as Pb. The energy densities reached in these collisions correspond to those of the early universe, less than a microsecond after the big bang. At these high energies protons, neutrons and gluons "melt" forming a Quark-Gluon Plasma (QGP) [13]. The experiment dedicated to these studies is ALICE, that uses a large TPC (in combination with a silicon vertex detector) as central tracking element, to allow for precise track resolution in this very high multiplicity events.

1.2.4 CP violation

One of the open questions arising from cosmology is the unbalanced amount of matter and antimatter in our universe. In cosmological searches no signatures of large amounts of antimatter were detected so far. A partial explanation is the CP violation⁵. CP violation was first discovered in Kaon systems. At the LHC due to the extremely large cross sections for $b - \bar{b}$ production, CP violation is studied in B-mesons decays. The Large Hadron Collider beauty (LHCb) experiment [10] is dedicated to precision measurements of the CP-violation and rare decays of B-Mesons.

1.3 The CMS Experiment

The CMS (Compact Muon Solenoid) [7, 14] is a general purpose detector, suitable for studying all the physics processes generated by the LHC proton proton collisions; in the design of the apparatus particular care has been taken to optimize the Higgs boson discovery potential, by ensuring:

- Good muon identification and momentum resolution over a wide range of momenta
- Good charged particle momentum resolution and high reconstruction efficiency
- Good electromagnetic energy resolution, good diphoton and dielectron mass resolution
- Efficient jet reconstruction
- Good transverse missing energy E_T^{miss} and dijet mass resolution, requiring hadronic calorimeters with a large geometric coverage and good hermeticity.

A general challenge to all subdetectors is the high particle multiplicity: The total cross section at 14 TeV is about 70 mb, leading on average to 23 collisions per bunch crossing⁶: mostly soft interactions, referred to as "minimum bias events", that generate about 3000 particles per

⁵Certain processes are not invariant over an inversion in P and C, where "P" refers to a mirror inversion in space and "C" to the exchange of a particles with their antiparticles.

⁶ $N_c = \mathcal{L} \sigma_{inel} \frac{3564}{2808} \Delta t$, where Δt is the average collision time (25 ns), and the fact that only 2808 out of the 3564 bunches are filled is considered [15].

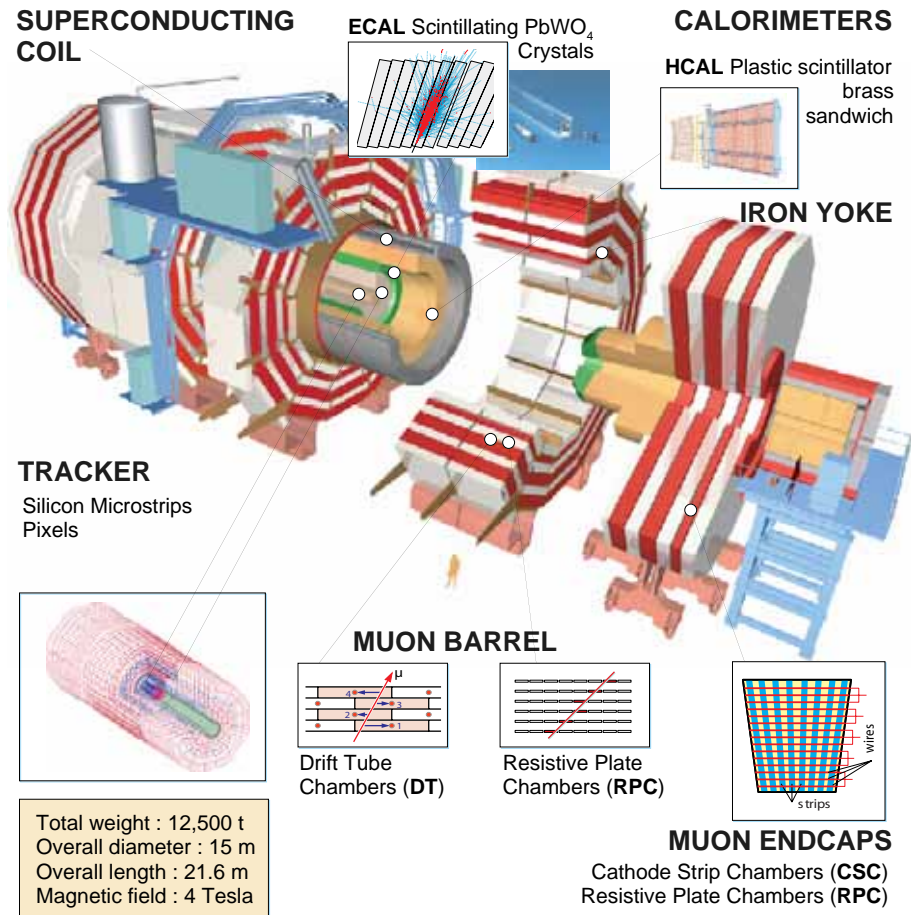


FIGURE 1.6: *The CMS detector and its layout. Close to the interaction point is an all silicon Tracker, that is surrounded by the Electromagnetic Calorimeter (ECAL) and the Hadronic Calorimeter (HCAL). All these systems are contained inside the superconducting solenoid. The detectors of the muon system: Drift Tubes (DT), Resistive Plate Chambers (RPC) and Cathode Strip Chambers (CSC) are embedded in the iron return yoke of the solenoid [17].*

bunchcrossing [16]. Such a crowded environment demands high granularity in all subdetectors, especially those located closer to the interaction point. An efficient trigger system must reduce the accepted rate below 100 kHz (starting from 40 MHz bunch crossing rate) without missing any interesting physics process.

The CMS experiment meets the above requirements. The layout of its subdetectors is illustrated in Figure 1.6. The magnetic field used for momentum measurements of the charged particles is generated by a large superconducting solenoid, and a special characteristic in the CMS design, is that the Tracker, the electromagnetic calorimeter and hadronic calorimeter are fully contained inside the magnet.

The signatures left by the particle species in the CMS detectors are sketched in Figure 1.7.

1.3.1 The Tracking System

The CMS Tracker is an all silicon Tracker with a pixel system populating the inner region surrounded by a silicon strip Tracker. The design and performance of the Tracker is discussed in detail in chapter 3.

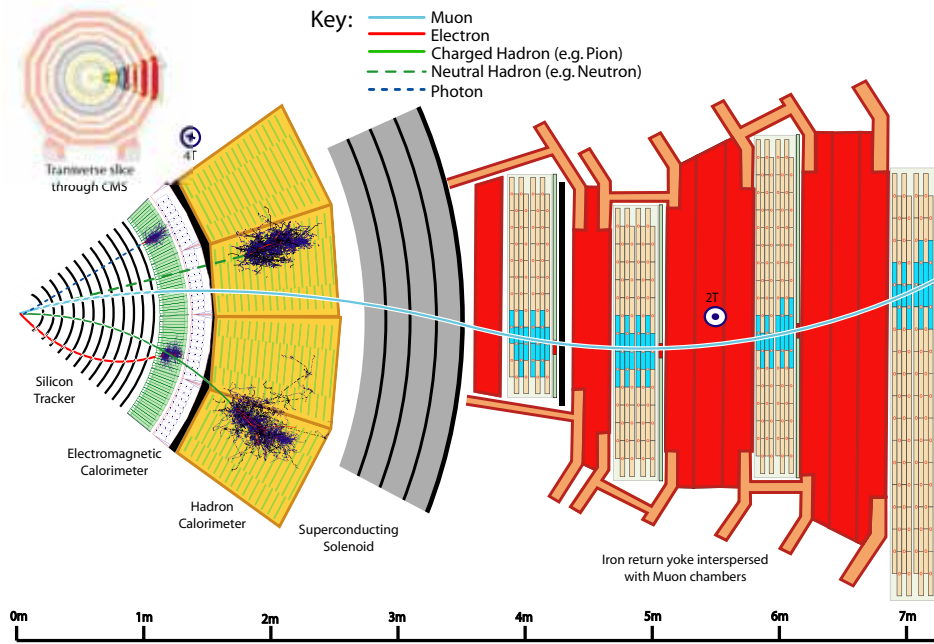


FIGURE 1.7: *Transverse slice through the CMS experiment: detector systems and particle identification [13].*

1.3.2 The Electromagnetic Calorimeter

The Electromagnetic Calorimeter (ECAL) is a homogeneous scintillator calorimeter made of about 80000 lead tungstate ($PbWO_4$) crystals [18]. These crystals feature small radiation length ($X_0 = 0.89\text{ cm}$), small Molière radius ($R_M \approx 2.2\text{ cm}$), fast light collection ($\approx 80\%$ of the light is collected within 25 ns.) and radiation hardness sufficient for the LHC operation with the drawback of only moderate light yield (100 photons/MeV $\approx 0.2\%$ of NaI). The crystals have a size of $2.2\text{ cm} \times 2.2\text{ cm} \times 23\text{ cm}$ in the barrel region and $3\text{ cm} \times 3\text{ cm} \times 22\text{ cm}$ in the forward region, providing despite the compact size a total radiation length of $X/X_0 = 26$ and $X/X_0 = 25$ respectively. The light is detected by Avalanche Photo Diodes (APDs) in the barrel and by more radiation tolerant Vacuum Photo-Triodes (VPT) in the endcaps. The ECAL provides an excellent energy resolution (better than 0.5% at energies larger than 50 GeV); its compact size is of fundamental importance for the design of the CMS as it allows to fit also the hadronic calorimeter inside the solenoid.

1.3.3 The Hadronic Calorimeter

The Hadronic Calorimeter (HCAL) [19] is made of four different sampling calorimeter systems. In the barrel region (HB) 50 mm thick brass layers are used as absorber material interleaved by 4 mm thick plastic scintillators with wavelength shifting plastic fibers. The endcaps (HE) have a similar design with 80 mm thick absorber layers. In the forward region (HF) steel is used as absorber material and quartz fibers emitting light due to Cherenkov radiation as active material. The HB is located inside the solenoid; but due to the limited space it has only an interaction length $\lambda/\lambda_0=6.5$ at $\eta = 0$ ⁷. A scintillator system outside the solenoid, exploiting the solenoid as absorber constitutes the HCAL Outer Barrel (HOB), that brings the total interaction length to $\lambda/\lambda_0=10$.

⁷ η is the pseudo rapidity which is defined as $\eta = -\ln \left[\tan\left(\frac{\Theta}{2}\right) \right]$, where Θ is the angle with respect to the beam axis.

1.3.4 The Magnet

The solenoid used in the CMS experiment is a superconducting magnet, that provides a homogeneous magnetic field of 4 T inside and 2 T outside . With 13 m in length and 5.9 m diameter it is large enough to house the complete Tracker and calorimetry systems. The solenoid uses Niobium Titanium (NbTi) as superconductive material encapsulated by copper and aluminum for mechanical stability. The solenoid has in total 2168 windings with a current I of about 20 kA and is housed inside a vacuum tank cooled at 4 K. With a stored energy of 2.7 GJ, it is the world largest superconducting magnet.

1.3.5 The Muon System

Muons will provide a clean signature of most of the physics processes the LHC is designed to explore. Fast muon identification and precise measurements of the transverse momentum are thus essential for the LHC experiments [13, 20]. In CMS the detectors of the muon system are embedded in a sandwich like layout in the iron return yoke of the solenoid. The yoke is thus also used as an absorber, stopping potentially high energetic particles, that were not absorbed by the hadronic calorimeter.

Three different types of gas detectors are used for the muon detection. Resistive Plate Chambers (RPC) are used in the barrel and the forward region for the trigger system. Precision measurements are obtained by the Drift Tubes (DT) in the barrel region and the Cathode Strip Chambers (CSC) in the forward region. In total the muon system has 195000 DT channels, 210816 CSC channels and 162282 RPC channels.

1.3.6 TOTEM

TOTEM is an independent experiment for the measurement of the total, elastic and diffractive cross section of p-p interactions. The detector will be installed in the forward region of both sides of CMS, and will add charged particle tracking and trigger capabilities to the CMS detector over a rapidity interval $3.1 < |\eta| < 6.8$ [11].

Chapter 2

Silicon Strip Detectors

Silicon detectors are widely used for the detection of ionizing radiation in medical applications and physics experiments. The operation principle of these detectors is similar to ionization chambers: Traversing charged particles (and photons) generate electron-hole pairs. The electron-hole pairs are separated in an electric field and are collected by the readout electrodes. The collected charge corresponds to the energy loss in the detector. In comparison with gas detectors, semiconductors offer several advantages. The mean energy to create an electron-hole pair is an order of magnitude lower thus good sensitivity with relatively low interaction length can be achieved. Furthermore the energy loss per unit distance in semiconductors is approximately three orders of magnitude higher thus requiring only thin layers of detector material. This results in combination with the high mobility of the charge carriers in a fast charge collection. In the CMS Tracker silicon pixel and strip sensors are employed for the track reconstruction of charged particles. These sensors have finely segmented readout electrodes providing a two or three dimensional position measurement of the traversing particles. In the following a brief overview of semiconductor radiation detectors is given, the signal formation in silicon strip sensors presented and phenomena of radiation damage introduced. This overview is based on the sources [21–24].

2.1 Interaction with Matter and Charge Generation

Radiation and charged particles are detected by their interaction with matter. Photons interact with the electrons (photoelectric effect, Compton scattering and pair-production¹) and with the nuclei (pair-production) of the detector atoms. Cross sections for the processes are shown in Figure. 2.1. In interactions due to the photoelectric effect the incident photon is completely absorbed freeing a bound electron. The cross section for the photoelectric effect is large at low energies. Silicon sensors are thus sensitive to visible and infrared light. At higher energies the cross section for the photoelectric effect decreases and Compton scattering is dominant - a process where a photon is transferring part of its energy to free or bound electrons. At energies above $\approx 10MeV$ pair production in the near field of the nucleus is the dominant interaction. In general the cross sections of Compton scattering and pair production are small and will not be detected by silicon sensors with a typical thickness of a few $100 \mu m$. Common to photon

¹In general the pair production in the field of the electron hull ($\kappa_e \propto Z$) can be neglected with those in the field of the nucleus ($\kappa_{nuc} \propto Z^2$).

interaction is that the intensity of the incident radiation is exponentially attenuated:

$$I = I_0 \exp^{-\nu x} \quad (2.1)$$

here ν is the inverse of the mean interaction length due to all processes:

$$\nu = \nu_{phot} + \nu_{compton} + \nu_{pair} \quad (2.2)$$

$$\nu = \frac{\sigma N_A \rho}{A} \quad (2.3)$$

where

σ ... Cross section

N_A ... Avogadro number

A ... Molecular weight

ρ ... Density of target medium

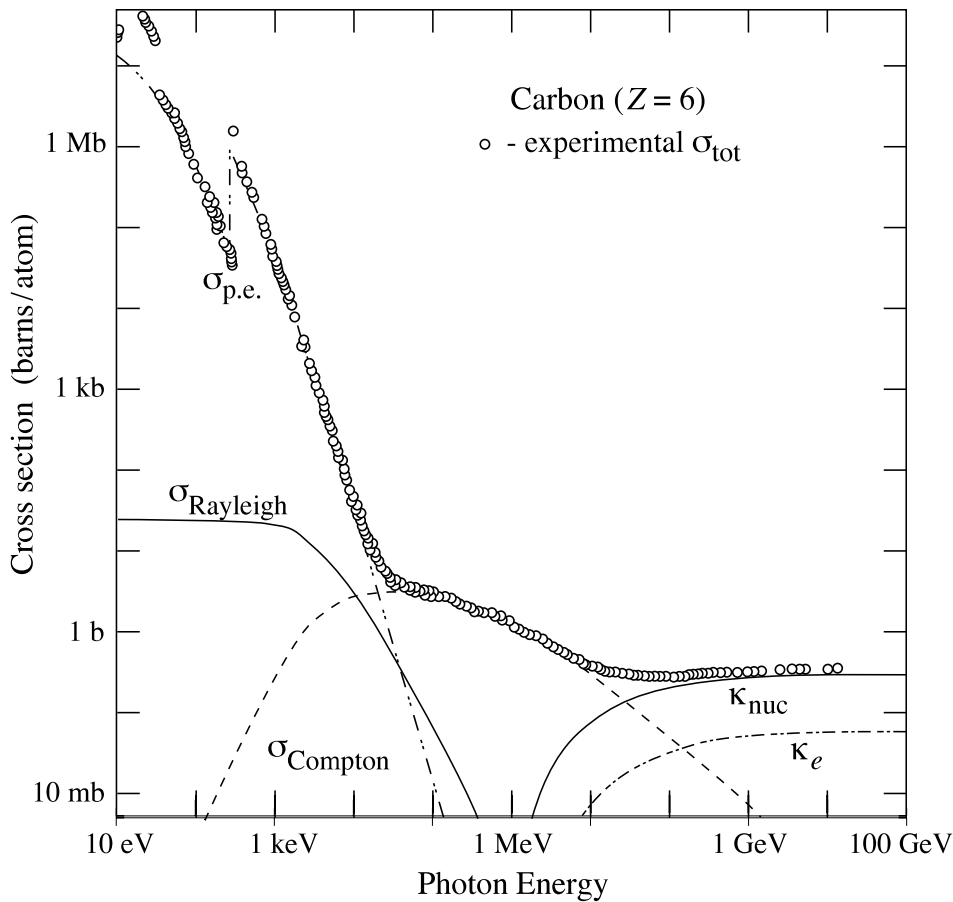


FIGURE 2.1: Total cross section for photon interactions: $\sigma_{p.e.}$... Photoelectric Effect, $\sigma_{Rayleigh}$... Rayleigh Scattering, $\sigma_{Compton}$... Compton Scattering, κ_{nuc} ... Pair Production in the field of the nucleus, κ_e ... Pair Production in the field of the electron hull.

Charged particles interact with matter via Bremsstrahlung, ionization and excitation. The cross sections depend on the particles energy and mass. Bremsstrahlung is the dominant process for electrons (with energies above 10 MeV), whereas heavier particles primarily interact via ionization and excitation. As an example for charged particle interaction, the mean energy loss of muons in copper is shown in Figure 2.2.

In a wide energy range the energy loss is described well by the Bethe-Bloch Formula² eqn.2.4.

²It is valid for all charged particles except electrons and positrons as it does not include energy loss due to Bremsstrahlung.

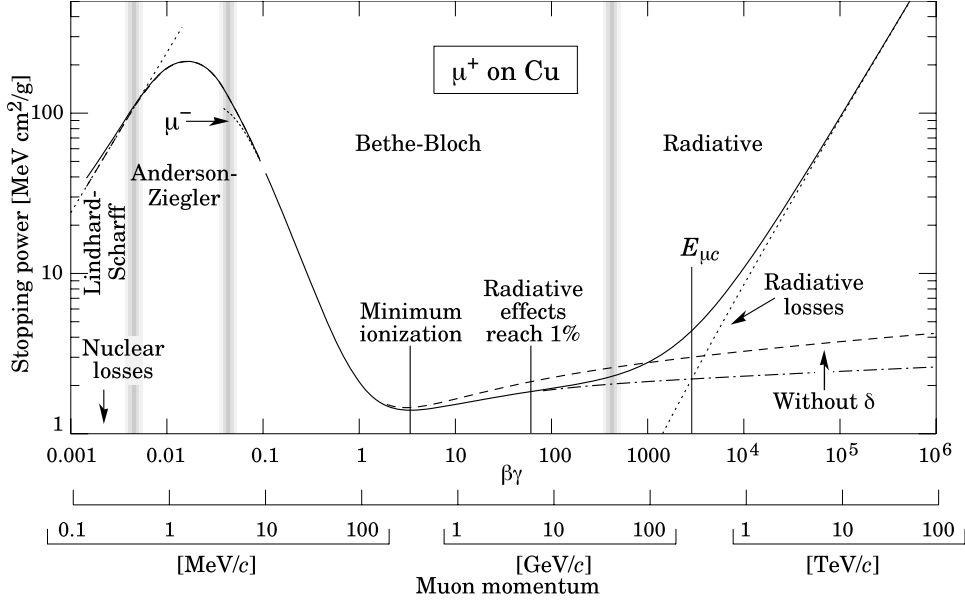


FIGURE 2.2: Stopping power ($\langle -1/\rho dE/dx \rangle$) of muons in copper.

The Bethe-Bloch formula gives the mean relative energy loss of charged particles due to excitation and ionization:

$$\frac{1}{\rho} \frac{dE}{dx} = -2\pi N_A r_e^2 m_e c^2 \frac{Z}{A} \frac{z^2}{\beta^2} \left[\ln\left(\frac{2m_e c^2 \gamma^2 \beta^2 W_{max}}{I^2}\right) - 2\beta^2 \delta - 2\frac{C}{Z} \right] \quad (2.4)$$

where

dE/dx ... Mean energy loss per unit path length [MeV/cm]

ρ ... Density of target medium

N_A ... Avogadro number

m_e ... Electron mass

r_e ... Classical electron radius ($r_e = e^2 / (4\pi\epsilon_0 m_e c^2) = 2.82 \cdot 10^{-13}$ cm)

$2\pi N_A r_e^2 m_e c^2$... 0.1535 MeV cm²/g

A, Z ... Nucleon number and atomic number of target medium

z ... Charge of the incident particle (projectile)

$\beta = v/c$ and $\gamma = 1/\sqrt{1 - \beta^2}$

I ... Mean ionization potential of target atoms

($I \approx 12 \cdot Z + 7$ eV $\forall (Z < 13)$; $I \approx 9.76 \cdot Z + 58.8 \cdot Z^{-0.19}$ eV $\forall (Z \geq 13)$)

W_{max} ... Maximum energy transfer in a single collision ($W_{max} \approx 2m_e c^2 \beta^2 \gamma^2$)

δ ... Density correction (polarisation of target medium screens electrical field of the projectile)

C ... Hull correction (at small projectile velocities only electrons in outer shells are excited)

For most media the minimum energy loss is for incident particles with $\beta\gamma \approx 2$. A particle with the corresponding momentum is referred to as MIP (Minimum Ionizing Particle). For higher energies the energy loss increases approximately logarithmically with $\beta^2 \gamma^2$ and for lower energies $\propto \frac{1}{\beta^2}$. The charge generated in the detector medium is the ratio of the lost energy along its path and the mean energy to generate an electron-hole pair I_0 ³ (1 is the path length):

$$N_{e^-, h^+ \text{ pairs}} = \frac{1}{I_0} \int_0^l \frac{dE}{dx} dx \quad (2.5)$$

³The mean energy necessary for generating an electron-hole pair is higher than the band gap, as momentum conservation leads to an excitation of phonons, requiring additional energy.

To relate the number of charges generated by ionization to thermally generated ones, basic properties of semiconductors are introduced in the following section.

2.2 Properties of Intrinsic Semiconductors

Most semiconductors crystals - such as silicon, germanium and diamond - have a diamond like (tetrahedral) lattice⁴. Each atom forms covalent bounds to its four nearest neighbors. In the energy band model the valence band is separated by a small gap from the conduction band. At low temperature the valence band is fully filled and the conduction band is empty. With increasing temperature electrons have a non vanishing probability to occupy the conduction band due to thermal vibration. The probability for an electron to occupy a state with the energy level E is function of the Fermi energy E_F and the temperature T described by the Fermi-Dirac statistic:

$$F(E) = \frac{1}{1 + e^{\frac{E-E_F}{kT}}} \quad (2.6)$$

The density of states $N(E_{kin})$ for fermions in a unit volume as a function of the kinetic energy E_{kin} is given by:

$$N(E_{kin}) dE_{kin} = 4\pi \left(\frac{2m}{h^2}\right)^{3/2} E_{kin}^{1/2} dE_{kin} \quad (2.7)$$

To calculate the concentration of electrons in the conduction band n , one has to integrate the density of states $N(E)$ over the occupation probability $F(E)$ and obtains:

$$n = \int_{E_C}^{\infty} N(E) \cdot F(E) dE = 2 \left(\frac{2\pi m_n kT}{h^2}\right)^{3/2} e^{-\frac{E_C-E_F}{kT}} = N_C e^{-\frac{E_C-E_F}{kT}} \quad (2.8)$$

where E_C is the energy and N_C is the effective density of states in the conduction band, m_n the effective mass of the electrons and $E_{kin} = E - E_C$. Unoccupied states in the conduction band are referred to as holes. For the density of holes p it follows similarly:

$$p = 2 \left(\frac{2\pi m_p kT}{h^2}\right)^{3/2} e^{-\frac{E_F-E_V}{kT}} = N_V e^{-\frac{E_F-E_V}{kT}} \quad (2.9)$$

where N_V is the effective density of states in the valence band and m_p the effective mass of the holes. For an intrinsic semiconductor the numbers of impurities are small compared to the number of thermally generated electron-hole pairs, and the number of holes and electrons is thus equal $p = n = n_i$ and can be written as:

$$n_i = \sqrt{np} = \sqrt{N_C N_V} e^{-\frac{E_C-E_V}{2kT}} = \sqrt{N_C N_V} e^{-\frac{E_G}{2kT}} \propto T^{\frac{3}{2}} e^{-\frac{E_G}{2kT}} \quad (2.10)$$

where E_G is the band gap. To operate a semiconductor as a radiation detector, the number of thermally generated electron-hole pairs must be small compared to the ones generated by ionization.

Following the example of [23] a signal to background estimation for pure (intrinsic) silicon is outlined. According to [25] the effective masses of the electrons and holes are $m_n = 1.18 m_e$ and $m_p = 0.81 m_e$, respectively at 300 K. Using eqn.2.10, the intrinsic density of thermally generated charge carriers n_i can be calculated yielding $\approx 10^{10} cm^{-3}$. For a typical strip detector with a pitch of 100 μm , 10 cm long strips and a thickness $d = 300 \mu m$ -the number of thermally generated electrons for a single strip at $T = 300 K$ equals:

$$N_{e^-,h^+therm} = n_i d A = 10^{10} cm^{-3} \cdot 0.03 cm \cdot 0.1 cm^2 = 3 \cdot 10^7 e^-, h^+ pairs \quad (2.11)$$

⁴Non elementary semiconductor such as GaAs have zinc-blende lattice.

In the same sensor a traversing MIP lose about 3.87 MeV/cm, generating according to eqn.2.5 ($I_0=3.66$ eV):

$$N_{e^-,h^+ \text{ pairs}} = \frac{3.87 \cdot 10^6 \text{ eV/cm} \cdot 0.03 \text{ cm}}{3.66 \text{ eV}} \approx 3.2 \cdot 10^4 \text{ } e^-, h^+ \text{ pairs} \quad (2.12)$$

The number of thermally generated electron-hole pairs thus exceeds the number of those generated by ionization by three orders of magnitude. Not only the resulting dark current, also the recombination of charge carriers created by ionization with the thermally generated ones prevents the use of pure silicon detectors at room temperature. Besides silicon, germanium and diamond are used in radiation detectors. Due to their large band gap of $E_G \approx 5.48$ eV diamonds are insulators at room temperature and thus can be used in pure form without cooling. In practical applications germanium detectors are operated in cold (77 K), whereas silicon sensors are generally not used in intrinsic form but as doped material forming a pn-junction.

2.3 PN-Junction Semiconductor Detectors

To minimize recombination and thus achieve a good charge collection efficiency silicon sensors are realised as a *pn-junction* that is reverse biased. As illustrated in Figure 2.3, a pn junction is a composite of two extrinsic semiconductors: p-type and n-type silicon. In p-type silicon a tiny fraction of the silicon atoms in the lattice has been replaced by elements with three valence electrons such as boron. The so called *Acceptor* creates an (initially empty) energy level slightly above the valence band, that is occupied at room temperature and thus leaves an electron vacancy (a hole) in the silicon that is freely mobile. In n-type silicon an element with five valence electrons (such as phosphor) is implanted in the silicon crystal. The additional electron introduced in the silicon crystal by the *Donor* is loosely bound resulting in an energy level slightly below the conduction band. At room temperature the n-type silicon thus has electrons as majority charge carriers and the p-type has holes.

If p-type and n-type silicon are brought into contact, thermal diffusion drives the majority charge carriers into the minority region. Due to the movement of the electrons and holes a space charge is build up that stops the diffusion process. The formula for the current density $\vec{j}(\vec{r})$ is given as:

$$\vec{j}(\vec{r}) = q \left(\mu \vec{E}(\vec{r}) N(\vec{r}) - D \vec{\nabla} N(\vec{r}) \right) \quad (2.13)$$

here \vec{E} is the electric field, q the charge, and $N(\vec{r})$ the carrier concentration. D is the the diffusion coefficient and depends on the temperature T and μ the mobility, and the charge of the charge carrier:

$$D = \frac{kT}{q} \mu \quad (2.14)$$

In equilibrium the current due to the drift in the electric field is counter balanced by thermal diffusion, and no net current is flowing ($\vec{j}(\vec{r}) = 0$). The voltage V_0 built up due to the diffusion process is:

$$V_0 = \frac{kT}{e} \ln\left(\frac{N_a N_d}{n_i^2}\right) \quad (2.15)$$

where N_a , N_d are the concentrations of the acceptors and donors.

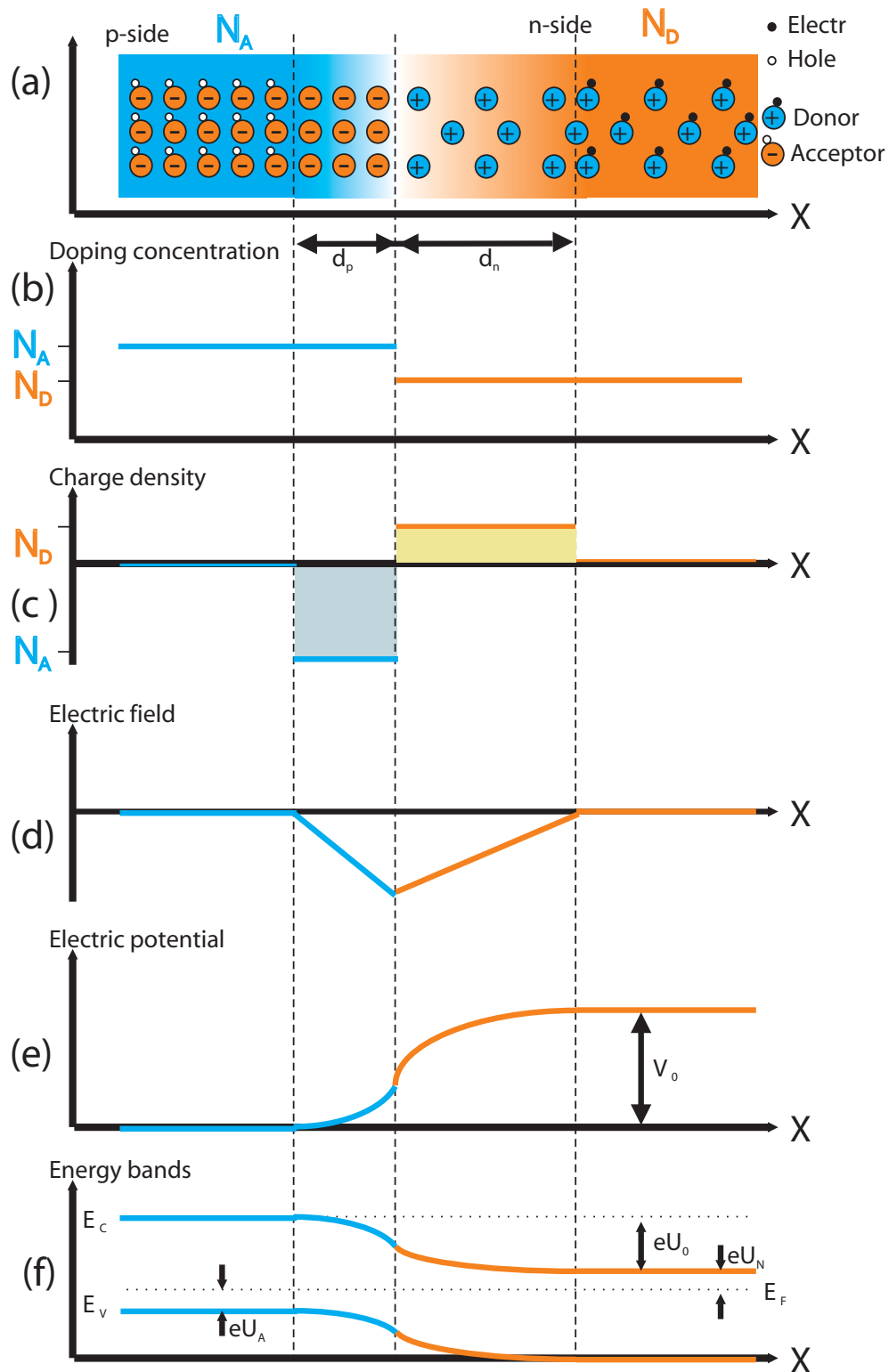


FIGURE 2.3: Abrupt pn-junction [26]: (a) Donor and acceptor distribution with their charge states. The doping concentrations are illustrated in (b) and the resulting charge distribution in (c), which has due to conservation of charge two areas of the same size. The resulting electric field (d), the electric potential (e) and the energy band structure (f) are shown.

2.3.1 Depletion Layer

Charge collection is only efficient in the region where there are no free charge carriers. This region is called the *depletion layer*. The depth of the depleted region W is a function of the potential difference V and the dopant concentrations N_a , N_d :

$$W = \sqrt{\frac{2\epsilon_0\epsilon_r V}{e} \frac{N_a + N_d}{N_a N_d}} \quad (2.16)$$

The depletion layer due to the built in voltage ($V = V_0$) extends for common dopant concentrations only to a small region ($O(10 \mu m)$). In silicon sensors the depleted region is enlarged by applying a reverse bias voltage. The voltage required for depleting an entire thickness d is the *full depletion voltage* V_{FD} :

$$V_{FD} = \frac{e}{2\epsilon_0\epsilon_r} d^2 \left(\frac{N_a N_d}{N_a + N_d} \right) \quad (2.17)$$

Usually the doping is strongly asymmetric and the depletion layer extends - due to charge conservation ($x_a N_a = x_d N_d$) - predominately into the low doped region. The concentration of the lower dopant becomes the effective doping concentration N_{eff} and eqn.2.17 can be approximated as:

$$V_{FD} \approx \frac{e}{2\epsilon_0\epsilon_r} d^2 N_{eff} \quad (2.18)$$

$$V_{FD} \approx \frac{e}{2\epsilon_0\epsilon_r} \frac{1}{\mu e} d^2 \frac{1}{\rho_{eff}} \quad (2.19)$$

Where the resistivity ρ is given by:

$$\rho = \frac{1}{\mu e N} \quad (2.20)$$

The full depletion voltage increases quadratically with the detector thickness and linear with the effective doping concentration N_{eff} (or the inverse of the resistivity). In order to keep the full depletion voltage low, the bulk material of silicon sensors is usually only lightly doped.

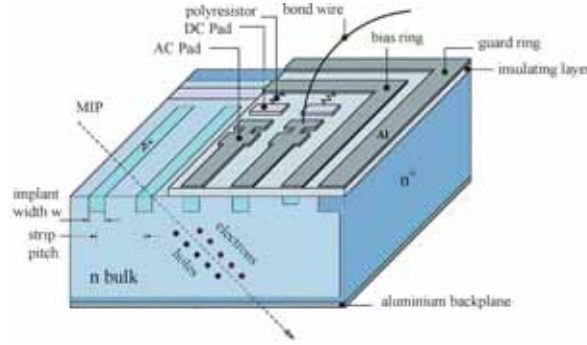
2.4 Silicon Strip Sensor Design

The basic design of a CMS strip sensor is illustrated in Figure 2.4. On a n-type bulk, strips of heavily doped p-type silicon are implanted. The distance between the strips - referred to as the pitch - determines the position resolution. More details on the position resolution shall be given in the chapter 8. The strips are insulated from the capacitively coupled readout electrodes by a thin SiO_2 layer. Metalizations on sensors are usually made of aluminium. Aluminium offers the advantage of a low resistivity, it has a good (mechanical) contact with Si and SiO_2 and allows for photo lithographic processing. For a good ohmic contact the bulk is connected via a strongly doped n-type layer to the backplane electrode.

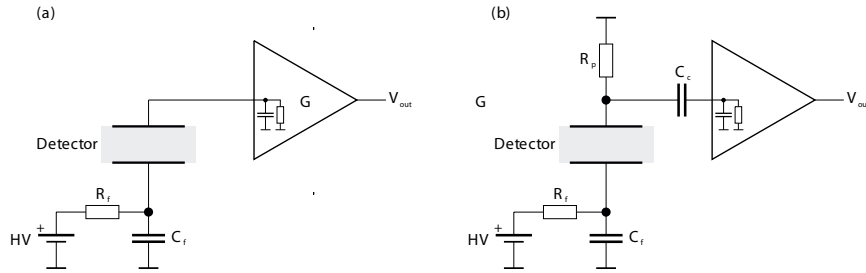
2.5 Readout and Mechanism of the Charge Collection

The measured quantity in a silicon strip sensor is the charge of the generated electron-hole pairs amplified electronically by a charge sensitive amplifier. In general each strip has its own amplifier⁵. As illustrated in Figure 2.5 the readout of a strip can be achieved by either coupling

⁵This is true for DC coupled detectors. AC coupling allows for interleaved strips. Due to capacitive coupling of neighboring strips the position resolution is not affected, as charge is divided position dependent.

FIGURE 2.4: *Silicon strip sensor layout [27].*

the strips directly to the amplifier (DC coupling) or via a capacitance (AC coupling). In case of the DC coupling all the leakage current collected by the strip flows to the amplifier. The leakage current changes with irradiation and bias voltage. Especially with irradiation the leakage current can become large with respect to the signal making the amplifier design difficult. In the AC coupling configuration the leakage current is blocked from the amplifier, thus AC coupling is the preferred choice.

FIGURE 2.5: *DC coupled readout (a); AC coupled readout (b); In both cases, the backplane bias voltage is filtered by an RC network [28].*

Regardless of the method of coupling, signal is induced on the readout strips as soon as the generated electron-hole pairs are separated in the electric field - and not, as one might naively assume, when charges are collected by the strips. The details of these processes are discussed in the following, as they will be the basis for the studies of the detector response, which are presented in chapter 8.

2.5.1 Mechanism of Charge Collection

The charge induced on a given electrode can be calculated with the help of the Shockley Ramo Theorem [29, 30]. An outline of the theorem is given following [31].

The problem of charge collection in strip sensors can be modeled as an ensemble of n grounded conductors and a point charge q_m , that induces charge on the electrodes. In this configuration the potential of the conductors is zero, ($V_i = 0$) and they have the induced charges q_i . To calculate the charge induced on conductor A, one can think of a second scenario where the charge q_m is removed and the potential of conductor A is raised to unit potential, whereas all other conductors remain grounded. The resulting potential is called *Weighting Potential* (for the electrode A). In this scenario the charges shall be denoted as \acute{q}_i where $\acute{q}_m = 0$. The potentials at the electrodes \acute{V}_i are 0 except $\acute{V}_A = 1$. The resulting potential at the location of the point charge q_m is \acute{V}_m .

The relation between the charges and the potentials in the two scenarios is given by Green's second identity:

$$\int V \Delta \dot{V} dv - \int \dot{V} \Delta V dv = \oint V \vec{\nabla} \dot{V} d\vec{n} - \oint \dot{V} \vec{\nabla} V d\vec{n} \quad (2.21)$$

where V and \dot{V} are describing electrical potentials:

$$\Delta V(r) = -\rho(r) \quad (2.22)$$

$$\Delta \dot{V}(r) = -\dot{\rho}(r) \quad (2.23)$$

and ρ is the charge density. If the boundaries are electrodes, or equipotential spheres around point charges, it follows from Gauss's law:

$$\oint_{S_i} V \vec{\nabla} \dot{V} d\vec{n} = -V_i \dot{q}_i \quad (2.24)$$

Using the above identity, applying eqn.2.21 and considering an ensemble where there are only electrodes in vacuum and no further charges in between, the left side of eqn.2.21 vanishes as ΔV respectively $\Delta \dot{V}$ is 0 and one yields.

$$\sum \dot{V}_i q_i = \sum V_i \dot{q}_i \quad (2.25)$$

Applying the above equation to the two scenarios it follows:

$$0 = 1 \cdot q_A + \dot{V}_m q_m \quad (2.26)$$

Renaming the Weighting field \dot{V}_m to $\Phi_w(\vec{r})$ and q_A to Q one gets the identity:

$$Q = -\Phi_w(\vec{r}) q_m(\vec{r}) \quad (2.27)$$

The induced charge on a given electrode can thus be computed if the Weighting potential (for the given electrode) is known at the location of the point charge. This method has been derived for electrodes in vacuum, it can however be shown [32] that it is also valid if the electrodes are embedded in a medium with fixed charges - an generalization of Shockleys theorem for media with moving charges is to be found in [33]. One should however notice that for the calculation of the Weighting potential only the geometry of the electrodes has to be considered (the media between them must not be taken into account). The Weighting potential is in general different from the electrical field in which the electrons are drifting.

For a parallel plate capacitor with the electrodes separated by d the Weighting potential equals:

$$\Phi_w = \frac{x}{d} \quad (2.28)$$

This is also a good approximation for the Weighting potential of thin silicon strip sensors with a large pitch. To check the validity of this approximation for the sensors used in the CMS Tracker the Weighting potential for "OB2" sensors (see Table 3.1) has been numerically solved using a program for electrostatic finite element analysis "Maxwell" [34]. For the calculation the problem has been modeled only in two dimensions disregarding effects at the ends of the strips. In this model the sensor geometry is described as a 500 μm thick silicon bulk with a back plane electrode and the readout electrodes of the strips⁶, that have a pitch of 183 μm and are 50 μm wide. The resulting Weighting field distribution is shown in Figure 2.6. In Figure 2.7

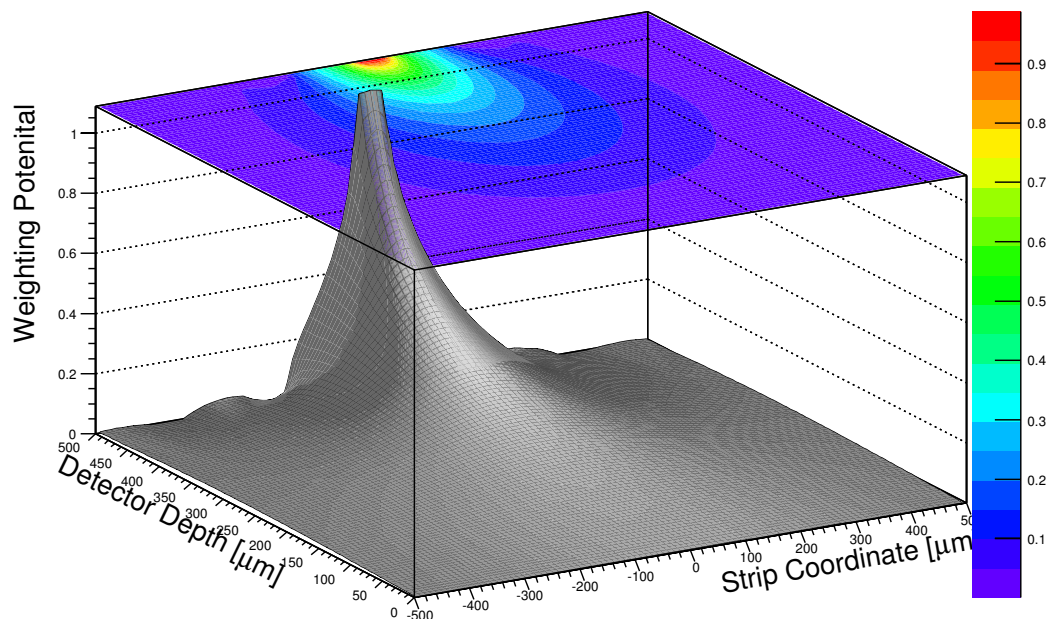


FIGURE 2.6: Weighting potential for 500 μm thick sensors with a pitch of 183 μm and a strip width of 50 μm .

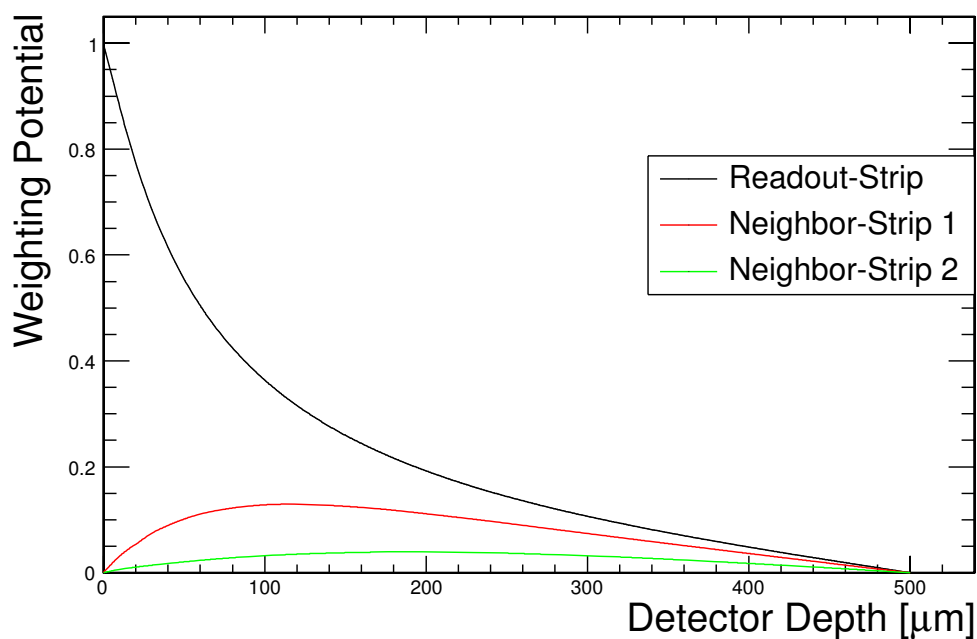


FIGURE 2.7: Cuts through the Weighting Potential. Potentials shown for charges drifting normal to the detector plane for the collecting strip and for its 1st and 2nd neighboring strip.

cuts through the Weighting potential are shown for charge carriers drifting perpendicular to the detector plane for the collecting strip, the first and second neighboring strip.

One sees from these plots that the calculated Weighting potential falls off faster from the readout electrode than the approximation for a parallel plate configuration. In general one will find that the smaller the pitch is, the bigger is the discrepancy between the parallel plate estimation and the real Weighting potential. It is interesting to notice that the neighboring strips will see a current while charge is drifting in the detector, as the Weighting potential may be small but is non-zero. The net signal induced (total charge) for neighboring electrodes will however integrate to zero (provided that the charge carriers are collected by an other electrode - i.e. that they are not trapped).

2.5.2 Time Evolution of Induced Currents

According to eqn.2.27, if a charge q_m is moving from \vec{r}_1 to \vec{r}_2 the charge induced on the readout electrodes will change by:

$$\Delta Q = -q_m(\Phi_w(\vec{r}_2) - \Phi_w(\vec{r}_1)) \quad (2.29)$$

In the detector charges are moving under the influence of the electric field $\vec{E}(\vec{r})$. Their velocity is a function of their mobility μ and the saturation velocity v_s :

$$\frac{d\vec{r}}{dt} = \frac{\mu\vec{E}(\vec{r})}{1 + \mu\vec{E}(\vec{r})/v_s} \quad (2.30)$$

For silicon v_s is in the order of $\approx 10^7 \text{ cm/s}$ thus for low field strength $\frac{d\vec{r}}{dt} = \mu\vec{E}(\vec{r})$ is a good approximation. The induced current on a given electrode can thus be written as:

$$i = \frac{dQ}{dt} = -q_m(\vec{r})\vec{\nabla}\Phi_w(\vec{r})\frac{d\vec{r}}{dt} \quad (2.31)$$

$$i = q_m(\vec{r})\vec{\xi}_w(\vec{r})\mu\vec{E}(\vec{r}) \quad (2.32)$$

Where $\vec{\xi}_w(\vec{r}) = -\vec{\nabla}\Phi_w(\vec{r})$ is the *Weighting field*. Eqn.2.32 is the differential form of the Ramo Shockley theorem. It will be used in the following to derive the time evolution of the induced current for the one dimensional case following [35].

The total induced current is due to the movement of both: electrons and holes. The drift of the electrons in the electric field $E(x)$ cause a current to flow in the depleted region of the sensor with the current density $j_e(x, t)$:

$$j_e(x, t) = -v_e n(x, t) = \mu_e E(x) n(x, t) \quad (2.33)$$

where $n(x, t)dx$ denotes the number of free (radiation generated) electrons in the layer $x, x + dx$.

The electrical field in which the charge carriers are drifting is a superposition of the internal field due to the space charges in the depletion layer and the applied bias voltage V :

$$E(x) = E_0 - \frac{\rho}{\epsilon_0\epsilon_r}x \quad (2.34)$$

⁶Notice that also the holes are collected by the p^+ strips, the Weighting potential has to be calculated for the aluminum strips, as Ramo's theorem is only valid for electrodes that are connected with negligible resistance to a certain potential. The p^+ strips are thus not to be considered as electrodes as they are connected with a relatively high resistance ($\approx 1M\Omega$) to ground.

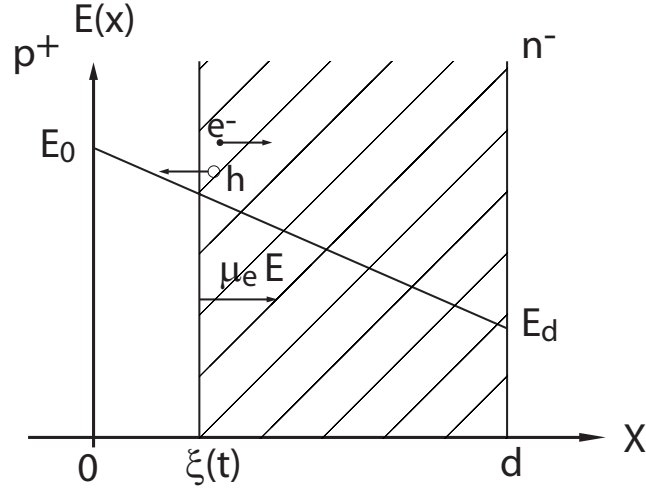


FIGURE 2.8: *Field Distribution in Detector and $\xi(t)$ the border of the drifting electrons.*

where the charge density $\rho = eN_{eff}$ and

$$E_0 = \frac{V + V_{FD}}{d} = \frac{V}{d} + \frac{\rho}{2\epsilon_0\epsilon_r}d \quad (2.35)$$

The moving electrons will induce according to eqn.2.32 a current on the readout electrode:

$$i_{ie}(t) = \mu_e e \int_{-\infty}^{\infty} \xi_w(x) n(x, t) E(x) dx \quad (2.36)$$

As illustrated in Figure 2.8 at the time t all electrons shall be confined in the region $\xi(t) < x < d$. For a Weighting field $\xi_w(x) = 1/d$ one obtains:

$$i_{ie}(t) = \mu_e e \frac{1}{d} \int_{\xi(t)}^d n(x, t) E(x) dx \quad (2.37)$$

The time dependence of the density of drifting electrons:

$$\frac{dn(x, t)}{dt} = \frac{\partial n}{\partial t} + \frac{\partial n}{\partial x} \mu E \quad (2.38)$$

can be calculated using the continuum equation:

$$\frac{\partial n}{\partial t} = \frac{1}{e} \frac{\partial j}{\partial x} \quad (2.39)$$

where j is given by eqn.2.33 and one obtains:

$$\frac{dn(x, t)}{dt} = \mu_e \frac{\partial E}{\partial x} n(x, t) \quad (2.40)$$

With the Poisson equation:

$$\frac{\partial E}{\partial x} = \frac{\rho}{\epsilon_0\epsilon_r} \quad (2.41)$$

one obtains for the density of the electrons for x within d , $\xi(t)$ an exponential increase with time:

$$n(x, t) = n_0(x) e^{\frac{\mu\rho}{\epsilon_0\epsilon_r} t} \quad (2.42)$$

The increase in density is due to the fact that electrons move faster at the border $\xi(t)$ than at the front ($E(\xi(t)) > E(d)$).

Assuming that the charge carriers are initially distributed homogeneously along the particles track ($n(x, 0) = n_0$), the induced current on the electrode connected to the $p+$ due to the moving electrons is given by:

$$i_{ie}(t) = \mu_e e \frac{1}{d} n_0 e^{\frac{\mu\rho}{\epsilon_0\epsilon_r} t} \left[E_0(d - \xi(t)) - \frac{\rho}{2\epsilon_0\epsilon_r} (d^2 - \xi(t)^2) \right] \quad (2.43)$$

The border $\xi(t)$ is moving with the velocity of the electrons located at ξ :

$$\frac{\partial \xi}{\partial t} = \mu_e E(\xi) = \mu_e E_0 \left(1 - \frac{\xi \rho}{\epsilon_0\epsilon_r E_0} \right) \quad (2.44)$$

At the time $t = 0$ $\xi(0) = 0$ thus integrating the above equation one obtains:

$$\xi(t) = E_0 \frac{\epsilon_0\epsilon_r}{\rho} \left(1 - e^{-\frac{\epsilon_0\epsilon_r}{\mu_e\rho} t} \right) \quad (2.45)$$

From this equation the collection time can be derived ($\xi(t_c^e) = d$):

$$t_c^e = \frac{\epsilon_0\epsilon_r}{\mu_e\rho} \ln \left(\frac{\frac{2V\epsilon_0\epsilon_r}{\rho d^2} + 1}{\frac{2V\epsilon_0\epsilon_r}{\rho d^2} - 1} \right) \quad (2.46)$$

Similar to the electrons the current induced by moving holes can be computed:

$$p(t) = p_0 e^{-\frac{\mu_p\rho}{\epsilon_0\epsilon_r} t} \quad (2.47)$$

$$i_{ip}(t) = \mu_p e \frac{1}{d} p_0 e^{-\frac{\mu_p\rho}{\epsilon_0\epsilon_r} t} \left[E_0(d - \xi_p(t)) - \frac{\rho}{2\epsilon_0\epsilon_r} (d^2 - \xi_p(t)^2) \right] \quad (2.48)$$

The border of the holes $\xi_p(t)$ is given by

$$\xi_p(t) = d e^{-\frac{\epsilon_0\epsilon_r}{\mu_p\rho} t} + E_0 \frac{\epsilon_0\epsilon_r}{\rho} \left(1 - e^{-\frac{\epsilon_0\epsilon_r}{\mu_p\rho} t} \right) \quad (2.49)$$

$$t_c^p = \frac{\epsilon_0\epsilon_r}{\mu_p\rho} \ln \left(\frac{\frac{2V\epsilon_0\epsilon_r}{\rho d^2} + 1}{\frac{2V\epsilon_0\epsilon_r}{\rho d^2} - 1} \right) \quad (2.50)$$

As electrons and holes are contributing to the induced current the total current equals:

$$i(t) = i_{ie}(t) + i_{ip}(t) \quad (2.51)$$

The equations presented have been derived assuming that the charge carriers are collected by the electrodes and not trapped in between. In combination with the simulated Weighting potential, the above equations will be used to model the induced current for the simulation of the signal forming in TOB sensors, that is presented in section 8.4.2.

2.6 Radiation Damage

At high radiation doses, silicon sensors suffer from radiation damage. The damage can be due to ionizing radiation mainly affecting the surface, and non ionizing energy loss that is primarily introducing damage in the bulk.

Surface damage is of concern in the insulating silicon oxide layer between the strips and the electrodes, where charge is generated by traversing photons and charged particles. Due to the insulating properties of this layer the charge is captured. In SiO_2 the mobility of electrons is two orders of magnitude higher than that of the holes, thus mainly holes are accumulated. The effect of the trapped positive charge is the accumulation of electrons at the Si/SiO_2 interface between the strips. The accumulated electrons form a conductive layer, which decreases the resistance between the strips and increases the interstrip capacitance. The increase of capacitance causes higher noise and degrades the spatial resolution. Surface damage also affects the readout electronics. Bulk damage is caused by radiation interacting with the sensors nuclei, introducing defects in the the lattice. Bulk damage arises mostly from (non ionizing) energy loss of heavy particles (neutrons, protons and pions) via strong or electromagnetic interaction. The damages in the bulk introduce new energy levels. Depending on the energy level within the band gap they lead to

- Charge trapping
- Change of the effective doping concentration
- Increasing leakage current

Energy levels that are close to the conduction or valence band trap electrons and holes generated from ionization which are then emitted back to the conduction band or valence band in a time that is typically longer than the read-out time of the connected electronics, making charge collection thus inefficient and degrading the signal to noise performance. Lattice defects are not only a function of the flux but also the transferred energy. At low energies the lattice is excited (phonons); at higher energies (≈ 25 eV) an atom can be displaced from its lattice position and moved to a inter lattice position, leaving a *Vacancy* and creating an *Interstitial* (the "Frenkel" defect). The atom involved in the interaction is referred to as the PKA (Primary Knock-On Atom).

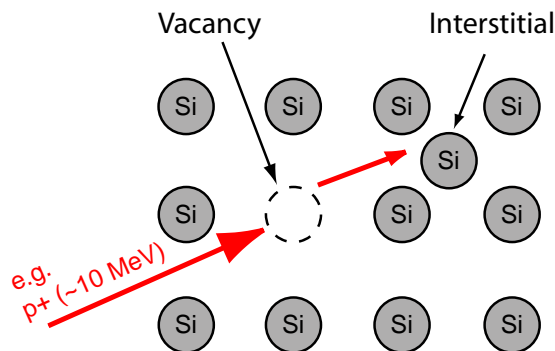


FIGURE 2.9: Creation of an interstitial-vacancy pair (Frenkel defect).

Depending on the energy of the PKA, the displaced atom can cause further damage in its vicinity resulting in cluster defects. Cluster defects are mainly due to interaction with uncharged hadrons reacting thus only via the strong interactions with the nucleus, whereas in interactions with charged hadrons the nucleus is partially screened by the electrons. Frenkel defects are not to be considered as stable defects. At room temperature vacancies and interstitials can move in the lattice and by chance an interstitial can compensate a vacancy or the defects can move

to the border of the crystal. With increasing temperature diffusion and therefore annealing will increase. There is however also a negative effect, *reverse annealing*, where radiation-induced inactive defects become active [36]. In general reverse annealing takes longer to develop than annealing. Therefore the ideal operation of a detector is at cold (to freeze the reverse annealing) interleaved with short periods in warm for the annealing.

Besides the discussed primary (unstable) defects there are also secondary defects where a vacancy or an interstitial is forming a stable complex with another lattice defect [22]: e.g. VP_s a vacancy next to a phosphor atom and VO_i Vacancy and oxygen atom as an interstitial. The first defect is neutralizing the donor level of the phosphor the second is generating an acceptor level.

2.6.1 Type Inversion

Although there are also defects creating donor levels, in general effects changing n-type to p-type material dominate. With accumulated radiation the n-type material will have increasing resistivity and further irradiation will form acceptor levels yielding to a p-type bulk. The thin higher doped n-type layer making the contact with the backplane does not invert and ensures operation as a diode. After type inversion however the detector can be only operated at full depletion, as the p-n junction is formed starting from backplane and holes would recombine in the undepleted region before being collected by the strips.

2.6.2 Thermal Runaway

Radiation induced energy levels in the middle of the band gap, leads to an increase of thermally generated electron-hole pairs. The leakage current in the detector thus increases with the absorbed flux:

$$\Delta I_R = \alpha \Phi \quad (2.52)$$

Where Φ is the particle fluence and $\alpha \approx 2 \cdot 10^{-17} A/cm$. The increased current however is not only increasing the noise, but also heating up the detector and thus in turn will further increase the leakage current. If the temperature increases beyond a critical temperature where the cooling can not maintain a stable temperature this will result in thermal runaway.

2.7 Summary

Basic principles of particle detection in silicon devices have been introduced. Charge collection and signal formation in silicon strip sensors have been discussed in detail. Radiation damage, which will affect both the CMS Tracker sensors and the front-end electronics, has been discussed. The effect of radiation-induced bulk damage (reverse annealing) is reduced at temperatures below 0°C. Furthermore, after accumulating a large hadron fluence, detectors will require low temperature operation also to avoid thermal runaway induced by the leakage current. For this reasons, the CMS Tracker is expected to be operated below -10°C.

Chapter 3

The CMS Tracker

The central part of the CMS detector is its all silicon Tracker. A robust and efficient track reconstruction is vital to the physics program of the CMS experiment. In the LHC, proton bunches are brought to collision at a constant rate of 40 MHz. At nominal luminosity of $10^{34} \text{ cm}^{-2} \text{ s}^{-1}$, on average about 20 single high momentum proton-proton collisions will take place in each bunch crossing, leading to ≈ 1000 charged particle tracks. The physics goals imply that the track of each single particle has to be resolved and the transverse momentum has to be measured with a relative precision of about 2% in the momentum range from 1 GeV/c to 100 GeV/c. The identification of decays of heavy objects such as "B-mesons" and τ leptons require good impact parameter resolution for tagging of secondary vertices. In addition to the requirements for efficient cooling and a mechanically stable support structure, the total material must be kept as low as possible. Both sensors and electronics have to be tolerant to high fluxes of ionizing and non ionizing radiation. To keep costs acceptable and to reduce risks of failure the use of established technologies is favored. The Tracker design is sketched in Figure 3.1. Close to the interaction point a silicon pixel Tracker is used for vertex finding and track seeding, surrounded by the silicon strip Tracker.

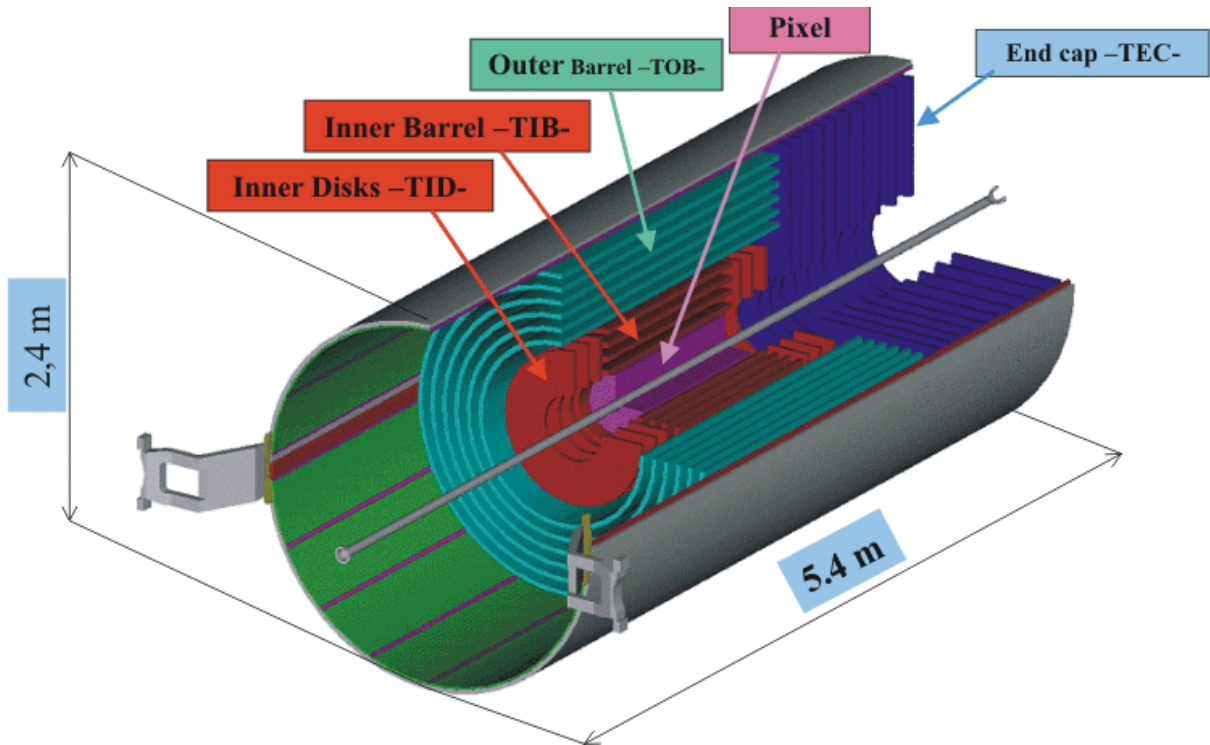


FIGURE 3.1: *Illustration of the subdetectors of the CMS Tracker.*

3.1 The CMS Pixel Detector

The inner region of the CMS Tracker is instrumented by a pixel detector [37]. The pixel detector as illustrated in Figure 3.2 has 3 layers at a radius of 4.4 cm, 7.3 cm and 11 cm from the beam axis and 2 turbine-like disks in the forward region, placed 34.5 cm and 36.5 cm away from the interaction point. The pixel detector is composed of 1440 modules with a total active area of

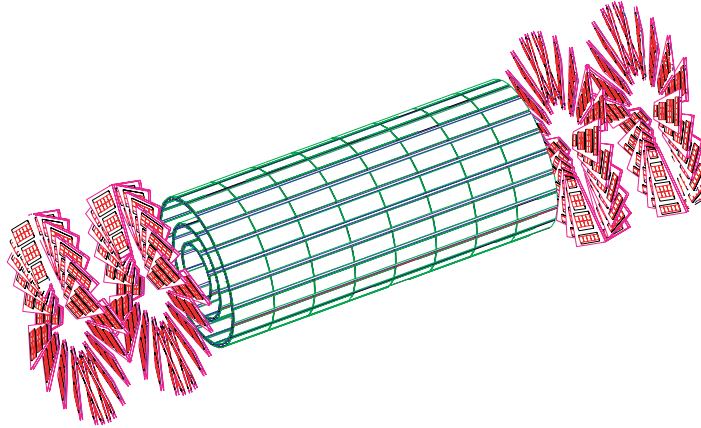


FIGURE 3.2: *The CMS pixel detector [37].*

$\approx 1m^2$. It is segmented into 66 million pixels with a size of $100\ \mu m$ in $(r-\phi)$ direction and $150\ \mu m$ in z direction. Charge sharing due to a Lorentz angle of about 23° yields a resolution of $\approx 10\ \mu m$. The pixel detector provides up to 3 high resolution 3D measurements; the high granularity ensures a low occupancy of $\approx 10^{-4}$ - vital for the track seeding and pattern recognition. As the pixel detector is closest to the interaction point and radiation doses scale roughly with $1/r^2$, it will suffer from the highest doses. To ensure stable operation, special radiation hard techniques have been developed. The sensors have a thickness of (only) $200\ \mu m$. The pixels are implemented in a *n-type on n-type* configuration and the bulk material is made of oxygenated silicon. Despite the resulting high radiation hardness, the pixel will age faster than the strip Tracker.

3.2 The CMS Silicon Strip Tracker

The CMS strip Tracker is surrounding the pixel detector. It is by far the biggest detector of this kind ever built. With a total area of about $206\ m^2$ of silicon it is substantially larger than the Tracker of the GLAST¹ ($74\ m^2$), ATLAS strip Tracker ($61\ m^2$), and more than an order of magnitude larger than the CDFII Tracker ($\approx 7.5\ m^2$) - the largest currently in operation. In Figure 3.3 a slice view shows a quarter of the pixel and strip Tracker.

In the central volume of the silicon strip Tracker [39] rectangular detectors are arranged on cylindrical shells, with the readout strips parallel to the beam axis (the z direction); this region is further split into Tracker Inner Barrel (TIB), made of four layers, and Tracker Outer

¹GLAST is a Gamma Ray Large Area Space Telescope, which contains a large silicon vertex detector [38].

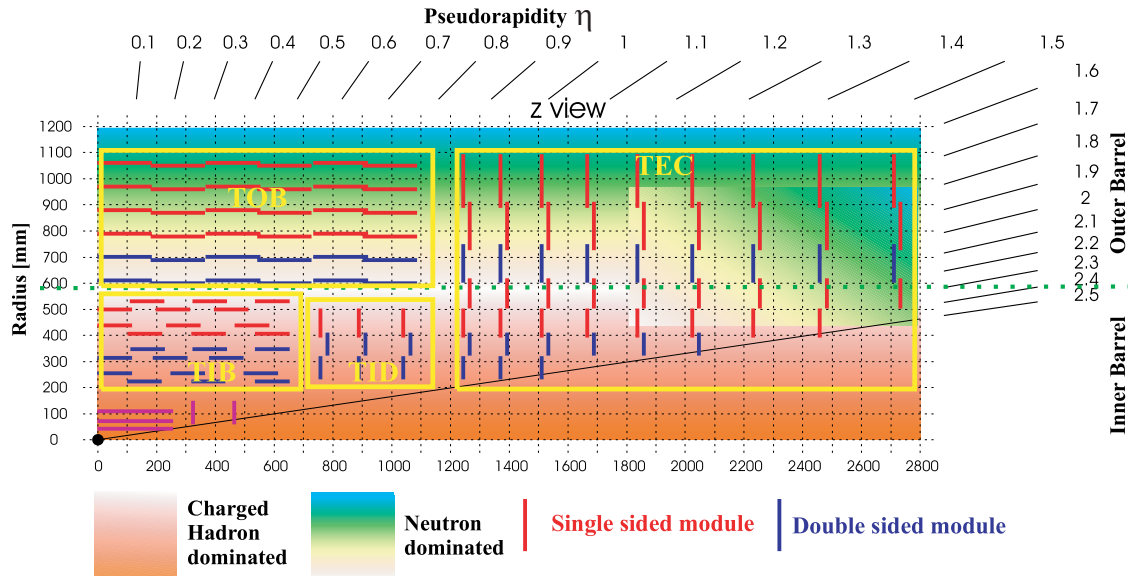


FIGURE 3.3: Cut through the CMS silicon strip Tracker (only a quarter is shown). The arrangement of the subdetectors TIB, TOB TID and TEC is shown. Modules in the inner layers of the Tracker provide measurements in the $r - \phi$ and z coordinates (blue color), detectors with $r - \phi$ measurements only are shown in red. In addition the dominant type of radiation is shown. The inner layers will experience radiation due to charged hadrons from the primary collisions, while the outer barrel will be dominated by neutrons scattered back from the ECAL [26].

Barrel (TOB), made of six layers. In the forward regions wedge-shaped detectors with radial readout strips are mounted on supporting disks. The sub detectors in the forward region are the TID (Tracker Inner Disks) made of 3 small disks, and the TEC (Tracker End Caps) made of 9 large disks. The orientation of the strips is chosen to optimize the precision of the transverse momentum measurement.

The Tracker has a good 4π coverage with 10 to 14 measurement layers in the region² $\eta < 2.4$. The inner 2 layers of the TIB and TOB, the rings 1 and 2 of the TID and 1,2 and 5 of the TEC are equipped with double sided modules. These modules (colored blue in Figure 3.3) are used to provide measurements of a space point, for ensuring a good pattern recognition and good matching between charged particle tracks and energy deposits in the ECAL crystals. They are made of two strip sensors mounted back to back. One sensor has the strips oriented along the beam axis (or radially for the end caps) the other is tilted by 100 mrad to provide an additional measurement along the strips. The sensors of the TIB are tilted by 9° from the tangential plane to compensate for the Lorentz-angle. The TOB does not implement a Lorentz-angle compensation.

3.2.1 Modularity of the Tracker

The CMS strip Tracker has a modular design. The smallest part of the system is a module. In total there are 15148 modules. In each of these modules a silicon strip sensor (two in the outer layers) are mounted on a carbon fiber/graphite support. Sensors and frames are isolated by a Kapton layer housing the leads for applying bias voltage to the sensors. The common front end electronics are soldered onto a multilayer ceramic hybrid. A glass pitch adapter connects the strips of the (first) sensor to the input pads of the readout chips. A TOB module is shown in Figure 3.4

² η is the pseudo rapidity which is defined as $\eta = -\ln \left[\tan\left(\frac{\theta}{2}\right) \right]$

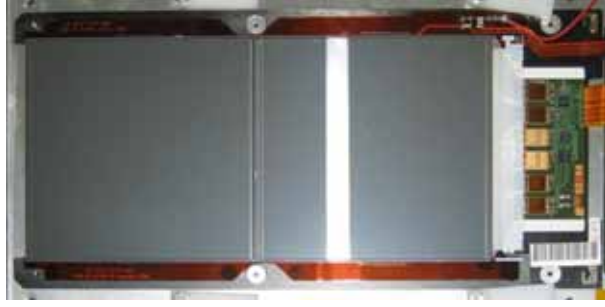


FIGURE 3.4: *TOB SS₄ Module, two OB2 sensors are bonded together and glued on a carbon fiber frame. Front end electronics is soldered onto the hybrid, connected by the pitch adapter to the readout strips; bias voltage is applied via a Kapton circuit.*

In case of the TIB and TID modules are directly mounted onto large carbon fiber support structures: - half-shells and disks respectively, as shown in Figure 3.5. A TIB layer is split in four half-shells along the $z=0$ and $y=0$ planes.

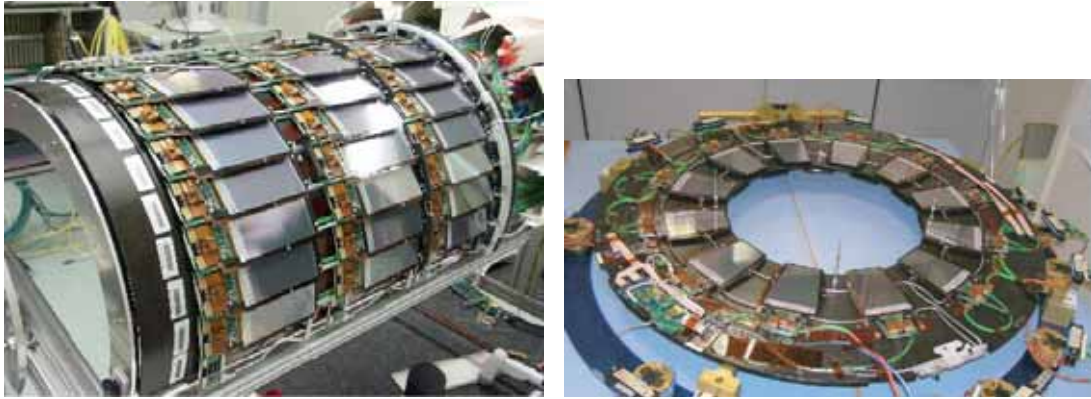


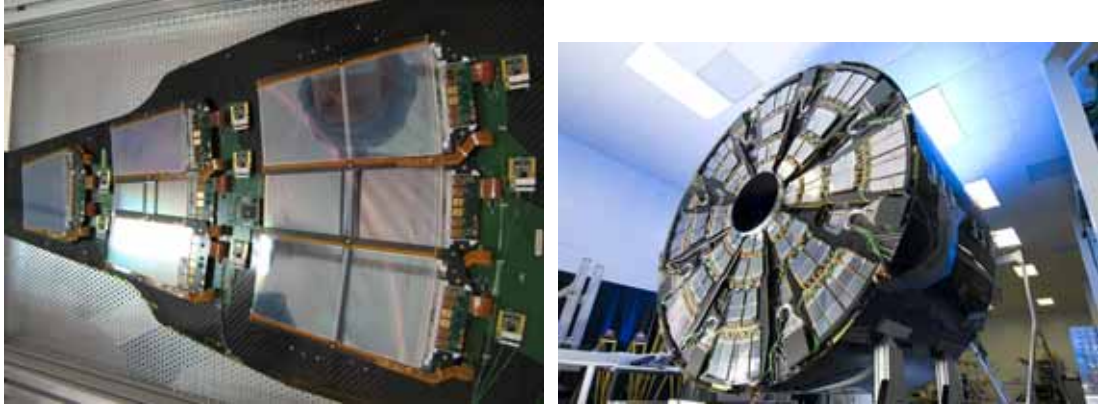
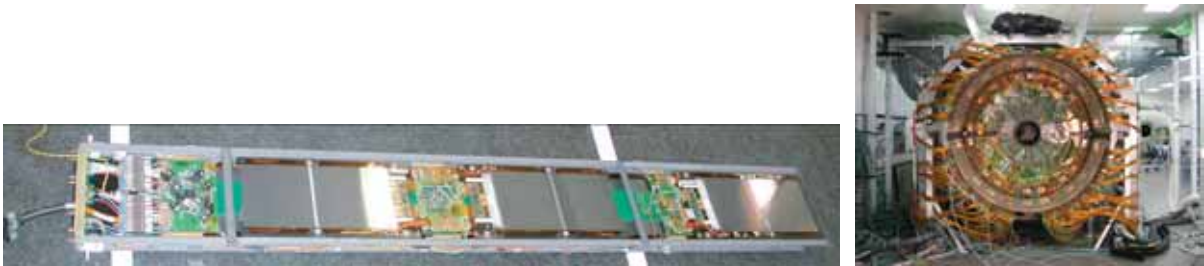
FIGURE 3.5: *Arrangement of the sensors for TID (left) and the TIB (right).*

The TOB and the TEC are organised in a more modular approach. Single modules are mounted on sub-assemblies. These are mechanical supports made of carbon fiber that house in addition the control electronics, optical data transmission, environmental sensors and have integrated cooling for the modules. The sub-assemblies are called "*Rods*" in case of the TOB and "*Petals*" in case of the TEC.

TEC Petals have modules arranged on both sides forming 7 rings in total. In the outermost disks, the inner rings that fall outside the acceptance ($|\eta| \geq 2.5$) are not populated, as shown in Figure 3.3. A single Petal covers 1/16 of a disk. In total there are 144 Petals in either side of the TEC (Figure 3.6).

The TOB is populated with Rods of different flavors. The two inner layers are populated with double sided Rods consisting of 12 modules where 2 modules are arranged for a stereo measurement. The modules have a pitch of $183 \mu\text{m}$ (4 readout chips). These Rods are referred to as *DS* Rods (Figure 3.7). Rods in the Layers 3-6 have 6 modules only but with a varying pitch. Rods in layers 3-4 have sensors with a pitch of $183 \mu\text{m}$ and are referred to as *SS₄* Rods, while Rods in layers 5 and 6 have sensors with a pitch of $183 \mu\text{m}$ and are referred to as *SS₆* Rods. In total there are 688 Rods in the TOB (Figure 3.7).

The geometry and design of the sensors are discussed in the following.

FIGURE 3.6: *TEC Petal left and (one) TEC (right) [40].*FIGURE 3.7: *TOB Rod (left) and fully integrated TOB containing 688 Rods (right).*

3.3 Design Choices of the Strip Sensors

The design of the CMS silicon strip sensors is described in [41, 42]. Strategies for radiation hardness are detailed in [43]; here an overview is given.

3.3.1 Geometry and Types

The geometry of the sensors has been optimized for 6" silicon wafers and full hermicity of the detection surface. Minimal but significant overlap is implemented in all surfaces in $r\phi$ and z views (rz and ϕ views for the forward). The resulting sensor types (Figure 3.8) are summarized in Table 3.1 for rectangular sensors in the TIB and TOB and the wedge shaped ones in Table 3.2 as used in the TID and TEC. The pitch of the sensors is tuned for the requirements of position (momentum) resolution and acceptable occupancy. The number of strips is always a multiple of 256, as this is the granularity of the readout electronics.

In the outer region particle flux and radiation are decreasing. To reduce the number of channels, sensors in the outer layers and rings have longer strips. In the TOB and the TEC rings 5-7, two sensors are bonded together: as a result, the modules have twice the strip length and thus twice the strip capacitance. This implies higher noise (see chapter 6) which is compensated by the use of 500 μm thick material, yielding larger signals.

3.3.2 Sensor Layout

The silicon strip sensors of the Tracker are highly boron doped p-type strips implanted in a lightly phosphor-doped n-bulk. To achieve a good ohmic contact to the backplane a thin layer of highly doped n-type silicon interfaces the bulk and the backplane. Although there are also radiation hard designs with n^- strips in a p^+ bulk, the p^+ strips have been preferred as the collected holes are less affected by the Lorentz drift. In addition the n^- strip configuration

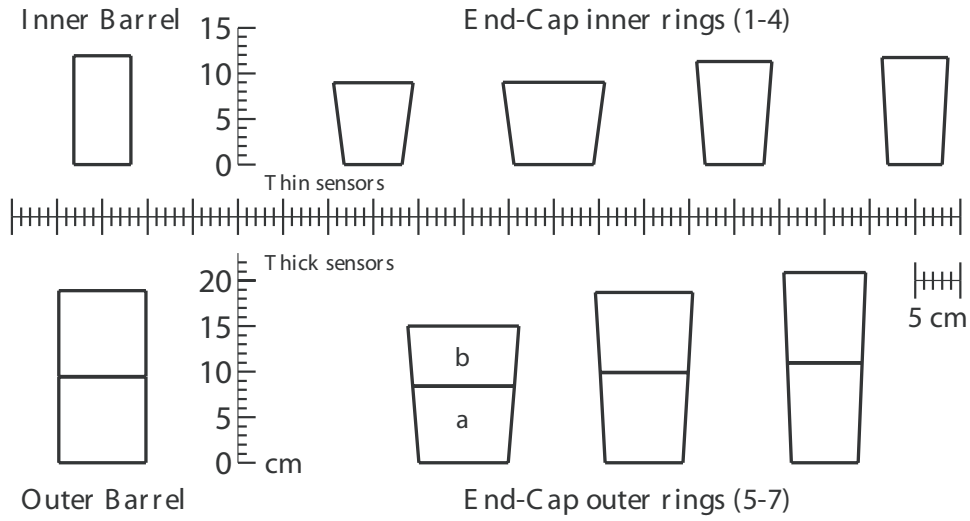


FIGURE 3.8: Shapes and dimensions of all the silicon detector types of the Tracker [39].

Type	Thickness [μm]	Length [mm]	Height [mm]	Pitch [μm]	Strips	Multipl.
IB1	320	63.3	119	80	768	1536
IB2	320	63.3	119	120	512	1188
OB1	500	96.4	94.4	122	768	3360
OB2	500	96.4	94.4	183	512	7056

TABLE 3.1: Inner barrel $320 \mu\text{m}$ thick sensors and outer barrel $500 \mu\text{m}$ thick sensors, geometrical dimensions and multiplicities [42]. In the TOB two sensors are bonded together resulting in modules having twice the length.

Type	Thickness [μm]	Length [mm]	Length [mm]	Height [mm]	Pitch [μm]	Strips	Multipl.
W1-TEC	320	64.6	87.9	87.2	81-112	768	288
W1-TID	320	63.6	93.8	112.9	80.5-119	768	288
W2	320	112.2	112.2	90.2	113-143	768	864
W3	320	64.9	83	112.7	123-158	512	880
W4	320	59.7	73.2	117.2	113-139	512	1008
W5a	500	98.9	112.3	84	126-142	768	1440
W5b	500	112.5	122.8	66	143-156	768	1440
W6a	500	86.1	97.4	99	163-185	512	1008
W6b	500	97.5	107.5	87.8	185-205	512	1008
W7a	500	74	82.9	109.8	140-156	512	1440
W7b	500	82.9	90.8	90.8	156-172	512	1440

TABLE 3.2: Geometrical dimensions and multiplicities for $320 \mu\text{m}$ thick ($W1 - W4$) and $500 \mu\text{m}$ thick ($W5a - W7b$) wedge-shaped sensors for TID and TEC [42]: $W1$ has two different versions for TID and TEC, whereas $W2$ and $W3$ sensors are used both in TID and TEC.

is problematic as the SiO_2 layer acquires positive charge which attracts thermally generated electrons of the bulk. The accumulated electrons can then electrically connect adjacent strips.

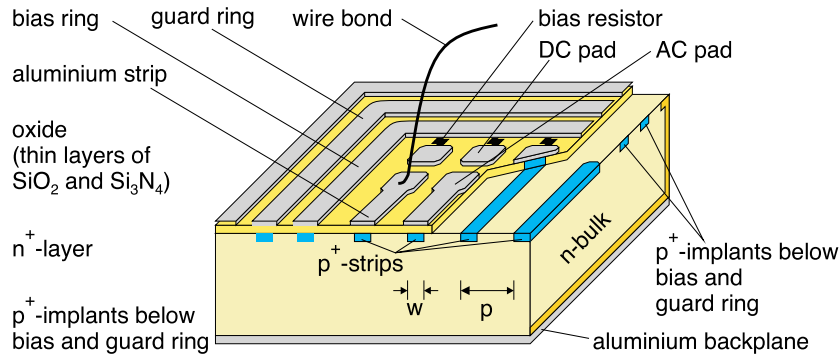


FIGURE 3.9: Silicon strip sensors for the CMS experiment [44].

The strips are read out via AC-coupling. Ideally the coupling capacitance should be large requiring a thin layer of SiO_2 . That would however increase the risk of *Pinholes* - an ohmic contact between the p^+ and the aluminum strips. Good coupling with enough tolerance against pinholes is achieved by using a sandwich of SiO_2 and Si_3N_4 as dielectric in between the p-strips and the aluminum readout strips. The aluminum strips are connected to ground via (intrinsic radiation hard) polysilicon resistors having a resistance of $\approx 2M\Omega$. The pitch of the sensors ranges from 80 to 200 μm , which is generally larger than in the Atlas strip Tracker ($\approx 80 \mu m$). However in the Atlas Tracker has a binary readout, whereas the analogue readout of the CMS Tracker results in slightly superior resolution due to interpolation of the position of charge deposition.

Stability to bias voltage is also a stringent requirement for longterm operation. High bias voltages will have to be applied in the beginning and the end of Tracker operation to ensure fully depleted sensors (Figure 3.12). The design of the sensors avoids high fields on the edges by use of guard rings (a ring at floating potential separating the bias ring from the ground ring). The aluminum readout strips overlap the p implants by a few μm to reduce edge effects. These overlaps ensure that most of the field lines are closing in the Al strips and not in the p strips. In this way, the region of highest field is transferred from the Si-bulk to the insulating SiO_2 layer, that has a much higher breakdown voltage. Sensors have been tested up to 550 V.

3.3.3 Radiation Hardness

The expected radiation doses for neutrons, photons and electrons are shown as a function of the radius in Figure 3.10. For small radii the radiation is dominated by charged hadrons, for the outer layers by neutrons backscattered by the ECAL, as illustrated in Figure 3.3.

Over the 10 years of operation, sensors in the inner layers of the strip Tracker will accumulate ionizing radiation of 60 *kGray* and non-ionizing radiation with an equivalent of $\approx 10^{14}$ neutrons (of 1 MeV) [42]. Surface damage is minimized by using silicon with a $\langle 100 \rangle$ orientation. Compared to a $\langle 111 \rangle$ orientation, the $\langle 100 \rangle$ configuration has an order of magnitude less dangling bonds (unbound valence electrons) on the surface. As shown in [45], this results in less trapped charges at the Si/SiO_2 interface. Furthermore the influence of the strip geometry on radiation induced effects has been carefully evaluated in [46]. It has been observed that radiation effects increase the inter-strip capacitance but decrease the backplane capacitance. Following that study a width to pitch ratio of 0.25 has been chosen, for which the two effects compensate, leaving the total strip capacitance constant as the accumulated radiation increases.

Doping concentration and thickness of the bulk have been balanced between the requirements of radiation hardness (favoring thin sensors with low resistivity), good signal (favoring thick

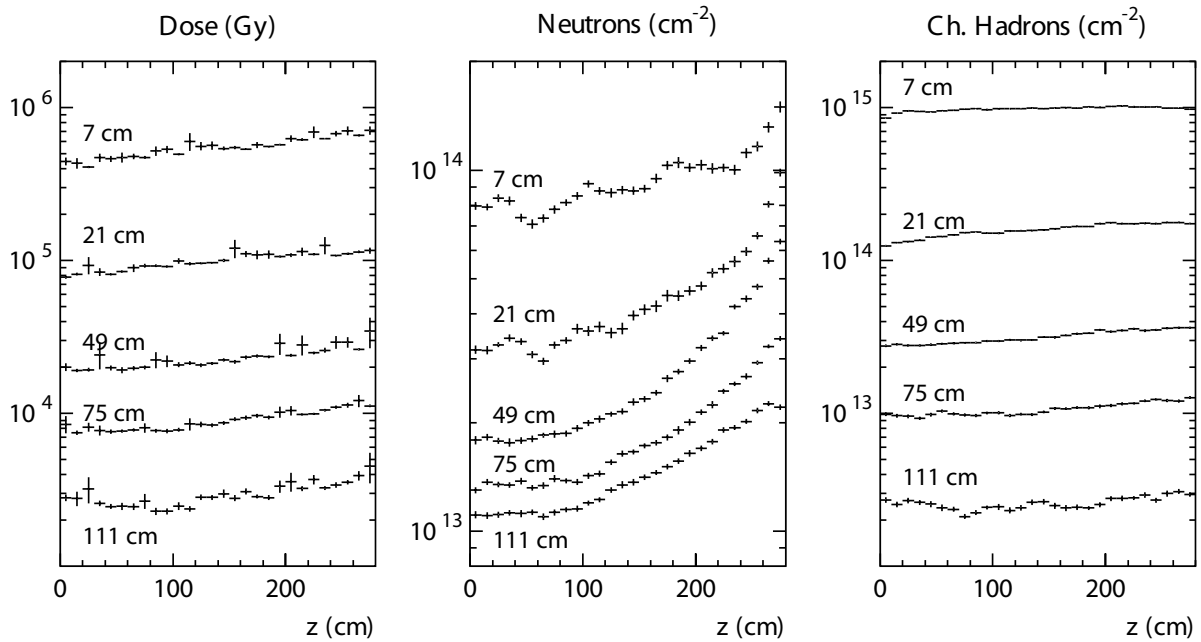


FIGURE 3.10: Predicted Radiation Dose, accumulated in 10 years of operation.

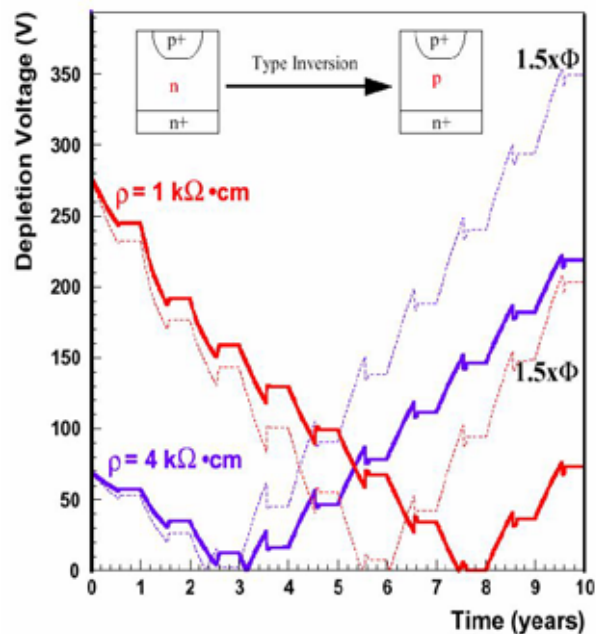


FIGURE 3.11: Predicted evolution of the depletion voltage for Inner Barrel sensors during 10 years of operation. Dotted lines are for a pessimistic scenario with 1.5 times the expected flux (giving 50% margin) [47].

sensors) and low full depletion voltage (favoring thin sensors with high resistivity). Sensors in the inner layer suffer from high radiation and are therefore made of low resistivity ($1.5\text{--}3\text{k}\Omega/\text{cm}$) $320\ \mu\text{m}$ thin silicon. Thin sensors are less affected by bulk damage due to radiation; the high doping concentration ensures low bias voltages after type inversion.

In the outer layers particle flux and radiation are lower; therefore longer strips and thick sensors are used. These thick sensors have a high resistivity ($3.5\text{--}7\text{k}\Omega/\text{cm}$) bulk material, to allow for full depletion voltages similar to the thin sensors. The depletion voltage for the barrel innermost layer is shown in Figure 3.11. The accumulated bulk damage decreases the effective dopant concentration, requiring less bias voltage for full depletion. After type inversion the effective doping concentration and depletion voltage increases. The steps in the graph result from estimated annealing and standby phases of Tracker operation.

3.3.4 Material Distribution of the Tracker

The total material in the Tracker is shown in terms of radiation length in Figure 3.12. The radiation length is the length after which an electron traversing the material has lost $1/e$ of its energy due to Bremsstrahlung; equivalently it is defined as $7/9$ of the mean free path length for pair-production by high energetic photons. Electrons traversing the Tracker will thus lose most of their energy due to Bremsstrahlung limiting the performance of the electromagnetic calorimeter that is surrounding the Tracker; pair production will increase the occupancy. In addition the material causes multiple scattering, thus reducing the momentum resolution for low p_T tracks. As seen from the right plot, a large contribution for $|\eta| > 1$ is due to services such as power cables and cooling. Power cables have already been optimized using aluminum in the Tracker volume, that have comparable electrical properties as copper but smaller radiation length due to the lower Z . The large amount of material for cooling reflects the demand of operating the Tracker at -10°C to prevent sensor damage due to reverse annealing, and - with accumulated radiation - thermal runaway.

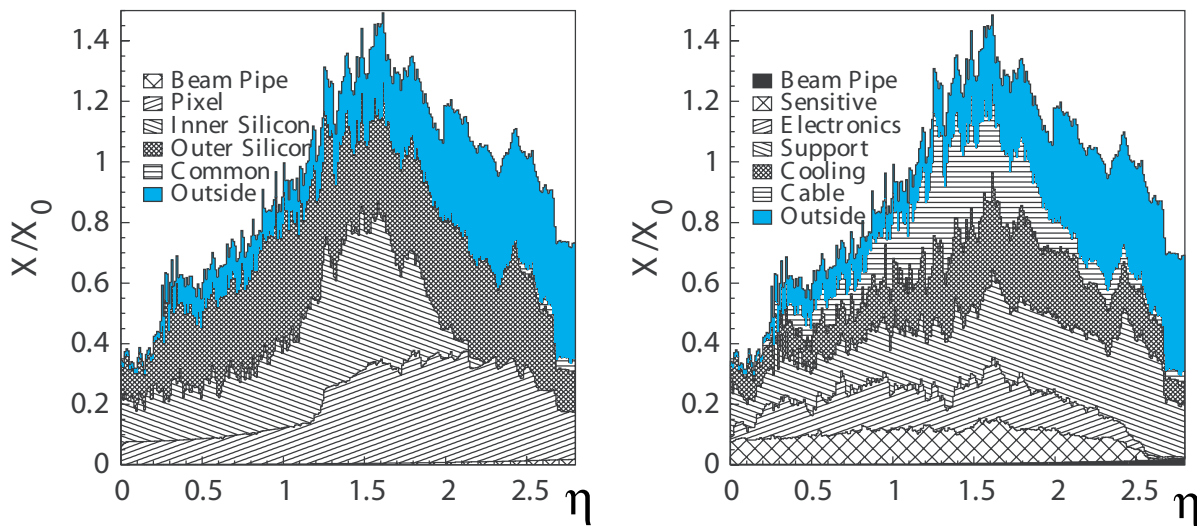
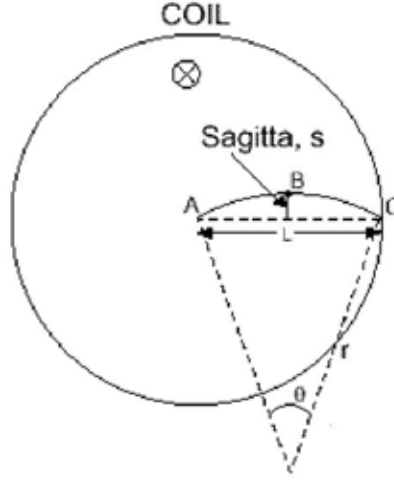


FIGURE 3.12: [39] Radiation length of the CMS Tracker as a function of pseudo-rapidity. The contributions of the subsystems are shown in the left plot, the right plot groups by functional components.

FIGURE 3.13: Definition of the sagitta s .

3.3.5 Tracker Performance

Momentum Resolution

The momenta of charged particles are measured in the Tracker via their curvature in the magnetic field. The trajectory of a charged particle in a static homogeneous magnetic field is a helix:

$$p_T^2 r = q \cdot p_T B \quad (3.1)$$

Expressing p_T in GeV/c, B in Tesla and R in meters, the equation can be rewritten as:

$$p_T = 0.3Br \quad (3.2)$$

The curvature is a function of the magnetic field B and the momentum normal to the magnetic field $p_T = m_0 v_T \gamma$. As shown in Figure 3.13 by measuring 3 points along the particles track, the sagitta can be obtained:

$$s = r - \sqrt{r^2 - \frac{L^2}{4}} \quad (3.3)$$

from which the curvature r and thus the transverse momentum can be calculated. The relative momentum resolution is derived in [48] for measurements in N_{hit} equidistant layers, where each layer has a position resolution of σ_{hit} :

$$\frac{\sigma(p_T)}{p_T} = \sigma_{hit} \frac{p_T}{0.3BL^2} \sqrt{\frac{720}{N_{hit}} + 4} \quad (3.4)$$

In addition one should keep in mind, that the hit resolution is subject to multiple scattering and is roughly given by:

$$\sigma_{hit} = \sqrt{\sigma_{int}^2 + \left(\frac{f(X/X_0)}{p} \right)^2} \quad (3.5)$$

where σ_{int} is the intrinsic resolution of the sensors, and $f(X/X_0)$ a function of the material and the geometry of the system.

To optimize the resolution of the transverse momentum, the two outermost layers of the Tracker - TOB layer 5 and 6 - house modules with smaller pitch than the other TOB layers.

The simulated momentum resolution is illustrated in Figure 3.14 demonstrating that the design provides in the central region a resolution better than 2% for particles up to 100 GeV. Combining eqn.3.4 and eqn.3.5 one sees, that for high momentum tracks the momentum resolution is limited by the intrinsic precision of the sensors, and for low momentum tracks by the Tracker material. The effect of the Tracker material is seen for low momentum muons in the range $|\eta| = 0$ to $|\eta| = 1.5$. At $|\eta| > 1.7$ the track resolution gets significantly worse, as in the projection along the z-axis less of the tracks path length is instrumented (see Figure 3.3). According to eqn.3.4 a reduced lever arm "L" degrades quadratically the resolution.

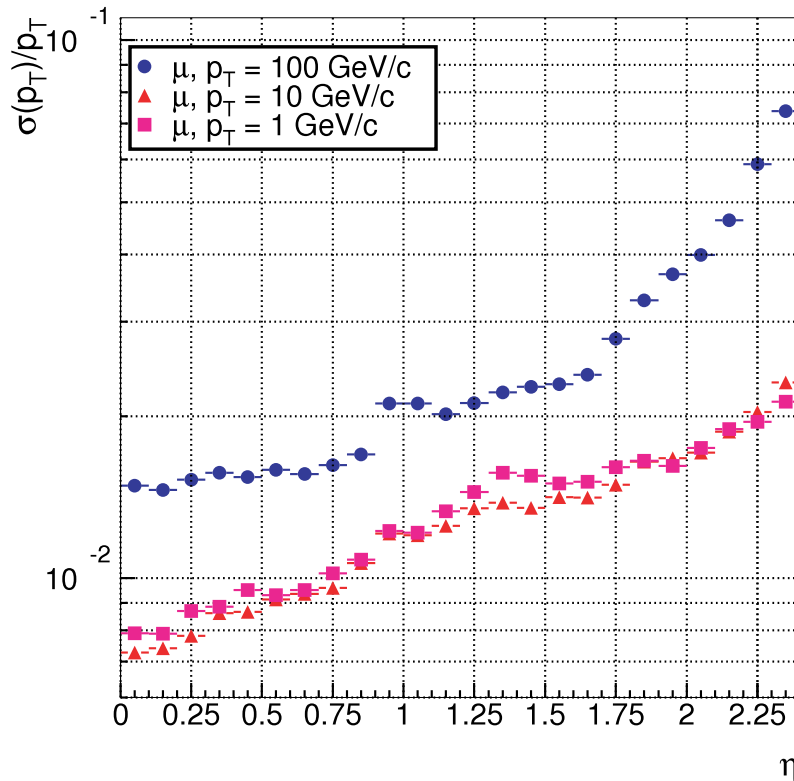


FIGURE 3.14: Transverse momentum resolution for different p_T as a function of the pseudo rapidity $|\eta|$ [49].

Track Reconstruction Efficiency

The track reconstruction efficiency simulated with muons and pions with transverse momenta of 1 GeV/c, 10 GeV/c and 100 GeV/c is shown in Figure 3.15. A track is considered to be reconstructed successfully, if it has a transverse momentum greater than 0.8 GeV/c, at least 8 hits, and is sharing at least 50% of the hits with the simulated track. This takes both properties of the detector and shortcomings of the reconstruction algorithm into account. For muons the track reconstruction is fully efficient over a large range of $|\eta|$. A small degradation is seen at $|\eta| = 0$ due to the gap of the two pixel halves and at $|\eta| > 2.25$ that is due to reduced coverage of the forward pixel discs.

For pions the reconstruction efficiency is between 75% and 95%, limited by hadronic interactions with the Tracker material. As shown in Figure 3.12, the total Tracker material increases from $X/X_0 \approx 0.8$ for $|\eta| = 1$ to $X/X_0 \approx 1.4$ for $|\eta| = 1.4$. The corresponding drop is clearly visible in Figure 3.15.

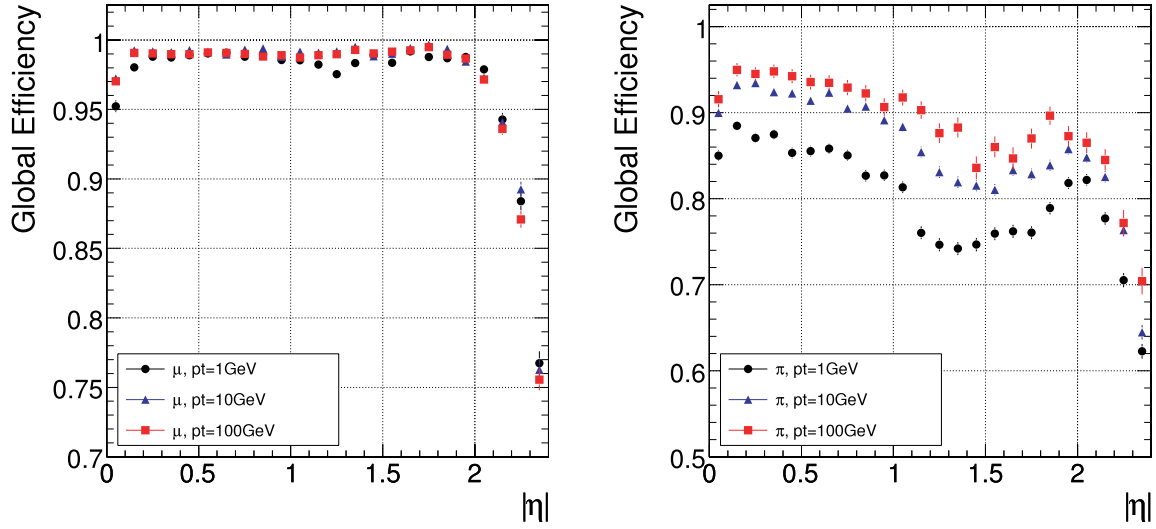


FIGURE 3.15: *Track reconstruction efficiency for muons (left) and pions (right) with $p_T = 1, 10$ and 100 GeV as a function of $|\eta|$ [50].*

3.4 Summary

The CMS Tracker instruments a cylinder with a diameter of 2.4 m and a length of 5.4 m. Its sensor are designed to operate for more than 10 years in a high-radiation environment. In the central region of the Tracker ($|\eta| < 1$), the momentum resolution is better than 2% for transverse momentum of $1 \text{ GeV}/c < p_T < 100 \text{ GeV}/c$. The track reconstruction is fully efficient for muons; for pions however, the efficiency degrades in the forward region due to hadronic interactions with the Tracker material.

Chapter 4

CMS Readout Electronics

The CMS Tracker readout electronics [28,51,52] has been designed to allow for efficient low noise charge readout in a severe radiation environment. Event reconstruction requires fast readout with a time resolution of 25 ns to resolve bunch crossings. The high granularity of the tracker implies a large number of channels leading to an enormous amount of data every bunch crossing. Bandwidth limitations require a selective readout. The *Level-1 Trigger* will search for signatures identifying potentially interesting events and triggering only for those a full readout. Therefore data have to be stored on the detector side until trigger decisions have been taken.

The readout of the tracker provides analogue pulse height information for each channel, which offers several advantages over binary readout. Among them are improved position resolution of the strip sensors by interpolation of the charge barycenter, offline common-mode noise subtraction and energy loss (dE/dx) measurements. Another benefit is the direct measurement of electronics noise - an important debugging tool for electronics crosstalk and the grounding scheme. Furthermore locating the digitization electronics outside the detector volume reduces power consumption. A significant fraction of the total material of the Tracker (Figure 3.12) is related to electronics and cooling. The power consumption of the electronics determines the cross sections of power cables, the amount of heat dissipated and hence the material required for cooling. Given the need to minimize the material in front of the surrounding ECAL, limiting the power consumption has been a basic requirement for the design of the electronics system.

4.1 System Overview

The schematic of the readout electronics is shown in Figure 4.1, which illustrates the data paths for the analogue readout and the digital control system.

Strips of the silicon strip detectors are read out by the front-end chip the *APV25* (Analogue Pipeline Voltage mode 0.25 μm process). This chip includes preamplification, analogue storage and pulse-shaping for 128 strips. The output of two APVs is multiplexed by the multiplexer (APVMUX) and converted to optical signals via the *Analogue Opto Hybrid* (AOH). Analogue data of 256 channels are transmitted sequentially via a single mode optical fiber to the *Front End Driver* (FED) located in the radiation protected counting room. At the FEDs data is converted from optical to electrical, demultiplexed, digitized and buffered for output.

The front-end chips are programmable and have to be configured prior to operation. The configuration and monitoring is performed by a dedicated control ring. Configuration commands are sent by the *Front End Controller* (FEC) digitally over optical fibers. At the detector side, the *Digital Opto Hybrid Module* (DOHM) performs the optical to electrical conversion and sends the commands, clock and trigger signals to the ring formed by the *Communication and Control Units* (CCU). The CCUs decode the information and pass them to the addressed devices. The data flow is bi-directional. Configuration parameters are read back, status information and environmental data collected by the *Data Conversion Units* (DCU) such as temperature, detector leakage

currents and voltages are transmitted to the FEC.

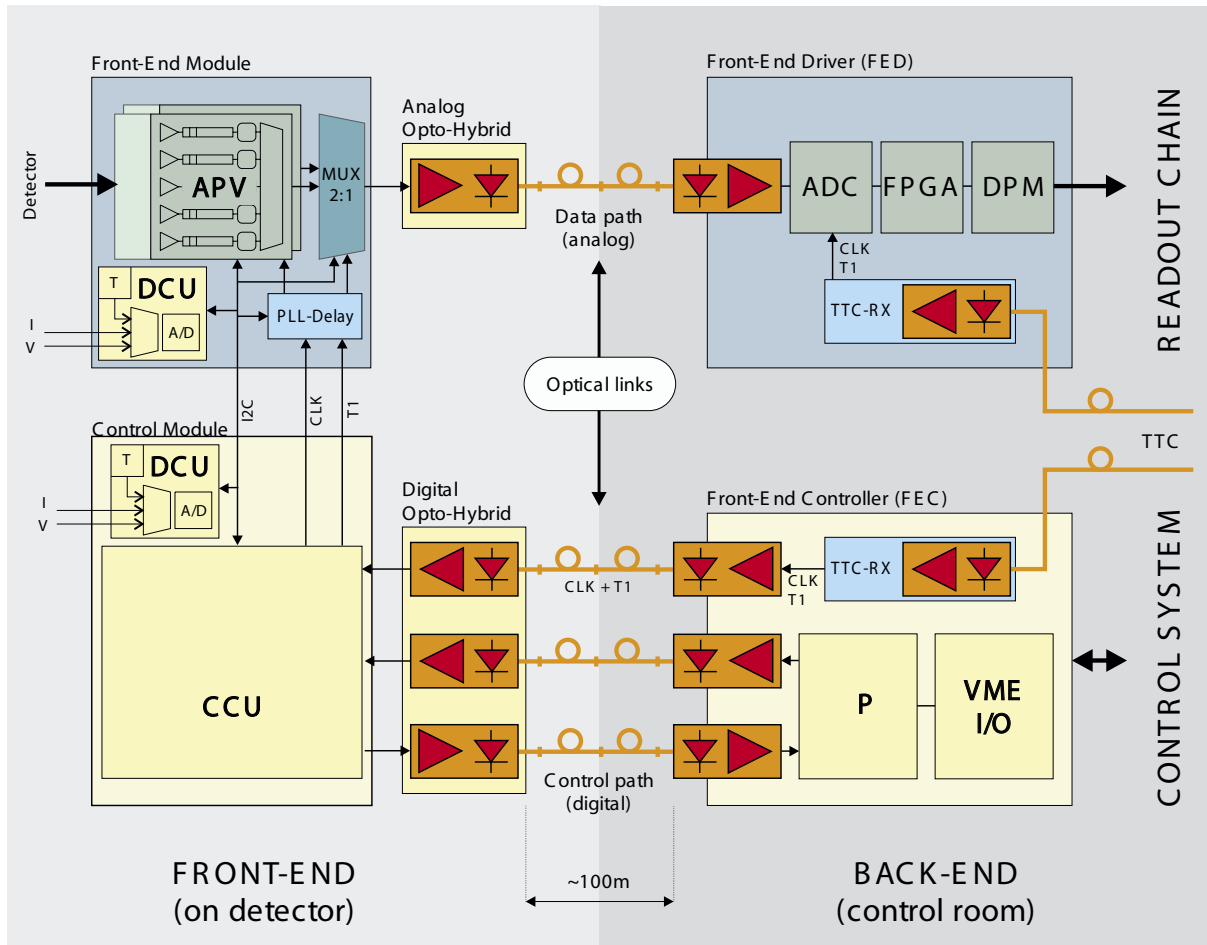


FIGURE 4.1: Overview of the CMS Tracker readout (top) - and control system (bottom) [28]. Transmission between the front-end electronics (left) and the back-end electronics (right) is established by optical links.

4.2 Radiation Hardness

The front-end electronics has been tested to sustain an accumulated irradiation of 20 Mrad (200 kGy) and a flux of $3 \cdot 10^{14}$ neutrons cm^{-2} with acceptable degradation of performance. The ASICs are manufactured in $0.25 \mu m$ CMOS (Complementary Metal Oxide Semiconductor) technology, which relies on the formation of small conductive layers near the gate electrodes and is therefore intrinsically tolerant to bulk radiation damage. Standard CMOS chips however suffer from effects of surface damage: The accumulation of radiation-induced positive charges in the oxide leads to threshold shifts and leakage currents. Hardness to surface damage has been achieved by selecting a submicron process, very thin oxide layers ($\approx 5 nm$) and special libraries for the chip design with enclosed gates geometries and guard rings [53]. The thin oxide layer reduces the interaction cross section with radiation, and in addition allows electrons to tunnel into the oxide¹, neutralizing the trapped charges.

As illustrated in Figure 4.2, due to the increased thickness of the oxide layer towards the contacting of the gate electrode, a conductive path is formed at the edges of the active area. The leakage current between drain and source can be significantly reduced by the enclosed gate

¹In general tunneling through the oxide layers is effective for a thickness less than $\approx 10 nm$.

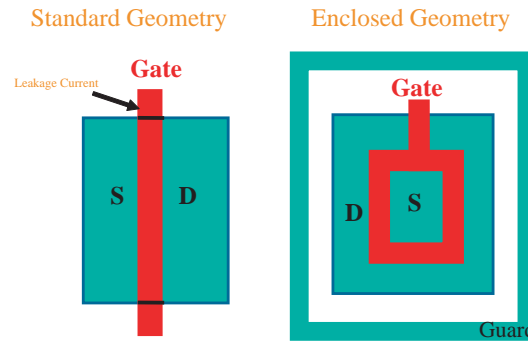


FIGURE 4.2: Radiation hard design of a MOS-FET. Leakage currents at the edges are eliminated by an enclosed geometry. A guard ring prevents creation of radiation induced parasitic bipolar devices.

design, where the oxide layer is thin over the entire boundary. Guard rings separating p-n borders prevent coupling of neighboring devices.

4.3 Front-End Electronics

The front-end hybrid integrates the front-end electronics of a single detector module, including four to six APV25 readout chips and three auxiliary chips: PLL, DCU and APVMUX.

The fast pulse shaping of the readout electronics requires for efficient charge detection, a synchronous readout in phase with the charge deposition. In order to compensate delays arising from signal propagation in optical and electrical lines and from the time of flight delays of particles emerging from LHC collisions, the clock and trigger signals are adjusted locally for each module by a programmable delay in the *Phase Locked Loop* (PLL) chip. The PLL chip decodes clock and trigger and adjusts the delays in coarse and fine steps. A coarse step is a full clock cycle and a fine step 1/24 of a clock cycle.

The APVMUX multiplexes the output of 2 APVs into one channel reducing the number of optical fibers required. Environmental conditions and status information are provided by the *Digital Control Unit* (DCU). The DCU has eight channels ², each equipped with 12bit ADC, monitoring several different parameters, including temperatures and leakage currents.

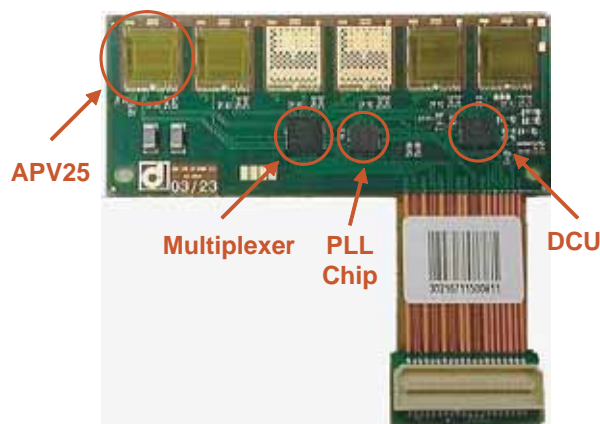


FIGURE 4.3: TOB Hybrid with frontend chips.

²Only 7 are available for external sensors, one of the channels is connected to an internal temperature sensor.

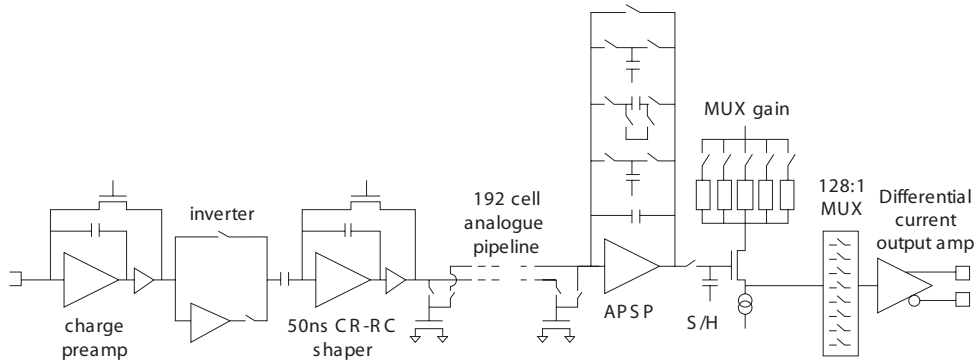


FIGURE 4.4: *Block Diagram of for one channel of the APV25 [28].*

4.4 Front-End Readout Chip APV25

The APV25 is the CMS front-end chip designed to readout out 128 strips, with a rate of 100 kHz and minimal dead time. The APV25 is a VLSI (Very large Scale Integration) circuit manufactured in a radiation hard CMOS 0.25 μm process. The chip has a digital part - the control interface for configuring the chip (via the I2C protocol [54]) - and an analogue one. Both parts have been optimized for power consumption resulting in 2.31 mW per channel (1.9 mW in the analogue part and 0.41 mW in the digital part) with the main contribution by the preamplifier with 0.9 mW.

The block diagram of Figure 4.4 shows the stages of the analogue part that are implemented for each of the 128 channels. A low noise charge sensitive preamplifier collects charge from a detector strip. To cope with either polarity, an inverter (with unity gain) can be switched into its output. Following that is a CR-RC pulse shaper with a time constant of 50 ns. In a narrow range the shaping can be tuned by shaping parameters, which modifying the rise and decay time. At every clock cycle the output of the CR-RC shaper is sampled and stored into a cell of the analogue pipeline. The pipeline buffers the data with a programmable latency of up to 160 clock cycles, allowing thus for a trigger decision within $\approx 4 \mu\text{s}$, well compatible with the estimated trigger decision latency of 3.2 μs (plus additional transmission delays). Cells in the pipeline flagged for readout are processed according to the selected operation mode by the Analogue Pulse Shaping Processor (APSP). The shaped signal is buffered and amplified with a fixed gain of 10. A following stage allows for a further amplification, by selecting between 5 gains steps (nominal, $\pm 10\% \pm 20\%$). The circuits are detailed in [55].

4.4.1 Operation Mode

The APV25 can be operated in three different modes: Peak, Deconvolution and Multi mode. In peak mode the APSP passes the data of a single pipeline cell to the output stage. The pulse shape of the signal is given by the CR-RC shaper. The resulting pulse is much longer than the 25 ns bunch crossing time, thus not suitable for LHC operation at high luminosity. To obtain pulses short enough for the resolution of bunch crossings, the deconvolution mode has been implemented. The deconvolution mode uses a discrete convolution algorithm, which calculates the weighted sum of three consecutive samples in the pipeline. The deconvolution mode is the default mode for LHC operation. The details of the algorithm will be discussed in chapter 8. The trigger logic of the APV requires a minimum dead time of 2 clock cycles between consecutive triggers. The Multi-mode copes with this limitation by reserving three consecutive pipeline cells for each trigger signal that are sent sequentially. This mode is not projected to be used in LHC operation but provides a tool for pulse shape calibration and analysis.

Pulse shapes for peak and deconvolution mode are shown in Figure 4.5.

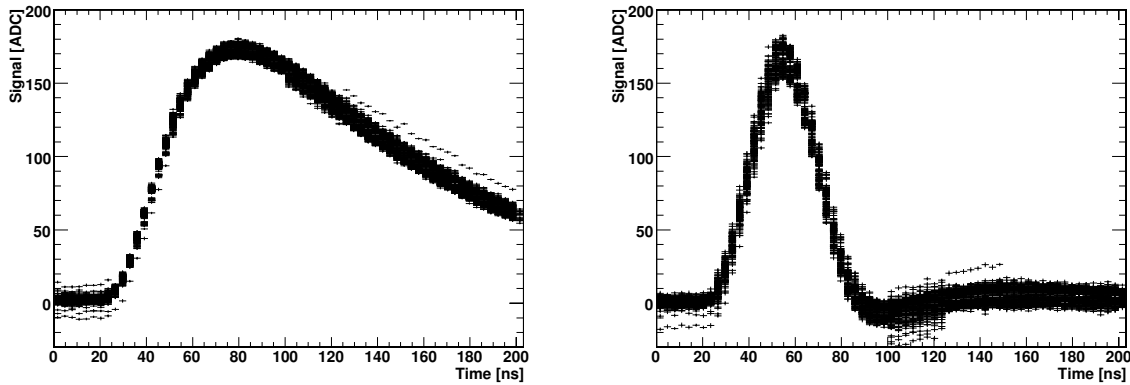


FIGURE 4.5: *Pulse shape in peak mode (left) and deconvolution mode (right) obtained by the internal calibration circuit. Diagrams show an overlay of all 128 strips of a single chip.*

4.4.2 Pipeline

The APV analogue pipeline has 192 cells, each of which is a capacitor for storing the data with two associated transistors, one for the write and one for the read operation. The pipeline is used to store data until a trigger decision is taken. Cells in the pipeline are not arranged as a shift register but they form a ring buffer. The operating principle is sketched in Figure 4.6. Cells of the ring are accessed by a read, a write pointer and a trigger pointer. The write and trigger pointers are "circulating" with the clock frequency, separated by a programmable latency of up to 160 cells (the remaining 32 serve as a buffer). At each clock cycle, a new data is written into the cell addressed by the write pointer. If a trigger command is received, in peak mode the cell accessed by the trigger pointer (in Deconvolution and Multi mode the actual and the following two cells) is flagged for readout by storing its address into the trigger FIFO (First In First Out buffer). The FIFO has 32 elements thus capable of storing 32 events in peak and 10 events in deconvolution and multi mode. With a given period (70 clock-cycles in 20MHz mode) the FIFO is queried. If the FIFO is not empty the read pointer will directly access the cell flagged by the FIFO starting the data transmission.

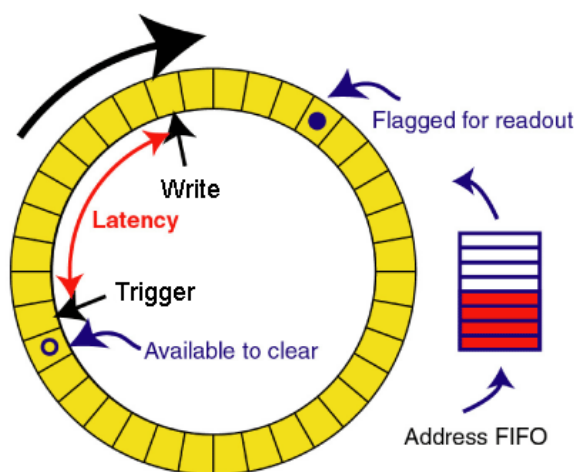


FIGURE 4.6: [56] Ringbuffer: *The trigger pointer is following the write point with a programmable latency. Upon receiving a trigger signal, the address of the trigger pointer is stored in the FIFO. A read pointer is accessing cells flagged by the FIFO.*

4.4.3 Amplification and Data Frame

The amplification of the APV25 has been tuned to the charge generated by MIPs traversing $320 \mu\text{m}$ thick silicon sensors. An input charge of $25 \cdot 10^3 e^-$ (corresponding to most the probable charge generated by a MIP) is translated into a current signal of $100 \mu\text{A}$; amplified by the output buffer this results in a signal of 1 mA .

The output of the chip is a differential current signal with a maximum amplitude from -4 mA to 4 mA , allowing thus a dynamic range of 8 MIPs. Data are transmitted in frames, consisting of a 12bit digital header (3 start bits (all high), a 8 bit pipeline column address and an error bit), followed by the analogue samples of 128 channels and a stop bit. The 128:1 multiplexing of the channels is implemented in multiple stages. As a consequence the order in which the channels are sent does not correspond to the order of the strips, but is given by eqn.4.1 where n is the position in the data frame.

$$\text{Channel No.} = 32 \cdot (n \text{ MOD } 4) + 8 \cdot \text{INT}(n/4) - 31 \cdot \text{INT}(n/16) \quad (4.1)$$

The resulting data frame is shown in Figure 4.7. When no data are queued for output, the chip is sending a synchronisation pulse, called *tickmark*. The tickmark is a digital "1" ($\hat{=}$ 8 MIPs) sent every 70 clock cycles ($1.75 \mu\text{s}$) and is used to ensure synchronisation of the back-end with the front-end electronics.

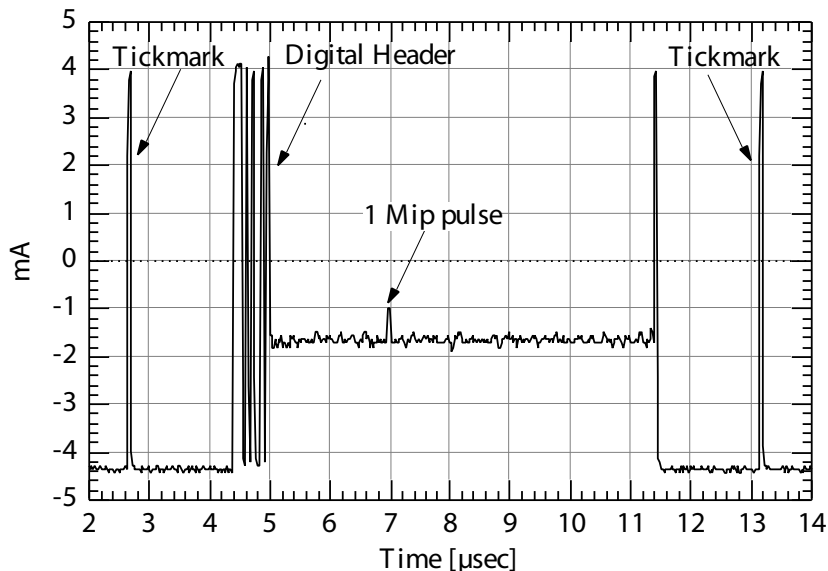


FIGURE 4.7: APV data frame [57]: The analog data of 128 strips is preceded by a 12 bit digital header and terminated by a stop bit. When no data are read out a synchronisation pulse is sent every 70 clock cycles.

The integrated multiplexer can be operated at 40 MHz and 20 MHz. 20 Mhz is the default as it allows for interleaving of the output of two chips³. A complete transmission takes 280 clock cycles or $7 \mu\text{s}$.

4.4.4 Internal Calibration Circuit

Integrated to the APV25 is a calibration circuit [58] providing test functionality of each single channel. A test pulse generator applies charge to the preamplifiers of a (selectable) group of 16 strips. The deposited charge and the delay between charge generation and sampling are programmable. The delay can be set in steps of 1/8 of a clock cycle (3.125 ns) allowing for the reconstruction of the pulse shape as shown in Figure 4.5.

³The 2:1 multiplexing is performed by the external APVMUX.

4.5 Optical Link System

The CMS Tracker is employing optical links [59, 60] in its readout and control paths. Optical links allow for a galvanic decoupling of the front and back-ends, high speed data transfer and are immune to electronics pickup. Most important, and essential for the entire detector performance, is the minimal contribution to the total Tracker material. That is not only due to the long radiation length of the fibers and their small volume (no electrical shielding needed), but also a consequence of the low power required for transmission.

In total about $40 \cdot 10^3$ optical links are used to readout the nearly 10 million detector channels; approximately 2500 links are used for the control system. The design of the optical link system is based on standard commercial components, with minor customization, which have been tested and qualified for the required radiation hardness, bandwidth and linearity. The analogue readout and the digital controls have most parts in common.

A single optical connection provides unidirectional data transfer. Amplitude modulated light is transmitted into a standard telecommunication single-mode optical fiber and received by a *positive-intrinsic-negative* diode (pin-diode).

The light transmitters are standard edge emitting semiconductor lasers in a custom package with minimal contribution to the total tracker material. The lasers have a wavelength of 1310 ± 25 nm and show a good linearity when biased properly. The required bias current is around 9 mA.

The optical link as illustrated in Figure 4.8 has three pluggable joints. Each of the optical connectors requires high mechanical precision, due to the small core diameter of the single mode fibers. The laser pigtailed are terminated by *MU* connectors, that are bundled in groups of 12 and connected at *Distributed Patch Panel* to a single readout ribbon. The ribbons have an average length of 5 m, and are routed outside of the Tracker volume to the *Patch Panel* where 8 ribbons are connected by the *MFS* connector to a *Multi Ribbon Cable* that carries the signal to the back-end. At the FED the single ribbons are attached by *MPO* connectors to the analogue receiver modules that have 12 input channels.

The transmitter module for the readout path the *Analogue Opto-Hybrid* (AOH) hosts three independent lasers, that are driven by an associated Linear Laser Driver (LDD) [62]. The LDD has an integrated I2C interface and allows for programming of gain and bias settings of individual lasers.

The gain setting defines the intensity of the emitted light and is necessary to operate the analogue receiver in the optimal dynamic range of the digitizer, adapting to variations in light efficiency of the optical links. A spread of the overall gain is expected due to variations of components, quality of optical connections, temperature dependence, and degradation of performance due to accumulated radiation doses.

The digital control ring has most components in common with the analogue readout. Only the photo diodes at the front-end and the transceivers at the back-end are different. The front-end module for the controls is the *Digital Opto Hybrid* (DOH), a transceiver equipped with 2 lasers, 2 pin diodes and an LDD.

Experimental results have demonstrated the excellent performance of the optical link system. The signal to noise ratio in the analog lines is in the order of 400 (52 dB) and the nonlinearity less than 2%. The digital link system has an error rate of approx 10^{-12} . Radiation hardness complies with the requirements. During CMS operation, with accumulated radiation, the bias current of the lasers is expected to increase by 50%, the linearity is not affected. Pin diodes for the front-end will have increased leakage currents, but will deliver sufficient photo current for stable operation.

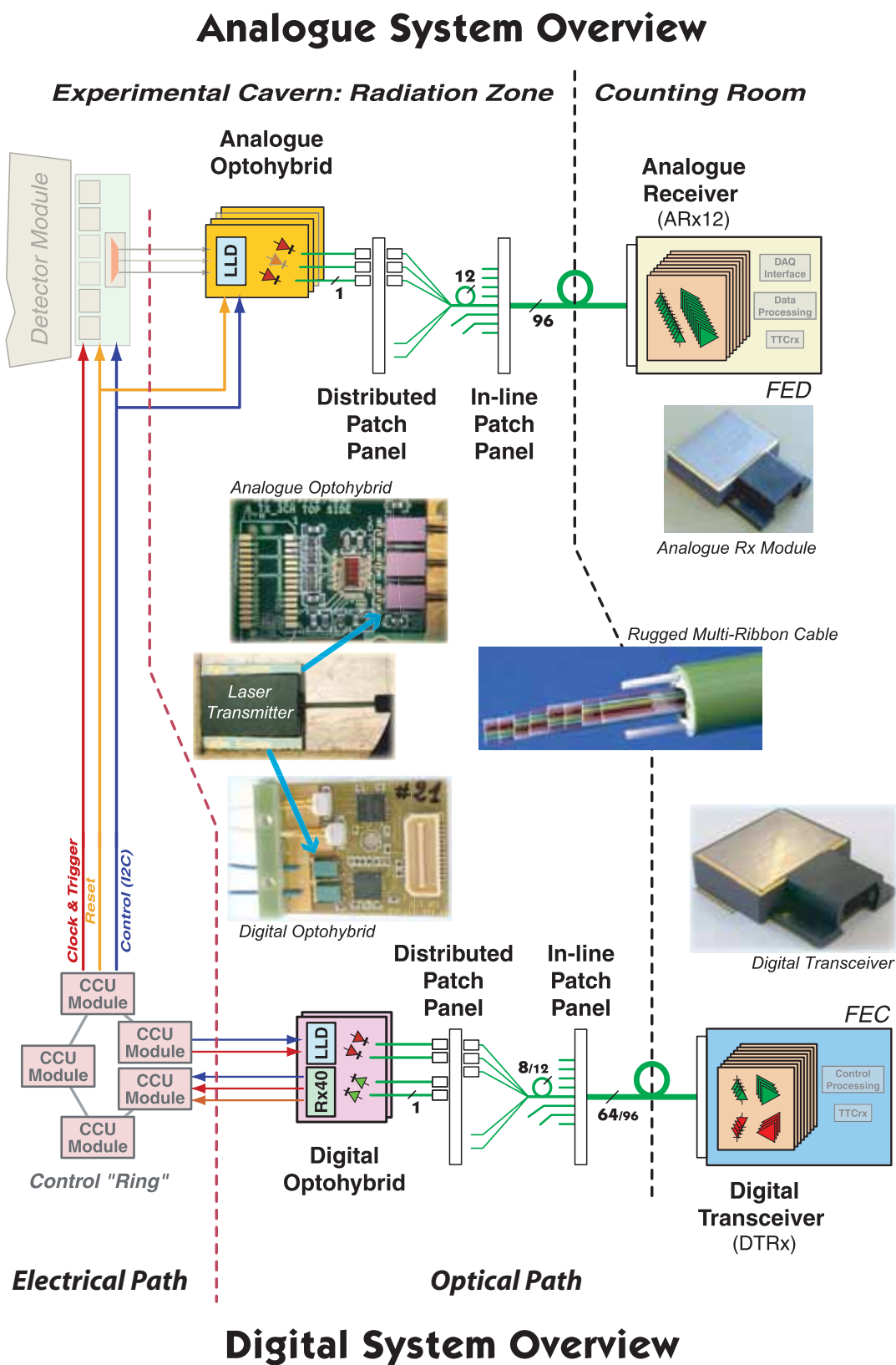


FIGURE 4.8: Optical readout and control system of the CMS Tracker. Diagram according to [61].

4.6 Control Architecture

The front-end electronics is highly configurable to be able to adapt to the different sensors used in the Tracker and to compensate for the expected change in performance due to irradiation. More than 10^5 programmable devices, distributed over the entire Tracker volume, need to be configured for operation and their status needs to be monitored.

A dedicated control hard- and software system [51, 63] ensures reliable read and write access to the front-end device registers.

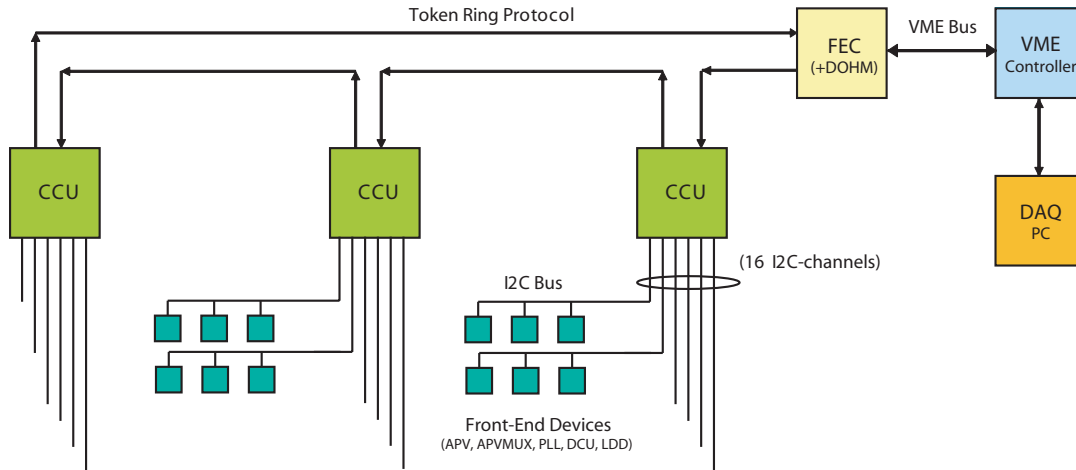


FIGURE 4.9: *Controlring Architecture* [28].

The topology of the control ring can be split in two layers of hierarchy. As sketched in Figure 4.9 the first layer is the communication between the CCUs and the FEC, and the second is the exchange of data between the CCUs and the front-end devices.

The lower level hierarchy is a bus architecture employing the I^2C protocol. A single CCU is the master of up to 16 channels. The channels are arranged so, that a single channels is associated to the devices belonging to a given detector module, and one channel is dedicated for the devices of the Communication and Control Unit Module (CCUM) - e.g its DCU and driver chips. Data requests are triggered at higher hierarchy and passed by the CCU to the addressed devices (e.g. the APV, PLL, APVMUX, DCU and LDD). At higher hierarchy, CCUs are daisy chained forming a logical ring. The ring communication is established via a Token Ring protocol [64]. In this standard protocol data are exchanged in frames that are passed from one node (i.e. the CCU) to the next. These data frames consist of the address of the receiver, the actual message and a part reserved to indicate the validity of the data - the token. If the ring is idle an empty data frame is circulating. A node wanting to transmit data is waiting for the arrival of such an empty frame and replacing it by the message to send and sets the token active. The frame is circulating until it is passed to its destination. There the token is changed from active to inactive and passed back onto the ring. When the data frame is then arriving at its origination by checking the token the originator can verify that the message has reached the destination. If there are further data to transmit a new data frame will be sent, otherwise an empty frame.

A special node in the token ring is the FEC. This is a VME based board housed in the counting room, the actual interface between the DAQ system and the front-ends. The FEC transmits and receives digital signals over ≈ 100 m long optical fibers. It is connected to the CCUs via the DOHM that performs the optical to electrical conversion (and vice versa).

A pre-requisite for the control ring operation is that all nodes must have different addresses. Address 0 is reserved for the FEC. The first two CCUs of the ring are also special nodes, as they have the additional functionality of controlling the LDD of the DOHM (the second CCU

performs the task in the case, that the first CCU is faulty and it is excluded from the ring). In the Outer Barrel, for the convenience of bookkeeping of CCU addresses, it has been chosen to reserve addresses "1" and "2" for the first and the second CCU in a ring, respectively, and use random addresses for the others in the available range of 8bits (CCU addresses are set by external jumpers).

The Token ring protocol has been chosen as it provides collision free exchange of data packets resulting in fast data exchange. It however relies on error-free operation of all nodes: a single faulty node breaks the entire ring. To improve robustness, redundancy has been implemented in the ring architecture, illustrated in Figure 4.10. Data transfer between the CCUs can be done via two channels A, and B. Channel A (default) connects the output of the CCU to the input of the following one, while by selecting channel B the following CCU is excluded from the ring and data are transferred to the next one.

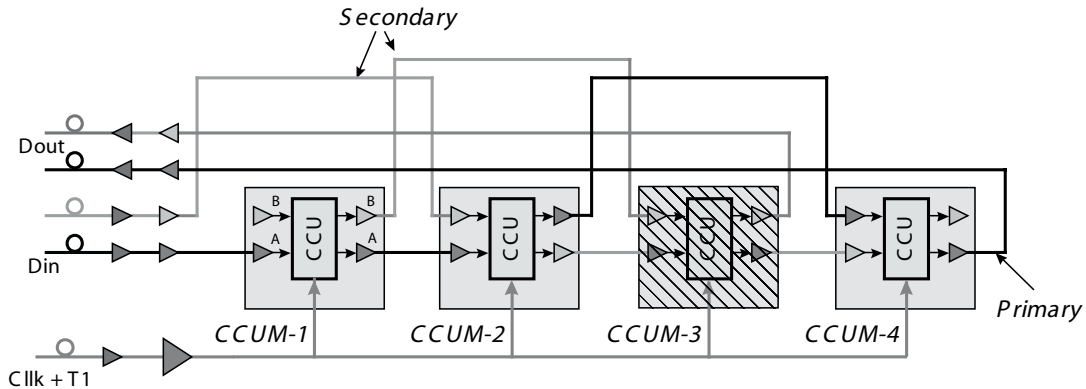


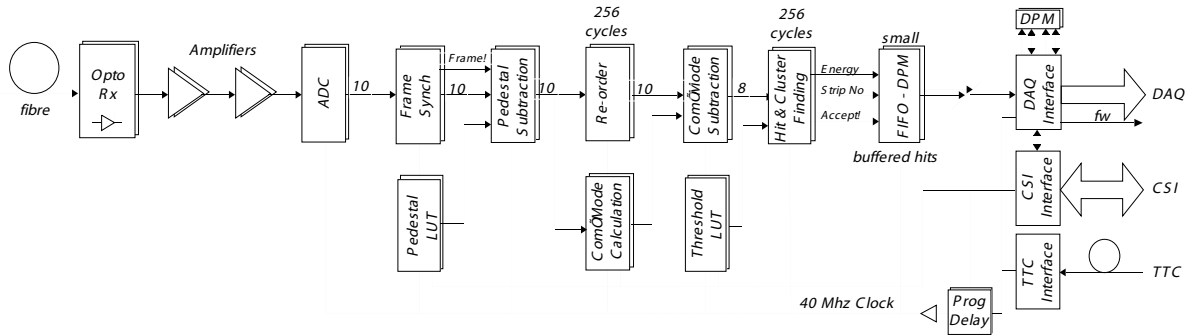
FIGURE 4.10: Redundancy scheme in the control ring architecture - CCUM 3 is being skipped.

With such scheme the ring however can still be broken, if two (or more) consecutive nodes are faulty.

4.7 Front End Driver

The Front-End driver receives analogue data via optical links from the front-end. It is the last element in the optical readout chain used for event building and data reduction. The FED is a VME-based board, that performs the optical to electrical conversion, fast digitization, simple data processing and buffering. To reduce the amount of custom electronic circuits, the FED employs *Field Programmable Gate Array* (FPGAs). The FED has four types of FPGAs: the delay FPGA for synchronisation with the data arrival, the Front End FPGA for header extraction, data processing and reduction, a back-end FPGA for event building and buffering and a VME FPGA for the control interface. For maximum flexibility each of the FPGAs can be updated via different firmware. A single FED processes data from 96 optical fibers, each of which carries data from 256 channels (strips). The FED has a modular design, that matches the layout of the optical cables: it has 8 identical front-end units, each of them processing data from a single ribbon (12 fibers). The Block diagram of Figure 4.11 shows the functionality implemented in the FED: An Optical receiver performs the optical to electrical conversion, the delay FPGA is adjusted for a synchronous readout with the data arrival determining the sampling point. Data are digitized with 10bit precision at a rate of 40 MHz. Depending on the readout mode, different stages of data processing follow. Finally the data are packed and buffered for output.

The FED can be operated in 4 different modes:

FIGURE 4.11: *Front end driver block diagram [51].*

- Scope Mode
- Virgin Raw Mode
- Processed Raw Mode
- Zero Suppressed Mode

4.7.1 Scope Mode

In Scope Mode digitization has to be triggered by a trigger signal. Following the trigger signal data are constantly sampled at the clock rate (40 Mhz) with 10 bit precision. The number of clock cycles can be set to a maximum of 1022. The scope mode is an important tool for FED debugging and time synchronisation.

4.7.2 Virgin Raw Mode

In Virgin Raw mode data sampling is not triggered by a trigger signal but by the identification of APV headers. Once a header is identified, data are sampled with 10bit resolution for 256 clock cycles. Without further processing, the data of each channel are sent to the back-end FPGA. This readout mode is used for noise and pedestal runs. It can be used in addition for debugging purposes in physics runs; due to the high data volume, it cannot be used for the normal CMS operation.

4.7.3 Processed Raw Mode

Data are treated as in the Virgin Raw Mode, then reordered and pedestal subtracted, before transmission to the DAQ interface.

4.7.4 Zero Suppression Mode

Zero Suppression Mode is the default mode for data taking as it results in the lowest data volume. Data is processed as in Processed Raw Mode. After the reordering and the pedestal subtraction, the common mode noise is subtracted. The common mode level is calculated event by event as the median of the 128 strips of a single APV. The cluster finding algorithm is then applied to the pedestal and common mode subtracted data. For each single channel (strip) two thresholds ($thresh1$, $thresh2$) are defined for the cluster-finding algorithm [65], where $thresh1 \geq thresh2$ and the thresholds are defined in units of ADC counts. The cluster finding algorithm is sketched in Figure 4.12. Clusters need to have at least one strip exceeding $thresh2$, or two neighboring strips must be above $thresh1$; two consecutive clusters must be separated by at least two strips below $thresh1$. Output for all strips not being identified to belong to a cluster are suppressed - hence

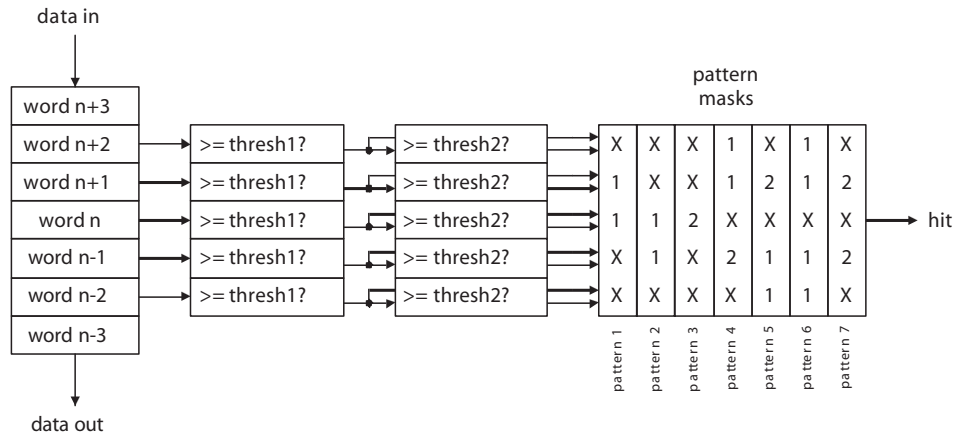


FIGURE 4.12: *Pattern identification for Cluster finding in Zero Suppression Mode [65]. A "2" in the pattern mask stands for a value \geq thresh2, "1" for \geq thresh1 and "X" for "dont care". Only data that matches one of the patterns is transmitted.*

the name Zero Suppression Mode. Further data reduction is achieved by restricting the output (which is the pedestal and common mode subtracted data of the strips forming a cluster) to 8 bits.

4.7.5 Data Readout

The FED is configured and can be readout via its VME interface. The data rate of this interface is however limited, allowing only for readout rates in the order of Hz , sufficient for testing and commissioning purposes. At nominal LHC operation however data will arrive at the average Level-1 Trigger frequency of about 100 kHz, and a FED will receive data at a rate of approximately 3 GB/s. To cope with this enormous data rates, the data are zero suppressed, and each FED is read out via Front-End Readout Links (FRL) [66] that are capable of data transfer rates up to 400 MB/s.

Chapter 5

The Cosmic Rack - A Large Scale Test Setup for the CMS Tracker

In order to operate successfully a device as complex as the CMS Silicon Strip Tracker, the properties of the hardware have to be characterized at a level that fully exploits the intrinsic detection potential of the Tracker. A number of issues have been identified, which need to be carefully studied to commission the detector, some of which concern the entire Tracker, while some are specific to the TOB:

- Validation of the grounding scheme and measurements of the noise performance.
- Measurements of the detector performance
 - Evaluation of the signal to noise ratio
 - Study of the time evolution of the detector response
 - Measurements of the inter-channel couplings
- Qualification of the geometrical precision of the detector subassemblies by track based alignment methods.

To study the above issues and to commission the data acquisition software and the reconstruction software with physics signals, a large scale test setup has been designed using TOB Rods in a dedicated mechanical support. In order to have results which are of relevance for the TOB, care has been taken to reproduce relevant design aspects and implement a large enough system size that accounts for the segmentation of the TOB, which is illustrated in Figure 5.1: the 344 Rods of each side of the TOB are organized in six layers, a layer is further segmented into cooling manifolds, control rings and readout groups. A cooling segment is formed by a group of rods that are served by the same cooling manifold ¹. A group of front-end electronics that is controlled by the same FEC is called a control ring [63]. A control ring never spans over two different cooling segments and contains between 4 and 10 Rods. Rods that share the same optical multi-ribbon cable are read out by the same FED are thus forming a *"Readout Group"*.

The realized test setup corresponds to a cooling segment, motivated by the implementation of a realistic grounding scheme (as will be discussed below), and has two control rings in order to study potential cross talk of the individual rings. The setup was operated successfully in test beams in 2004 [67], and in 2005 it has been fitted with a low-jitter cosmic trigger for tracking cosmic particles - hence the name *"Cosmic Rack"*.

¹Each Rod contains a small cooling pipe that removes the heat from the silicon detectors and the front-end electronics. The Rod cooling pipes are fed by manifolds located on the TOB end surfaces.

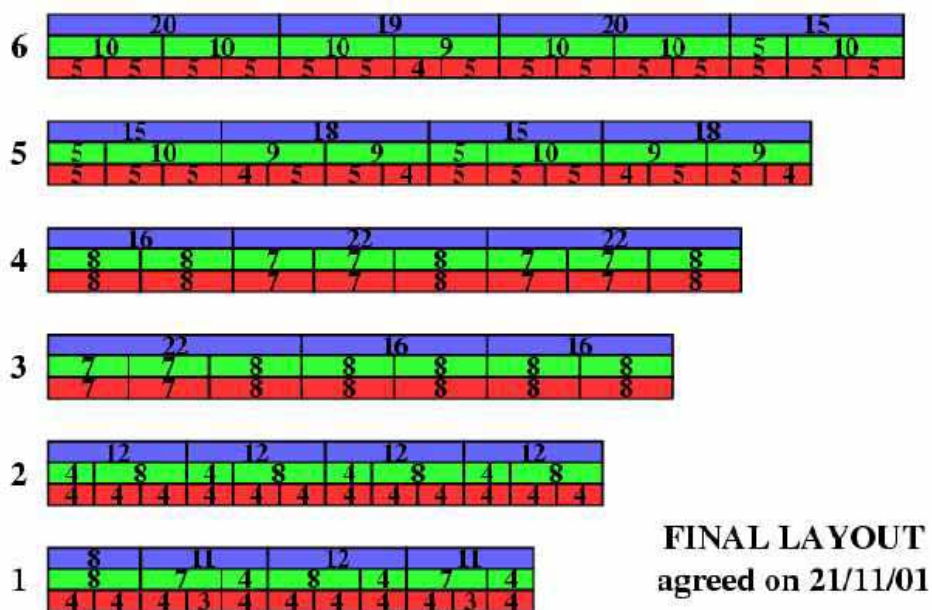


FIGURE 5.1: Organisation of 688 Rods in the TOB: The 344 Rods on each TOB side are grouped into: 22 cooling groups (blue), 46 control loops (green) and 67 optical readout cables (red).

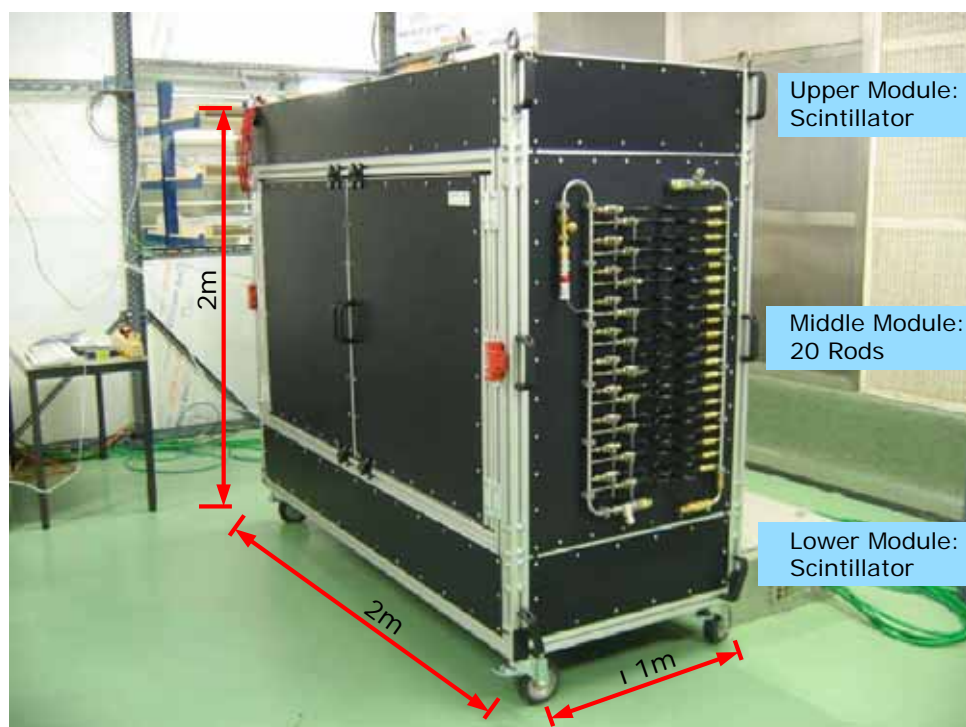


FIGURE 5.2: Picture of the Cosmic Rack in the laboratory [68].

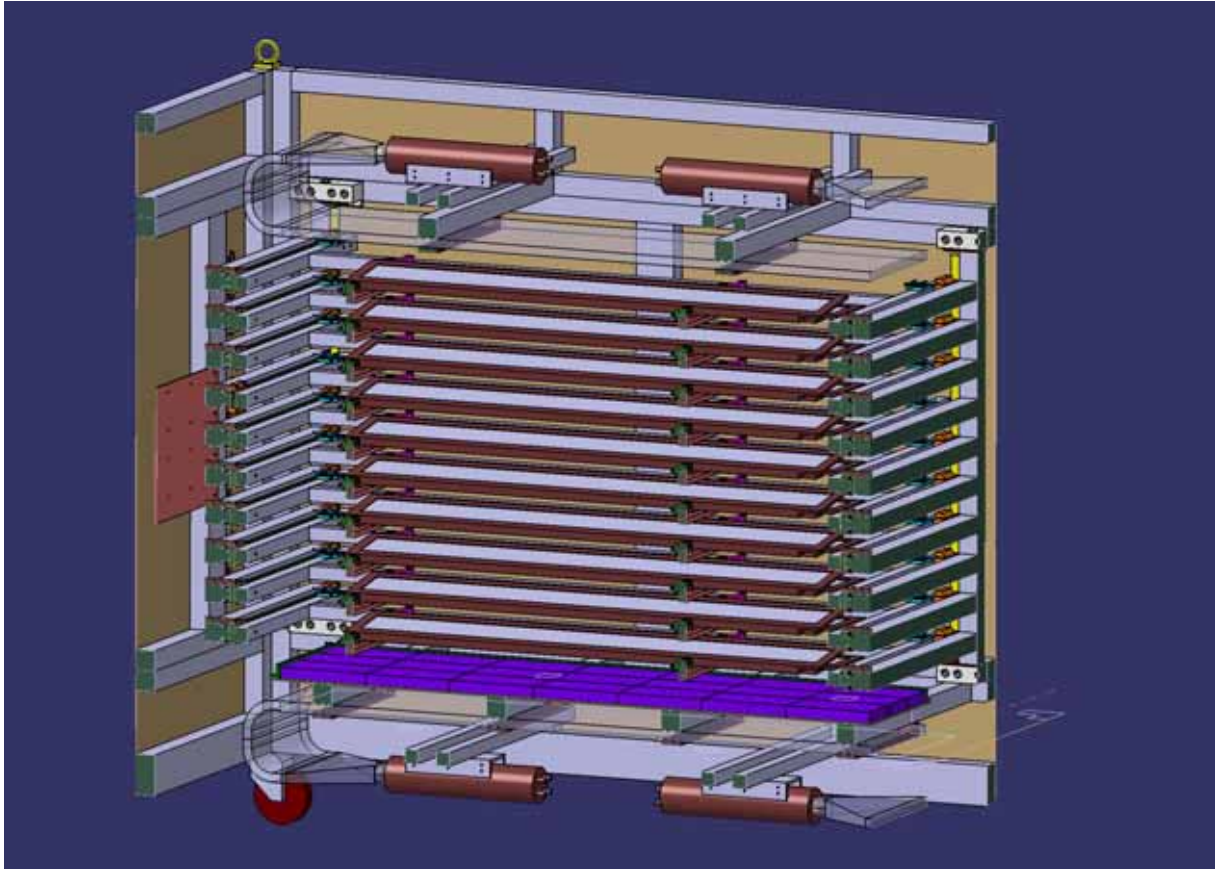


FIGURE 5.3: *Cosmic Rack drawn in section: the Cosmic Rack has 10 layers, each of which providing space for two Rods; for the trigger system, large plastic scintillators are mounted on top and bottom, each of which is equipped with two photo-multiplier tubes; a lead layer above the lower scintillator is filtering low momentum particles [69].*

5.1 Cosmic Rack Mechanics

The Cosmic Rack is organized in three modules (see Figure 5.2): an upper and a lower part housing the scintillators for the trigger system, and a central module where up to 20 rods are arranged in 10 layers (Figure 5.3). This modular design allows the use in the test beam or tracking of cosmic muons. Further details on the cosmic rack mechanics can be found in [70].

5.1.1 Cosmic Rack Geometry

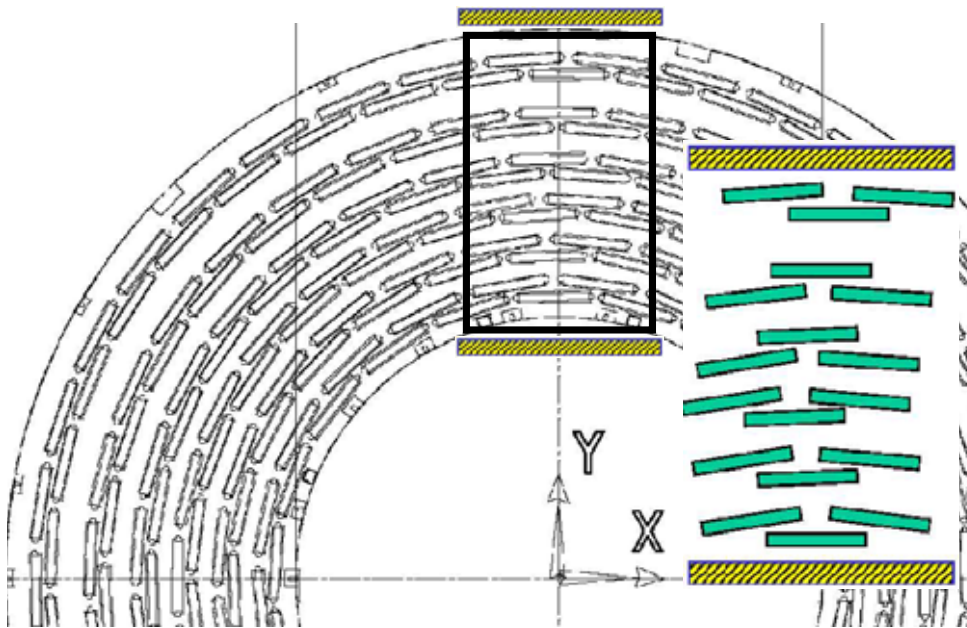


FIGURE 5.4: *Slice of the TOB cut along the r - ϕ plane [68].*

The Cosmic Rack approximates a slice of the TOB. A real slice - illustrated in Figure 5.4 - is however mechanically too complicated. The final design is realized with 10 (instead of 6) layers. All relevant geometrical aspects of the TOB were taken into account, with a layout optimized for tracking cosmic particles. The distance between the layers (86 mm) and the angle of the Rods (8.5°) are the average values of the TOB. Each of the 10 layers can be populated with 2 Rods (being flexible in the actual population). In the construction care has been taken to achieve a mechanical precision better than $500 \mu\text{m}$, in order to obtain a good track reconstruction efficiency even prior alignment of the setup.

5.2 Services and Grounding Scheme

5.2.1 Cooling

The Cosmic Rack has a dedicated C_6F_{14} cooling unit, that serves the direct cooling of the Rods. The coolant temperature can be regulated over a wide range, down to -20°C . The Cosmic Rack is housed inside an environmental chamber that can be cooled down to -20°C , allowing thus for measurements at the Tracker operating temperatures. In order to prevent condensation of the Rods, the interior of the Cosmic Rack is flushed with dry air.

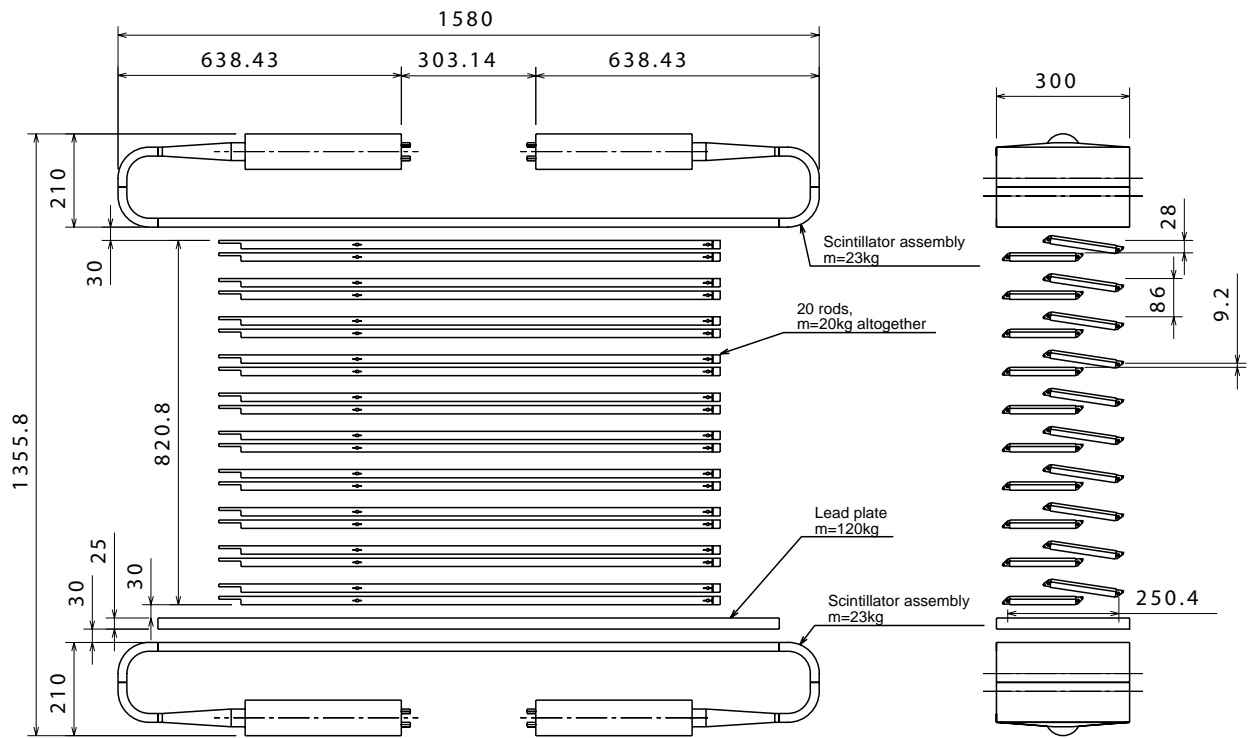


FIGURE 5.5: Dimensions of the Cosmic Rack and the scintillator system [69].

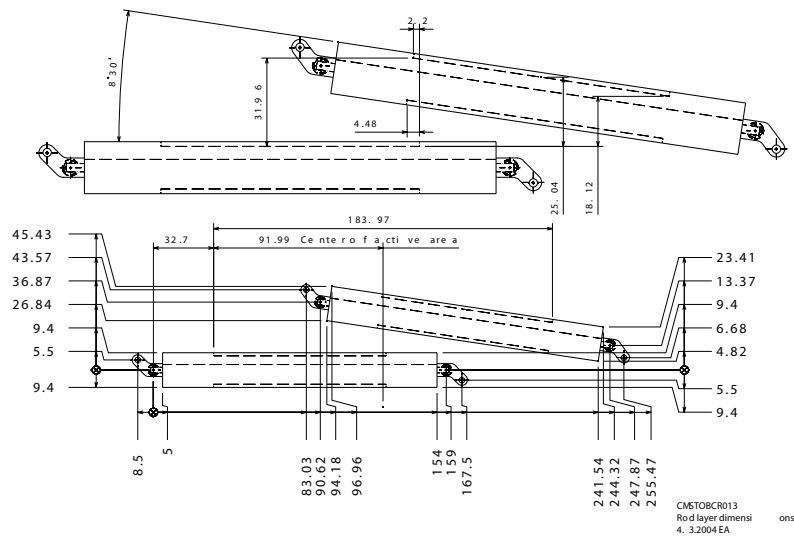


FIGURE 5.6: Arrangement of two Rods in a given layer. The Rod in the upper position is tilted by 8.5°, and the active sensor areas overlay by about 4 mm [69].

5.2.2 Grounding Scheme

In the TOB a number of Rods that are served by the same cooling manifold varies between 8 and 22. Cooling pipes are made of a Cu-Ni alloy, and all joints are soldered, therefore the Rods belonging to the same cooling segment have the mechanical structures electrically connected together. For each Rod, the power return line is connected to the manifold through a dedicated multi wire cable. So the manifold serves as local ground for all the Rods of a cooling segment. Different manifolds are then connected together and to the main support structure of the Outer Barrel through a system of metallic strips and rings.

In designing the Cosmic Rack, care has been taken to reproduce the grounding scheme of a TOB cooling segment, in order to be able to test it and validate it before the actual start of the TOB assembly. However, contrary to the TOB, in the Cosmic Rack the cooling manifolds are made of plastic, with quick connections to the Rod pipes. To recover the possibility of implementing the same grounding scheme as in the TOB, a copper bar has been added close to the Rod ends, and to which the ends of the Rod cooling pipes are connected with multi wire cables.

5.3 Data Acquisition System

5.3.1 Power Supply System

The Cosmic Rack power system uses prototypes of the final Tracker power supplies. Two CAEN EASY 4000 Crates with a total of 10 power supply modules of Type 4601H and two of 4601F (for the controls) are installed. These power supply modules are made up of 2 power supply units, each able to provide low voltage (1.25 V and 2.5 V) and high voltage (two individual channels adjustable up to 600 V) for a single Rod. The 48 V DC main power for these crates is supplied by an AC-DC of a pre-series type. The power supplies are controlled via a CAEN SY1527 mainframe with one branch-controller. The power supplies can be controlled locally or remotely via a telnet session or a dedicated graphical user interface. A small Programmable Logic Controller (PLC) interlock system measures the temperature of the ambient air and the temperature of the cooling lines of two selected Rods in the Cosmic Rack. To prevent the system from being powered with insufficient cooling thresholds for the air and coolant temperature have been set that - if exceed - will trigger a power down of all Rods.

5.3.2 Control and Readout Hardware

The Cosmic Rack DAQ control and readout system is made of final (or late stage prototype) Tracker components; for the studies presented in this thesis the following configuration was in use:

- 1 VME crate with final power supply
- 1 SBS VME crate controller (not final)
- 4 FEDs 9U
- 1 FEC 9U
- 1 CAEN 48V 5 kW AC-DC power supply (not final)
- 1 CAEN SY1527 mainframe with one A1676 branch controller
- 2 CAEN Easy 4000 Crates
- 10 CAEN Easy 4601H PSMs
- 2 CAEN Easy 4601F PSMs (for the controls - not final)

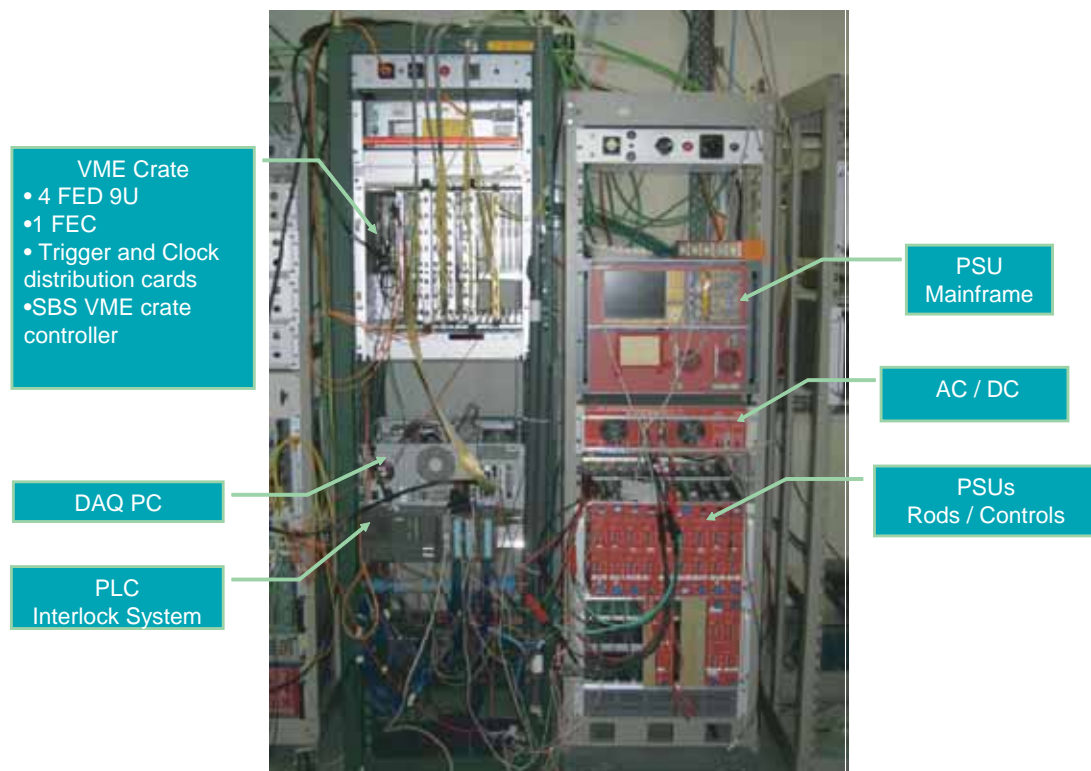


FIGURE 5.7: *Picture of the Cosmic Rack data acquisition system.*

5.4 Cosmic Trigger System

The readout electronics of the CMS Tracker works with a 40.8 MHz clock that is derived from the LHC machine, and synchronized to the arrival of the particles emerging from the LHC collisions, whereas in the Cosmic Rack the charge deposition due to impinging cosmic particles is in random phase with the clock. In order to be able to study the signal to noise ratio of the detectors with cosmic particles, and to characterize the time evolution of the physics signals and of the electronics coupling of neighboring channels, the trigger system must be able to select only tracks that are synchronous, within 2-3 ns, with the rising edge of the internal clock to simulate correctly the LHC operation environment. In addition, the difference in time between the signals collected in the various layers has also a time jitter, caused by the spread in the incident angles of the muons. The trigger system must therefore select tracks with a limited spread around a preferential incident angle. The obvious choice is to select vertical tracks, for which the rate is the highest. Finally, the trigger must deliver a decision within $4 \mu\text{s}$ after the actual charge deposit, to cope with the length of the readout pipeline that holds 192 samples.

A trigger system meeting all the above requirements has been realized using standard instrumentation components [71]. It is based on two large plastic scintillators mounted on top and on bottom of the Cosmic Rack, covering the active area of the Rods. Each scintillator is equipped with Photo Multiplier Tubes (*PMTs*) on both sides (Figure 5.8). A lead plate of 25 mm thickness is placed just above the bottom scintillator to avoid triggering on low energy particles.

The top and bottom *PMTs* on each side of the Cosmic Rack are connected to a coincidence unit, after delaying the signal of top scintillator by 3 ns, corresponding to the time of flight of straight relativistic particles. This first coincidence rejects tracks impinging on the Cosmic Rack with large incidence angles. The signals from the two sides are sent to a further coincidence unit that has a time window large enough to account for the propagation of the signals over the entire length of the two scintillators. The purpose of this second coincidence is to reduce background from noise in the scintillators and in the *PMTs*. This part of the logic provides good trigger signals for vertical particles, but its timing suffers from the jitter due to the large size of the scintillators, and it is therefore not suitable for gating the internal electronics trigger. For this purpose, the signals from the two upper scintillators are also sent to a mean timer unit, which provides a signal that corresponds to the mean arrival time on the two sides, delayed by a fix amount. This signal carries the precise information on the arrival time of the particle on the surface of the top scintillator. The signal from the mean timer is sent to a further coincidence unit together with the basic trigger signal, suitably delayed, so obtaining a signal that has a well defined delay with respect to the arrival time of the particle on the top scintillator. This final trigger signal is then sent to a gate that only accepts triggers within a window of 5 ns of the electronics clock. The phase of the clock in the different layers is then adjusted to account for the travel time of vertical relativistic muons from the top scintillator to each layer.

With the logic described the trigger rate is approximately 1 Hz, translating to about 1 hit per module every 25 s.

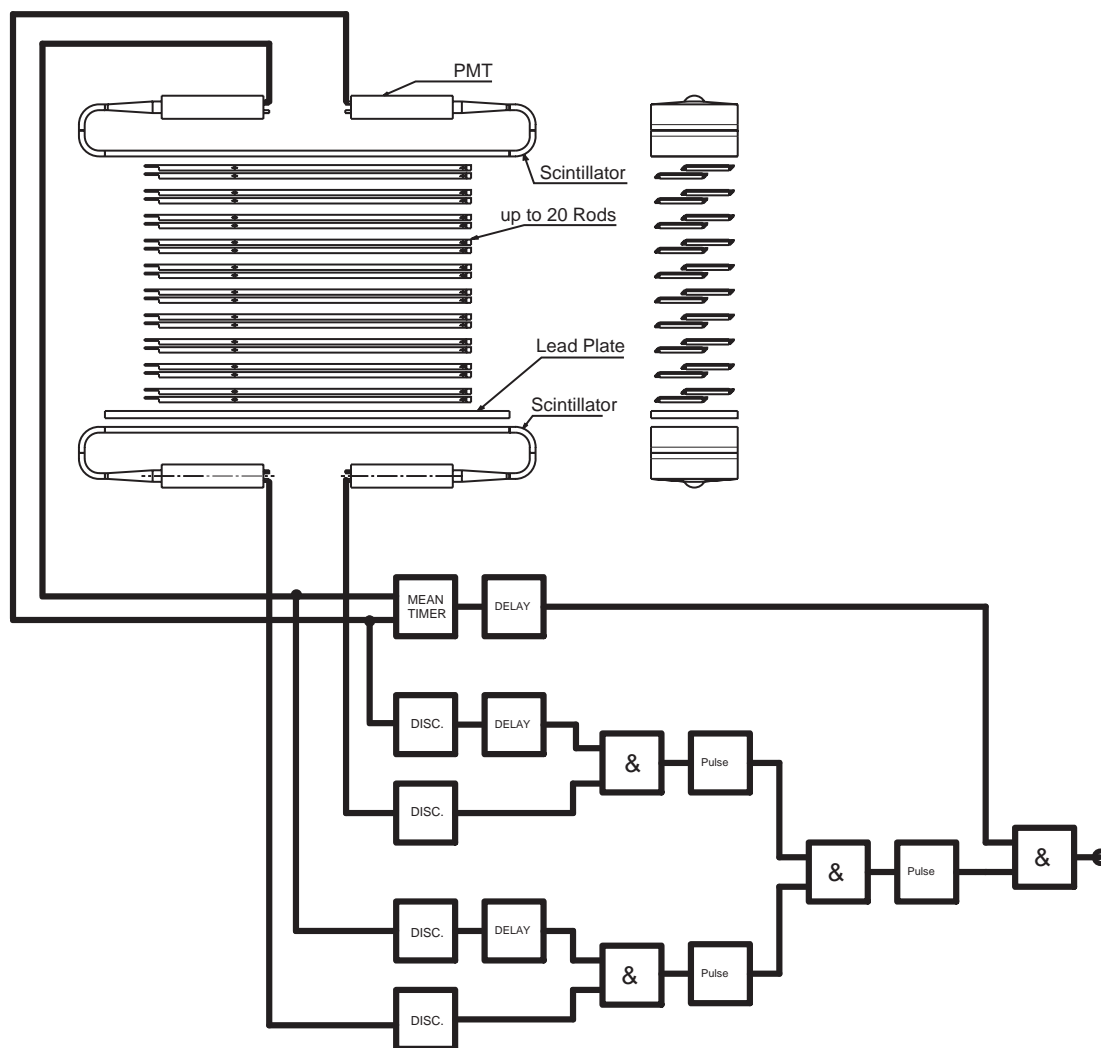


FIGURE 5.8: *Logic of the cosmic trigger. The mean timer provides a signal synchronous with the particle traversing the upper scintillator independent of the impact point. In addition the implicit coincidence for the signals of both scintillators reduces the rate of false triggers due to noise. Coincidences with tight time windows of the photomultiplier signals of either side, allow for a restriction in track inclination.*

5.5 Filtering Low Momentum Particles

The lower scintillator module of the Cosmic Rack is equipped with a 25 mm thick lead plate, in order to absorb secondary particles and low momentum muons. The stopping power of such layer can be determined from the graph of Figure 5.5, where the absorption range R of is given by:

$$R = \rho \cdot d \quad (5.1)$$

where ρ is the density and d the thickness of the absorber. The absorption range of the lead ($\rho = 11.8 \text{ g/cm}^3$) layer in Cosmic Rack is about 29.5 g/cm^2 , yielding for muons (mass $M=0.106 \text{ GeV}$) an R/M of about $280 \text{ g/(cm}^2 \text{ GeV)}$. Thus muons with an energy less then 120 MeV will be stopped in the absorber, before reaching the lower scintillator, and will not generate a trigger signal.

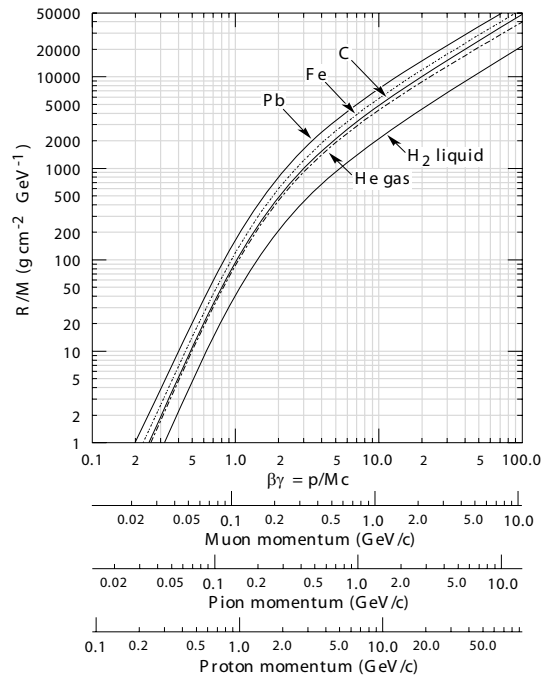


FIGURE 5.9: Range of heavy charged particles in hydrogen, helium, carbon, iron and lead. (M is the mass of the incident particle, R is the range in g/cm^2) [72].

5.6 Summary

The Cosmic Rack is a setup designed to track cosmic muons with TOB detectors. It is operated with final Tracker power supplies, the final control and readout system and serves for testing and characterization of the hardware and the development of the data acquisition and reconstruction software. Its low jitter trigger system, allows the selection of tracks synchronous with the fast readout electronics, thus detailed studies on the time evolution of the detector response can be performed. Furthermore with its geometry, that is optimized for tracking cosmic particles, the CMS reconstruction software can be tested, and alignment studies can be carried out. The Cosmic Rack was operated during several months. The analysis of the recorded data is described in the following chapters.

Chapter 6

Studies of the Noise and Grounding Scheme

6.1 Introduction

Low electronics noise is crucial to the operation of silicon strip sensors as the charge generation for a typical detector thickness ($\approx 500 \mu m$) is of the order of $40000 e^-$ and no intrinsic amplification (as for example in gas detectors) takes place. One of the design aspects of the Cosmic Rack was to validate in a large scale system the noise performance of the Tracker Outer Barrel and study effects arising from different grounding schemes and power supply systems. In this chapter noise measurements in both readout modes of the APV25, the peak and deconvolution mode will be presented. These measurements have been performed at room temperature and at $-10^\circ C$. Different grounding configurations have been evaluated and power supplies tested. Furthermore the correlation of noise between neighboring strips has been studied.

6.2 Expected Noise Performance

6.2.1 General Concepts

The theoretically predicted noise performance of TOB modules in combination with the readout electronics will be derived below. General concepts of electronics noise sources will be explained following [73].

A current I , due to the movement of N charge carriers distributed along the path of length l , can be written as:

$$I = \frac{q_e v N}{l} \quad (6.1)$$

where q_e is the charge of the carriers, and v is their average velocity.

In an actual measurement one observes that the current is not constant, but is subject to random fluctuations - electronics noise. Noise sources are either represented as voltage sources e_n or current sources i_n , with the spectral noise density defined as:

$$e_n^2(f) = \frac{dV_{noise}^2}{df}; \quad i_n^2(f) = \frac{dI_{noise}^2}{df} \quad (6.2)$$

As seen from eqn.6.1 electronics noise can be caused either by variation of the velocity (Thermal Noise) or by the fluctuating number of charge carriers N (Shot Noise). All ohmic conductors are subject to thermal noise. The spectral power density of thermal noise is given by

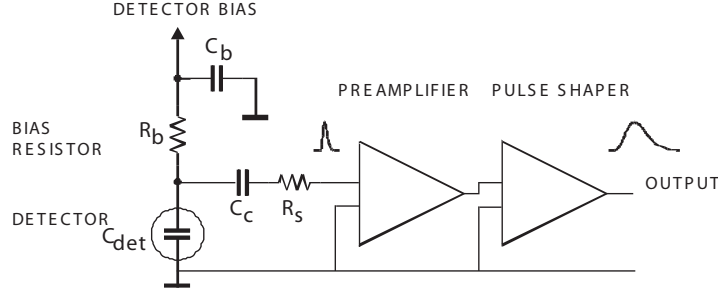


FIGURE 6.1: Schematics of strip sensor and front end electronics [73].

$\frac{dP_{noise}}{df} = 4kT$ (where kT is the thermal energy), which translates for a resistance R to a noise voltage density of:

$$e_n^2 = 4kTR \quad (6.3)$$

or a current density of:

$$i_n^2 = \frac{4kT}{R} \quad (6.4)$$

Shot noise is an effect arising from the discrete nature of charge. It is found in non-ohmic conductors such as p-n junctions. The spectral noise density for shot noise depends on the (DC) current I and the charge of the charge carriers q_e :

$$i_n^2 = 2q_e I \quad (6.5)$$

Both thermal noise and shot noise are white noise sources i.e. their noise spectrum is constant for all frequencies ($e_n(f) = \text{const}$, $i_n(f) = \text{const}$).

The measured noise on the output e_{on} however depends on the transfer function of the system $A(f) = \frac{U_{out}(f)}{U_{in}(f)}$ and can be written (generalized for frequency dependent noise) sources as:

$$e_{on}^2 = \int_0^{\infty} A^2(f) \cdot e_n^2(f) df \quad (6.6)$$

6.2.2 Noise of Silicon Strip Sensors

The equivalent circuit diagram of a silicon strip sensor with connected readout electronics is given in Figure 6.1. A given strip with capacitive coupled readout is represented by its total capacitance C_{det} , a coupling capacitance C_c , the resistance of the connection line to the amplifier R_s , the bias resistor R_b and a filtering capacitance of the bias circuit C_b .

The noise sources of this circuit are summarized in Figure 6.2, derived under the assumption that C_b and C_c can be considered as shorts. Noise sources appearing in this figure are grouped into parallel and serial noise sources. Serial noise sources are shown as voltage sources and parallel sources as current sources.

Equivalent Noise Charge

The noise of a system can be quoted for example as the RMS of a noise voltage or a current. However for systems in which a charge is measured, the noise is often quoted in terms of the Equivalent Noise Charge (ENC). The ENC is defined as the charge that, if injected in the input, gives a S/N ratio of 1.

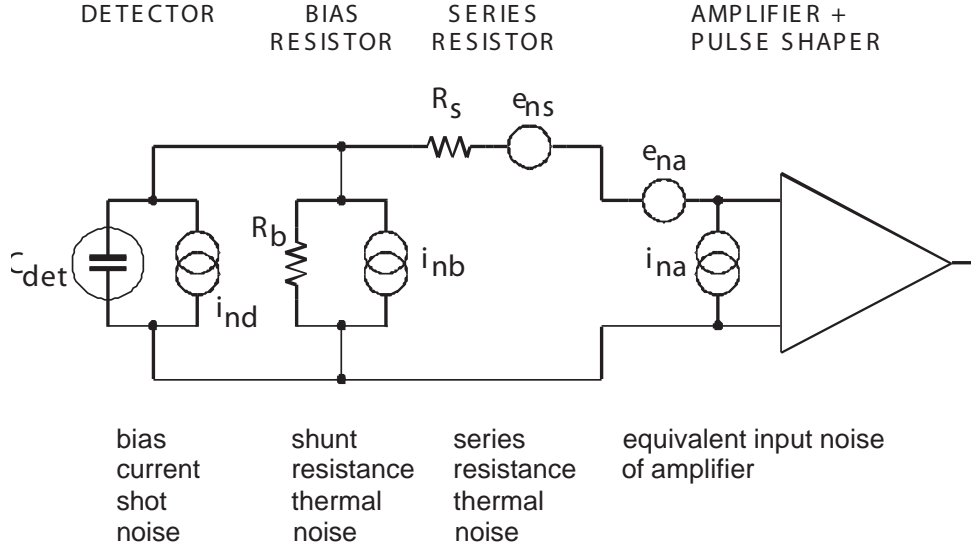


FIGURE 6.2: Equivalent circuit for noise analysis [73].

For the circuit shown in Figure 6.2 the ENC can be written as [73]:

$$Q_n^2 = i_n^2 \tau F_i + C^2 e_n^2 F_v \frac{1}{\tau} \quad (6.7)$$

Where i_n^2 includes the parallel (current) noise sources:

$$i_n^2 = 2q_e I_b + \frac{4kT}{R_P} + i_{na}^2 \quad (6.8)$$

and e_n^2 the serial (voltage) noise sources:

$$e_n^2 = 4kT R_S + e_{na}^2 \quad (6.9)$$

F_i and F_v are called *shaping factors* and depend on the pulse shaping function:

$$F_i = \frac{2}{T_S} \int_{-\infty}^{\infty} |W(t)|^2 dt F_v = \frac{T_S}{2} \int_{-\infty}^{\infty} \left| \frac{W(t)}{dt} \right|^2 dt \quad (6.10)$$

Where T_s is the characteristic shaping time (e.g. the peaking time τ) and $W(t)$ is the pulse response of the system - normalized to 1 at the peaking time. In case of a CR-RC shaper $W(t)$ is given by

$$W(t)_{CR-RC} = \frac{t}{\tau} e^{1-\frac{t}{\tau}} \quad (6.11)$$

Thus for a simple CR-RC shaper

$$F_i = F_v = \frac{e^2}{8} \quad (6.12)$$

The different noise sources and their approximate contribution are evaluated for TOB modules in Table.6.1. The total noise is approximately 1300 e^- in peak mode and 2200 e^- in deconvolution mode. As expected for a well designed system, the biggest contribution is coming

from the amplifier itself, and it is mainly caused by shot noise and thermal noise on the current path of the transistors; it has been parametrized as (Appendix A.2):

$$Q_N^{RMS} = a + C_{det} \cdot b \quad (6.13)$$

For non-irradiated sensors shot noise from the bias current can be neglected, and the second biggest contribution comes from the thermal noise of the aluminum readout strips. With accumulation of irradiation, the bias current will increase from 2 nA to 1500 nA [74] and will contribute additional noise of about $930 e^-$ in peak mode and $450 e^-$ in deconvolution mode, resulting in a total expected noise of about $1600 e^-$ in peak mode and $2200 e^-$ in deconvolution mode.

Noise Source	Type	ENC (RMS e^-)	Peak Mode Useful Expression at T=20°C	Deconvolution Mode
Reverse bias current I_b	parallel	$\frac{1}{q_e} \frac{e}{\sqrt{8}} \sqrt{2q_e I_b \tau}$	$\approx 108 \cdot \sqrt{I_b(\mu A) \tau(ns)}$ (34 e^-)	$\times 0.44$ (15 e^-)
Shunt resistance R_b	parallel	$\frac{1}{q_e} \frac{e}{\sqrt{8}} \sqrt{\frac{4kT}{R_b \tau}}$	$\approx 24 \cdot \sqrt{\frac{\tau(ns)}{R_b(M\Omega)}}$ (135 e^-)	$\times 0.44$ (60 e^-)
Metal strip resistance R_s	series	$\frac{1}{q_e} \frac{e}{\sqrt{8}} \sqrt{4kT \frac{R_s/3}{\tau}} C_{tot}$	$14 \cdot C_{tot}(pF) \cdot \sqrt{\frac{R_s(\Omega)}{\tau(ns)}}$ (532 e^-)	$\times 1.54$ (820 e^-)
Front-end electronics	series	$a + C_{det} \cdot b$	$246 + 36 \cdot C_{tot}(pf)$ (1218 e^-)	$396 + 60 \cdot C_{tot}(pf)$ (2016 e^-)
Total			$\approx 1340 e^-$	$\approx 2180 e^-$

TABLE 6.1: Noise sources, types and equivalent noise charges (ENC) evaluated for the CMS TOB read-out system [51]. In the evaluation of the contribution from the metal strip resistance, the effective resistance for the noise is taken to be approximately a third of the strip resistance. This is a transmission line effect taking into account that the resistance is distributed over the total strip length. The values in brackets are calculated for a TOB module using $T_s = 50 ns$, $R_{bias} = 1.6 M\Omega$, $R_{metal} = 100 \Omega$, $C_{tot} = 27 pF$ and $I_b = 2 - 1500 nA$ (the high leakage current is expected after 10 years at LHC) [74]. Parameters for the readout electronics are taken from [57]. The factors for the deconvolution mode are derived in the Appendix B, they can be roughly estimated considering that in the deconvolution mode the effective shaping time is $\tau/2$.

6.3 Common Mode Noise

In addition to the noise sources discussed above, a system can also be subject to noise sources originating from the power supplies or electronics pickup. Noise from such sources often affects many channels simultaneously, and is therefore referred to as *Common Mode Noise*. For an example one might think of a system with floating ground potential, electronics pickup of the line will thus add a signal to all channels that are using this as a reference potential. Typical examples of sources for common mode noise are electronics pickup via the ground path and

noise originating from the power supplies as illustrated in Figure 6.3. Other effects that can appear as common mode noise, are vibrations that change stray capacitances and thermal effects. Potential sources of common mode noise should be identified and removed, as much as possible.

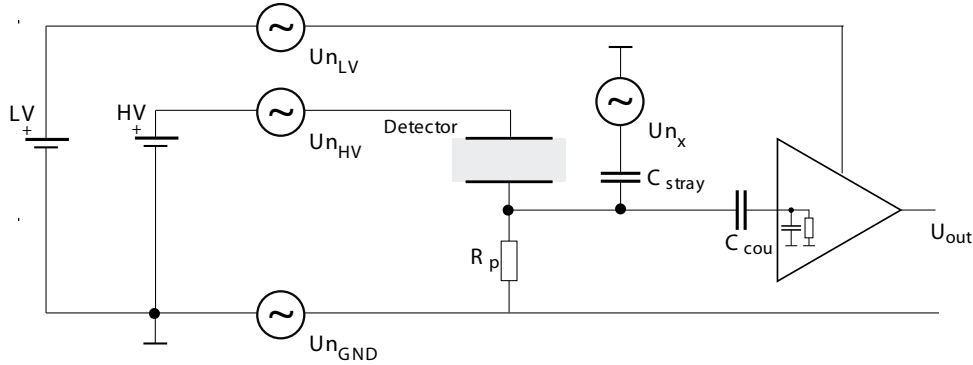


FIGURE 6.3: Example of common mode noise sources. $U_{nGND}, U_{nLV}, U_{nHV}$ include noise of the low and high voltage power supplies and pickup on the transmission lines. The strips can couple via stray capacitances and inductive pickup to external electronics signals (such as clock and data transmission lines), which become source of noises pickup U_{nX} .

For the calculation of the common mode noise, the terms and definitions described below are used.

6.3.1 Terms and Definitions

The data processed by the front-end electronics can be split into the following contributions: a physical signal $S(i, k)$, a baseline shift $P(i)$ called "pedestal", the intrinsic noise fluctuations $N_{cms}(i, k)$, and a common mode shift $C(j, k)$ that affects a readout group j ($i \subset j$), where i refers to the channel number and k to the event number.

$$ADC(i, k) = S(i, k) + P(i) + N_{cms}(i, k) + C(k, j) \quad (6.14)$$

In the absence of a physical signal the pedestal is calculated as the average of the raw data over n events:

$$P(i) = \frac{1}{n} \sum_{k=1}^n ADC(i, k) \quad (6.15)$$

The *Raw Noise* is defined as the variance of the raw signal:

$$N_{raw}(i) = \sqrt{\frac{1}{n} \sum_{k=1}^n (ADC(i, k) - P(i))^2} \quad (6.16)$$

The common mode level can be (in some cases) estimated event by event, and subtracted from the raw data. Then the common mode subtracted noise can be defined as:

$$N_{cms}(i) = \sqrt{\frac{1}{n} \sum_{k=1}^n (ADC(i, k) - P(i) - C(j, k))^2} \quad (6.17)$$

To estimate the common mode level (or shift), a model has to be chosen, which should reflect the way the common mode noise couples to the a suitably chosen group of channels k (e.g. a

readout group, or a power group). For an equal coupling of the common mode to the channels, the mean and the median are suitable estimators. In case of the mean, the common mode level is calculated as:

$$C(j, k) = \frac{1}{g} \sum_{i=1}^g (ADC(i, k) - P(i)) \quad (6.18)$$

for the g strips belonging to the group j , in event k .

In the CMS tracker the common mode subtraction is performed on the group of channels read out by the same front-end chip; the common mode level is calculated as the median of the pedestal subtracted signals. The median is preferred over the mean as (thanks to the low occupancy) it is not influenced by charge deposition due to physics events.

The common mode noise is the RMS of the common mode level in a sample of events. Since the common mode noise and the intrinsic noise are uncorrelated, the Raw Noise can be written as:

$$N_{raw}(i) = \sqrt{N_{cms}(i)^2 + RMS(C(j, k))^2} \quad (6.19)$$

6.4 Measured Noise Performance

6.4.1 Scaling to Tickmarks

An evaluation of the noise in ADC counts, does not provide a complete estimate of the absolute performance of the system, since the output of the readout chain scales with the gain of the optical link, which depends on the performance of the laser, the efficiency of the connections and the settings chosen for the laser driver. An absolute calibration of the readout chain can be obtained, for example, by comparing signals with known charge depositions (e.g. minimum ionizing particles traversing the detectors at normal incidence). Alternatively a sufficient precise calibration of the chain can be obtained in a simple way, from the tickmarks (the synchronisation pulse of the APVs). A tickmark has a defined height of 8 mV, which is approximately equal to the output of the APV25 for an input signal of 200000 e^- [75]. To be able to do this scaling, the tick height is extracted from a timing run performed with the same settings as the pedestal run¹. Having measured the pulse height of the tickmark, the conversion from the noise in ADC counts to the equivalent noise charge is thus given by:

$$noise_{ENC} = noise_{ADC} \cdot \frac{200000}{tickheight[ADC]} e^- \quad (6.20)$$

Although the ENC calculated by this method is not accurate to the percent level, it removes the dependence on the optical gain (see Figure 6.4) and gives results that are comparable with the measurements of signal to noise and the estimated noise performance.

6.4.2 Tests of the Grounding Scheme

The grounding scheme of the Cosmic Rack has been designed to reproduce the TOB. A few open issues on the TOB grounding scheme have been studied with the Cosmic Rack to find the optimal configuration.

Tests were carried out in peak mode on a SS6 rod. The tests focused on the module position six, which is the first module on the bus (see Figure 6.5), and which has been observed to be

¹The header of a data frame contains samples of the same height as the tickmark, but this information is removed in the FED 9U and not accessible.

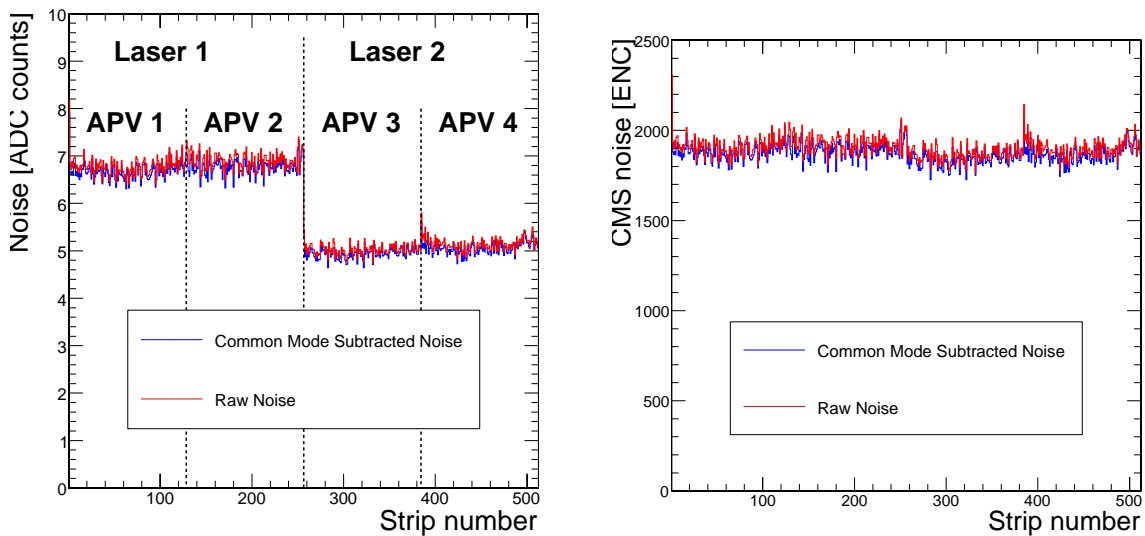


FIGURE 6.4: Noise profile of raw and common mode subtracted noise for SS_4 modules in deconvolution mode. The plot in ADC counts (left) shows a jump at the border of the APV pairs caused by different optical gain of the two optical channels. The scaling to tickmarks (right) removes this effect.



FIGURE 6.5: Module numbering for single sided rods.

the most sensitive to common mode noise. The module is facing the CCUM, which contains all clock and control data lines, and it is the first on the power bus and it is thus affected by the currents drawn from all other modules. First it has been observed, that connecting the power return line of the rod to the cooling pipe has a stabilizing effect on the rod electronics. The connection is realized by a few cm long wire (called "YW") that is joining the rod power return line and the cooling manifold supplying the rod. The difference in performance with and without this ground connection is illustrated in Figure 6.6.

Since it is a single point connection having a length of a few cm, it has a significant inductive impedance at frequencies in the MHz range. To further improve the stability of the system new interconnect cards were tested that introduce further connections between the return line and the cooling pipes (see Figure 6.7). As the noise profile is flat and the common mode noise low, the effect of these additional connections is marginal. However a visible effect was observed for the outermost strips of a sensor, as indicated in Figure 6.8. As no negative side effects were measured, these additional connections were implemented in the final design of the interconnect cards used in the TOB.

The powering scheme for the CMS Tracker foresees two power cables connected in series. The first cable is routed inside the Tracker volume, and is made of aluminum to reduce the contribution to the total Tracker material; it has a length of about 5 m. Outside the Tracker such cable is connected in a patch panel box to a second cable, that reaches the power supply at the back end; the second cable is made of copper and has a length of approximately 35 m.

For the copper cables two types have been designed: the Multi Service Cable (MSC) and the Low Impedance Cable (LIC) [76]. The LIC is a multiconductor cable with complex layout optimized to reduce the self inductance and maximize the distributed capacitance, and thus

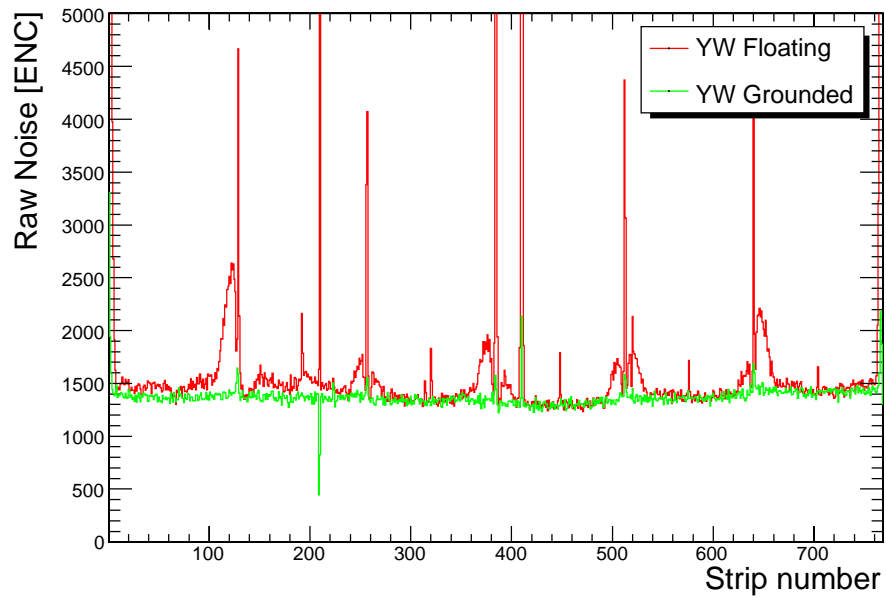


FIGURE 6.6: *Effect of the connection between the cooling pipe and the return line of a rod. "YW Grounded" indicates that the connection is in place, "YW Floating" means that the connection is not made.*

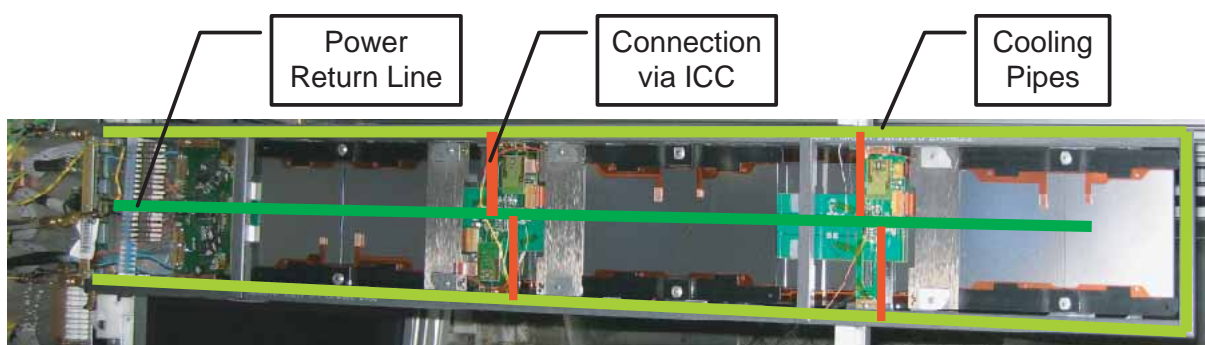


FIGURE 6.7: *Illustration of the influence of the Rod Inter-Connect Cards (ICC) on the grounding scheme.*

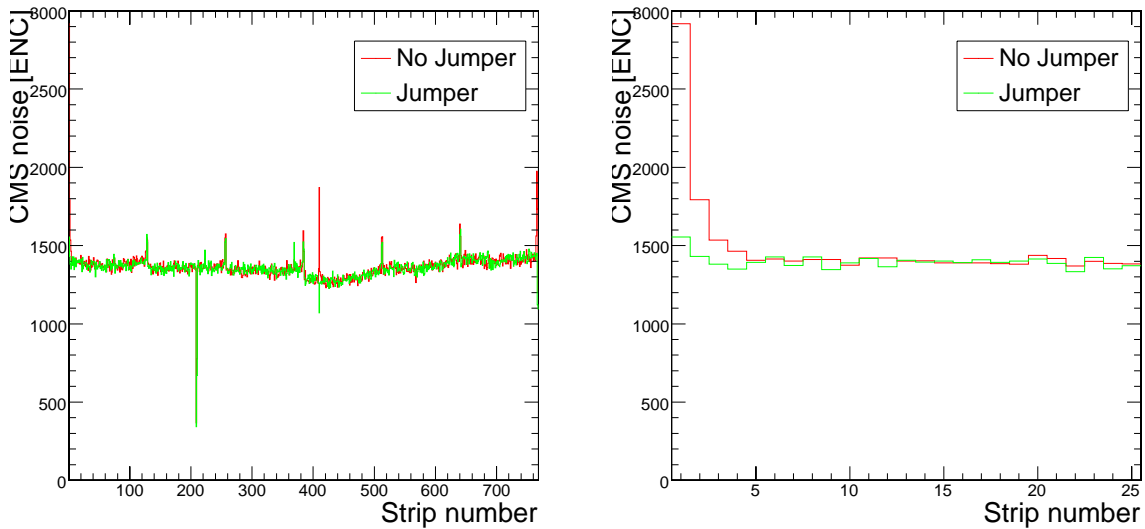


FIGURE 6.8: *Effect of grounding connection in the Rod interconnect card. The general noise profile is unaffected, however the noise for the outermost strips is significantly reduced.*

minimize the impedance. The MSC cable has a conventional layout, with twisted pairs used for the sense wires, and large single conductors for the power lines. A comparison between the MSC cable and the LIC cable is shown in Figure 6.9. The LIC cable shows significantly less common mode noise than the MSC cable. The additional common mode noise of the MSC cable however is flat and the (median) common mode subtracted noise is about the same for both cables.

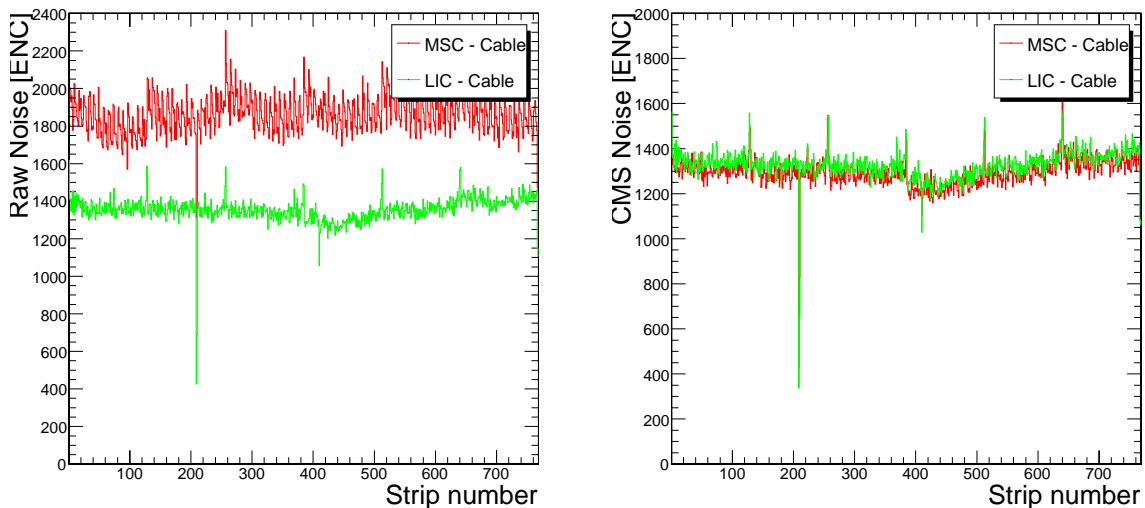


FIGURE 6.9: *Comparison of the power cables. The LIC cable has significantly lower common mode noise than the MSC cable. The common mode subtracted noise is not influenced.*

6.4.3 Study of the Noise Profile

The default common mode subtraction implemented in the FEDs consists in subtracting the median of the pedestal subtracted readings of the 128 channels of a readout chip.

A typical noise profile in the final grounding configuration and with final power supplies is

shown in Figure 6.10 . The noise profile is flat and the common mode noise is low. Due to the serial readout however low frequency noise modulating the analog data transmission can still appear.

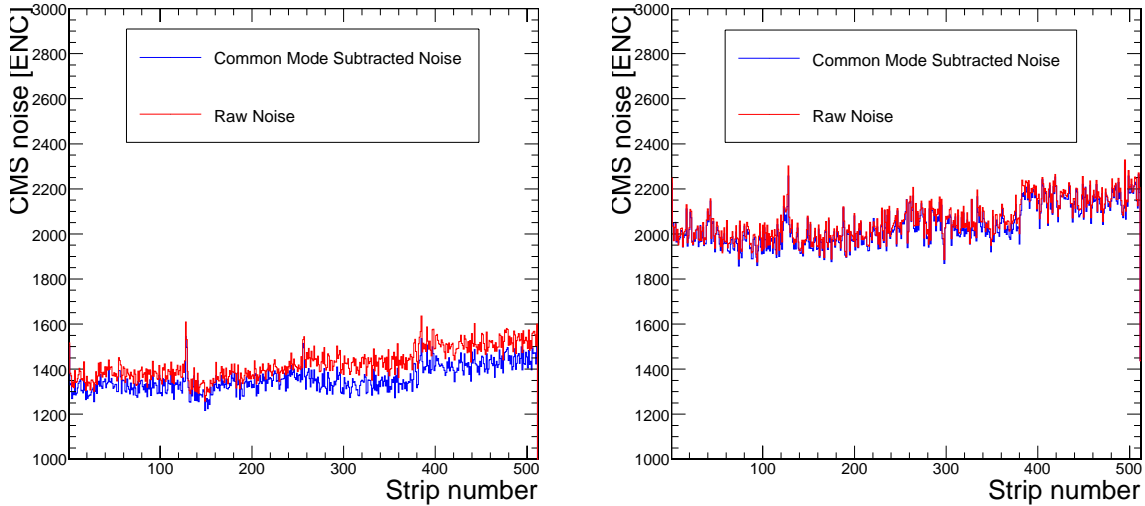


FIGURE 6.10: Typical noise profile of raw and common mode subtracted noise for SS_4 modules in peak (left) and deconvolution mode (right).

In some cases on module position 6 of a rod a slight deviation of the otherwise flat profile is found as shown in Figure 6.11 . These data have been processed with a more sophisticated common-mode subtraction algorithm, applied offline. The baseline of the chip is described by a line with nonzero slope, determined event by event, and such slope is subtracted from the pedestal subtracted raw data ("linear" common mode subtraction). The principle is illustrated in Figure 6.12. Such a procedure removes the additional noise in module 6 and restores the flat noise profile as demonstrated by the rightmost plot of Figure 6.11.

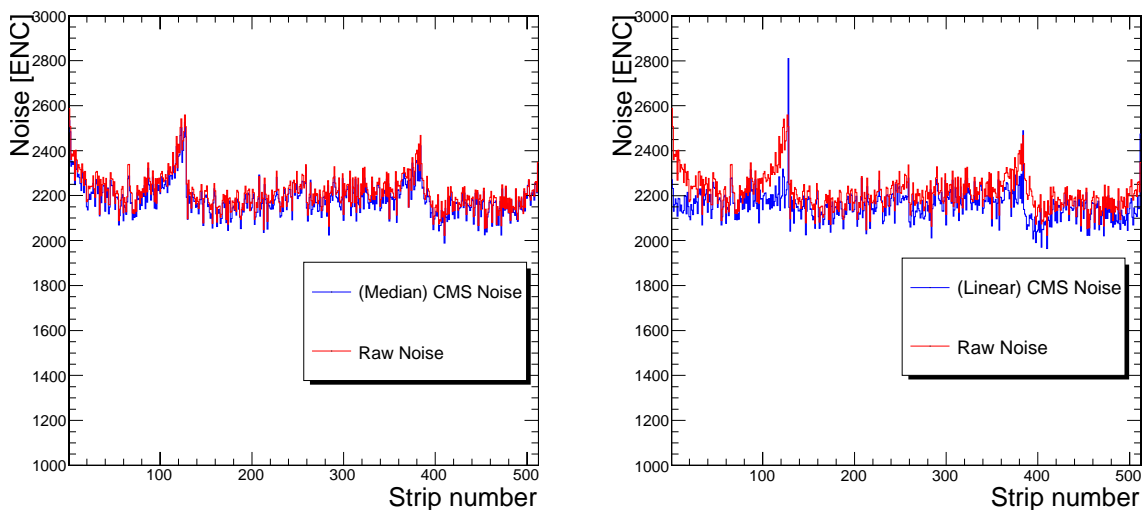


FIGURE 6.11: Non-flat profile (left); effect of linear common mode subtraction (right).

A summary of noise measurements on final rods for the Cosmic Rack is given in Table 6.2. The measurements have been performed in with fully biased detectors (HV=300V, 400V) in

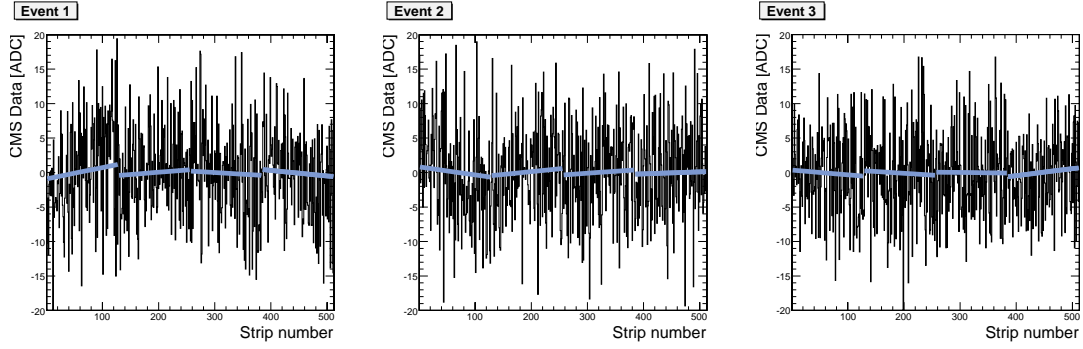


FIGURE 6.12: Illustration of the linear common mode subtraction. The baseline in a chip is described by a line with non zero slope, event by event.

TABLE 6.2: Summary of noise measurements with the Cosmic Rack. Values quoted in ENC have been obtained using the method of scaling to tickmarks. The noise performance for different rod types is quoted separately, "All" indicates the cumulative performance without distinction of the rod type. The measured values of the common mode subtracted noise are in good agreement with the predictions shown in Table 6.1 (e.g. compare the values measured at 20°C for peak mode and deconvolution mode with the prediction of 1300 e^- , 2200 e^- respectively).

Run # Pedestals	Run # Timing	APV Mode	Temp [°C]	Rod- Type	CMS Noise [ENC]		RAW Noise [ENC]	
					Mean	Rms	Mean	Rms
200287	200285	PEAK	20	ALL	1388	67	1505	78
				SS4	1348	61	1529	80
				DS	1398	64	1499	76
200682	200680	PEAK	20	ALL	1398	68	1436	69
				SS4	1358	64	1409	65
				DS	1408	66	1443	68
400124	400120	PEAK	20	SS6	1314	60	1750	118
200275	200285	DECV	20	ALL	2105	94	2129	94
				SS4	2087	94	2113	94
				DS	2110	93	2133	94
200326	200329	DECV	20	ALL	2056	97	2163	106
				SS4	2065	100	2227	98
				DS	2054	96	2147	102
400206	400205	DECV	20	SS6	1992	99	2356	124
200905	200910	PEAK	-10	ALL	1231	60	1259	59
				SS4	1188	54	1221	53
				DS	1238	58	1265	58
200923	200910	PEAK	-10	ALL	1266	245	1367	298
				SS4	1223	249	1335	302
				DS	1273	244	1372	297
200911	200910	DECV	-10	ALL	1878	86	1916	86
				SS4	1851	91	1892	90
				DS	1883	85	1920	85
200920	200910	DECV	-10	ALL	1880	88	1909	87
				SS4	1851	91	1885	88
				DS	1885	87	1913	86
200916	200910	DECV	-10	ALL	1942	91	1975	92
				SS4	1906	96	1942	95
				DS	1948	89	1980	90

peak mode and deconvolution mode at room temperature (coolant temperature set to 15°C , air temperature inside the Cosmic Rack, measured to be 20°C) and at the tracker operating temperature (coolant temperature set to -20°C ; cold room set to maximum cooling; air temperature measured to be $\approx -10^{\circ}\text{C}$).

The common mode noise is low and gives negligible contribution to the total noise. The measured noise values are in good agreement with the expected values. The decrease of noise observed when comparing data at room temperature and data at -10°C cannot be explained by the decreasing thermal noise of the bias resistor and aluminum strips, but it is likely dominated by effects of the readout electronics.

6.4.4 Tests of the Tracker Power Supply

Initial tests of the CAEN 4601H power supply system showed that a large common mode noise on the TOB rod detectors was caused by a low frequency oscillation in the CAEN power supply (Figure 6.13).

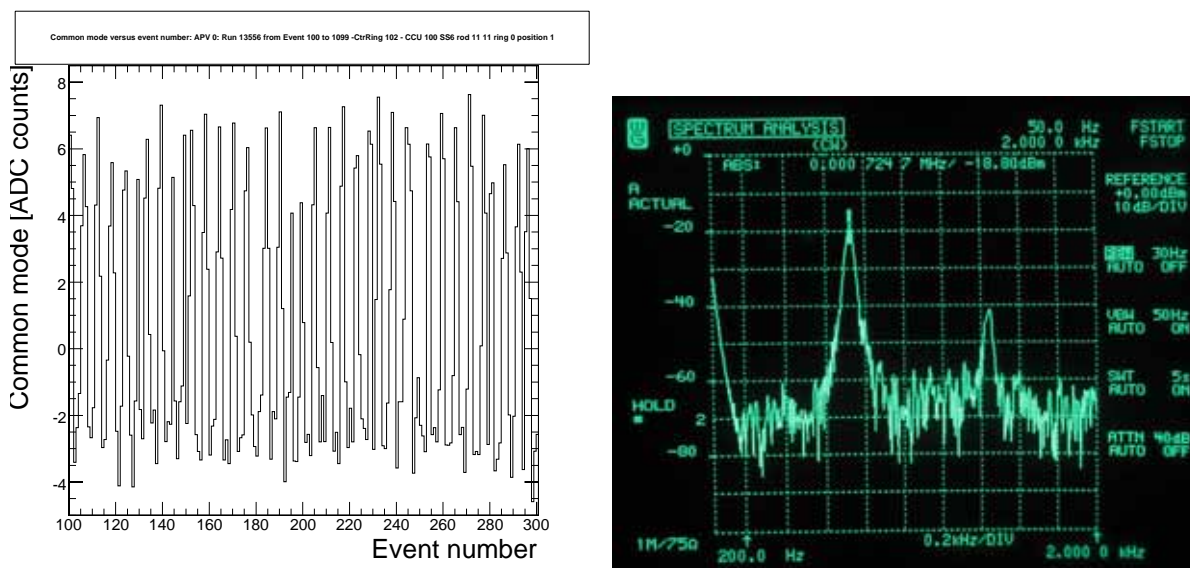


FIGURE 6.13: Oscillations of the power supply system shown for an SS6 rod powered via a 50 m long LIC cable. The periodic fluctuations in the common mode level (left) are due to oscillations on the power lines. A screenshot of the measured spectrum (right) shows a clear peak at 724 Hz.

Further investigation carried out following suggestions of [77, 78], showed that the frequency was inversely proportional to the square root of the supply cable length, indicating a \sqrt{LC} oscillation with the inductance supplied by the power cable.

The results of measurements with different LIC cable lengths and loads are summarized in Figure 6.14. In addition the power supplies were tested using a dummy load (consisting of a resistance of $0.6\ \Omega$ in parallel with a capacitance of $1500\ \mu\text{F}$ for both the 1.25 V and the 2.5 V line) instead of a rod. With this dummy load no oscillation was observed.

The results were presented to CAEN; following these observations the power supplies were modified by increasing the bandwidth of the feedback amplifier. Tests with these modified power supplies showed a steady DC voltage with no oscillations (Figure 6.15). Although the source of the oscillation has been removed, its origin is not yet fully understood. Positive feedback however has been excluded from the possible causes, as the oscillations are stable with an amplitude of a few millivolt, while positive feedback oscillations should rapidly grow in amplitude until the supply shuts off from over voltage.

One hypothesis that fits all the data is that the oscillations are caused by a shock exciting an LC resonant circuit, that is composed of the power and sense lines in the LIC cable and the load

Rod Type	LIC Cable Length [m]	Frequency [Hz]
SS4		
	35	1084
	50	947
	70	820
DS	85	732
	35	566
	50	420
	85	371

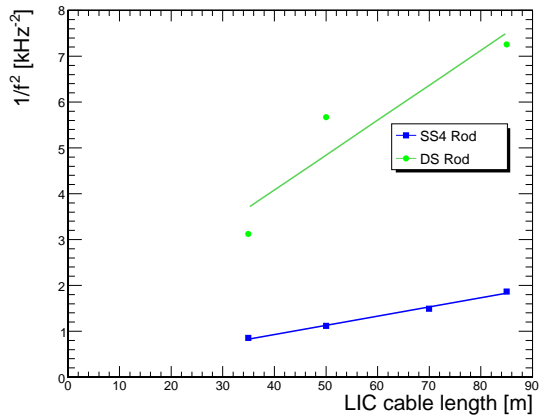


FIGURE 6.14: Dependence of the oscillation frequency on the length of the power cable and the load. The double sided rod (DS) has a higher capacitance than the Single Sided Rod (SS4) and therefore the oscillation has a lower frequency. The frequency also approximately scales with $1/\sqrt{l}$ where l is the length of the LIC cable (the inductance of the following aluminum cable of 5 m length is neglected).

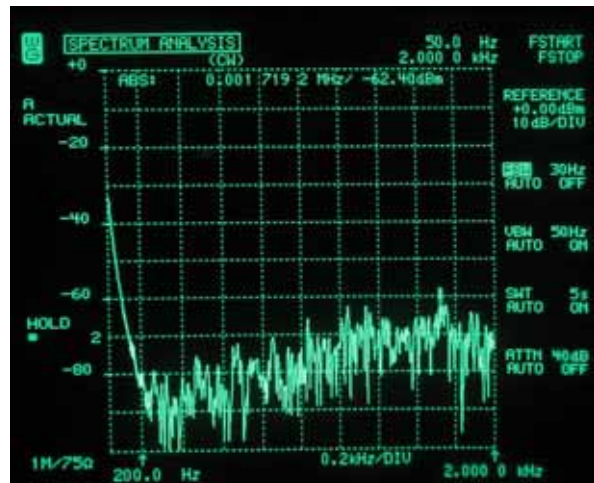
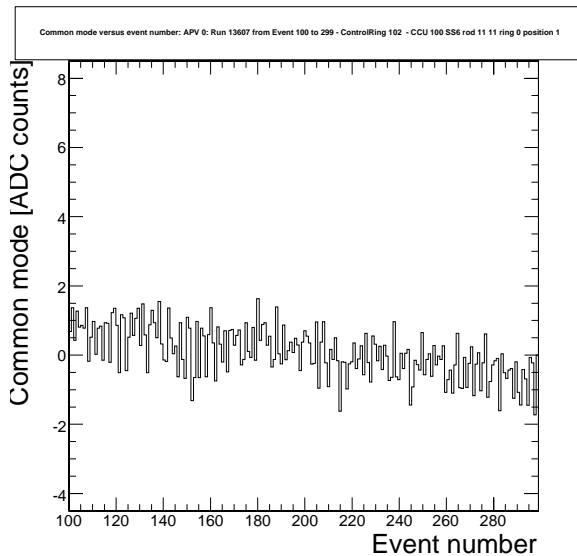


FIGURE 6.15: Power supply after modification by CAEN: The fluctuations of the common mode are significantly reduced (left) and no peaks are found in the spectrum (right).

capacitance. The shock is provided by the variation in the current drawn by the rod, occurring when the front-end electronics is biased. This hypothesis is also consistent with the observation that a constant load (a dummy RC circuit) does not produce oscillations. The CAEN supply had originally a very low cutoff frequency on the feedback amplifier. This is presumably to guard against positive feedback oscillation, but was apparently too low in bandwidth to prevent for the LC oscillations.

6.5 Noise Correlations

Due to properties of the system, fluctuations of different channels can be correlated. One example of a correlation is common mode noise, a positive correlation among the strips of the relevant group. In addition, also intrinsic noise can show significant correlations between

different channels due to electronics coupling. In the following, a study of correlation between neighboring channels in TOB sensors will be presented. The general concept should however be also applicable to other subdetectors.

6.5.1 Estimate of Noise Correlation in Silicon Strip Sensors

A detailed discussion of correlated noise in silicon strip sensors is given in [79], showing that in general the noise fluctuations of neighboring channels have a negative correlation, arising from the capacitive coupling of the strips.

A silicon strip sensor with associated readout electronics can be modeled as a capacitive network, as shown in the block diagram of Figure 6.16.

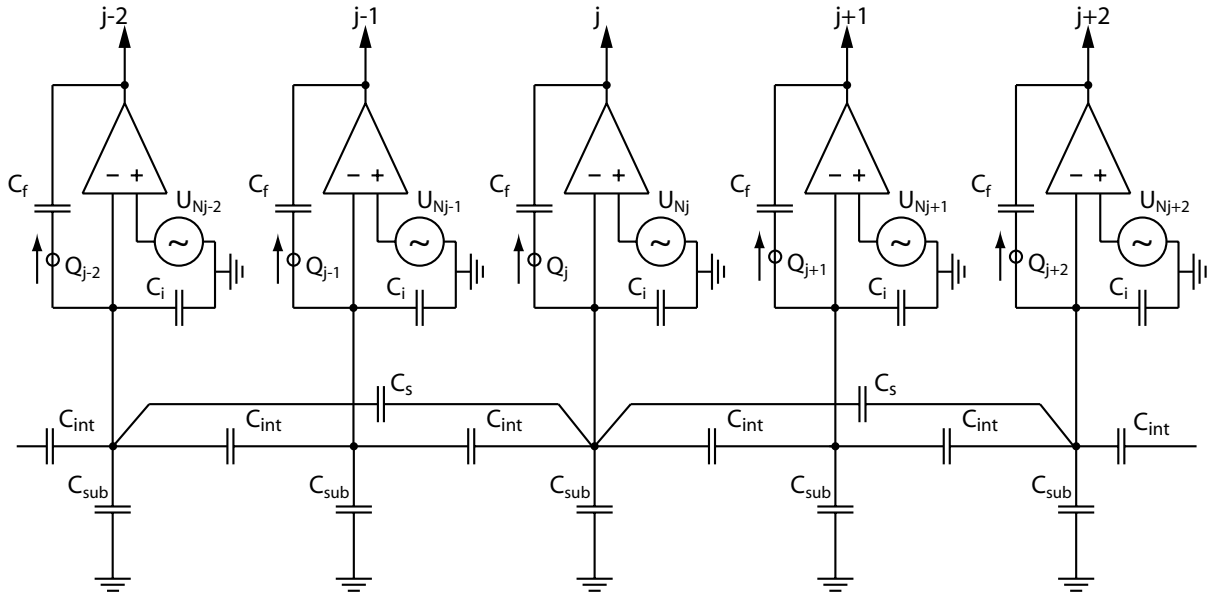


FIGURE 6.16: *Equivalent circuit diagram of a silicon strip sensor with connected readout electronics [79].*

In this diagram strips are coupled via the capacitance C_{sub} to the backplane, and to neighboring strips via the inter-strip capacitance C_{int} . A direct coupling of second neighboring strips is given by the capacitance C_s . Each strip is read out by a charge sensitive amplifier that has an open-loop gain A , a feedback capacitance C_f and an input capacitance C_i . Where C_i refers to the "cold" input capacitance of the amplifier (i.e. without considering the feedback), which is given in good approximation by the input capacitance of the input transistor of the amplifier. We will assume in the following that the effective capacitance ($A \cdot C_f$) of an amplifier is large

and thus the input of a charge sensitive amplifier can be considered as a virtual ground.

In the presence of a noise voltage of U_{nj} , the equivalent noise charge for the corresponding amplifier (according to eqn.A.17, substituting C_{det} , by C_{tot}) is given by:

$$Q_{Nj} = -U_{Nj} \cdot (C_i + C_f + C_{tot}) \quad (6.21)$$

where C_{tot} is the total strip capacitance seen by the amplifier:

$$C_{tot} = 2C_{int} + 2C_s + C_{sub} \quad (6.22)$$

Q_{Nj} is driven by a noise voltage, that is also seen by the surrounding network, and causing a charge deposition on the neighboring capacitances:

$$U_{Nj} = -\frac{Q_{Nj}}{C_{tot} + C_i + C_f} = -\frac{Q_j}{C_{tot} + C_i} = \frac{Q_{Ci}}{C_{Ci}} = \frac{Q_{Csub}}{C_{sub}} = \frac{Q_{Cint}}{C_{int}} = \frac{Q_{Cs}}{C_s} \quad (6.23)$$

As the effective capacitance of the amplifier is dominating over the C_{int} and C_{sub} , the charge on the interstrip capacitance Q_{Cint} is in good approximation equal to the charge flowing to the neighboring channel and it follows:

$$\frac{Q_{j+1}}{Q_{Nj}} = \frac{Q_{j-1}}{Q_{Nj}} = -\frac{C_{int}}{C_{tot} + C_i + C_f} \quad (6.24)$$

Similarly for the second neighbors:

$$\frac{Q_{j+2}}{Q_{Nj}} = \frac{Q_{j-2}}{Q_{Nj}} = -\frac{C_s}{C_{tot} + C_i + C_f} \quad (6.25)$$

Intuitively the anti-correlation can be understood as follows: due to conservation of charge, the noisedriven charge Q_j in the feedback capacitance of amplifier "j", is supplied by the surrounding network:

$$Q_j + Q_{Ci} + Q_{Csub} + Q_{j+2} + Q_{j+1} + Q_{j-1} + Q_{j-2} = 0 \quad (6.26)$$

where according to eqn.6.23, the relation between the equivalent noise charge Q_{Nj} and the charge Q_j deposited on the feedback capacitance is given by:

$$Q_j = Q_{Nj} \cdot \frac{C_{tot}}{C_{tot} + C_f} \quad (6.27)$$

Estimates of the capacitance of the TOB sensors, and of the preamplifier of the APV25 are given by eqn.8.43, eqn.8.47, eqn.8.46 and Table.8.4. The input capacitance of the APV25 is about $C_i = 7 \text{ pF}$, the feedback capacitance $C_f = 0.15 \text{ pF}$, the total strip capacitance $C_{tot} = 1.4 \text{ pF/cm}$. For SS4 modules the interstrip coupling is about $C_{int} = 0.43 \text{ pF/cm}$ and the coupling to the second neighbor $C_s = 0.1 \text{ pF/cm}$. For strips of approximately 19 cm length, the expected correlation between neighboring strips is about -24% (eqn.6.24) and between second neighbors about -6% (eqn.6.25). The correlations for SS6 modules can be derived analogously, giving -26% for the correlation between neighboring strips and -6% for the second neighbors. These

predictions refer to samples measured at the same time and therefore apply to peak mode. The correlation in deconvolution mode can be expressed in terms of the signal samples in peak mode; the signal in deconvolution mode at the sampling time "i" d_i can be written as:

$$d_i = w_1 \cdot p_i + w_2 \cdot p_{i-1} + w_3 \cdot p_{i-2} \quad (6.28)$$

where p_i are the samples in peak mode and w_i the weights.

The correlation in deconvolution mode for a strip d and its neighbor \hat{d} therefore equals:

$$\text{corr}(d, \hat{d}) = \frac{\langle d \cdot \hat{d} \rangle}{\langle d \rangle} = \quad (6.29)$$

$$= \frac{(w_1^2 + w_2^2 + w_3^2) \langle p \cdot \hat{p} \rangle + 2w_2(w_1 + w_3) \langle p_k \cdot p_{k-1} \rangle + 2w_1 \cdot w_3 \langle p_k \cdot p_{k-2} \rangle}{(w_1^2 + w_2^2 + w_3^2) \langle p \cdot p \rangle + 2w_2(w_1 + w_3) \langle p_k \cdot p_{k-1} \rangle + 2w_1 \cdot w_3 \langle p_k \cdot p_{k-2} \rangle} \quad (6.30)$$

This expression contains correlations between signals at different sampling times, for which we do not have a prediction. Therefore the expected correlations in deconvolution mode cannot be derived from the values in peak mode. Correlations in both readout modes are measured from the data, as discussed in the following.

6.5.2 Measurements

The correlation between the noise of neighboring channels has been measured with the Cosmic Rack. The analysis has been carried out using the noise analysis package described in [80].

The correlations between two strips k, j is given by:

$$\text{corr}(k, j) = \frac{\sum_{i=1}^N (k_i - \bar{k}) \cdot (j_i - \bar{j})}{\sigma_k \cdot \sigma_j} \quad (6.31)$$

where $k(j)$ is the pedestal and common mode subtracted data of strip k (j) and \bar{k}, \bar{j} is the mean of $k(j)$, which - depending on the common mode subtraction algorithm can be different from zero.

For a measurement of the correlation, the common mode needs to be correctly subtracted. The effect of different common mode subtraction algorithms is illustrated in Figure 6.17 (peak mode) and Figure 6.18 (deconvolution mode). When a median common mode subtraction is applied, the noise correlation profile shows a strong dependence of the strip position with increasing correlation at the outer strips of a chips. This is an effect of common mode noise, that is not coupling in the same way to all strips (see section 6.4.3), and can be reduced with a linear common mode subtraction. The noise profile after linear common mode subtraction is not perfectly flat, indicating that there are some higher order effects in the common mode. Nevertheless for the purposes of the following studies these higher order effects are negligible, and the results presented in the following are obtained using a linear common mode subtraction.

The correlation profiles for SS4 (OB2) modules in peak mode are shown in Figure 6.19 and in Figure 6.20 for the deconvolution mode. The corresponding plots for SS6 (OB1) modules are shown in Figure 6.21 (peak mode) and in Figure 6.22 (deconvolution mode). Measurements of several runs are summarized in Table.6.3.

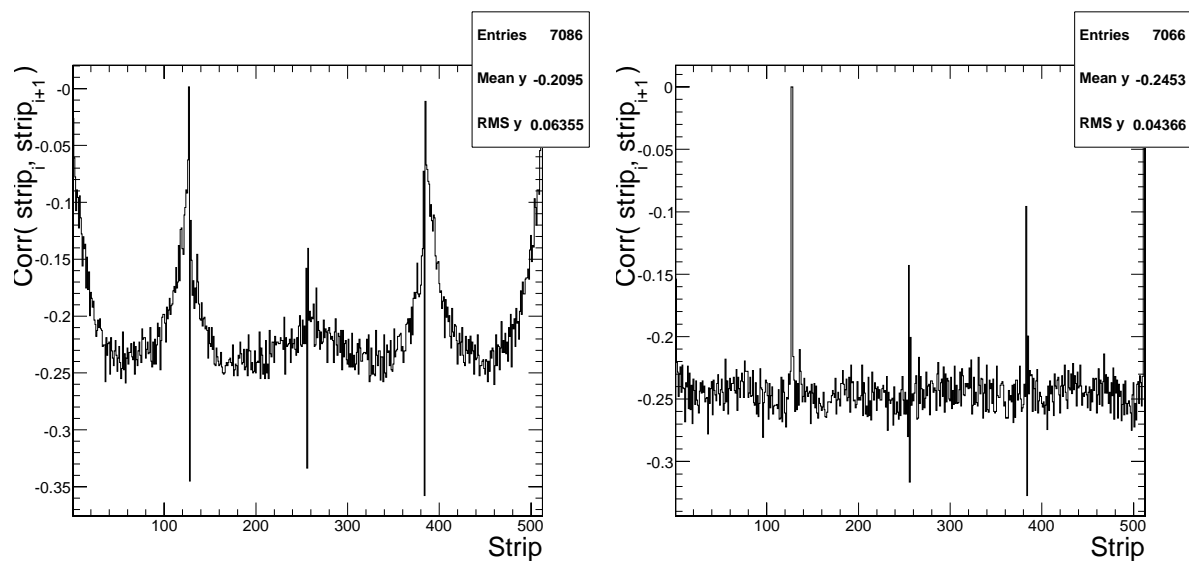


FIGURE 6.17: *Effect of the common mode subtraction on the correlation profile in peak mode. The plots show module position 6 of an SS4 rod, which is known to be influenced most by the common mode. Correlations with median common mode subtraction left, linear common mode subtraction right. (The spikes at the chip borders require further investigation.)*

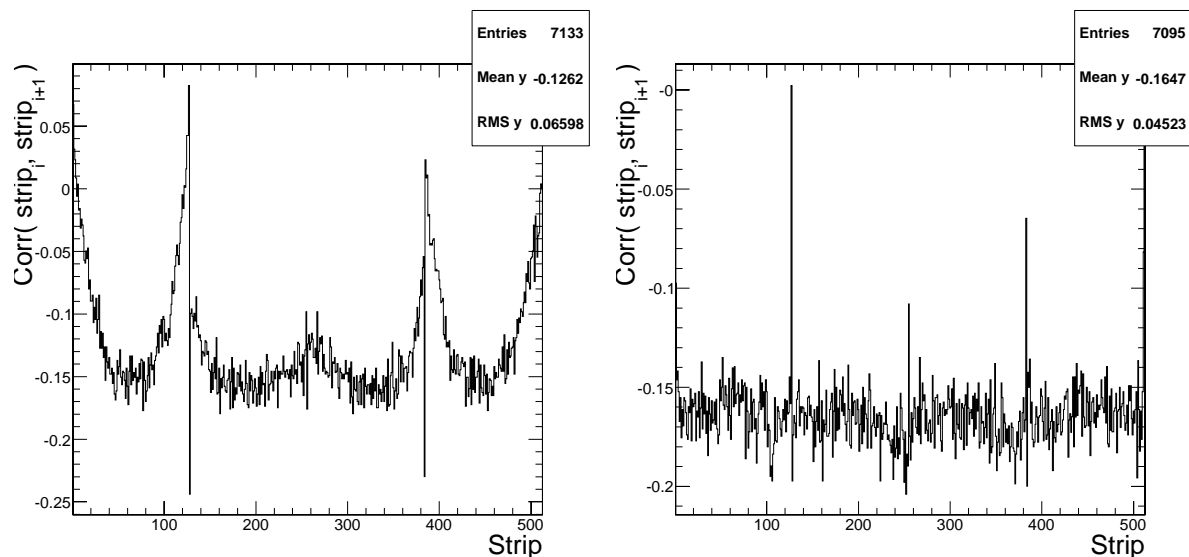


FIGURE 6.18: *Effect of the common mode subtraction on the correlation profile in deconvolution mode. The plots show module position 6 of an SS4 rod. Correlations with median common mode subtraction on the left side, linear common mode subtraction on the right.*

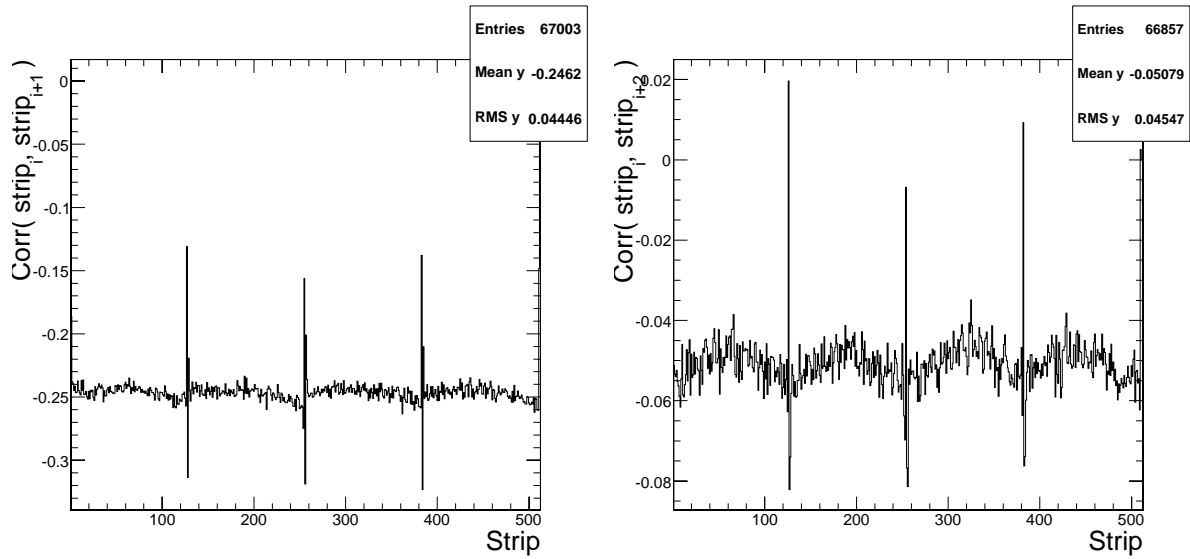


FIGURE 6.19: Noise Correlation for SS4 modules in peak mode. Correlation between neighboring strips (left) and second neighbors right.

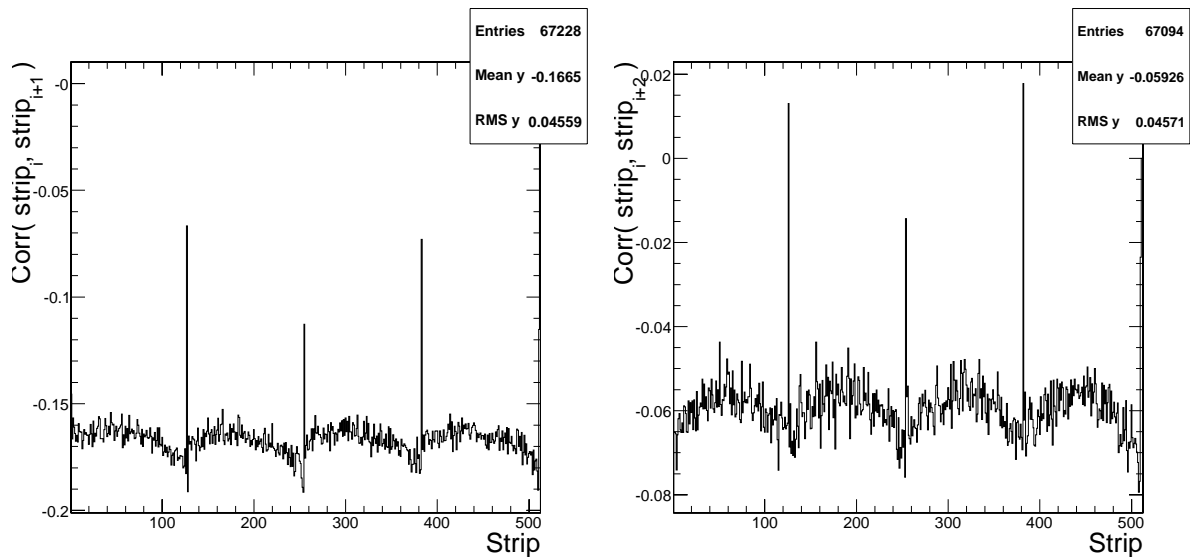


FIGURE 6.20: Noise Correlation for SS4 modules in deconvolution mode. Correlation between neighboring strips (left) and second neighbors right.

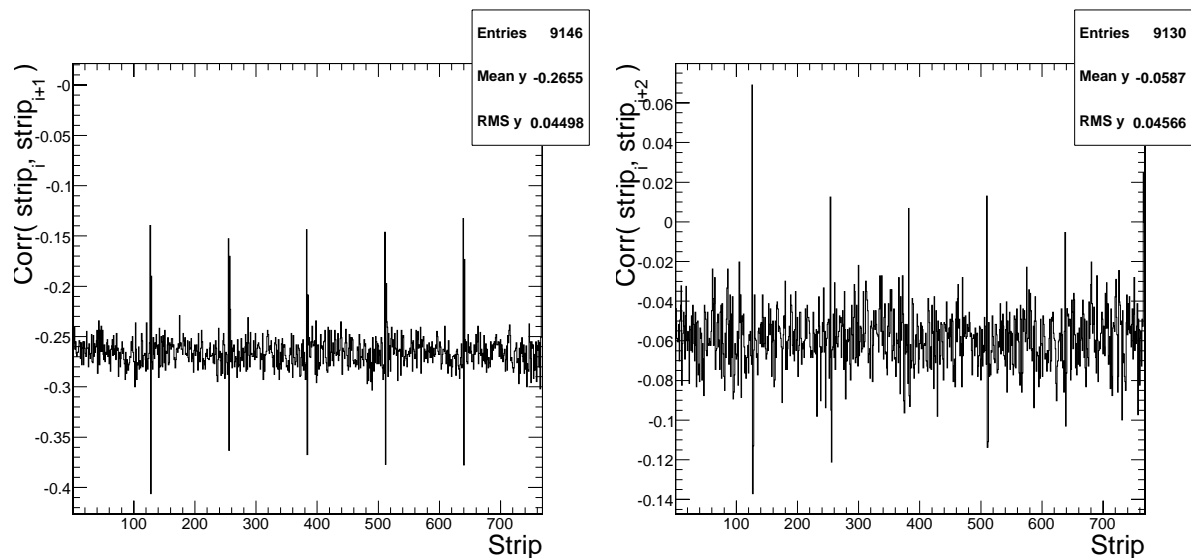


FIGURE 6.21: Noise Correlation for SS6 modules in peak mode. Correlation between neighboring strips (left) and second neighbors right.

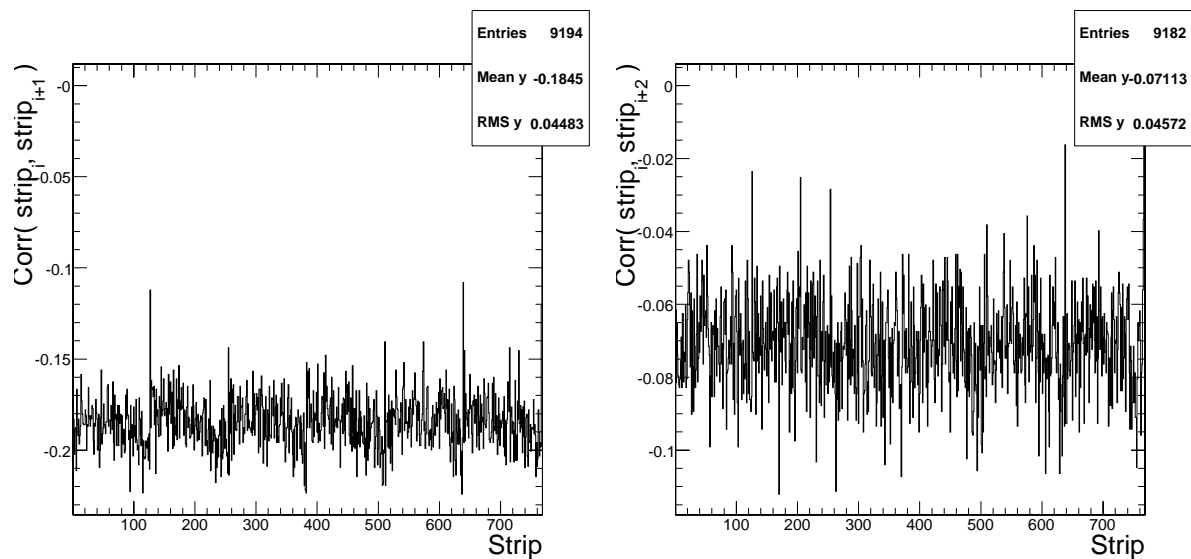


FIGURE 6.22: Noise Correlation for SS6 modules in deconvolution mode. Correlation between neighboring strips (left) and second neighbors right.

Run	Module	Mode	Correlation First Neighbor		Correlation Second Neighbor	
			Mean [%]	RMS [%]	Mean [%]	RMS [%]
200287	SS4	PEAK	-24.6	4.4	-5.1	4.5
400124	SS4	PEAK	-24.5	4.4	-5.0	4.6
400124	SS6	PEAK	-26.6	4.5	-5.9	4.6
200275	SS4	DECV	-16.7	4.6	-5.9	4.6
200326	SS4	DECV	-16.6	4.6	-5.9	4.6
400206	SS4	DECV	-16.9	4.5	-6.1	4.5
400206	SS6	DECV	-18.5	4.5	-7.1	4.6

TABLE 6.3: *Noise correlations in peak and deconvolution mode for SS4 and SS6 modules after linear common mode subtraction. Noise in neighboring strips (and also second neighbors) shows a significant anti-correlation. The effect is higher in peak mode than in deconvolution mode and slightly stronger for SS6 than SS4 modules. The measurements are reproducible with good accuracy.*

The measured anti-correlation of neighboring strips is larger for SS6 than for SS4 modules as one expects from the larger inter-strip capacitances. The measurements are in good agreement with the estimation in peak mode. The (anti-)correlations in deconvolution mode are smaller than in peak mode.

6.6 Summary

A comprehensive noise analysis has been carried out using data collected with the Cosmic Rack. The calibration of the readout chain with the APV synchronisation pulses, yields absolute measurements of the noise in ENC. The measured values ($\approx 1400 e^-$ in peak mode and $\approx 2100 e^-$ in deconvolution mode) are in good agreement with the expectations ($\approx 1300 e^-$ and $\approx 2200 e^-$ respectively).

The grounding scheme of the TOB has been studied and the final scheme validated; a significant improvement is found, when the power return line is soldered to the ground, defined by the cooling pipes. The final design of the interconnect cards implements additional ground connections between the return line and the cooling pipes, that reduce the noise of the outermost strips of the detector, with no negative side effect.

A study of the CAEN 4601H power supplies revealed that they introduce significant common mode noise to the front end. After giving feedback to the supplier, the bandwidth of the feedback loop was increased and the problem disappeared.

The correlation of the noise between neighboring strips has been studied; significant values of about -25% in peak mode and -16% in deconvolution mode have been found; such values are compatible with the expectations from capacitive couplings of neighboring strips.

Chapter 7

Tracking Cosmic Particles

Test beams and cosmic rays as well as lasers and radioactive sources are commonly used to test particle detectors. Compared to the other sources of physics signals, cosmic rays offer the possibility to illuminate large detector surfaces in any laboratory location, albeit at low rate, and without control of the particle energy. For these reasons cosmic rays are primarily used for long term tests and commissioning of large detector assemblies.

A setup designed to track cosmic muons with TOB detectors - the Cosmic Rack- has been operated for several month in different conditions to establish stability, robustness and performance of the TOB subassemblies (Rods). Following an introduction to the cosmic spectrum at sea level, the measurements performed with the Cosmic Rack will be presented.

7.1 Cosmic Radiation

A short introduction to the cosmic radiation shall be given in the following. Further information can be found in [72, 81, 82]. Cosmic Rays were discovered by Victor Hess in 1912, when he observed in a balloon experiment an increasing discharge of an electroscope when ascending. First the effect was attributed to electromagnetic radiation, later however it was discovered that the radiation must be a flux of charged particles, as a deflection by the earth magnetic field was observed.

At sea level the spectrum of charged particles is dominated by cosmic muons. They originate in the interaction of high energetic primary cosmic particles - mostly protons ($\approx 90\%$) and alpha particles ($\approx 9\%$) - with the nuclei of the outer atmosphere. In these collisions predominately pions are produced directly or as secondary particles, due to the decay of instable products (e.g. kaons). Charged pions decay through weak interaction into muons and muon neutrinos:

$$\pi^+ \rightarrow \mu^+ + \nu_\mu \quad (7.1)$$

$$\pi^- \rightarrow \mu^- + \bar{\nu}_\mu \quad (7.2)$$

while neutral pions decay into two photons. Muons have a lifetime of ($2.2 \mu s$), due to the time dilatation at relativistic speeds, they can travel long path lengths before decaying. As the cross sections for interactions of muons with matter are small, most of the muons generated in the atmosphere, reach the sea level before decaying. The muons interact mostly by ionization and loose about $2 GeV$ traversing through the atmosphere. The energy spectrum shows a decrease of the flux for increasing energies, and the mean energy of muons observed at sea level is about $4 GeV$.

7.1.1 Spectrum and Angular distribution

Cosmic Muons arrive at the earth surface with an approximate rate of $0.01 Hz/cm^2$. According to [72] the spectrum, neglecting effects due to muon decay, is proportional to $E_\mu^{2.7}$. This

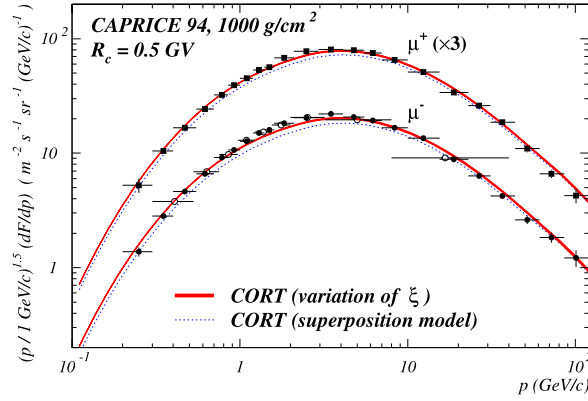


FIGURE 7.1: *Differential momentum spectra of positive and negative muons at ground level [84].*

approximation is however only valid for high-energy muons ($E > 100 \text{ GeV}$). Muons in the low momentum region have been measured in the Caprice balloon experiment [83]. The differential spectrum illustrated in Figure 7.1 is in not very intuitive units. For better demonstration the spectrum has been unfolded and fitted in [85] (with a parametrization similar to those presented in [86]):

$$\frac{dI(p)}{dp} = p^{-1.5} \exp^{A+B \cdot \ln(p)+C \cdot \ln(p)^2+D \cdot \ln(p)^3} \quad (7.3)$$

Where p is the muon momentum in GeV/c . The constants A, B, C, D obtained by fitting the combined flux for positive and negative charged muons are given in Table 7.1. This fitted

A	B	C	D
3.266	0.946	-0.402	1.87e-2

TABLE 7.1: *Constants obtained by fitting the data points listed in [87] of the Caprice94 balloon experiment using eqn.7.3.*

spectrum agrees well with the Caprice data in the range from 0.25 GeV to 100 GeV (Figure 7.2). The integral flux is $87 \text{ GeV}^{-1} \text{m}^{-2} \text{s}^{-1} \text{sr}^{-1}$. The spectrum peaks around 500 MeV and the mean energy is $\approx 4 \text{ GeV}$.

The cosmic flux depends not only on the energy but also on the incident angle. The angular distribution as a function of the zenith angle is approximately given by:

$$I(\theta) = I_v \cos^2(\theta) \quad (7.4)$$

where at ground level according to [88] the integral flux of particles I_v (with less than 10 GeV) is $0.83 \cdot 10^{-2} \text{ s}^{-1} \text{cm}^{-2} \text{sr}^{-1}$.

The total rate of cosmic passing through a horizontal surface of size S is given by:

$$R = \int_0^{2\pi} \int_0^{\frac{\pi}{2}} I(\theta) \cdot S \cdot \cos(\theta) \cdot \sin(\theta) \cdot d\theta \cdot d\phi = \frac{\pi}{2} \cdot S \cdot I_v \quad (7.5)$$

When measuring rates, deviations from the calculation (eqn.7.3) have be expected due to the deflection of primary cosmic radiation and secondary particles. Especially in the low momentum region ($< 10 \text{ GeV}$), the spectrum and more importantly the flux are influenced by the solar activity, the earth magnetic field and atmospheric depth. Therefore the numbers presented have a certain error.

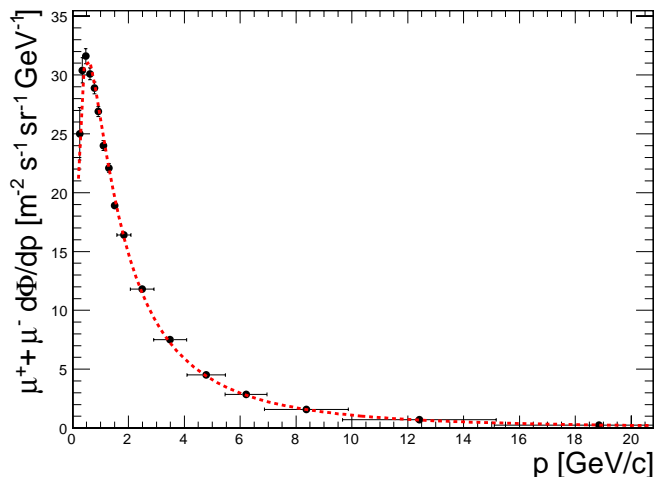


FIGURE 7.2: *Differential flux of cosmic muons at sea level. Fitted spectrum and data points from Caprice94.*

7.1.2 Measured Rates

To validate the Cosmic Rack trigger system, the rates of the individual photomultipliers and groups of photomultipliers connected in coincidence have been measured. The counts obtained for a sampling interval of 100 s are summarized in Table 7.2.

PMT	Counts/100s
TOP_A	26933
TOP_B	18446
BOT_A	18450
BOT_B	22726
TOP_A & TOP_B	15340
BOT_A & BOT_B	13401
TOP_A & BOT_A	1178
TOP_B & BOT_B	1171
TOP_A & TOP_B & BOT_A & BOT_B	1110

TABLE 7.2: *Trigger rates from the individual photomultiplier tubes (and coincidences) for a sampling time of 100s and a pulse width of 25ns. "TOP" indicates the photo multipliers attached to the top and "BOT" to the bottom scintillator. "A" is the side of the scintillators close to the module position six of the Rods and "B" is close to the module position one of the Rods.*

The total rate of the trigger system (11.1 Hz) agrees well with those determined with a custom simulation of the Cosmic Rack trigger system giving 9.5 Hz. The rates for the top and bottom scintillators however are a factor 2-3 higher than the expected value of 55 Hz derived from eqn.7.5. Due to the tight window for the coincidence this cannot be explained by noise, and it is an effect seen by both PMTs of the same scintillator, therefore it must originate from physics effects not described by eqn.7.5 (an example might be showers originated in the material above the Cosmic Rack).

7.2 Tracking Cosmics

7.2.1 Reconstruction Chain

Necessary prerequisites for the data reconstruction is a mapping of the readout channels and their geometric position in the detector. This mapping is obtained in multiple steps:

- Mapping between the channels in the readout system and the control ring.
- Mapping between the address of a module in the control ring and its *DCUID*, the identifier of the DCU on the hybrid, that is a unique number in the entire Tracker.
- Mapping between the DCUIDs and the sensitive volume describing the sensors in the Tracker geometry, that are identified by the *GeomDetId*.

The geometric representation of the detector is done in a hierarchical form. The used *DDD* (Detector Description Database) [89] file format is based on the Geant4 [90] geometric description. In the DDD file format, volumes are defined and material properties such as radiation length are assigned to them. The volumes are nested in a hierarchical way: child volumes are placed into a surrounding parent volume. For example a sensitive volume (the actual sensor) is defined and embedded into a volume describing a module, modules are then placed into a Rod and so forth. The geometry files are not only used to determine the hit positions in space but also to provide information of the distribution of material in the Tracker volume - important for estimation of multiple scattering and to determine the deposited energy.

For the analysis of data taken with the Cosmic Rack, a geometry description of the setup has been built. To use as much as possible of existing code, standard files for the description of the TOB-Rods have been used; Rods have been placed in space according to the geometry of the Cosmic Rack. The support structures for the Rods (the Cosmic Rack mechanics) has not been simulated.

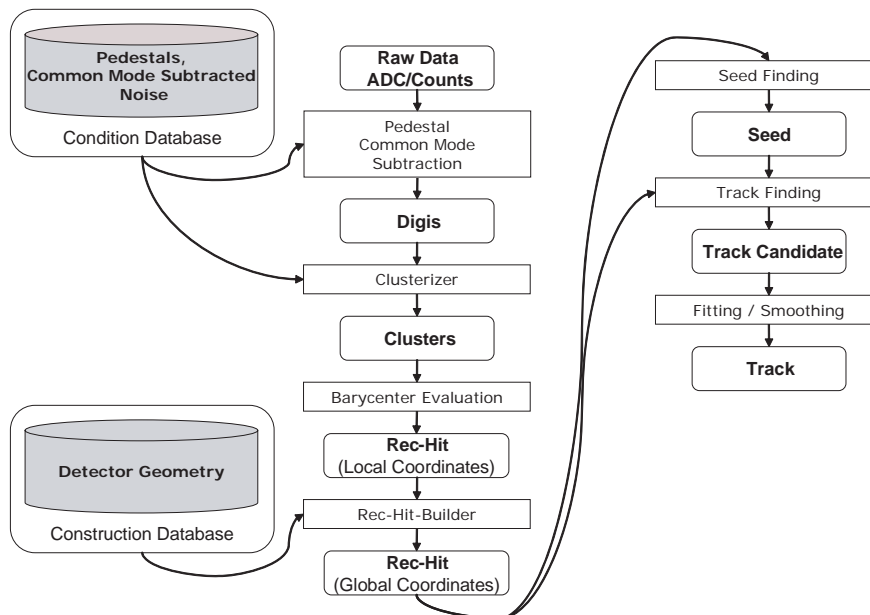


FIGURE 7.3: Steps for the reconstruction of tracks in CMSSW.

For the reconstruction of events in the Cosmic Rack, the standard CMS software CMSSW [91] has been used. The data flow for the reconstruction of tracks is sketched in Figure 7.3. The reconstruction is starting with the data files from the Readout-Unit applications of the data acquisition framework (XDAQ) [7, 66, 92]. These files contain essentially the ADC counts seen by the FEDs for the individual channels (strips) for each event (trigger). Depending on the readout mode of the FED, the raw data need to be pedestal and common mode subtracted using data from a separate "pedestal run" that is stored in the calibration database.

The result are *Digis*, assigning a value for each strip that is proportional to the deposited charge. From these Digis clusters are identified - a group of neighboring strips where charge exceeding certain thresholds has been deposited. The thresholds are usually defined in terms of the common mode subtracted noise, that is retrieved from the calibration data base. *RecHits* describe the position of the charge deposition, which is the estimator of the particle crossing point. RecHits are first computed in the local frame (reference system of the sensor) using the charge barycenter and the (estimated) track direction. A special group of hits are the *Matched RecHits* (a tool for the pattern recognition) that combine the information from a r-phi detector and the corresponding stereo detector to form a 3D space point. The matching hit is projected on a layer in-between the r-phi and stereo detector and thus depends on the angle of the passing particle, therefore the matching has to be redone once the track direction is known. Using the information of the geometric detector description, the hit position is then translated to the global reference system.

The track reconstruction [50, 93] itself can be split into the following tasks:

- Seed Finding

- Pattern Recognition

- Fitting and Smoothing

The seed finding provides a first estimate of a candidate track; it is done combining pairs or triplets of hits and fitting a helix to them. Starting from the seed, the track is successively build using a Kalman filter technique. Detectors with hits are sorted according to the order in which they would be crossed by a particle. Compatible hits are found by propagating the trajectory to the next detector surface and evaluating the compatibility (χ^2/ndof) of this estimated impact point with the hits on the detector. If a compatible hit is found, the trajectory is updated using the information of the hit and then propagated to the next detector surface. Once all compatible hits have been found and the full track information is available, the "track fitting" starts for the re-evaluation of the hit estimations. The fitting process starts from the seed and is applied iteratively to the following hits using the updated trajectory information at each stage. If the fitting is successful "smoothing" starts, which is a backward fitting using the trajectory state found in the fitting process and propagating it in the backward direction towards the seed. The resulting track provides optimal estimates for the track parameters and hits.

7.2.2 Software Settings

The results presented in the following have been obtained using CMSSW_1.2.3 software, adapted to the requirements of the Cosmic Rack geometry. For the cluster finding the standard clusterizer ("*ThreeThresholdStripClusterizer*") has been selected, that is applied on pedestal and common mode subtracted ¹ data. This clusterizer identifies clusters on basis of three cuts: a cut on the seed strip (the strip with the highest signal), its neighboring strips and the total cluster charge. The cut on the signal of neighboring strips has been set to 3σ , the cut for the seed strip to 4σ and the total cluster charge has to exceed $5\sigma_{clu}$, where the cluster noise σ_{clu} is defined as:

$$\sigma_{clu} = \sqrt{\left(\frac{1}{n} \sum \sigma_i^2\right)} \quad (7.6)$$

where σ_i is the common mode subtracted noise of the strips contributing to the cluster ². The tracking of cosmic particles requires some adoptions compared to tracking during LHC operation. In general not more than one track is expected, and tracks are not coming from the origin. For reconstruction of tracks in the Cosmic Rack, the *CosmicSeedFinder* and the *CosmicTrackFinder* have been employed for the track reconstruction.

The parameters of the *CosmicTrackFinder* for the minimum number of hits in a track have been set to 4 and the $\chi^2/ndof$ of the track finder to a large value of 2000, in order to accommodate for misalignment, multiple scattering and bad estimations of the seed direction and the matched RecHits. As there are only very few events in the Cosmic Rack with more than one track, this high cut does not compromise the effectiveness of track reconstruction.

7.2.3 Measurements on the Track Distribution

The scintillators cover an area that is larger than the sensitive areas of the Rods. It is found, that approximately 70% of the triggers correspond to tracks fullfilling the above defined criteria. A cosmic particle passing through the Cosmic Rack is shown in Figure 7.4. The numbers of hits per track are shown in Figure 7.5, where the matched hits from a pair of r-phi / stereo detector are counted as a single hit. The number of hits can exceed the numbers of layers, as modules in a Rod have an overlap, and also sensors of neighboring Rods in the same layer have an overlap of approximately 12 strips. The angular distribution of the reconstructed tracks in the Cosmic Rack is shown in Figure 7.6 in the coordinate systems of the scintillators (as defined in the figure caption).

Relevant for the deposited charge and cluster shape are the angles of the tracks in the coordinate system of the crossed detector. In this local coordinate system u is the direction across the strips, v along the strips and w normal to the module plane. In Figure 7.8 the distribution of the local track angles is shown. Due to the geometry of the system and the trigger acceptance, most of the particles cross the sensor almost perpendicular to the detector plane.

¹The common mode has been calculated as median of all strips of a given chip

²In a more recent version of CMSSW this definition this has been changed to $\sigma = \sqrt{(\sum^n \sigma_i^2)}$.

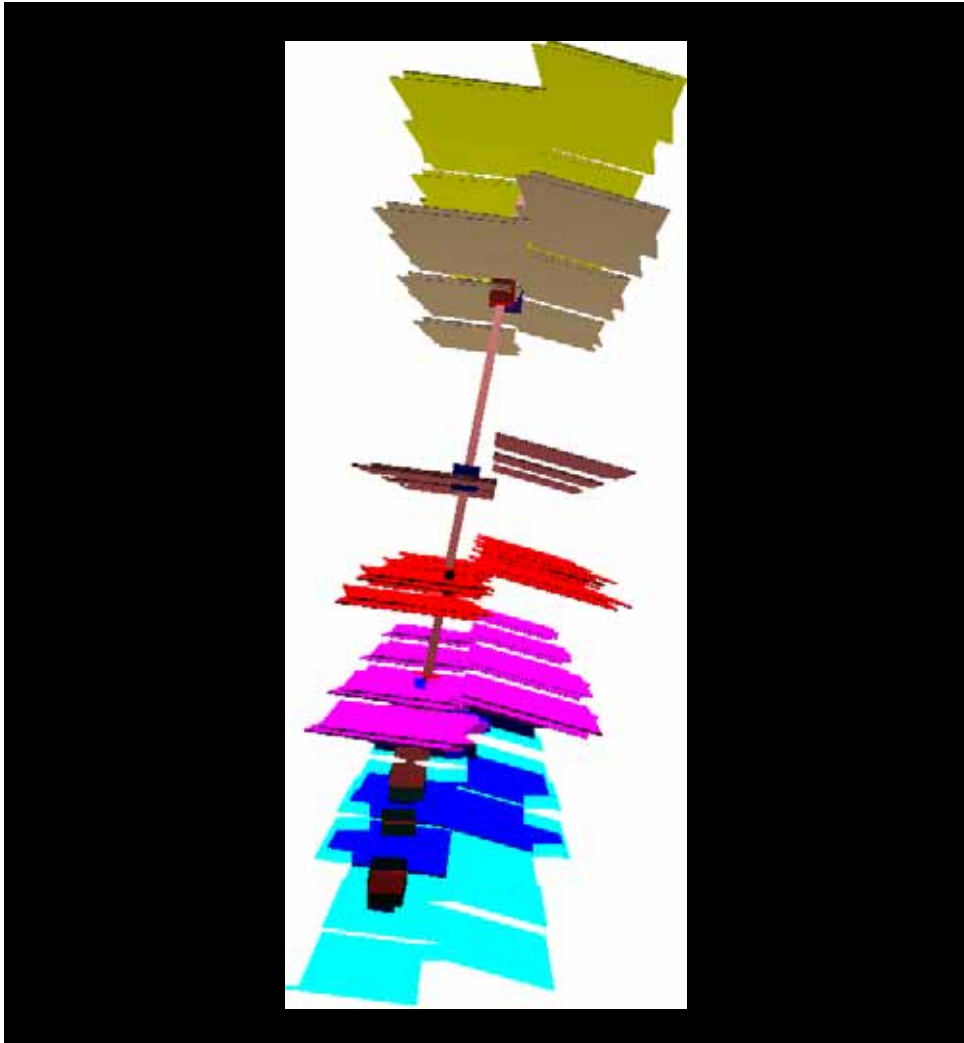


FIGURE 7.4: *Event display showing a particle passing through the Cosmic Rack.*

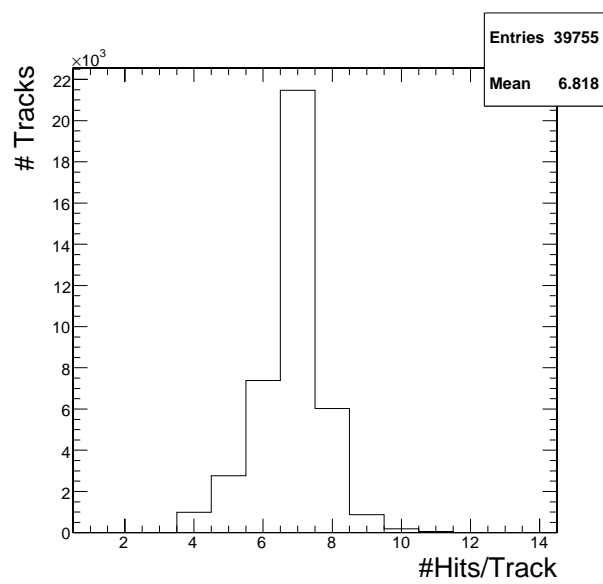


FIGURE 7.5: *Number of hits per track. In this plot matched RecHits are counted as a single hit.*

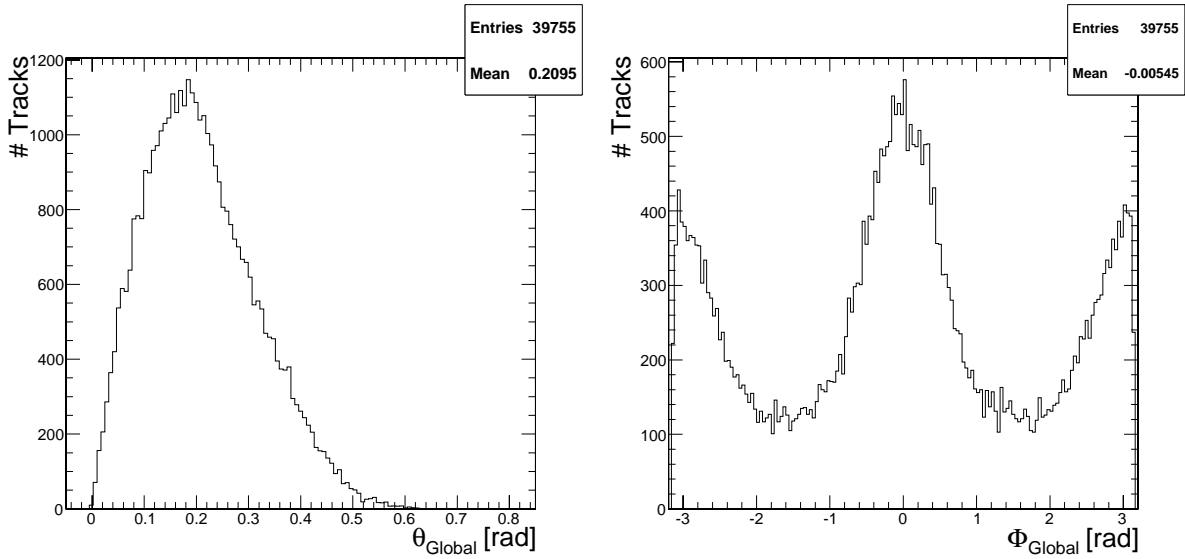


FIGURE 7.6: Angular distribution of cosmic tracks in the global coordinates system (defined by the scintillators). θ is the angle normal to the scintillator plane and $\phi = \text{atan}(x/z)$ the azimuthal angle where x is along the short and z along the long side of the scintillators.

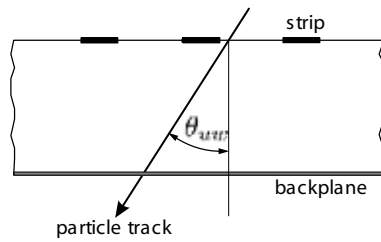


FIGURE 7.7: Definition of Θ_{UW} .

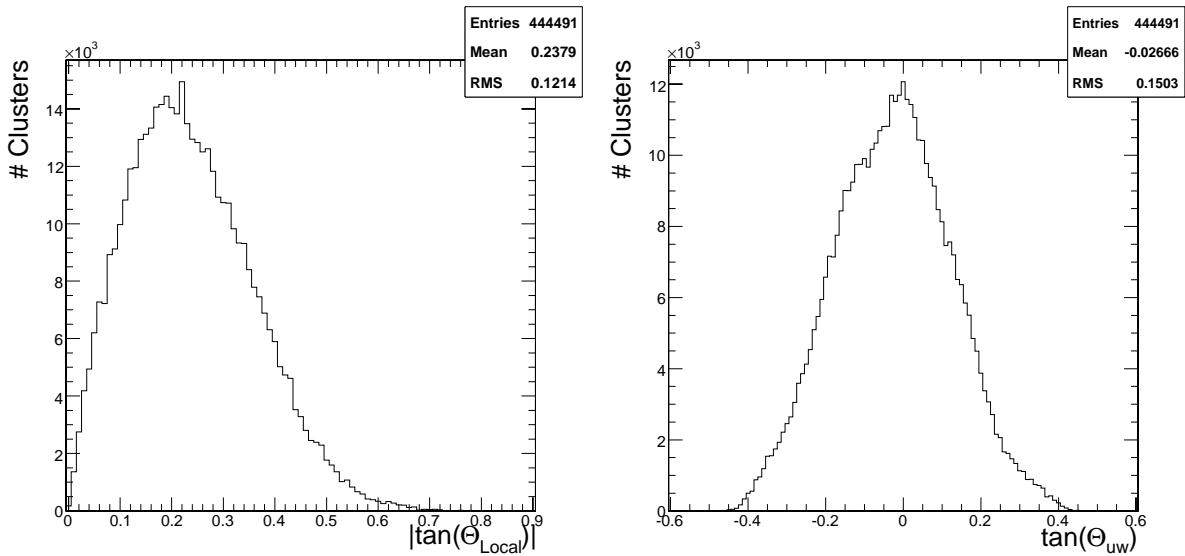


FIGURE 7.8: Angular distribution of cosmic tracks in the coordinated system of the crossed detector. Shown in the left is the angle Θ_{local} of the track with respect to the normal of the module plane, and on the right the angle Θ_{UW} (as defined in Figure 7.7).

7.3 Cluster Properties

Plots presented in the following take only clusters into account that have been identified to belong to a particles track, in order to unfold effects of the track angle on the cluster charge and cluster size.

7.3.1 Signal to Noise

The signal to noise ratio (S/N) is a key parameter for the tracking performance. A large S/N ensures high efficiency of hit reconstruction and allows the measurement of charge sharing between neighboring strips, improving the resolution through the calculation of the charge barycenter. Due to the high radiation environment of the CMS Tracker, the S/N ratio will decrease with time - roughly it is expected to decrease by a factor 1.5 in 10 years of operation [94]. Therefore a large margin in the beginning is necessary.

The mean energy loss of a charged particle in the sensor is described by the Bethe-Bloch formula. The deposition of charge is however a statistical process, where in each single interaction of the incident particle with the medium the transferred energy varies. For thin layers of materials (as in the case of the 500 μm thin silicon strip sensors) these fluctuations are non negligible and are described by a Landau distribution.

Furthermore for a given value of the energy released by the crossing particle, the number of generated electron hole pairs is also subject to variations, as part of the energy is transferred to vibrations of the lattice atoms (phonons). The mean number of generated electron hole pairs N for the transferred energy E is:

$$N = \frac{E}{\epsilon} \quad (7.7)$$

where ϵ is the mean energy for the generation of an electron-hole pair; the fluctuations around the mean value are described by the *Fano Factor* F :

$$\langle N^2 \rangle = FN = F \frac{E}{\epsilon} \quad (7.8)$$

where according to [95] F is ≈ 0.111 for silicon. Further fluctuations are due to variations of the charge collection efficiency (trapped charges), jitter of the readout electronics and electronics noise. The Most Probable Value (*MPV*) of the S/N distribution is taken as the S/N estimator. The MPV is a more stable estimator than the average of the S/N distribution, which is sensitive to the long tail at high values (refer to the left plot of Figure 7.10), which in turn is affected by saturation of the readout electronics. To accommodate for all the variations described above the MPV has been obtained by fitting the measured S/N distribution with a Landau function that is convoluted with a Gaussian.

Expected Energy Loss

Considering the spectrum of cosmic muons and the cutoff due to the lead absorber in the Cosmic Rack, the muons can be treated in good approximation as MIPs ($\beta\gamma = 2$). Muons with the minimal energy to pass the lead absorber ($\approx 120 \text{ MeV}$) will loose on average only about 10% more energy than a MIP. The mean energy loss for a MIP in silicon is according to [72] $1.66 \text{ MeV g}^{-1} \text{ cm}^2$. In 500 μm thick silicon (2.33 g/cm^3) that translates to a mean energy loss of 193 keV , which in turn corresponds to 53000 electron-hole pairs, using the value of 3.66 eV per pair created. The scaling factor between the average value and the MPV for the energy loss in 500 μm thick silicon has been estimated from Figure 7.9 (by interpolation) to be 0.76, which yields a MPV of ≈ 40000 electron-hole pairs for a MIP.

In the following the signal to noise ratio presented is defined as the total charge of the cluster divided by the (common mode subtracted) noise of the seed strip. When tracking cosmics, the

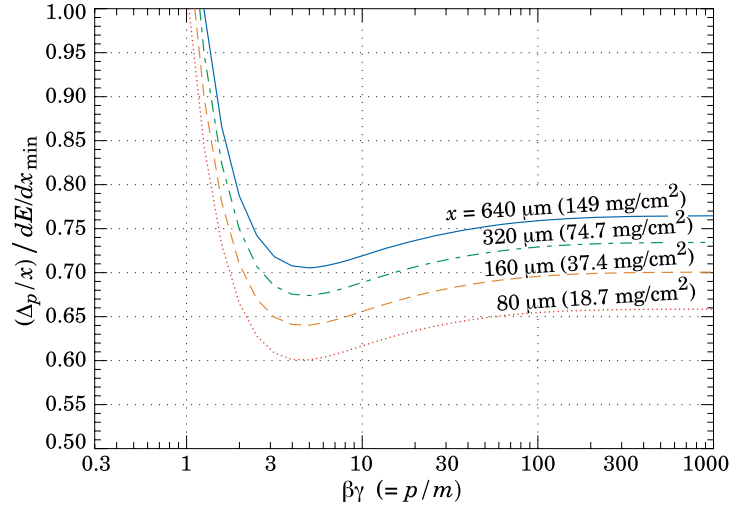


FIGURE 7.9: Most probable energy loss in silicon, scaled to the mean loss of a minimum ionizing particle, $388 \text{ eV}/\mu\text{m}$ ($1.66 \text{ MeVg}^{-1}\text{cm}^2$) [72].

track inclination can vary in a wide range, limited only by the acceptance of the system. In order to unfold the effect of different path lengths (shown in Figure 7.10), the measured signal can be re-scaled to the path of a perpendicular particle by multiplying it by $\cos(\theta)$, where θ is the angle between the track and the direction normal to the sensor plane³. Figure 7.11 shows the signal to noise ratio (normalized to the path length) for SS4 modules at room temperature in peak and deconvolution mode. The distribution is well described by the Landau function (convoluted with a Gaussian). A signal to noise ratio of about 20 is measured in deconvolution mode and 30 in peak mode. Further measurements are summarized in Table 7.3.

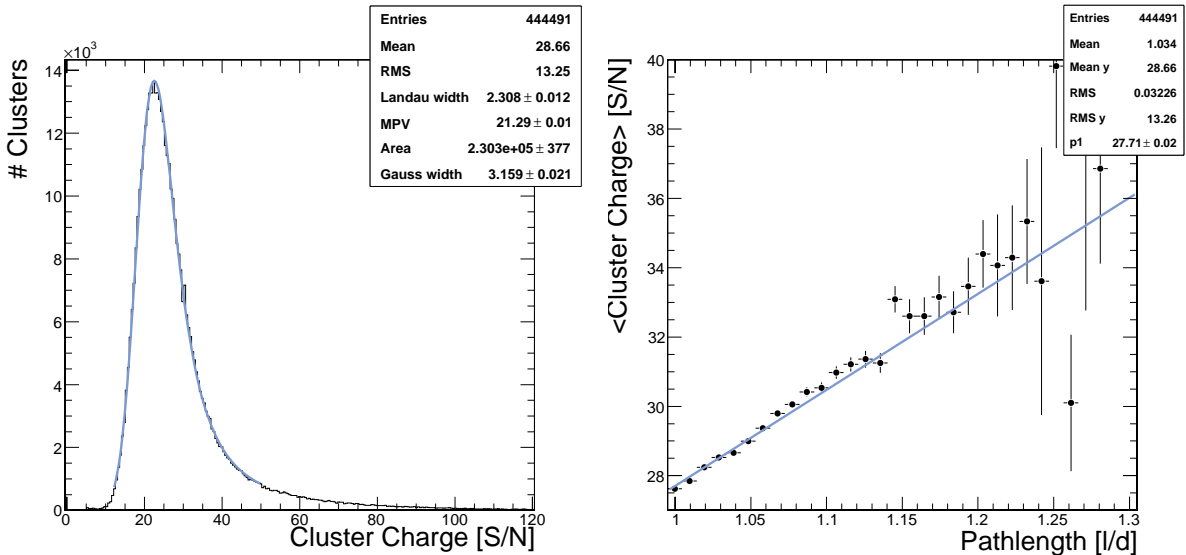


FIGURE 7.10: Signal to noise ratio in deconvolution mode for SS4 (OB2) modules. For all clusters without path length correction (left) and as function of the path length (right). The mean of the deposited charge is proportional to the path length in the sensor.

³There is a second order effect on the MPV of the distribution as the mean energy loss scales with the path length. The MPV/mean ratio increases with the path length as illustrated in Figure 7.9.

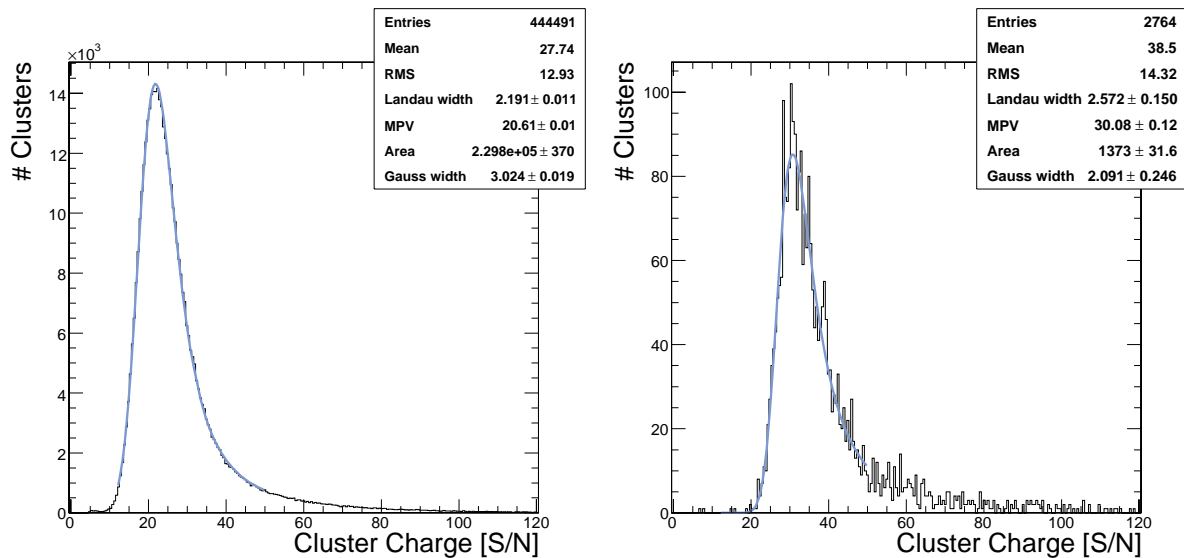


FIGURE 7.11: Signal to noise ratio (path length corrected) in deconvolution mode (left) and peak mode (right) for OB1 modules at room temperature.

Cluster Size

The cluster size has been studied in both readout modes and as a function of the track inclination. The distribution of clusters recorded in deconvolution mode in SS4 modules is shown in Figure 7.12 along with their dependence on the track angle.

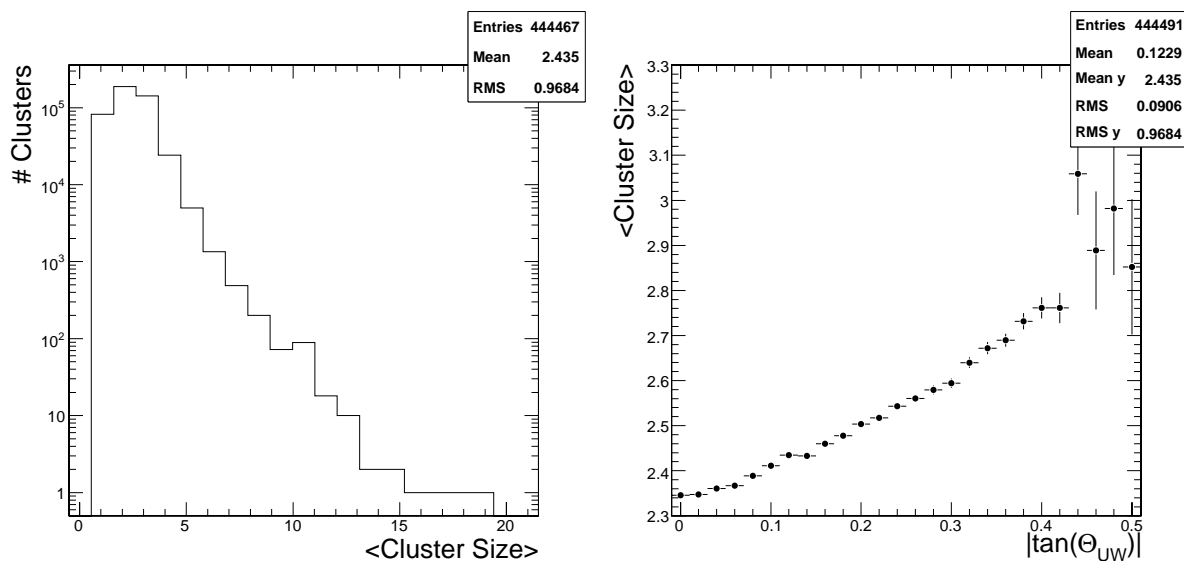


FIGURE 7.12: Cluster size in deconvolution-mode for SS4 modules: distribution of the cluster sizes for all tracks (left), cluster size as a function of the crossing angle θ_{UW} (right).

For perpendicularly tracks, one would expect, that the charge may be shared at most between two neighboring strips, and therefore the cluster size should never be larger than two strips. Particles with the largest inclinations that triggered a readout had a $\tan(\Theta_{UW}) = 0.5$ (see Figure 7.8), corresponding to a spread of the charge over a distance of $250 \mu m$, and therefore a maximum cluster size of 3 strips for SS4 modules. As seen from Figure 7.12, a few very large cluster were recorded ($n_{strips} > 10$); such effect appears to be due to the interaction of high energetic muons, generating a shower in the Cosmic Rack. An example of a wide cluster is given

in Figure 7.13. The full display of the event (Figure 7.14) shows the shower developing in the Cosmic Rack.

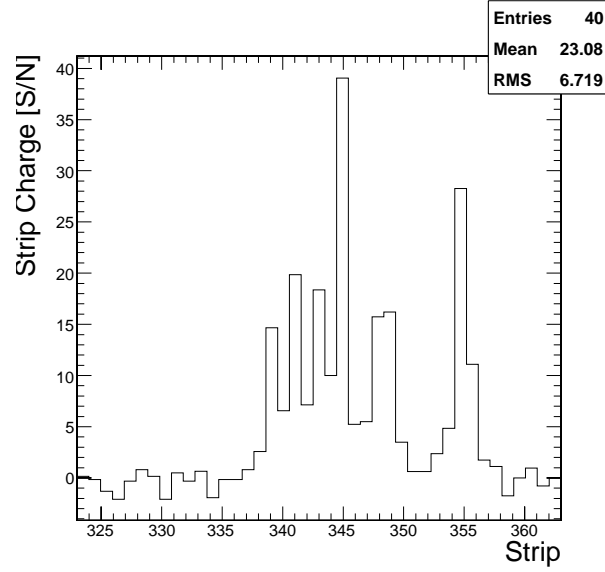


FIGURE 7.13: *Shape of a wide cluster and neighboring strips.*

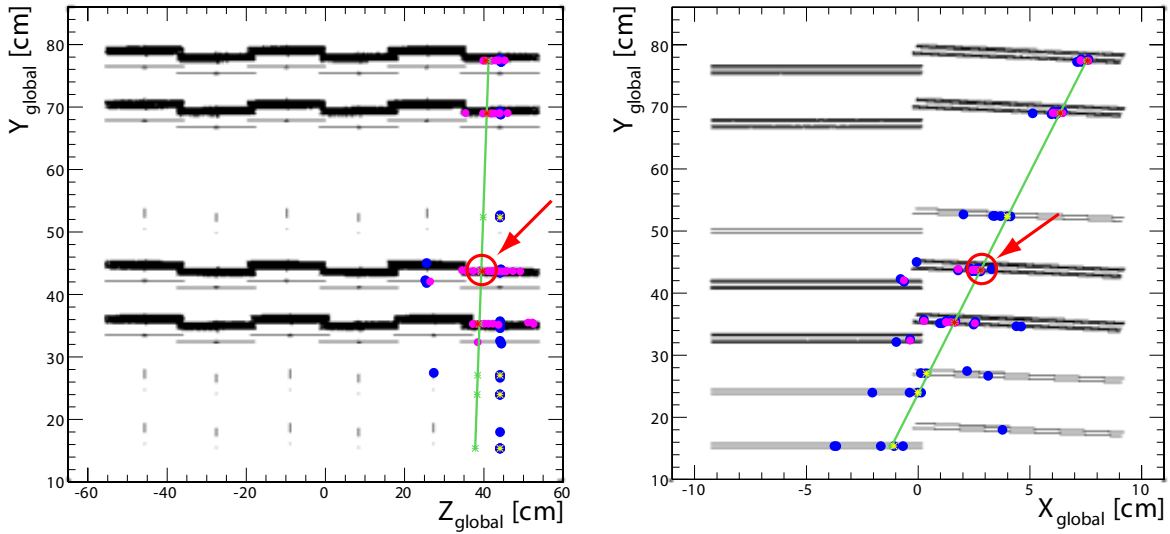


FIGURE 7.14: *An event in the Cosmic Rack with high multiplicity: yz-view (left) yx-view (right). RecHits are colored blue, matched RecHits purple and the track is in green. The cluster with the large width shown in Figure 7.13 is indicated by the arrow.*

The distribution of the cluster size for tracks almost perpendicular to the sensor ($|\Theta_{UW}| < 0.05$) is shown in Figure 7.15. The most probable cluster size is two in deconvolution mode, and one in peak mode. Since the S/N ratio is larger in peak mode than in deconvolution mode, and the thresholds for accepting strips in the cluster reconstruction are defined in terms of noise, the cluster size would be expected to be larger in peak mode, if charge sharing was the dominant effect. As will be shown in the following chapter the observed cluster size can be explained by capacitive coupling.

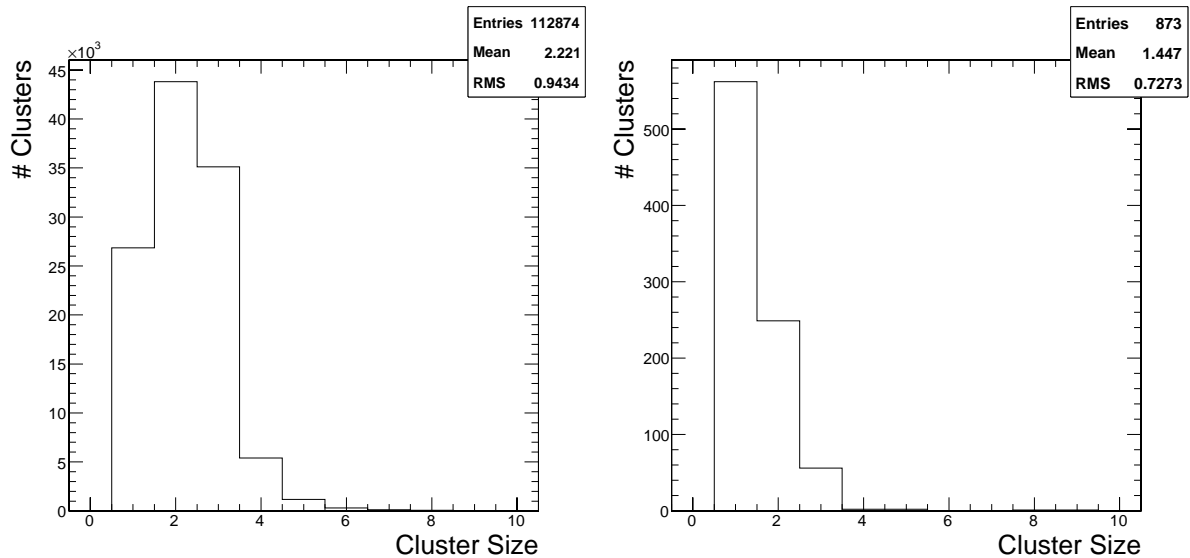


FIGURE 7.15: *Distribution of cluster size for almost perpendicular crossing tracks ($|\Theta_{UW}| < 0.05$) in deconvolution-mode (left) and peak-mode (right).*

7.4 Summary

The S/N ratio in peak and deconvolution mode has been measured. At room temperature with path length correction a ratio of 20 in deconvolution and 30 in peak mode was observed. This is in good agreement with the estimated charge generated by a MIP of 40000 electron-hole pairs and the expected noise of $\approx 2100e^-$ in deconvolution mode and $\approx 1400e^-$ in peak mode. The dependence of the cluster size on the track angle has been studied. For perpendicularly passing particles, clusters are larger than one would expect from charge sharing between neighboring strips, and the cluster size distribution is significantly different in peak and deconvolution mode. Surprisingly the cluster size in deconvolution mode is larger than in peak mode. This effect will be subject of the following chapter studying the detector response. The measurements on the S/N ratio and the cluster size are summarized in Table 7.3.

Run Nr.	Gate [ns]	APV Mode	Module Type	MPV [S/N]	Number Clusters	Cluster Size	# Clusters $ \Theta_{UW} < 0.05$
Room Temperature (20°C), Cluster Cuts: 3σ (side), 4σ (seed), 5σ (cluster)							
400301	5	PEAK	SS4	30.1	2764	1.45	873
400301	5	PEAK	SS6	29.4	3013	1.51	902
400364	5	DECV	SS4	19.9	4817	2.01	1525
400364	5	DECV	SS6	19.4	5208	2.03	1535
200379	5	DECV	SS4	20.6	333575	2.21	83126
200397	5	DECV	SS4	20.7	407352	2.23	1036696
200401	5	DECV	SS4	20.6	444491	2.22	112874
200786	-	PEAK	SS4	30.0	387350	1.92	98130
Cold Temperature (-10°C), Cluster Cuts: 3σ (side), 4σ (seed), 5σ (cluster)							
200881	-	PEAK	SS4	32.5	289068	2.01	72682
Room Temperature (20°C), Cluster Cuts: 2σ (side), 3σ (seed), 5σ (cluster)							
400301	5	PEAK	SS4	30.8	2776	1.79	879
400301	5	PEAK	SS6	31.9	3023	1.86	907
400364	5	DECV	SS4	21.4	4824	2.65	1529
400364	5	DECV	SS6	21.0	5212	2.67	1539
200401	5	DECV	SS4	22.3	444883	2.89	112941

TABLE 7.3: *Signal to noise ratio for SS6 (OB1) and SS4 (OB2) sensors normalized to path length and mean cluster size for particles close to normal incidence. The runs in peak mode 200786 and 200881 have been taken without a gate. The resulting jitter of up to 25 ns between the deposition has a small effect on the S/N ratio but measurable influence on the cluster size. As will be shown in the following this is due to the dependence of the coupling on the sampling point.*

Chapter 8

Detector Response

To fully exploit the potential of the CMS Tracker the precise knowledge of the detector response is crucial. The optimization of the sampling point in time, of the cluster finding algorithm and hence of the spatial resolution, require a detailed understanding of the time evolution of the signals and of the spatial profile for different track incidence angles. With the Cosmic Rack the detector response has been studied by tracking cosmic muons.

8.1 Reconstruction of the Pulse Shape

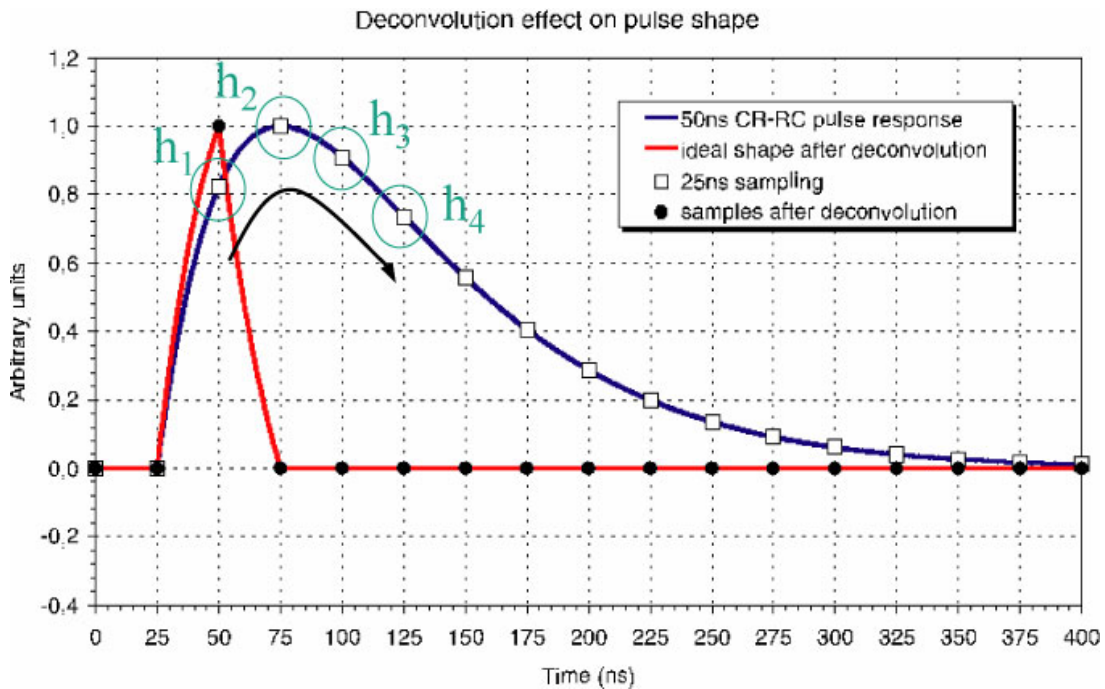


FIGURE 8.1: *Ideal pulse shape in peak and deconvolution mode (for a charge deposited at $t=25$ ns) [96].*

The CMS readout electronics is designed to cope with the LHC bunch crossing rate of 40 MHz. At each bunch crossing on average about 20 proton proton collisions are expected to take place (in high luminosity operation), translating to about 1000 charged particles crossing the Tracker. Thus ideally the detector response should reach its maximum within 25 ns and should be rapidly dropping to zero afterwards. Implementing such short pulses with conventional filtering techniques requires fast charge collection, low detector capacitances and high bandwidth of the front end electronics. The higher bandwidth however not only increases the electronics

noise (as seen in from Table 6.1 the dominating serial noise is proportional to $\sqrt{1/\tau}$), but also leads to increased power consumption.

For the CMS Tracker readout chips (the APV25) - a new approach has been adopted, that is based on a discrete convolution filtering technique [97]. The pulse shaping in the fundamental mode (the peak mode) is performed by a simple CR-RC shaper with a time constant $\tau = 50 \text{ ns}$ that is ideally sampled at its maximum (the sampling point can be tuned). In deconvolution mode the pulse from the shaper is sampled at three equidistant points in time. A weighted sum of the samples is then computed and passed to the output.

The ideal pulse shapes for peak and deconvolution mode are shown Figure 8.1. In peak mode the signal has significant size even 150 ns after the charge deposition, whereas in deconvolution mode it is confined within one bunch crossing. The peak mode has lower noise compared to the deconvolution mode (by approximately a factor of 2/3), and will be used for debugging and testing purposes in the low luminosity phase of LHC operation. The default mode of operation is the deconvolution mode, required for an efficient pattern recognition for the track reconstruction at nominal luminosity. In the following, the principles of the deconvolution mode will be outlined and the weights of the convolution derived.

8.1.1 APV25 Deconvolution Mode

The APV25 deconvolution mode uses a discrete convolution filter. As illustrated in Figure 8.2 the principle of the deconvolution mode is to apply the inverse transformation $w(t)$ of the pulse-shaping circuits $h(t)$, in order to obtain the original detector signal $s(t)$.

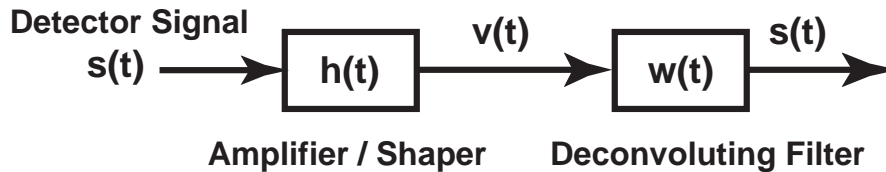


FIGURE 8.2: Schematic of the pulse shaping process.

Without the deconvolution filter the detector response $v(t)$ is the convolution of the detector signal $s(t)$ with $h(t)$ the signal shaping due to the integrator and CR-RC pulse shaper:

$$v(t) = \int_{-\infty}^t h(t - \hat{t}) s(\hat{t}) d\hat{t} \quad (8.1)$$

If $s(t)$ and $v(t)$ are only measured in equidistant points in time i , this can be written as a matrix equation:

$$V_i = \sum_j H_{ij} S_j \Rightarrow \mathbf{V} = \mathbf{H}\mathbf{S} \quad (8.2)$$

Where H_{ij} corresponds to $h(t_i - t_j)$ and S_i to $s(t_i)$.

In order to obtain the detector signal $s(t)$ from $v(t)$ one has to apply the inverse transformation:

$$\mathbf{S} = \mathbf{W}\mathbf{V} = \mathbf{H}^{-1}\mathbf{H}\mathbf{S} \quad (8.3)$$

This general mechanism will now be tailored to the scenario of the CMS detector. The pulse-shaping $h(t)$ for an integrator followed by an CR-RC pulse shaper with a time constant τ

(normalized to 1 for $t = \tau$) equals:¹

$$h(t) = \frac{t}{\tau} e^{1 - \frac{t}{\tau}} \quad (8.4)$$

The pulse shaper of the front end electronics has a time constant of 50 ns and the sampling is done at time intervals $\Delta t = 25$ ns therefore:

$$\Delta t = \frac{\tau}{2} \quad (8.5)$$

For the pulse shaping coefficients $h_n = h(t_n)$ at the discrete sample points $t_n = n\Delta t$ one thus obtains:

$$h_n = \frac{ne}{2} e^{-\frac{n}{2}} \quad n = 0, 1, 2, 3 \dots \quad (8.6)$$

It can be shown that three samples are sufficient for constructing the deconvoluted pulse shape, which is given by:

$$s_n = w_1 h_n + w_2 h_{n-1} + w_3 h_{n-2} \quad (8.7)$$

The discrete weights w_i are calculated from the inverse of \mathbf{H} and they are:

$$w_1 = \frac{2}{\sqrt{e}} = 1.2131 \quad (8.8)$$

$$w_2 = -\frac{4}{e} = -1.4715 \quad (8.9)$$

$$w_3 = \frac{2}{e\sqrt{e}} = 0.4463 \quad (8.10)$$

Nominally, the deconvoluted signal is confined within a bunch crossing, since it is different from 0 only for $n = 1$:

$$s_n = 0 \quad \forall n \leq 0 \quad (8.11)$$

$$s_n = w_1 h_1 = 1 \quad \forall n = 1 \quad (8.12)$$

$$s_n = \frac{e}{2} e^{-\frac{n}{2}} \left[\frac{2}{\sqrt{e}} n - \frac{4}{e} (n-1) \sqrt{e} + \frac{2}{e\sqrt{e}} (n-2) e \right] = 0 \quad \forall n > 1 \quad (8.13)$$

8.1.2 Measurements of the Pulse Shape

The pulse shape in deconvolution mode has been measured with the Cosmic Rack by tracking cosmic particles and varying the delay between the charge deposition and the readout.

The APV25 front end chip is controlled by various parameters. Their influence on the pulse shape is described in [98]. For the studies with the Cosmic Rack the chips have been operated using the values proposed for 30°C.

To evaluate the capability of the setup in reconstructing the pulse shape, data from the internal calibration circuit were compared to physics data. The modules were operated with a bias voltage of 300 V, and the gate of the trigger system was set to 5 ns. In the calibration mode the delay steps are 3.125 ns while for the physics run data were collected every two fine delay steps (corresponding to $2 \cdot 25/24$ ns). The result of this measurement is shown in Figure 8.3. The plot shows the mean of the signal to noise ratio of the cluster seed, where only clusters that belong to a track have been selected. If the track has hit the module but no cluster has been found a S/N of 0 was used. This causes a more rapid drop when the signal efficiency is low, but is more suitable for this test compared to omitting these "missing" clusters. The FWHM is in both cases ≈ 30 ns demonstrating the low jitter of the trigger system.

¹This is a simplification assuming that $s(t)$ is fast compared to τ and can be modelled as a Dirac delta pulse.

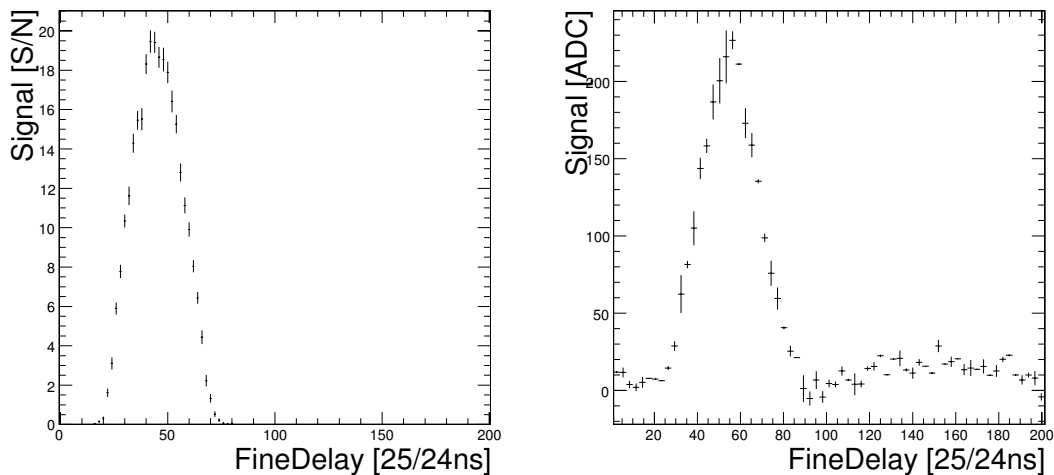


FIGURE 8.3: Comparison of the pulse shape obtained from tracking cosmics (left) and the internal calibration circuit (right).

8.2 Cluster Analysis

A cluster is a set of neighboring strips that have collected charge from a traversing particle. The strip with the highest signal is referred to as the seed. To define a cluster in the CMS offline analysis three cuts are applied. A threshold defines the minimum signal of a seed, and another threshold is used for accepting neighboring strips, that are added to the cluster. A third threshold is then defined on the total signal of the cluster².

Different effects contributing to cluster size and spatial resolution are discussed below, following [99].

8.2.1 Spatial Resolution

If the track coordinate is estimated from the position of a single strip, the position resolution is solely defined by the pitch P , and can be written as:

$$\langle \Delta x^2 \rangle = \frac{1}{P} \int_{-P/2}^{P/2} x^2 dx = \frac{P^2}{12} \quad (8.14)$$

and therefore the resolution σ is $P\sqrt{12}$, which is referred to as binary resolution. In the CMS Tracker the pitch ranges from $80 \mu m$ to $220 \mu m$, corresponding to a binary resolution from $23 \mu m$ to $64 \mu m$. If the pulse height is readout, when a particle leaves charge on neighboring strips, the signals can be interpolated to improve the position resolution. Assuming that the

²All cuts are applied on pedestal and common mode subtracted data and defined as a signal to noise ratio.

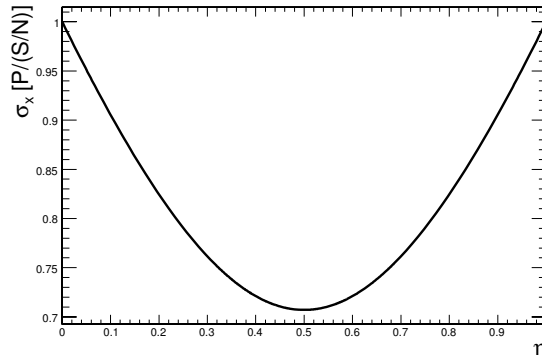


FIGURE 8.4: Resolution in terms of pitch P divided by the signal to noise ratio (S/N) as a function of η , assuming linear charge sharing between two adjacent strips.

amount of charge collected by a strip is inversely proportional to the distance of the impact point from that strip ("linear" charge sharing), the hit position can be estimated as:

$$x = x_L + P\eta \quad (8.15)$$

where η is defined as:

$$\eta = \left(\frac{S_R}{S_L + S_R} \right) \quad (8.16)$$

and S_L and S_R are the signals collected on the "left" and "right" strip and x_L is the coordinate of the left strip. The achievable resolution is in principle only limited by the signal to noise ratio. For example in case of two strips sharing the charge, the resolution can be calculated from the above formula using error propagation:

$$\sigma_x = \frac{1}{S/N} P \left(\sqrt{1 - 2\eta + 2\eta^2} \right) \quad (8.17)$$

Thus for a signal to noise ratio S/N larger than $\sqrt{12}$ the resolution obtained by calculating the charge barycenter should be better than the binary resolution. The resolution as a function of η is shown in Figure 8.2.1. This is however a simplified model. In a real system due to threshold effects (for the definition of the clusters) the resolution will be worse. Also linear charge sharing is an idealization, which is in practice only seen if the extension of the charge cloud matches the pitch and electronics crosstalk is negligible. Effects of charge sharing will be discussed in the following section.

8.2.2 Charge Sharing and Electronics Coupling

Effects that contribute to the cluster size can be classified into two categories: charge sharing and electronics crosstalk. We will assume in the following that electronics crosstalk is independent of the position where the charge was generated, while charge sharing indicates processes where the charge is shared among consecutive strips depending on the position of the charge deposition.

As discussed in section 2.5, in the case of the p-doped strips of the CMS sensors, the cluster size depends only on the collection of the holes. We will therefore focus on the drift and collection of holes in the following.

Diffusion

A particle traversing a sensor generates charge in a region of $\approx 1 \mu m$ around its trajectory. The charge carriers drift in the electric field following the field lines. Thus most of the charge is

collected by the nearest strip, however due to diffusion a small amount of the charge may be collected by neighboring strips.

Diffusion of the charge carriers is caused by multiple collisions of the charge carries with each other and the spread can be described with a gaussian distribution. The number N of particles in a distance $r + dr$ from their origin at a given time t is given by:

$$\frac{dN(r, t)}{N} = \frac{1}{\sqrt{4\pi Dt}} \exp^{-\frac{r^2}{4Dt}} dr \quad (8.18)$$

where D is the diffusion coefficient, a function of the thermal energy kT and the mobility μ , and the charge q :

$$D = \mu \frac{kT}{q} \quad (8.19)$$

The spread due to diffusion is given by the diffusion coefficient and the drift time t_{drift} :

$$\sigma = \sqrt{2Dt_{drift}} \quad (8.20)$$

In first approximation one can estimate the drift time of the charge cloud that is generated homogeneously along the particles track over the entire sensor thickness d by its mean:

$$t_{drift} = \frac{d/2}{\mu U_b/d} \quad (8.21)$$

With this approximation the diffusion width at the readout electrodes can be written as:

$$\sigma = d \sqrt{\frac{kT}{q} \frac{1}{U_b}} \quad (8.22)$$

Evaluating the above equation for CMS TOB modules ($d=500 \mu\text{m}$), biased with a voltage $U_b = 300 \text{ V}$ one obtains for $T = 300\text{K}$ a diffusion width³ of $5 \mu\text{m}$. The diffusion is small compared to the sensor pitch ($O(100\mu\text{m})$). Thus charge sharing will only take place in a narrow region in the middle between two strips as illustrated in Figure 8.5. For a charge cloud located

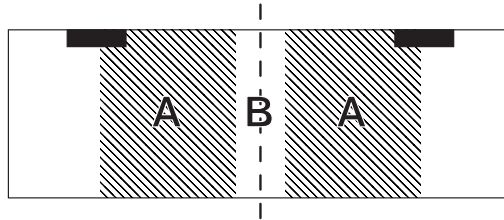


FIGURE 8.5: Charge carriers will drift - following the electrical field lines - towards the closest strip. Charge sharing (driven by diffusion) will only take place in a region B around the border of the strips, whereas in region A the charge will be collected mostly by the closest strip [99].

³Note that the spread due to diffusion is the same for electrons and holes.

at a distance x from the center of the two strips, that reaches the readout electrodes after a drift time t , the fraction of charge collected by the furthest of the two strips is given by:

$$\frac{dN(x, t)}{N} = \frac{1}{\sqrt{4\pi Dt}} \frac{1}{2} \int_x^\infty \exp^{-\frac{r^2}{4Dt}} dr = \frac{1}{2} \left(1 - \text{Erf} \left(\frac{x}{\sqrt{4Dt}} \right) \right) \quad (8.23)$$

If the charge cloud is distributed along a particles track, the distribution has to be integrated over all t, x . For charge depositions along tracks perpendicular to the sensor, an approximation can be given by assuming an average drift time and using the formula above. As illustrated in Figure 8.6 fractions of charge collected on the two strips vary almost linear with the coordinate of the charge deposition, but only in a narrow region with a width of $\sigma = \sqrt{2Dt_{drift}}$. Outside this region the charge is almost entirely collected by the nearest strip.

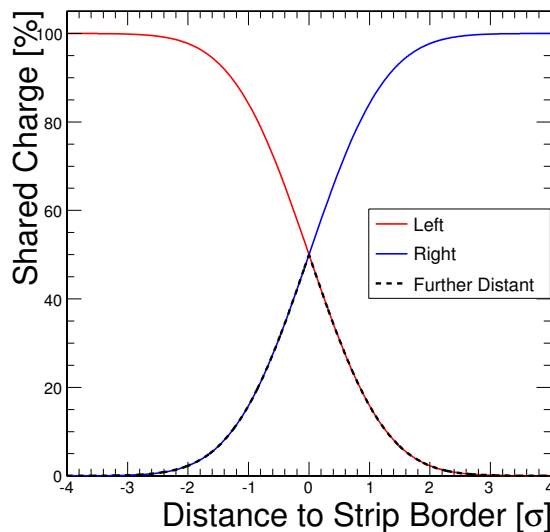


FIGURE 8.6: Fraction of charge carriers collected by the left, right or further distant strip for particles crossing perpendicular to the sensor plane as a function of the coordinate of the charge deposition, in units of diffusion lengths (0 corresponds to the middle point between the two strips).

Track Inclination

The charge released in the sensor can be spread over more than one strip due to the inclination of the impinging particle (Figure 8.7). The extension of the charge deposition is given by the track inclination θ_{UW} and the thickness of the sensor d :

$$L = d \tan(\theta_{UW}) \quad (8.24)$$

Lorentz Angle

If charges drift in a magnetic field their motion is affected by the Lorentz force (see Figure 8.8):

$$\vec{F} = q \left(\vec{E} + \vec{v} \times \vec{B} \right) \quad (8.25)$$

The angle between the drift direction and the electric field is called the *Lorentz angle*. Assuming constant mobility of the charge carriers μ and \vec{B} being perpendicular to \vec{E} the tangent of the Lorentz angle can be calculated by:

$$\tan \theta_{uw} = B\mu \quad (8.26)$$

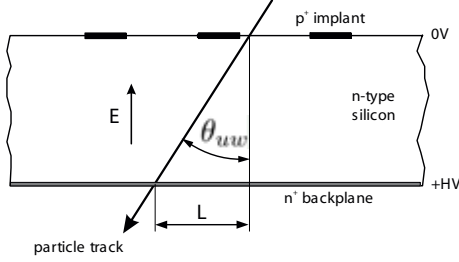


FIGURE 8.7: *Extension of the charge cloud due to the track inclination.*

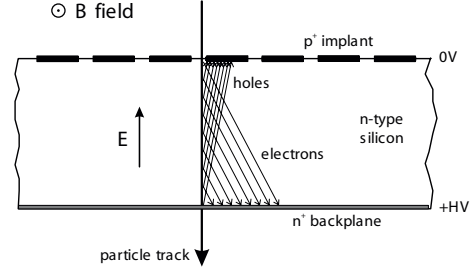


FIGURE 8.8: *Extension of the charge cloud due to the Lorentz angle.*

The Lorentz angle is different for holes and electrons. In the CMS Tracker, due to the 4 Tesla magnetic field, a Lorentz angle of about 10° for the holes is expected. The Lorentz angle is independent of the track inclination and contributes to the charge spread in the same way as an inclined track. If this additional spread is not wanted, the orientation of the sensors can be chosen to compensate for the Lorentz angle and keep minimal cluster size for the high momentum tracks emerging from the primary vertex.

8.3 Measurements of the Electronics Crosstalk

In order to measure the crosstalk, the effect of charge sharing needs to be disentangled. To perform this study it is useful to introduce the η function. This is a function of the signal of the seed strip and its highest neighboring strip, given by:

$$\eta = \frac{S_R}{S_L + S_R} \quad (8.27)$$

where S_L refers to the signal of the "left" strip and S_R refers to the signal of the "right" strip, independently of which of the two is the seed strip.

From the measured distribution of the η -function for a data sample where the detectors have uniform illumination, estimates of charge sharing, capacitive coupling and S/N can be derived. It is therefore also referred to as "Response-function". To understand the properties of this distribution one can consider the following two extreme cases: for ideal linear charge sharing all values of η between 0 and 1 have the same probability, and therefore the η values should have a flat distribution. On the contrary, if there is no charge sharing, either the left or the right strip collects all the charge and the distribution of the η -function should have two peaks: one at 0 (the left strip collects all charge) and the other at 1 (the right strip is collects all the charge).

Figure 8.9 shows the distribution of the η -function for an SS4 Rod in the Cosmic Rack. The area where charge sharing takes place is small compared to that where charge is collected by one strip only. The peaks are not exactly at 0 and 1 but shifted towards the middle. This effect is due to electronics coupling, occurring when a fixed fraction of the signal collected by a strip is transferred to the neighbor. Fluctuations due to noise determine the width of the peak.

The distribution of the η -function can be used to estimate the width of the region in which charge sharing takes place (region "B" in Figure 8.5): the area under the gaussian peaks is proportional to the region where the signal is collected by a single strip, and the remaining area is proportional to the region where charge sharing occurs.

Charge sharing versus Track Angle

In the absence of a magnetic field the track inclination is the main contribution to charge sharing. This can be verified by plotting the η -function for different track samples. The distribution of

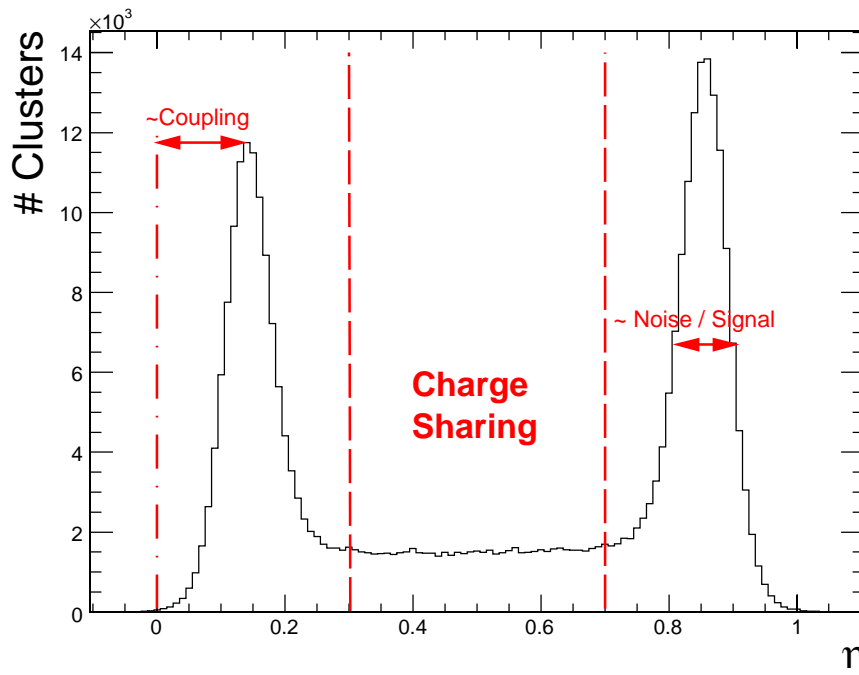


FIGURE 8.9: *Distribution of η -function for modules of SS4 Rods from the data collected with the Cosmic Rack.*

the η -function in Figure 8.9 was obtained without applying any cuts on the selected tracks. The region of charge sharing is rather small, which follows from the acceptance of the Cosmic Rack and its trigger system, that is largest for perpendicular tracks, as seen from the corresponding distribution of the (local) track angles θ_{UW} (Figure 8.10).

To illustrate the effect of the track inclination on the charge sharing, two cuts on the local track angle have been selected. The left plot of Figure 8.11 shows the distribution of η for tracks with large inclination ($\theta_{UW} \geq 0.4$). The cut has been selected such that the extension of the charge matches the pitch. This results - as expected - in almost linear charge sharing. The plot on the right contains tracks almost perpendicular to the detectors ($\theta_{UW} \leq 0.1$) and shows minimal charge sharing.

Measurement Method

As demonstrated above, charge sharing can be effectively controlled by cutting on the local track angle. For particles traversing the detectors perpendicularly there is negligible charge sharing between neighboring strips and coupling is the dominating source for clusters with more than one strip. An estimate of the coupling can be derived from the η distribution (right plot of Figure 8.11): If the charge is deposited on the left strip only, the signal of the right strip is due to coupling, $S_R = cS_L$ and η is written as:

$$\eta = \frac{S_R}{S_L + S_R} = \frac{c \cdot S_L}{S_L(1 + c)} = \frac{c}{1 + c} \quad (8.28)$$

Similarly for the other peak, where the right strip is the seed, $S_L = cS_R$ and η is written as:

$$\eta = \frac{S_R}{S_L + S_R} = \frac{S_R}{S_R \cdot (1 + c)} = \frac{1}{1 + c} \quad (8.29)$$

Using the positions of these peaks to calculate the coupling however, results in an overestimation of the coupling, since the η function selects by definition the neighboring strip with the higher

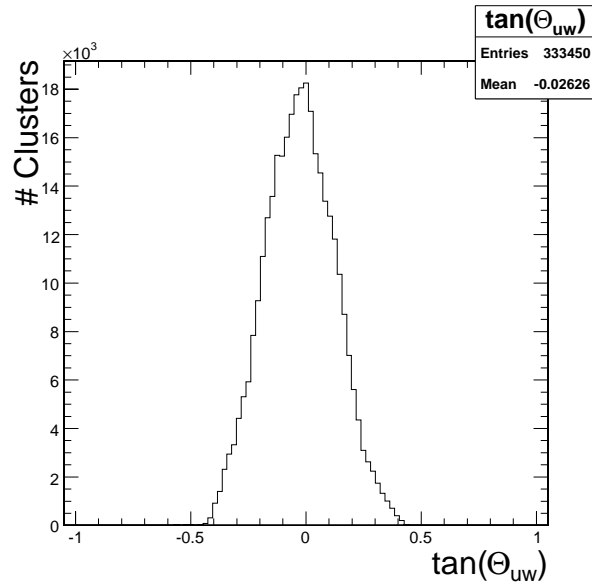


FIGURE 8.10: *Distribution of the local track angle θ_{UW} in the Cosmic Rack.*

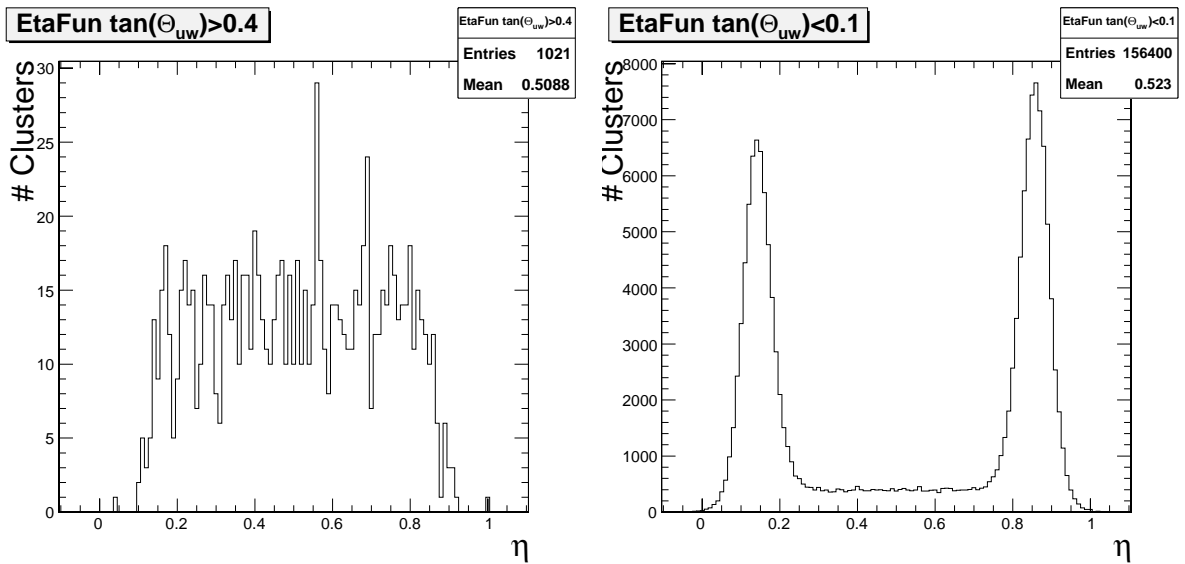


FIGURE 8.11: *Distribution of the η -function for tracks with an inclination of $|\theta_{UW}| > 0.4$ (left) and almost perpendicular to the detectors $|\theta_{UW}| < 0.1$ (right).*

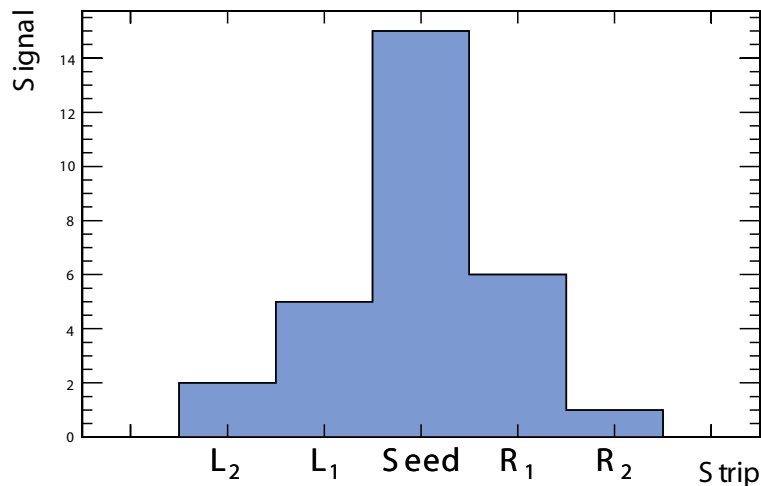


FIGURE 8.12: *Example of a cluster with seed and neighboring strips.*

signal, i.e. the one of the two that had a more positive noise fluctuation. Therefore a different approach has been developed. The coupling of a strip to its nearest neighbors c_1 (in the absence of charge sharing) is defined as:

$$c_1 = \frac{S_{L1} + S_{R1}}{2S_{Seed}} \quad (8.30)$$

where S_{L1} (S_{R1}), indicate the signal of the left (right) neighbor of the seed strip as shown in Figure 8.12. If the correlation between the noise of the side strips can be neglected, this definition removes the bias discussed above.

In analogy to the coupling c_1 to the nearest neighbors, also a coupling to the second c_2 and third c_3 can be defined:

$$c_i = \frac{S_{Li} + S_{Ri}}{2S_{Seed}} \quad (8.31)$$

For the analysis a cut on $|\Theta_{UW}| < 0.1$ was chosen to minimize charge sharing, while keeping sufficient statistics. In addition to the angular cut for steep inclined tracks the bias voltage has been set to a high value of 300 V to minimize diffusion. It is important to notice that to obtain unbiased results all clusters have to be included in the distribution, even if the neighboring strips are below threshold. A custom cluster analysis has therefore been tailored using pedestal subtracted and common mode subtracted strip signals. The measured distribution of the coupling parameter c_1 (defined according to eqn.8.30) is shown in Figure 8.13. This distribution is well modelled by a Gaussian plus a tail at positive value. The tail is due to residual charge sharing, the width is due to the noise of the side strips, and the position of the peak of the Gaussian (basically unaffected by the presence of the tail) is the estimator of the coupling.

The couplings shown above are defined only for a given sampling point in time; their time evolution will be discussed in the next section.

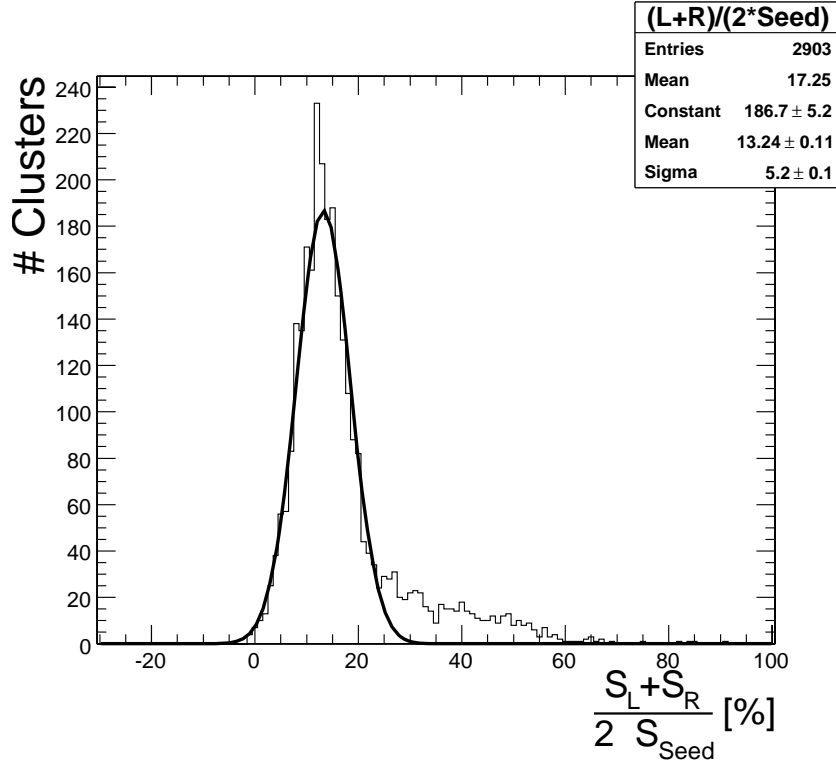


FIGURE 8.13: Distribution of c_1 for all modules of a given Rod. The measured coupling is 13.2%

8.4 Time Evolution of the Coupling

The coupling of neighboring strips show a dependence of the sampling point in time. This can be qualitatively understood if the sensor is modelled as RC-network with different time constants for the strips that are collecting the charge, and the ones that have a signal due to coupling only. In the Cosmic Rack the time dependence has been measured, by changing the delay between charge deposition and readout. Figure 8.14 and Figure 8.15, show the resulting plots in peak mode for SS4 and SS6 modules, respectively. The corresponding plots in deconvolution mode are shown in Figure 8.16 for SS4 and in Figure 8.17 for SS6 modules. In these plots, in addition to the coupling coefficients c_1 , c_2 and c_3 , the time evolution of the signal in the strips is shown.

These figures show that the coupling strongly depends on the sampling point of time. Of special interest are the coupling coefficients at the ideal sampling time, defined as the one for which the seed strip is has maximum signal. Technically this has been implemented fitting the signal in peak mode with a CR-RC pulse shape⁴ [100]:

$$S_{peak}(t) = A \frac{t}{\tau} e^{-\frac{t}{\tau}} \quad (8.32)$$

For the data in deconvolution mode the deconvolution algorithm is applied to the above function obtaining.

$$S_{Deconv}(t) = 1.2131 \cdot S_{peak}(t - 25 \text{ ns}) - 1.4715 \cdot S_{peak}(t) + 0.4463 \cdot S_{peak}(t + 25 \text{ ns}) \quad (8.33)$$

Figure 8.18 shows that these functions describe well the measured pulse shape of the seed strip.

The measurements of the coupling coefficients for SS4 and SS6 modules, peak and deconvolution mode at the optimal sampling time are summarized in Table 8.2. Couplings have a strong

⁴To accommodate for the jitter of the trigger logic and the charge collection time the function for the fit has been convoluted with a Gaussian

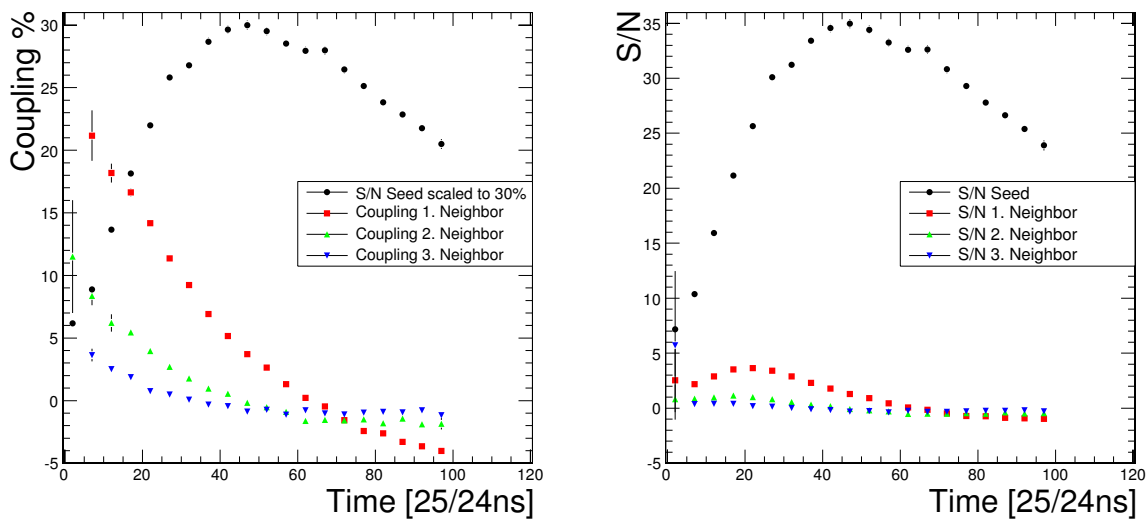


FIGURE 8.14: Time evolution of coupling coefficients (left) and the signal in the seed strip and neighboring strips (right) for SS4 modules in peak mode.

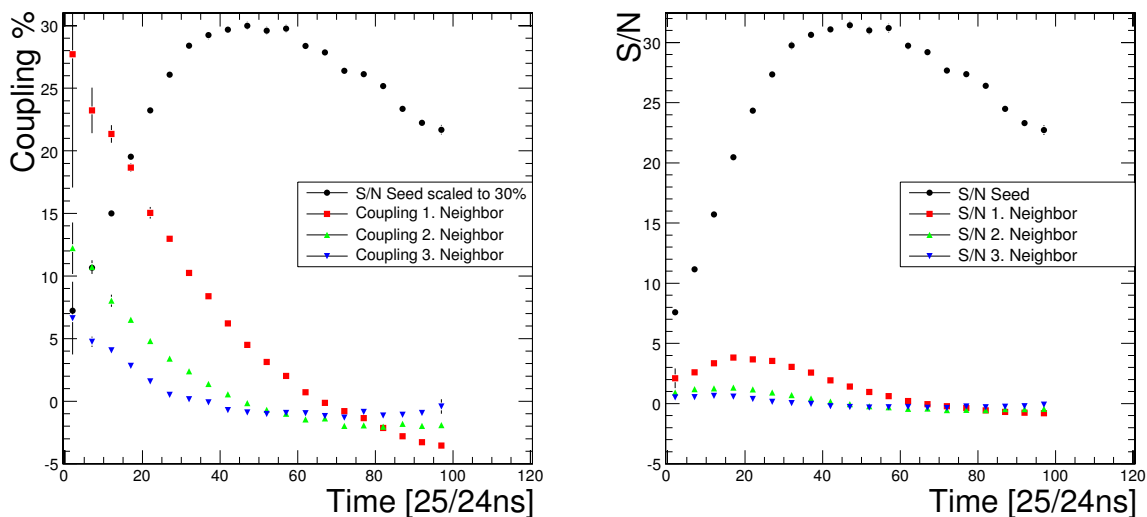


FIGURE 8.15: Time evolution of coupling coefficients (left) and the signal in the seed strip and neighboring strips (right) for SS6 modules in peak mode.

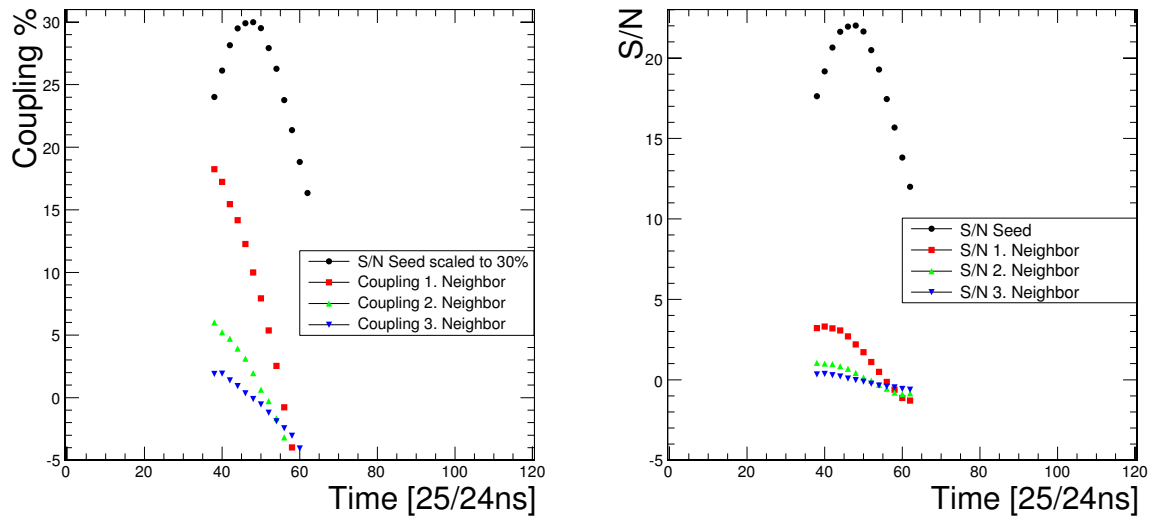


FIGURE 8.16: Time evolution of coupling coefficients (left) and the signal in the seed strip and neighboring strips (right) for SS4 modules in deconvolution mode.

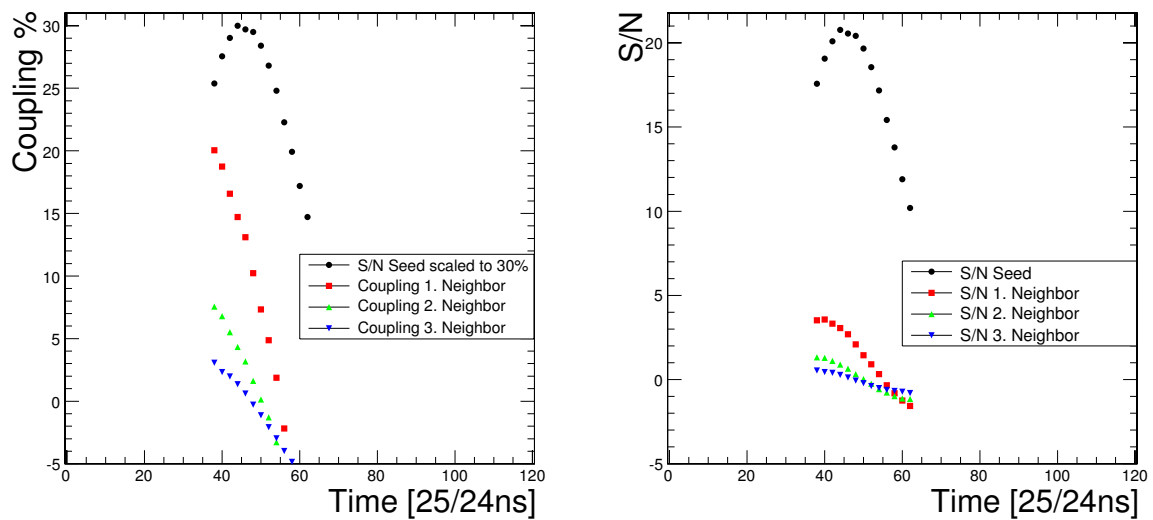


FIGURE 8.17: Time evolution of coupling coefficients (left) and the signal in the seed strip and neighboring strips (right) for SS6 modules in deconvolution mode.

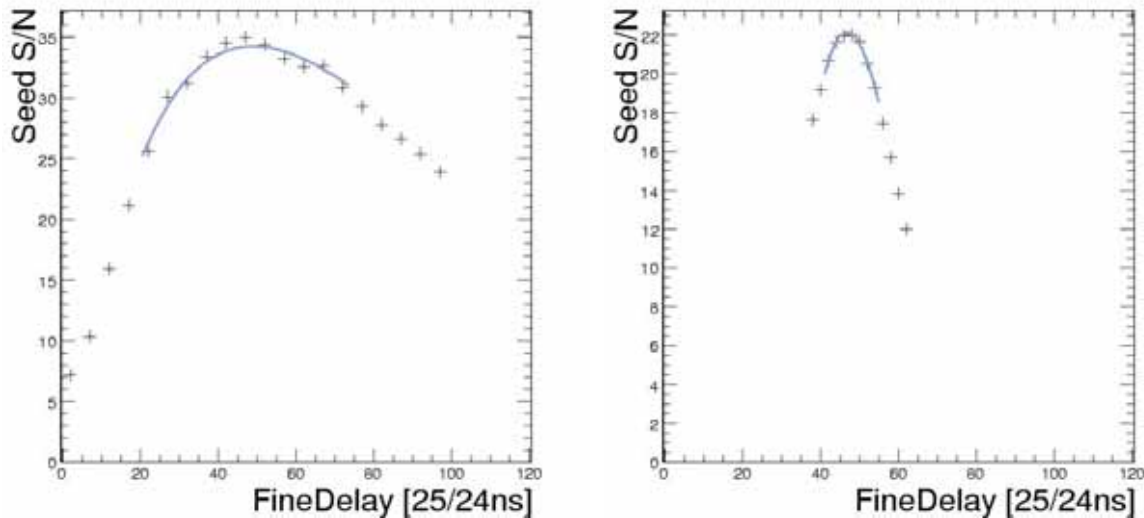


FIGURE 8.18: Determining the optimal sampling point of time. The Signal of the seed strip and the fit functions for the pulse shapes are shown for peak (left) and deconvolution mode (right).

TABLE 8.1: Coupling coefficients at optimal sampling time

Run Nr.	Bias Voltage	APV Mode	Module Type	C_1 [%] (t_{opt})	C_2 [%] (t_{opt})	C_3 [%] (t_{opt})	C_1 [%] (t_{DECV})	C_2 [%] (t_{DECV})	C_3 [%] (t_{DECV})
400301	300	PEAK	SS6	4.3	-0.2	-0.9	14.4	4.4	1.2
400301	300	PEAK	SS4	3.3	-0.3	-0.8	12.5	3.2	0.6
400364	300	DECV	SS4	11.3	2.6	0.2			
400364	300	DECV	SS6	13.8	3.7	1.0			
400305	200	PEAK	SS6	4.8	0.2	-0.9	14.1	4.4	1.5
400305	200	PEAK	SS4	3.8	-0.3	-0.8	12.3	3.3	0.5

TABLE 8.2: In peak mode in addition to the optimal sampling point of time the coupling coefficients are also quoted 25 ns before " t_{DECV} " as this corresponds to the sampling point used in the deconvolution mode.

dependence on the sampling point of time ($\approx 1\%/ns$)! The coupling coefficients for deconvolution mode are in good agreement with those in peak mode measured 25 ns before the peak. Thus the deconvolution algorithm as implemented on the APV25 seems to have a negligible contribution to the coupling.

8.4.1 Verification of Measured Coupling Coefficients

Couplings coefficients have been measured analyzing only clusters from events with almost perpendicular tracks, hence clusters where charge was deposited mostly on one strip only. In the following, the validity of these coupling coefficients will be verified by analyzing clusters where charge has been shared between two neighboring strips.

A simple model for clusters where charge has been deposited on two strips is presented in Figure 8.19. Charge is deposited only on the two strips A and B , the signal of the outer strips X and Y is due to coupling and noise only. For convenience A is taken to be the seed strip and B the highest neighbor. The charges deposited on strips A and B are denoted a and b , respectively.

The signal on strip A is composed by the charge deposited on that strip and coupling from

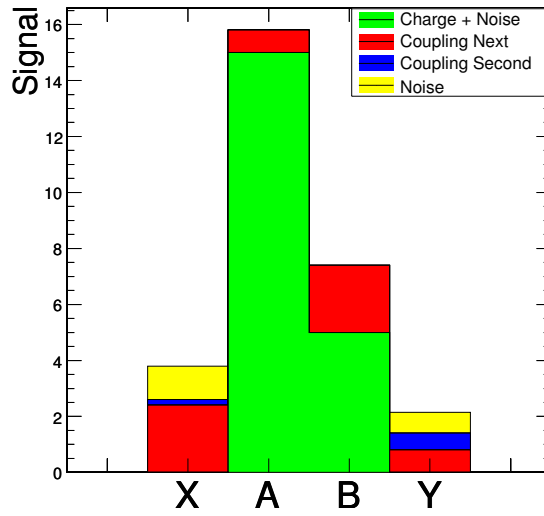


FIGURE 8.19: Model for clusters where charge has been deposited on two strips.

the charge b of strip B via the coefficient c_1 and similarly for strip B; therefore the total charge in strip A and B is given by:

$$A = a + c_1 \cdot b \quad (8.34)$$

$$B = b + c_1 \cdot a \quad (8.35)$$

The signal in the outer strips X and Y is given by the coupling from the charges a and b via first and second neighbor coupling coefficients c_1 , c_2 and noise.

$$X = c_1 \cdot a + c_2 \cdot b \quad (8.36)$$

$$Y = c_1 \cdot b + c_2 \cdot a \quad (8.37)$$

This model can be tested against reconstructed clusters from the data, as follows:

- Select clusters where charge is deposited on two strips only (A,B,X,Y are measured).
- Solve the equation system 8.35 for a and b using the measured couplings c_1 and c_2
- Calculate the expected signal X_{calc} , Y_{calc} using eqn.8.37.
- Compare the predicted values X_{calc} , Y_{calc} with the measured ones (X,Y).

For the selection of cluster where charge is deposited on two strips, no restriction in the track inclination has been applied and the signal on B was requested to exceed the following threshold:

$$B > a \cdot c_1 + 2 \cdot noise \quad (8.38)$$

This selection is motivated as follows: If there would be no charge on strip B ($b=0$) there would be a contribution due to coupling ($a \cdot c_1$) and noise. By requiring that the signal of B exceeds the expected coupling by twice the noise, we select mostly clusters with charge deposited on more than one strip.

If the model is valid, then the differences between measured values and calculated values for X,Y should differ only by the noise, which is in agreement with the results of the test shown

in Figure 8.20. The mean of the difference between the estimated and measured values of X, Y normalized to the noise is compatible with 0 and the spread is ≈ 1 . These values have been obtained fitting a gaussian distribution to the histograms. The small tails that observed may be due to clusters where charge has been deposited on more than two strips.

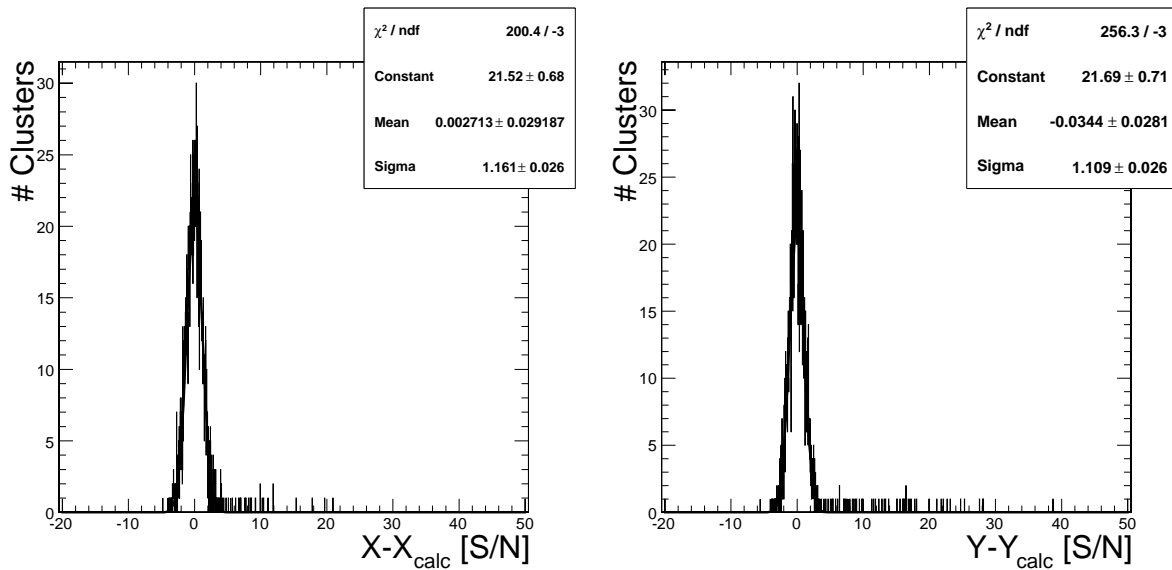


FIGURE 8.20: *Difference between estimated signal of the side strips due to coupling and the measured signals.*

In the following paragraph a prediction for the coupling coefficients is derived from simulation of the electric circuits of the front end electronics and the strip sensor.

8.4.2 Spice Model of the Coupling

The inter-strip capacitive coupling in silicon strip sensors could explain at least partially, the observed coupling between the signals of neighboring readout channels. Capacitive coupling is often estimated, modelling the silicon strip sensor as a capacitive network [101]. A simple representation is shown in Figure 8.21, where C_{int} denotes the inter-strip capacitance, C_{sub} the capacitance of a strip to the backplane, C_{Cou} the coupling capacitance to the read out electronics.

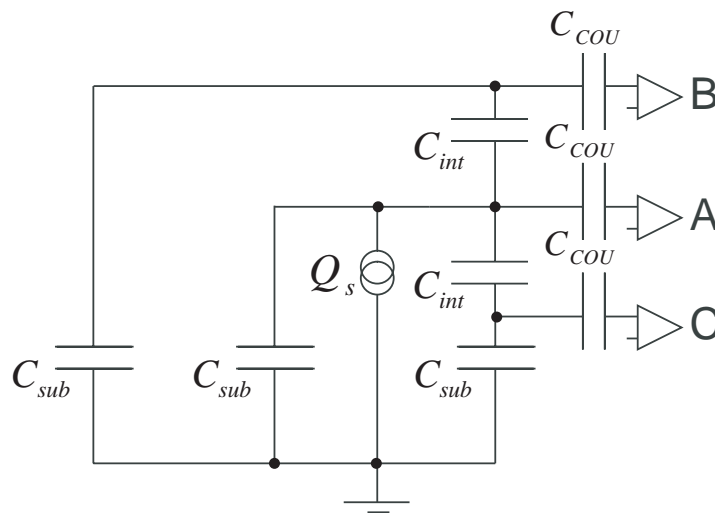


FIGURE 8.21: *Model of AC-coupled microstrip detector according to [101].*

For the fraction of charge that is coupled to strip B when the charge $Q_S = Q_A + Q_B + Q_C$ has been deposited on strip A , one gets:

$$c_1 = \frac{Q_B}{Q_A + Q_B + Q_C} = \frac{C_B}{C_A + C_B + C_C} \quad (8.39)$$

The effective input capacitance of a charge sensitive amplifier C_{ampl} is considered to be large with respect to the coupling capacitance C_{cou} , thus the total input capacitance (C_{cou} and C_{ampl} in series) can be approximated as C_{cou} . Typically the coupling capacitance C_{cou} is one or two orders of magnitude larger than the strip to backplane capacitances C_{sub} , the parallel connection of C_{cou} and C_{sub} is therefore in good approximation C_{cou} .

Thus the effective capacitances C_A, C_B, C_C for the charge Q_s to be collected by the amplifier A, B and C is given by:

$$C_A = C_{cou} \quad (8.40)$$

$$C_B = C_C = \frac{C_{int} \cdot C_{cou}}{C_{int} + C_{cou}} \approx C_{int} \quad (8.41)$$

and the coupling eqn.8.39 becomes:

$$c_1 \approx \frac{C_{int}}{C_{cou}} \quad (8.42)$$

This model however is too much simplified as it neglects the resistances of the sensor and the input impedance of the amplifier. For a more detailed study on the couplings, a Spice simulation has been developed, modelling the silicon strip sensor as an R-C network and generating an equivalent circuit for the APV25 preamplifier and pulse shaper (the freely available LT-Spice circuit simulation has been used [102]).

The R-C network of the silicon strip sensor has been modelled following the design presented in [103]. The circuit diagram is illustrated in Figure 8.4.2.

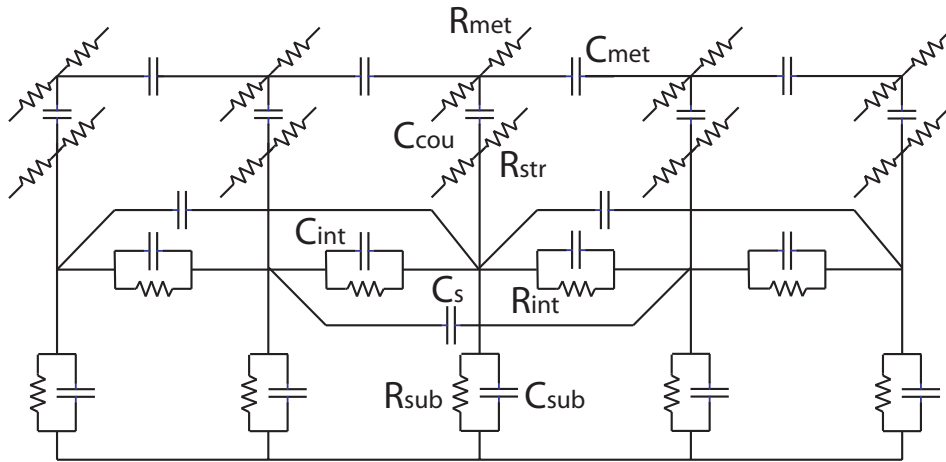


FIGURE 8.22: Schematic representation of a silicon strip sensor.

The capacitances and resistances of the sensor circuit have been evaluated for TOB SS4 sensors (also known as OB2). The total capacitance C_{tot} of a strip is composed of the the capacitance to the backplane C_{sub} and couplings to the first and second neighbors, C_{int} and C_s . In [104] an approximation of C_{tot} is given by assuming a linear dependence on the w/p ratio:

$$C_{tot} = C_{sub} + 2C_{int} + 2C_s = A + B(w/p) \quad (8.43)$$

where analyzing data available in literature, the constants $A = (0.971 \pm 0.027 \text{ pf/cm})$ and $B = (1.731 \pm 0.075 \text{ pf/cm})$ have been determined. All TOB modules have a w/p ratio of 0.25 thus: C_{tot} is approximately 1.4 pf/cm .

The capacitance of a single strip to the backplane is dependent on the sensor thickness d the pitch p and the w/p ratio. According to [105] it can be estimated by:

$$C_{sub} = \epsilon_0 \epsilon_{SI} \frac{p}{d + pf(w/p)} \quad (8.44)$$

Where $\epsilon_0 = 8.85 \cdot 10^{-14} \text{ As/(Vcm)}$ is the dielectric constant of vacuum and $\epsilon_{SI} = 11.7$ the relative dielectric constant for silicon. $f(w/p)$ is given by:

$$f(w/p) = -0.00111(w/p)^2 + 0.0586(w/p) + 0.240 - 0.651(w/p)^{-1} + 0.355(w/p)^{-2} \quad (8.45)$$

For CMS strip sensors that have a width to pitch ratio of 0.25, f equals 0.316. For OB2 sensors that have a pitch $p = 183 \mu\text{m}$ and a thickness $d = 500 \mu\text{m}$ one obtains $C_{sub} = 0.34 \text{ pf/cm}$.

A linear dependence of the coupling capacitance to the second neighbor on the pitch has been found in [104]⁵:

$$C_s = 0.145 \text{ pf/cm} - p \cdot (0.00027 \text{ pf cm}^{-1} \mu\text{m}^{-1}) \quad (8.46)$$

For OB2 sensors one obtains: $C_s = 0.096 \text{ pf/cm}$

Having determined C_{tot} , C_{sub} and C_s , the inter-strip capacitance C_{int} can be calculated using eqn.8.43:

$$C_{int} = \frac{C_{tot} - C_{sub} - 2C_s}{2} \quad (8.47)$$

For OB2 sensors one obtains: $C_{int} = 0.43 \text{ pf/cm}$

Values for coupling capacitances, resistances of the p^+ strips and the aluminum strips have been chosen according to the measurements presented in [41] and [106]. There the coupling capacitances have been measured on test structures having a pitch of $122 \mu\text{m}$ and a length of 4.413 mm yielding an average value of 23 pf . Thus (assuming a linear scaling with the pitch) for a pitch of $183 \mu\text{m}$: $C_{cou} = 80 \text{ pf/cm}$. Measurements on the inter-strip resistance have been performed in [41] quoting an average value of $\rho = 118 \Omega/\text{square}$ for the p^+ strips and $24.4 \text{ m}\Omega/\text{square}$ for the aluminum strips. The resistance for a strip of length l , with a width w and a resistivity ρ is given by:

$$R = \rho \cdot \frac{l}{w} \quad (8.48)$$

Thus the p^+ strip have a resistance of $R_{str} = 26 \text{ k}\Omega/\text{cm}$ and $R_{met} = 5.3 \Omega/\text{cm}$ per cm length. The inter-strip capacitances of the aluminum strips C_{met} are small compared to those of the p^+ implanted strips as the medium is air and the thickness of the metal implants is of the order of $1 \mu\text{m}$. The values used for the simulation are summarized in Table 8.3. The preamplifier and pulse shape have been modelled, following the schematics provided by [107]. In the simulation of the front end electronics (Figure 8.4.2) also the resistance of the pitch adapter has been taken into account. The resistance of the pitch adapter varies, according to [108], between 24Ω for the shortest and 60Ω for the longest strips. For the simulation a value of 45Ω has been chosen. The parameters used for the simulation of the readout electronics are specified in Table 8.4.

⁵Equation (2) of this reference is incorrect it should be $C_s = 0.145 - 0.00027 \text{ pF}$.

OB2 Strip Sensor		
R_{met}	Resistance aluminum strip	$5 \Omega/cm$
R_{str}	Resistance p+ strip	$26 k\Omega/cm$
R_{sub}	Resistance strip-bulk	$1 T\Omega/cm$
C_{sub}	Backplane capacitance	$0.3 pf/cm$
C_{cou}	Coupling capacitance	$80 pf/cm$
C_{int}	Inter-strip coupling capacitance	$0.43 pf/cm$
C_s	Second neighbor coupling capacitance	$0.1 pf/cm$
R_{int}	Inter-strip resistance	$1 T\Omega/cm$
C_{met}	Capacitance between adjacent metalizations	$1 fF/cm$
R_{bias}	Bias resistor	$1.6 M\Omega$

TABLE 8.3: Parameters for modelling the OB2 strip sensor. All parameters, except R_{bias} scale with the strip length.

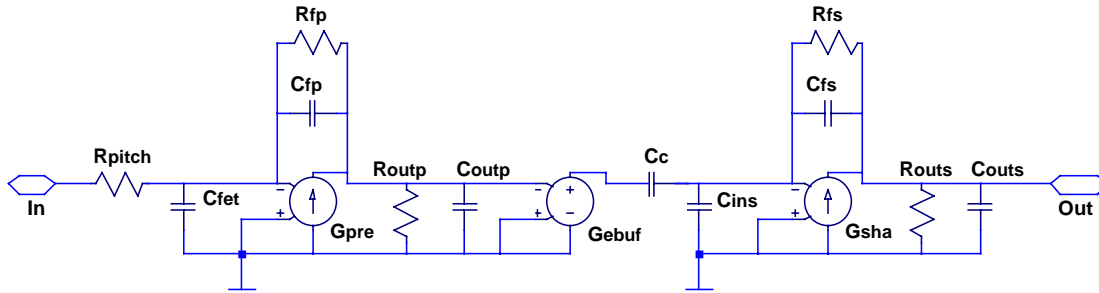


FIGURE 8.23: Preamplifier and pulse shaper.

Pitch Adapter		Source Follower	
Rpitch	45 Ω	Gebuf	-1
Preamplifier		Shaper	
Cfet	7 pf	Cc	1.4 pf
Gpre	8 mA/V	Cins	0.5 pf
Cfp	0.15 pf	Gsha	0.8 mA/V
Rfp	50 $M\Omega$	Cfs	0.2 pf
Routp	1 $M\Omega$	Rfs	500 $k\Omega$
Coutp	0.5 pf	Routs	1 $M\Omega$
		Couts	1 pf

TABLE 8.4: Parameters of the preamplifier and pulse shaper for the APV25.

The input current to the simulation has been modelled according to section 2.5. The parameters used in the model are a resistivity of $5 \text{ k}\Omega/\text{cm}$ for a bias voltage of 300 V , assuming a mobility of $1450 \text{ cm}^2/\text{Vs}$ for the electrons and $450 \text{ cm}^2/\text{Vs}$ for the holes; the charge collection times are 7 ns for electrons and 22 ns for holes, respectively. The pulse shapes for the induced currents are shown in Figure 8.24. The left plot is the signal obtained from eqn.2.43 to eqn.2.51 the right is obtained numerically using the simulated weighting potential (Figure 2.7) following eqn.2.36 and eqn.2.42.

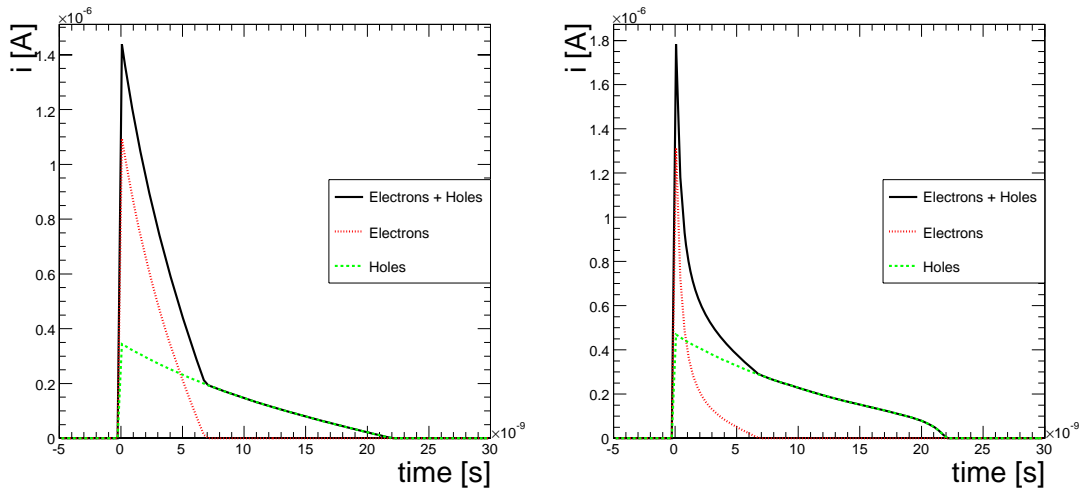


FIGURE 8.24: Current induced on the readout electrode. For a weighting potential of $1/d$ (left), and with the simulated weighting potential (right).

The time evolution of the signal on seed and side strips obtained from the simulation are shown in Figure.8.25.

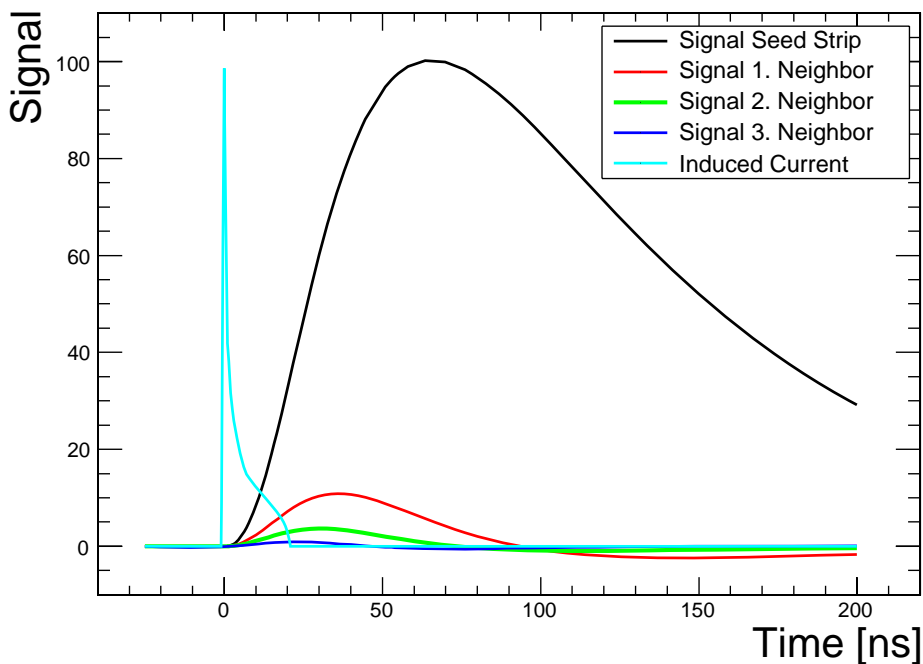


FIGURE 8.25: Results from Spice simulation: Signal shapes of the seed and neighboring strips in peak mode for a charge deposition at $t=0$.

Although the simulated shaping time has a peaking time of 65 ns, larger than the measured one, the simulated coupling coefficients are in good agreement with the measurements: the model predicts couplings of about 5% at the peaking time of the seed strip and about 13% 25 ns earlier, compared to the measured values of 12% in peak mode and 4% in deconvolution mode.

8.4.3 Effect on the Position Resolution

Due to the small diffusion length of the charge carriers and the strong couplings of neighboring strips, the center of gravity is not an optimal estimator for the particle impact point: several alternative methods are discussed in [99]. A method that takes couplings and deviations from linear charge sharing correctly into account is the *eta correction algorithm*. The approach is based on the assumption that the η -function is monotonically increasing when the point of charge deposition is moving closer to the right strip. Thus when knowing $p(\eta)$ - the distribution of η the position of the charge deposition can be calculated by:

$$x(\eta) = x_L + P \frac{\int_{-\infty}^{\eta} p(\eta') d\eta'}{\int_{-\infty}^{\infty} p(\eta') d\eta'} \quad (8.49)$$

8.5 Summary

Contributions of charge sharing to the cluster size have been discussed and evaluated, demonstrating that in the absence of a magnetic field the spread of the charge cloud contributes significantly to the average cluster width only for inclined tracks. The pulse shape in the peak and deconvolution mode has been reconstructed with ns resolution. The coupling between signals of neighboring strips has been determined. The coupling parameters have strong time dependence and have been determined to be 12% in deconvolution and 4% in peak mode at the optimal sampling point. From the time evolution of the coupling parameters the mechanism of the coupling has been found to be the same in peak and deconvolution mode and the differences arise from the different sampling points only. A simple model has been developed to describe the observed cluster size in terms of charge sharing and coupling to first and second neighbors. The measured coupling parameters have been validated with this model finding excellent agreement. A Spice simulation of the silicon strip sensors as an RC network and its readout electronics has been developed, obtaining predictions for the coupling parameters consistent with the measurements.

Chapter 9

The CMS Tracker Alignment Strategy

9.1 Introduction

The performance of the CMS experiment depends strongly on the position resolution of the Tracker. The Tracker sensors have an intrinsic resolution ranging from $10 \mu\text{m}$ to $50 \mu\text{m}$. The effective resolution however is affected by the knowledge of the relative position of the sensors with respect to each other and the global CMS reference frame, i.e. their alignment.

For technical and economical reasons, a large complex structure like the CMS Tracker, with more than 15000 detectors, cannot be built with a precision comparable with the intrinsic resolution of the sensors. Estimations of the achievable precision of the Tracker structures are presented in [109] and are summarized in Table 9.1.

TABLE 9.1: *Expected misalignment of the Strip Tracker subdetectors and their components [109].*

	TOB $\Delta\mu\text{m}$	TIB $\Delta\mu\text{m}$	TEC $\Delta\mu\text{m}$
Sensor vs. Module	± 10	± 10	± 10
Module vs. Rod / Module vs. Petal	± 100	± 100	± 100
Rod vs. Cylinder / Petal vs. Disk	$\pm 100 - 500$	± 200	$100 - \pm 200$
Cylinder vs. Cylinder / Disk vs. Disk	$\pm 100 - 500$	$\pm 100 - 500$	$\pm 100 - 500$

This misalignment of the sensors increases the hit to track residuals, and thus worsens the position resolution. In order to avoid a degradation of the detector performance, the misalignment needs to be recovered. Ideally a precision higher than the intrinsic precision is desired. Some physics goals e.g. the precision measurements of the W^\pm bosons, require even a position resolution of $10 \mu\text{m}$ in the r-phi plane [7]. This precision can only be achieved with track-based alignment. This method however relies on an efficient track reconstruction and therefore requires an already pre-aligned system. In the Tracker alignment strategy three steps are foreseen: the processing of survey information, the use of data from the laser alignment system, and finally track-based alignment [7, 110].

9.2 Survey

During Tracker construction the precision of the different components has been measured with Coordinate Measurement Machines (*CMM*) or other survey methods such as photogrammetry [7]. The results of these measurements are stored in a database and are used to correct the ideal geometrical description of the Tracker for the measured displacements and deformations. In some

cases the metrological information is acquired only on samples, and no direct corrections can be applied, but the statistically quantified assembly precision is used to estimate the placement uncertainty. The so called *alignment position errors* are then taken into account for the initial track reconstruction leading to an improved efficiency.

9.3 Laser Alignment System

The Laser Alignment System *LAS* [7, 110, 111] has been developed to measure the relative displacement of the Tracker subdetectors. It contributes to the determination of the initial positions for the alignment, and will provide a constant monitoring of possible deformations, that might be caused by thermal stress, by the strong field of the CMS solenoid and electrical currents in the Tracker, or by long term effects on the mechanics due to irradiation. The components of the LAS are shown in Figure 9.1.

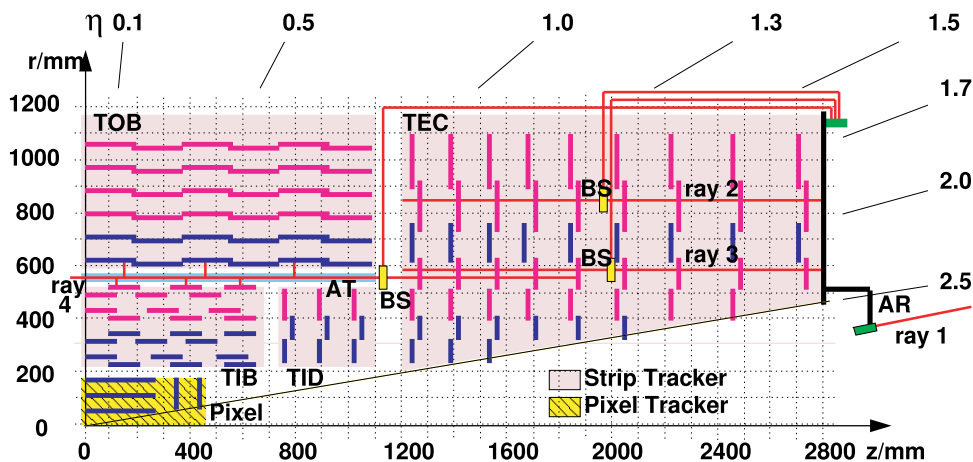


FIGURE 9.1: *The laser alignment system of the CMS Strip Tracker. Infrared lasers are placed outside the volume. The beams are distributed over the Tracker by a system made of beam splitters, labeled as BS, the Alignment Ring (AR) and Alignment Tubes (AT). The system provides measurements of the relative positions of TIB, TOB and TEC. In the TEC modules, the aluminum bias layer has a hole in the area of expected light penetration allowing for a measurement of the relative positions of all TEC disks - in the TIB and TOB only the inner layers are measured [7].*

In the LAS, solid state Nd-Yag lasers with a wavelength of 1075 nm are used. Silicon sensors are partially transparent to this infrared wavelength: charge (via the photo electrical effect) is generated in the sensors, and several layers can be penetrated. To improve the transparency, modules shined on by the laser system have an anti-reflection coating. The generated charge is then measured by the front-end electronics. Although the generated charges are low ($S/N \approx 1$) a significant signal can be measured by pulsing the laser and averaging over several pulses. From the signals the position of the laser crossing is determined and - as the laser beam passes the modules on a straight line - the relative displacement of the sensors can be determined. The lasers are placed outside the Tracker volume, and a system of beam splitters distributes several beams inside the Tracker. The expected accuracy of the LAS is about $100 \mu\text{m}$. More detailed information can be found in [111].

9.4 Track Based Alignment

The ultimate precision in the knowledge of the detector positions is expected to be achieved with track-based alignment methods [27, 112, 113]. The first step is to build a model, describing the impact points (the crossings positions of traversing particles) on the detectors $\vec{f}(\vec{p})$ as a function of the parameters \vec{p} , where \vec{p} is including alignment and track parameters. In the next step the model is linearized:

$$\vec{f}(\vec{p}) = \vec{f}(\vec{p}_0) + \mathbf{A}(\vec{p} - \vec{p}_0) + O\left((\vec{p} - \vec{p}_0)^2\right) \quad (9.1)$$

with

$$\mathbf{A} = \frac{\partial \vec{f}}{\partial \vec{p}_{\vec{p}=\vec{p}_0}} \quad (9.2)$$

In the linear approximation, the higher order terms $O\left((\vec{p} - \vec{p}_0)^2\right)$ are neglected. The residuals \vec{z} , the difference between the fitted $\vec{f}(\vec{p})$ and the measured positions \vec{y} are then given by:

$$\vec{z}(\vec{p}) = \vec{y} - \vec{f}(\vec{p}_0) - \mathbf{A}(\vec{p} - \vec{p}_0) \quad (9.3)$$

The alignment parameters are then determined by minimizing the weighted residuals - here referred to as the χ^2 function:

$$\chi^2 = \left(\vec{y} - \vec{f}(\vec{p}_0) - \mathbf{A}(\vec{p} - \vec{p}_0)\right)^T \mathbf{V}^{-1} \left(\vec{y} - \vec{f}(\vec{p}_0) - \mathbf{A}(\vec{p} - \vec{p}_0)\right) \quad (9.4)$$

A common approach is the minimization by the least squares, leading to the equation system:

$$\vec{p} = \vec{p}_0 + (\mathbf{A}^T \mathbf{V}^{-1} \mathbf{A})^{-1} \mathbf{A}^T \mathbf{V}^{-1} (\vec{y} - \vec{f}(\vec{p}_0)) \quad (9.5)$$

This equation system can be solved in principle by inversion. For the CMS Tracker due to the large number of detectors and large number of tracks needed for alignment, this matrix would be $O(10^6 \times 10^6)$ and can not be solved directly. Instead different approaches have been developed that are described in the following, after an introduction to track and alignment parameters used by the different algorithms.

9.4.1 Alignment and Track Parameters

A detailed discussion can be found in [27, 114]. The main concepts are summarized in the following.

Alignment Parametrization

The alignment of the Tracker can be done in different levels of hierarchy: individual sensors, or composite structures such as Rods, Layers or full subdetectors can be aligned. In the following these objects - illustrated in Figure 9.2 - are referred to as *alignables*.

The alignment parameters describe the position and orientation of an alignable as deviations from the nominal positions. Assuming only incremental changes, the alignment parameters are linearized. For practical reasons two coordinate systems are used: local and global coordinates. In the local coordinate of an alignable, a point is described by the vector $\vec{q}(u, v, w)$ where \vec{u} , \vec{v} and \vec{w} are the basis vectors of the local coordinate system. In the global coordinate system the positions of alignable objects are given by a the vector \vec{r}_0 that defines the position of its

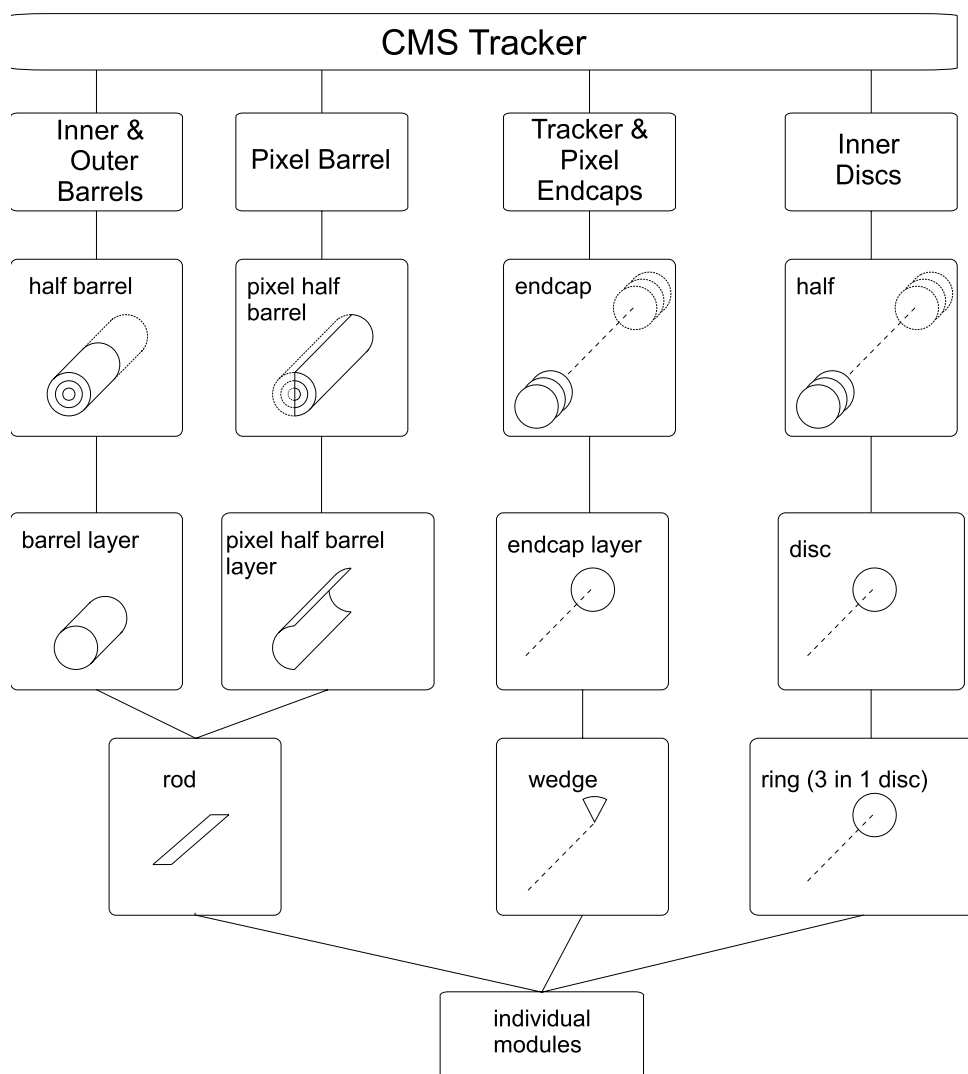


FIGURE 9.2: Hierarchical representation of alignable objects in the CMS alignment framework [27].

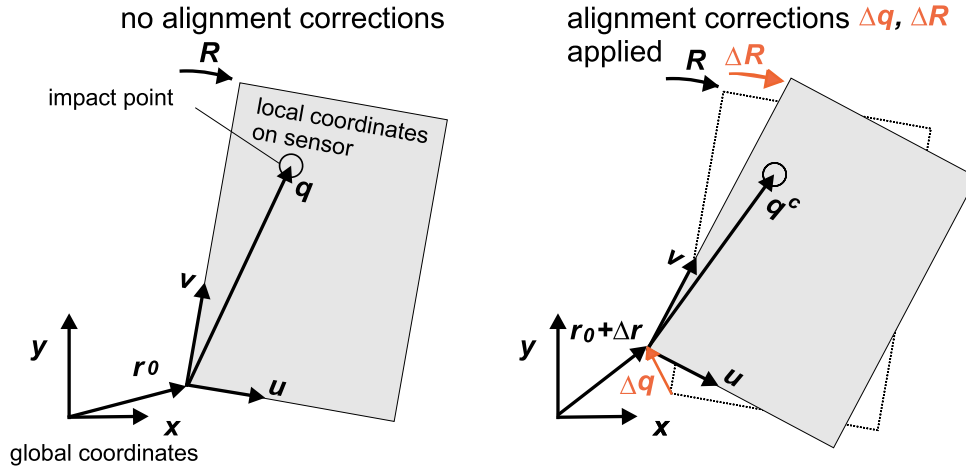


FIGURE 9.3: Two-dimensional illustration of the dependence of the local coordinates \vec{q} on the alignment corrections $\Delta\vec{q}$ and $\Delta\mathbf{R}$.

center, and a rotation matrix \mathbf{R} that gives its orientation in the CMS coordinate system. The rotations are defined around \vec{r}_0 and therefore do not result in an additional shift of the alignable. The transformation between a point \vec{q} in the local coordinate system and the global coordinates $\vec{r}(x, z, y)$ is given by:

$$\vec{r} = \vec{r}_0 + \mathbf{R}^T \cdot \vec{q} \quad (9.6)$$

The alignment corrections are (small) shifts $\Delta\vec{q}$ and rotations $\Delta\mathbf{R}$ preferably defined in the local frame as illustrated in Figure 9.3. With these alignment corrections eqn.9.6 becomes:

$$\vec{r} = \vec{r}_0 + \mathbf{R}^T \Delta\mathbf{R} (\vec{q} + \Delta\vec{q}) \quad (9.7)$$

Alternatively they can be seen as corrections in the global frame $\Delta\vec{r}$, ΔR :

$$\vec{r} = \Delta\vec{r} + \vec{r}_0 + \mathbf{R}^T \Delta\mathbf{R} \cdot \vec{q} \quad (9.8)$$

Where:

$$\Delta\vec{r} = \mathbf{R}^T \Delta\mathbf{R} \cdot \Delta\vec{q} \quad (9.9)$$

A linearisation of the rotations is possible, if the rotations are small i.e. $\sin(x) \approx x$ and $\cos(x) \approx 1$. The rotation matrix $\Delta\mathbf{R}$ can then be written as:

$$\Delta\mathbf{R} = \Delta\mathbf{R}_\alpha \cdot \Delta\mathbf{R}_\beta \cdot \Delta\mathbf{R}_\gamma \quad (9.10)$$

with:

$$\Delta\mathbf{R} = \begin{pmatrix} 1 & \Delta\gamma & \Delta\beta \\ -\Delta\gamma & 1 & \Delta\alpha \\ -\Delta\beta & -\Delta\alpha & 1 \end{pmatrix} \quad (9.11)$$

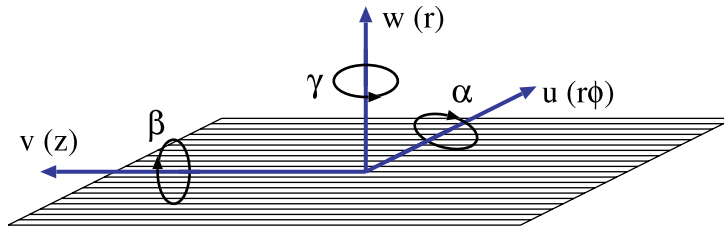


FIGURE 9.4: Definition of the local coordinate system [27].

The six alignment parameters are therefore of the form:

$$a = \begin{pmatrix} \Delta u \\ \Delta v \\ \Delta w \\ \Delta \alpha \\ \Delta \beta \\ \Delta \gamma \end{pmatrix} \quad (9.12)$$

The definition the local coordinate system is shown in Figure 9.4.

Track Parametrization

Tracks of charged particles in a constant magnetic field (as it is the case for the CMS Tracker) are helices. Five parameters and a reference surface are sufficient to describe a track:

$$\tau_i = \begin{pmatrix} u_p \\ v_p \\ \frac{du}{dw} \\ \frac{dv}{dw} \\ \kappa \end{pmatrix} \quad (9.13)$$

The reference surface is the first surface crossed by the particle and u_p and v_p are the impact points of the reference plane, $\frac{du}{dw}$, $\frac{dv}{dw}$ the tangents in local coordinates, κ defines the curvature.

9.5 Alignment Algorithms for Track based alignment

For the alignment of the CMS Tracker three algorithms are under development: the Millepede algorithm [115], a Kalman-Filter based method [116,117], and the Hits and Impact-Points algorithm [114].

9.5.1 Hits and Impact-Points Algorithm

In the Hits and Impact Point (*HIP*) algorithm, eqn.9.5 is solved only for the alignment parameters, while the track parameters are taken from the track reconstruction. With this simplification, the global χ^2 function can be minimized by minimizing the (weighted) hit to impact point residuals for each alignable individually. An illustration is given in Figure 9.5.

The advantage of the *HIP* method is that only small matrices (6x6) have to be inverted, which is fast and numerically exact. The algorithm neglects correlations between the alignables, that are given by the dependence of the track parameters on the alignment parameters. To account for correlations, the *HIP* algorithm has to be applied iteratively, where after each iteration the tracks are refitted according to the new detector positions.

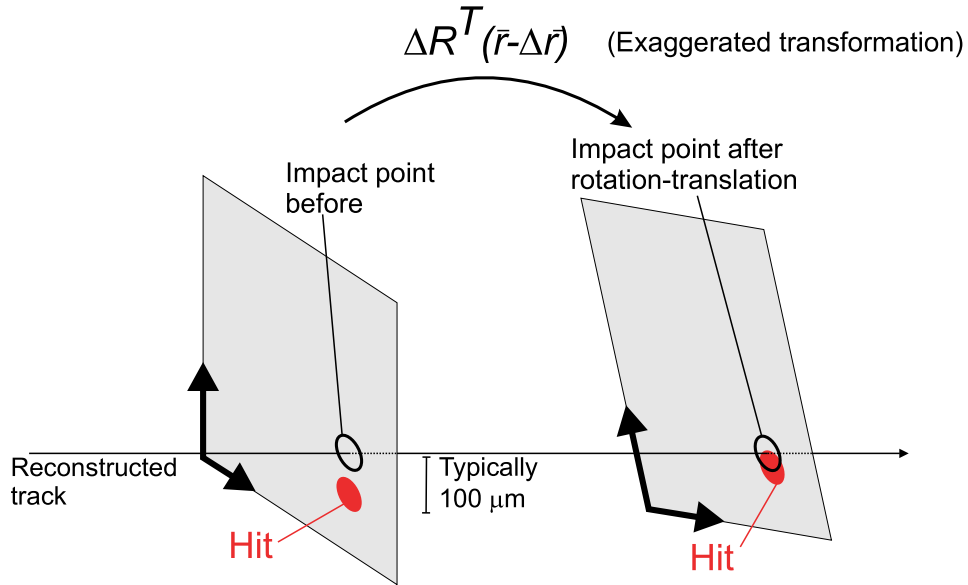


FIGURE 9.5: Principle of the HIP algorithm [113]. The impact points are the crossings of the estimated track with the detector and the hits refer to the positions measured by the detector. The alignment parameters are calculated, such that the (weighted) residuals between all hits and impact points on a given detector are minimized.

9.5.2 Kalman Filter Algorithm

The Kalman filter method was proposed rather recently and so far has not been applied on a real large scale system; the results on simulations are however encouraging. It is an iterative algorithm, where the alignment parameters are updated after each processed track. It is referred to as "global method", since correlations of alignment parameters are explicitly taken into account and for each track the alignment parameters of all detectors are updated (not only those of the detectors crossed by the particle).

For large systems with many alignment parameters it has been proposed [117] to restrict the correlations only to significant ones. That requires some "book-keeping" but allows for a formulation which does not require the inversion of large matrices.

The convergence of the Kalman filter alignment algorithm depends on the initial positions and can therefore benefit from survey measurements and the Laser Alignment System data. The strengths of the approach is that a refinement of the alignment parameters can be achieved only processing a new set of tracks, without reprocessing the full data set, furthermore the convergence of the alignment parameters can be observed by the evolution of their covariance matrix.

9.5.3 Millepede Algorithm

The Millepede algorithm is the most advanced alignment algorithm and has been successfully applied for the H1 and CDF trackers, will be used for the LHCb and in a variant for ATLAS. It is a non-iterative algorithm performing a simultaneous fit of all track and alignment parameters.

The parametrization is divided into two parts: the local and the global parameters. The local parameters α are the track parameters that change from track to track. The alignment parameters a are referred to as global parameters, since they are common to the complete data set. With this classification, eqn.9.3 for the residuals z_k can be written as:

$$z_k = y_k - \left[\sum_{j=1}^n a_j D_{k,j} + \sum_{l=1}^p \alpha_l \delta_{k,l} \right] \quad (9.14)$$

where y_k is the vector of measurements, $D_{k,j} = \frac{\partial f_k}{\partial a_j}$ the derivatives with respect to global parameters and $\delta_{k,l} = \frac{\partial f_k}{\partial \alpha_l}$ the derivatives with respect to local parameters.

Local and global parameters are determined by minimizing the residuals z_k via the least squares leading to the equation system:

$$\left(\begin{array}{c} \mathbf{D}^T \\ \hline \delta^T \end{array} \right) \left(\begin{array}{c} V^{-1} \\ \hline \end{array} \right) \left(\begin{array}{c} \vec{z} \\ \hline \end{array} \right) = \left(\begin{array}{c} \mathbf{D}^T \\ \hline \delta^T \end{array} \right) \left(\begin{array}{c} V^{-1} \\ \hline \end{array} \right) \left(\begin{array}{c|c} \mathbf{D} & \delta \\ \hline \end{array} \right) \left(\begin{array}{c} \vec{a} \\ \hline \vec{\alpha} \end{array} \right) \quad (9.15)$$

Where V^{-1} is the variance matrix of \vec{y} . For the Millepede alignment algorithm the measurements y_k are assumed to be uncorrelated and V^{-1} is thus a diagonal matrix with entries $\frac{1}{\sigma_k^2}$. Under this assumption eqn.9.15 can be written in general form as:

$$\left(\begin{array}{c} \vec{b}_1 \\ \hline \vec{b}_2 \end{array} \right) = \left(\begin{array}{c|c} \mathbf{C}_{11} & \mathbf{C}_{21}^T \\ \hline \mathbf{C}_{21} & \mathbf{C}_{22} \end{array} \right) \cdot \left(\begin{array}{c} \vec{a} \\ \hline \vec{\alpha} \end{array} \right) \quad (9.16)$$

To solve this equation for the parameters a and α , the matrix \mathbf{C} needs to be inverted¹:

$$\left(\begin{array}{c|c} \mathbf{B} & -\mathbf{B} \cdot \mathbf{C}_{12} \cdot \mathbf{C}_{22}^{-1} \\ \hline -\mathbf{C}_{22}^{-1} \cdot \mathbf{C}_{12}^T \cdot \mathbf{B} & \mathbf{C}_{22}^{-1} - \mathbf{C}_{22}^{-1} \cdot \mathbf{C}_{12}^T \cdot \mathbf{B} \cdot \mathbf{C}_{12} \cdot \mathbf{C}_{22}^{-1} \end{array} \right) \cdot \left(\begin{array}{c} \vec{b}_1 \\ \hline \vec{b}_2 \end{array} \right) = \left(\begin{array}{c} \vec{a} \\ \hline \vec{\alpha} \end{array} \right) \quad (9.17)$$

Where \mathbf{B} is given by:

$$\mathbf{B} = (\mathbf{C}_{11} - \mathbf{C}_{12} \cdot \mathbf{C}_{22}^{-1} \cdot \mathbf{C}_{12}^T)^{-1} \quad (9.18)$$

¹ $A^{-1} = \frac{adj(A)}{det(A)}$

9.5.4 Matrix Partitioning

If just the alignment parameters \vec{a} need to be determined, the inversion of the full matrix \mathbf{C} can be avoided:

$$\vec{a} = \mathbf{B} \cdot \vec{b}_1 + \mathbf{B} \cdot \mathbf{C}_{12} \cdot \mathbf{C}_{22}^{-1} \cdot \vec{b}_2 \quad (9.19)$$

The special solution for the track parameters for the case that the alignment parameters are zero shall be denoted as $\vec{\alpha}^*$ and is according to eqn.9.16 given by:

$$\vec{\alpha}^* = \mathbf{C}_{22}^{-1} \cdot \vec{b}_2 \quad (9.20)$$

If $\vec{\alpha}^*$ is known, 9.19 can be written as:

$$\vec{a} = \mathbf{B} \cdot \vec{b}_1 + \mathbf{B} \cdot \mathbf{C}_{12} \cdot \vec{\alpha}^* \quad (9.21)$$

Thus with eqn.9.21 the sub vector \vec{a} can be determined performing only the inversion of the $n \times n$ matrix \mathbf{C}_{11} and the $p \times p$ matrix \mathbf{C}_{22} . This method is not an approximation but the exact solution for the alignment parameters, since the local parameters are solved implicitly.

The inversion of the full matrix \mathbf{C}_{22} can be simplified due to its special structure. As the measurements between different tracks are uncorrelated \mathbf{C}_{22} can be written as a diagonal matrix with the matrices $\mathbf{\Gamma}_i$ and eqn. 9.16 becomes:

$$\begin{pmatrix} \sum \mathbf{C}_i & \cdots & \mathbf{G}_i & \cdots \\ \vdots & \ddots & 0 & 0 \\ \mathbf{G}_i^T & 0 & \mathbf{\Gamma}_i & 0 \\ \vdots & 0 & 0 & \ddots \end{pmatrix} \cdot \begin{pmatrix} \vec{a} \\ \vec{\alpha}_i \\ \vdots \end{pmatrix} = \begin{pmatrix} \sum \vec{b}_i \\ \vdots \\ \vec{\beta}_i \\ \vdots \end{pmatrix} \quad (9.22)$$

The symmetric matrices \mathbf{C}_i include only derivatives with respect to global parameters, while the symmetric matrices $\mathbf{\Gamma}_i$ contain only derivatives with respect to local parameters. The index i indicates the i^{th} partial measurement, i.e. the i^{th} track. The matrices \mathbf{G}_i are rectangular and include both derivatives with respect to local and global parameters; \vec{b} contains products of global derivatives and $\vec{\beta}$ contains products of local derivatives.

To solve this equation system (analog to eqn.9.20), first the special solution of track parameters $\vec{\alpha}_i$ is determined:

$$\vec{\alpha}_i^* = \mathbf{\Gamma}_i^{-1} \cdot \vec{\beta}_i \quad (9.23)$$

Then the global parameters \vec{a} are obtained according to eqn.9.21:

$$\vec{a} = \left(\sum_i \mathbf{C}_i - \sum_i \mathbf{G}_i \mathbf{\Gamma}_i^{-1} \mathbf{G}_i^T \right)^{-1} \cdot \left(\sum_i \vec{b}_i - \sum_i \mathbf{G}_i \left(\mathbf{\Gamma}_i^{-1} \vec{\beta}_i \right) \right) \quad (9.24)$$

The strength of this approach is that the size of the matrix that needs to be inverted has only the size of the number of global parameters independent of the number of tracks that are used for the alignment. Nevertheless for a large number of global parameters the inversion of the above matrix (9.24) can still become complex and computing intensive. For the Millepede algorithm inversion methods have been developed, that make use of the sparseness (most entries are zero) of the matrix. In the new implementation of Millepede (MillepedeII) eqn.9.24 can be solved alternatively to inversion of the matrix \mathbf{C} by minimization which is much faster and numerically more accurate. Studies have shown [27] that the full CMS Tracker alignment can be achieved on a single PC within 1h.

Constraints

Another benefit of the Millepede is the possibility of constraining ambiguous solutions of the alignment parameters. Explicit (linear) relations between the alignment parameters can be formulated in the form:

$$\mathbf{f}^T \cdot \vec{a} = \vec{f}_0 \quad (9.25)$$

Such constraints can be taken into account by the method of Lagrange multipliers, where the equation system is enhanced by these additional equations becoming:

$$\left(\begin{array}{c|c} \mathbf{C} & \mathbf{f} \\ \hline \mathbf{f}^T & \mathbf{0} \end{array} \right) \begin{pmatrix} \vec{a} \\ \vec{\lambda} \end{pmatrix} = \begin{pmatrix} \vec{b} \\ \vec{f}_0 \end{pmatrix} \quad (9.26)$$

This allows for example for a simultaneous alignment of objects of different hierarchies, e.g. Rods and individual modules. In this case the constraint equations for the modules (of) a given Rod would have to fulfill the side conditions that net translations of the modules is zero - as this would correspond to the movement of a Rod and shall be applied therefore on the Rod level.

A detailed discussion of the Millepede algorithm and in particular the MillepedeII implementation can be found in [118].

Chapter 10

Alignment by Tracking Cosmic Particles

10.1 Introduction

The detectors in Cosmic Rack are aligned with the Millepede algorithm, using tracks from cosmic particles. The parameters steering the alignment, and the settings of the alignment algorithm are described, and validated with a Monte-Carlo simulation of the Cosmic Rack. Subsequently the procedure is applied to the real system; the results are studied to evaluate the achieved precision, and to investigate possible systematic effects. A quantitative measurement of the geometrical precision of fully assembled TOB Rods is derived. Results from data samples collected at room temperature and at the Tracker operating temperature are compared, to look for possible deformations induced by temperature variations.

10.2 Measurement Setup

The alignment studies were carried out with the Cosmic Rack equipped with 8 double sided (DS) Rods and 6 single sided (SS) Rods arranged in 7 layers, representing more than 2% of the channels of the TOB. All of the Rods were equipped with OB2 sensors, that have a pitch of $183 \mu\text{m}$. In total 132 modules were in the Cosmic Rack, which corresponds to 84 "alignable Dets", as the CMS alignment framework treats pairs of r-phi and stereo detector as a single "glued detector".

10.2.1 Estimation on Multiple Scattering

Important for the performance of all track based alignment methods is the quality of the used tracks, i.e. the hit to track residuals should be ideally dominated by the misalignment.

This is however only partially fulfilled for the low momentum tracks recorded with the Cosmic Rack. Due to the broad energy spectrum (see Figure 7.2) of cosmic muons, peaking at low energies, and the limited stopping power of the lead absorber, multiple scattering gives a large contribution to the hit-to-track residuals, which limits the performance of the alignment method, and complicates significantly the task. In addition the momentum of individual particles is not measured, hence it is not possible to assign to each track an accurate estimate of the multiple scattering and therefore an optimized statistical weight.

An approximate estimate of the effect of multiple scattering for the Cosmic Rack is given in the following. Using a gaussian approximation, the average angle under which a particle with momentum p and charge z is scattered, when crossing a layer of material with thickness x and

Type	Material	ρ	X_0	Thickness	x	x/X_0
		$[g/cm^3]$	$[g/cm^2]$	$[\mu m]$	$[g/cm^2]$	
Silicon Sensor	Si	2.33	21.82	500	$1.2 \cdot 10^{-1}$	$5.3 \cdot 10^{-3}$
Rod PCB Carrier	G10-FR4	1.8	30.1	1000	$1.8 \cdot 10^{-1}$	$6.0 \cdot 10^{-3}$
Rod PCB Lines	Cu	8.9	12.86	70	$6.2 \cdot 10^{-2}$	$4.8 \cdot 10^{-3}$
Total						$1.6 \cdot 10^{-2}$

TABLE 10.1: *Material distribution of TOB sensors and the Rods bus. Material properties from [72].*

a radiation length X_0 , is given by:

$$\theta_0 = \frac{13.6 \text{ MeV}}{\beta c p} z \sqrt{x/X_0} [1 + 0.038 \ln(x/X_0)] \quad (10.1)$$

For TOB Rods, the minimal amount of matter is traversed for particles crossing only the silicon sensors and the bus. The contributions to the traversed material in this special case are listed in Table 10.1 summing up to a total radiation length of $x/X_0 = 1.6\%$. According to eqn.10.1, particles with a momentum of $1 \text{ GeV}/c$ are scattered by 1.4 mrad , when crossing a Rod.

The above estimate represents the lower limit of the traversed material. Further contributions to the traversed material are given by the front-end chips, the analog optical hybrids, the CCUM, cooling pipes and other components such as connectors, capacitors and cooling fluid. The average radiation length is about $x/X_0 = 5\%$ for double sided Rods and $x/X_0 = 3\%$ for single sided Rods¹, which translates to an average scattering angle for particles with a momentum of $1 \text{ GeV}/c$ of 2.7 mrad and 2 mrad , respectively. In the Cosmic Rack the distance between the layers is 86 mm , so just considering the effect of multiple scattering from one layer to the next one, the contribution to the residuals is about $200 \mu m$.

Although the effect of multiple scattering is large for tracks in the Cosmic Rack, it does not exclude a precise alignment. Misalignment mainly translates to a non-zero mean of the residuals, whereas multiple scattering is random and only contributes to the width of the residual distribution. Thus with sufficiently large data samples, a high precision alignment can be obtained despite the smearing caused by multiple scattering.

10.3 Alignment with the Millepede Algorithm

For the alignment of the Cosmic Rack the Millepede algorithm has been selected, as it is the most advanced algorithm and has been already successfully applied in large experiments. Its powerful outlier rejection is effective for alignment with low momentum particles, and it allows for the simultaneous alignment of objects in different levels of hierarchy, which facilitates the determination of the displacement of the modules within the Rod frame.

The Data flow for the alignment with Millepede is shown in Figure 10.1: the tracks obtained from the standard track reconstruction are refitted, taking updated alignment parameters and alignment position errors into account. In the following step "Mille", the local and global derivatives are calculated, and are written into a binary file, together with the measured hit positions. This event file and an (optional) text file with constraint equations for the alignment parameters are read in by a stand-alone Fortran program "Pede", that builds the matrices for the linear fit and determines the alignment parameters.

In principle no iterations are required, as the Millepede algorithm performs a simultaneous fit for the track and alignment parameters, and is thus taking correlations of the alignment pa-

¹This estimate is taken from the geometric description files of the CMS Tracker [119].

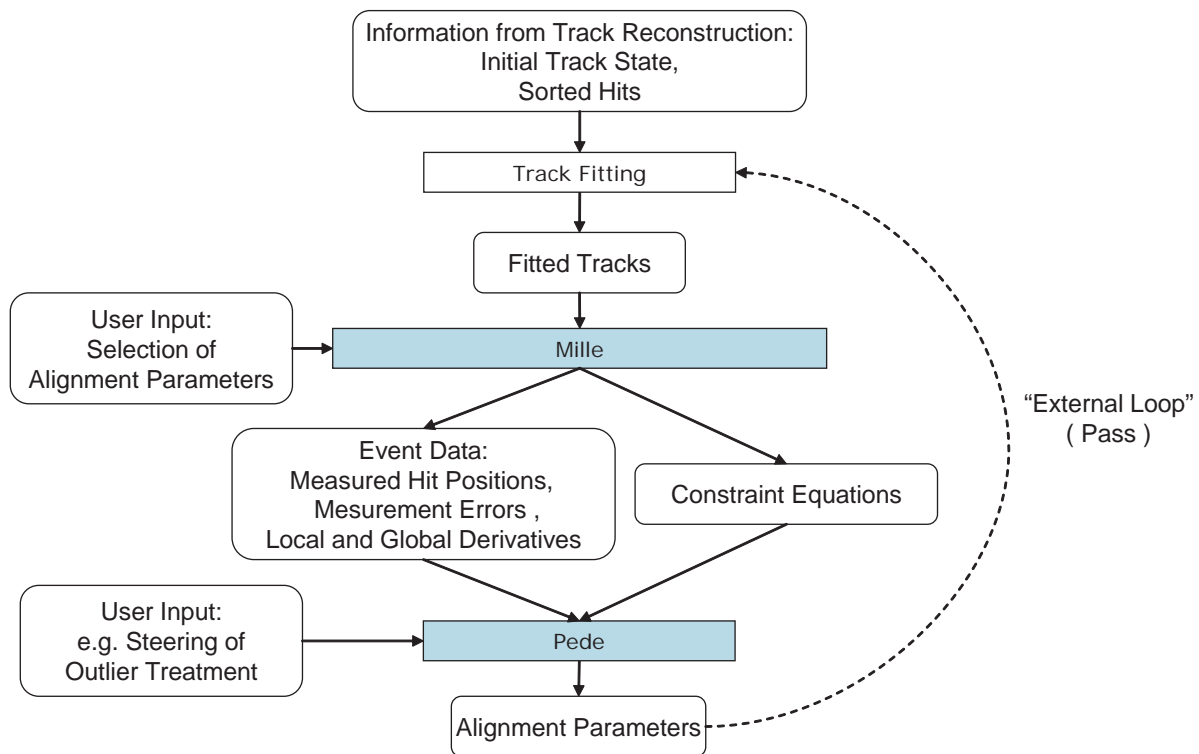


FIGURE 10.1: Data-flow for the alignment with Millepede algorithm.

rameters correctly into account. The linearization of the track model is however a simplification, and in general the derivatives depend on the starting positions. Furthermore relations between the alignment parameters can be hidden from the alignment algorithm. Therefore - depending on the initial misalignment - the solution of the fit can be improved processing the data set several times. At each new pass the tracks are refitted with the updated alignment parameters. Typically after the second pass the ultimate precision is already achieved.

10.3.1 Definition of the Reference System

In track-based alignment methods, the alignment parameters are determined by minimizing the hit-to-track residuals (track χ^2). The determination of the alignment parameters can give however ambiguous solutions, as certain transformations may exist, under which the χ^2 remains unchanged. Obvious examples for these χ^2 -invariant transformations are *Global shifts* - a uniform offset of all alignable objects or *Global rotations*. Depending on the geometry of the system, the samples of tracks and the alignment parameters chosen, also scaling transformations, shearing and torsions can be χ^2 invariant. A detailed discussion on χ^2 -invariant transformations is given in [27].

For the Cosmic Rack alignment to ensure that there is a unique solution for the alignment parameters, two double sided Rods are kept fixed to implicitly define a reference system. As illustrated in Figure 10.2, one Rod is fixed in all degrees of freedom and the other is fixed in translations, but free in all rotations. The two DS Rods have been selected such, to have the maximal "lever arm" between them.

10.3.2 Selection of Alignment Parameters

For the alignment of the Cosmic Rack setup, a two step strategy has been chosen. In the first step the alignment is carried out only at the level of Rods, and in the second step (starting from the aligned positions of the first step) Rods and individual sensor modules, in the following

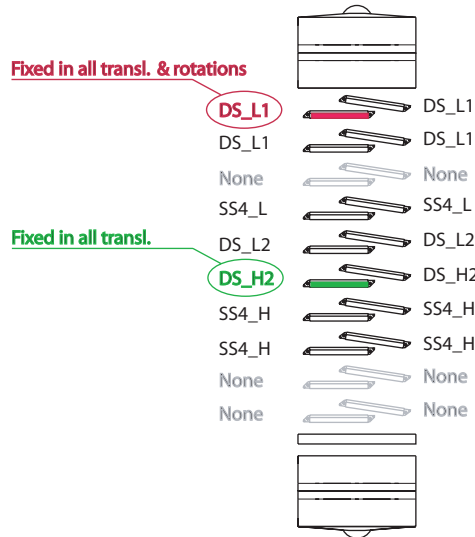


FIGURE 10.2: Configuration of the Cosmic Rack. For the definition of a reference system two double sided Rods are fixed: one is fixed in all degrees of freedom, the other in translations only.

referred to as "Dets", are aligned. With this two-step alignment, non-linearities in the track model are taken into account, and in addition the number of alignment parameters can be kept low in each pass. The definition of the alignment parameters for Rods and dets is illustrated in Figure 10.3.

The selection of parameters is summarized in Table 10.2. In the first pass, Rods are aligned in the translation and rotation degrees of freedom ("u", "v", "w" and " α ", " β ", " γ "), with the exception of the two Rods used to define the reference system, as discussed above. Single sided Rods are not aligned in "v" (the coordinate along the strips) as the precision in this view is only about $20\text{cm}/\sqrt{12}$, and therefore the results obtained for the alignment parameters would depend more on the non-uniform illumination of the detectors, than on a real misalignment [120].

In the second pass the dets are aligned in "u", "v" and " γ ", and simultaneously Rods are aligned in "u" and "v". In order to avoid ambiguous solutions, the alignment parameters of the modules are constrained to solutions which do not correspond to a uniform translation of the Rod to which they belong. The Rods defining the reference system are treated as in the first pass, and similarly, single-sided Rods and modules are not aligned in the "v" coordinate.

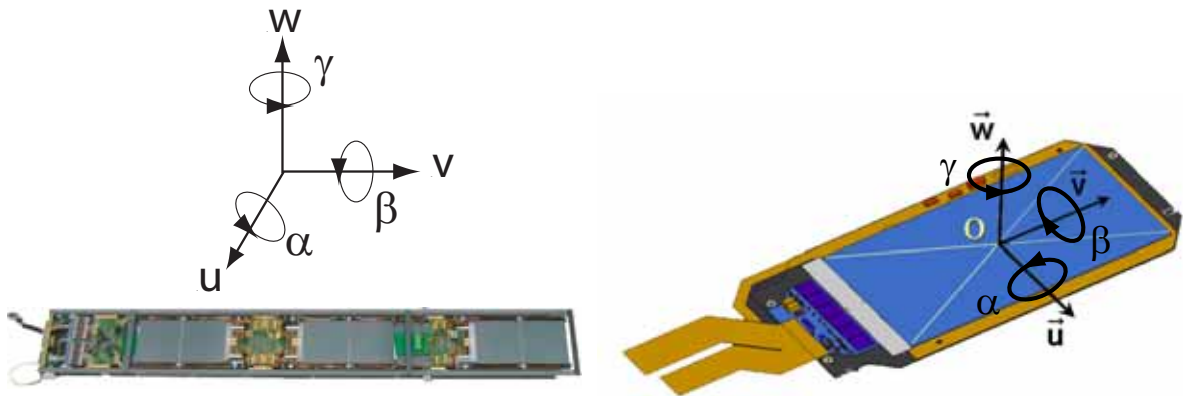


FIGURE 10.3: Definition of the alignment parameters for a TOB subassembly "Rod" (left) and a detector module "Det" (right).

	u	v	w	α	β	γ
Fixed Rods						
DS Layer 3	0	0	0	0	0	0
DS Layer 8	0	0	0	1	1	1
Aligned Rods						
SS-Rods	1	0	1	1	1	1
DS-Rods	1	1	1	1	1	1

	u	v	w	α	β	γ
Fixed Rods						
DS Rod Layer 3	f	f	f	0	0	0
DS Rod Layer 8	f	f	f	0	0	f
Aligned Rods						
SS-Rods	1	0	0	0	0	0
DS-Rods	1	1	0	0	0	0
Dets						
Dets SS	1	0	0	0	0	1
Dets DS	1	1	0	0	0	1

TABLE 10.2: Selection of the alignment parameters for the alignment of Rods only (left), and the alignment of Rods and dets (right). "0" indicates that the degree of freedom is not aligned, "f" keeps the degree of freedom of the higher level object (Rod) fixed and forces the alignment parameters of its components to result in no shift or rotation of their parent object. Degrees of freedom marked with "1"; are aligned, and if the aligned object is a composite the alignment transformations of its components are constrained such that they do not introduce additional global shifts or rotations of the parent object.

10.3.3 Track Reconstruction and Selection

Tracks used for the alignment have been reconstructed, without taking into account uncertainties in the track propagation due to material effects such as energy loss and multiple scattering. The tracks reconstructed in this way correspond to a straight lines, that best fit to the measured hit positions, where the weight of the hits is only given by the measurement resolution of the corresponding sensors. However, neglecting effects from multiple scattering in the track fit results (for the low momentum tracks) in large residuals. In order to avoid loss of track reconstruction efficiency, only tracks with an estimated χ^2/ndf greater than 2000 are rejected. Such a loose cut is necessary, as the estimated hit position error only accounts for the intrinsic resolution of about $50 \mu m$, while multiple scattering and misalignment results in residuals in the order of mm. For the selection of tracks used in the alignment, no further cut on the χ^2/ndf is applied; in order to have well defined residuals in "v", tracks are required to have at least 4 hits in glued-Dets.

10.3.4 Outlier Rejection

The least squares fitting method finds the optimal solution only if the errors of the measurements are gaussian distributed [118]. Data sets with non gaussian errors, can yield biased values for the alignment parameters. Therefore especially for the tracks of cosmic particles, where the effect of multiple scattering is large, and cannot be estimated correctly, because the momentum is not measured, the treatment of "outliers" is important.

In the MillepedeII algorithm the treatment of outliers can include the rejection of entire tracks and down-weighting of individual data points. For the Cosmic Rack alignment only the rejection of entire tracks has been selected. This method performs several internal iterations, in each iteration the track parameters are determined (using the updated alignment parameters from the previous iteration) and those with a too large χ^2/ndf get rejected and are not used for the determination of the global (alignment) parameters. In the following iteration the cut on the χ^2/ndf is tightened.

The outlier rejection is steered by three parameters: a χ^2 cut² for tracks the first iteration, the χ^2 cut for the second iteration, and the maximum number of iterations. For the studies

²This value is a measure for the χ^2/ndf of the tracks but does not correspond exactly to it. More details can be found in [118].

presented in the following, the χ^2 cut for outliers in the first iteration was set to 20000, and for the second to 40.5. Convergence is assumed and no further iterations are carried out, if the improvement in the χ^2 for the global parameters from the current iteration to the previous one is less than a given value (set to 0.9), or if a maximal number of iterations is carried out (set to 29).

10.4 Test of the Alignment Procedure with a Simulation

In order to evaluate the performance and limits of the alignment algorithm in a controlled environment, the alignment is tested first with a Monte-Carlo simulation of the setup.

The simulation is implemented in the standard CMS software framework CMSSW, that uses GEANT [90] for the simulation of the passage of particles through matter, modelling particle decays, electromagnetic and hadronic interactions. The output of this step is the amount of charge deposited in the different detectors ("hits"). The hits are then processed simulating the detector response, to produce the "digis", the signals issued by the front-ends. The digis are then processed with the same cluster finding and track reconstruction algorithms as the real data.

In order to simulate correctly the particles recorded with the Cosmic Rack, a cosmic muon generator was set up, with a spectrum described by the parametrization of eqn.7.3 and Table 7.1. In order to mimic the acceptance of the Cosmic Rack trigger system, only events are processed, in which particles are crossing the areas of the top and bottom scintillators, furthermore a minimum energy of 120 MeV is required, which accounts for the cut introduced by the lead absorber. The same configuration of the Rods as in the real system is used; the material of the mechanical structure supporting the Rods is not taken into account.

In the simulation of the passage of cosmic muons through the Cosmic Rack, i.e. the deposition of charge at the sensors, the detectors are placed at nominal positions (in the following referred to as "true positions"). The performance of the alignment algorithm is then tested by introducing an artificial misalignment at the step of track reconstruction. Ideally the alignment algorithm should correct for the misalignment introduced, and the differences between the positions after alignment and the true positions - i.e. the remaining misalignment - should be small.

The Millepede algorithm is tested with two misalignment scenarios. In the first scenario only Rods are misaligned and aligned and in the second Dets and Rods are misaligned and aligned. The results of the studies presented in the following were obtained using a sample of 50000 events, which corresponds to 20000 tracks fulfilling the track selection criteria.

10.4.1 Misalignment of Rods

The performance of the alignment algorithm at the level of Rods is evaluated. For the misalignment used in this test, the two Rods defining the reference system remain at nominal positions, for the other a realistic misalignment is applied. The alignment is carried out in two external loops. The selection of alignment parameters for the first and second pass is done according to Table 10.2 - "alignment of Rods only". The initial misalignment and the comparison with the true positions after the first pass are shown in Table 10.3, the results after the second pass are listed in Table 10.4.

Already after the first pass the alignment parameters are determined with good precision. In the second pass a further significant improvement is obtained in "u" and "v". This effect is mostly due to a correlation of " β " with "u" and "v" for glued Dets, that is introduced by the current implementation of the alignment framework. For the glued-Dets the hit position is estimated by projecting the hit strips in the stereo module and the corresponding r-phi module onto a virtual plane (located in the middle of the two detectors). The point of intersection gives the measured hit position. This estimate however depends on the projection angle, that is given

Parameter		Misalignment		Aligned vs. True	
		Mean [μm]	RMS [μm]	Mean [μm]	RMS [μm]
Rods	u	-558	251	-19	22
	v	348	292	67	272
	w	635	375	-5	17
		Mean [mrad]	RMS [mrad]	Mean [mrad]	RMS [mrad]
	α	-0.53	0.58	-0.27	0.15
	β	-7.40	4.64	0.03	0.36
	γ	0.28	0.26	-0.02	0.02

TABLE 10.3: Alignment with simulated tracks, misalignment scenario "Rods only": the initial misalignment and the difference to the true positions after the first pass of the alignment are shown.

Parameter		Relative Shifts		Aligned vs. True	
		Mean [μm]	RMS [μm]	Mean [μm]	RMS [μm]
Rods	u	13	21	-6	5
	v	-94	278	-27	10
	w	-2	11	-7	20
		Mean [mrad]	RMS [mrad]	Mean [mrad]	RMS [mrad]
	α	-0.04	0.01	-0.31	0.16
	β	-0.01	0.10	0.01	0.37
	γ	0	0	-0.02	0.02

TABLE 10.4: Alignment with simulated tracks, misalignment scenario "Rods only": the relative shifts and the difference to the true positions after the second pass of the alignment are shown.

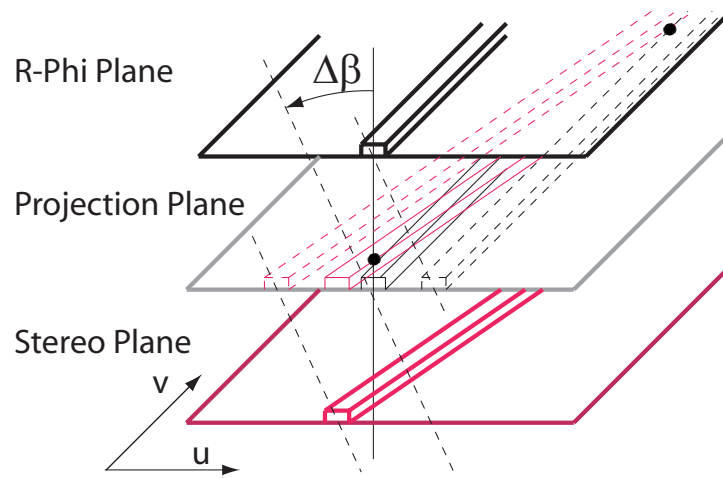


FIGURE 10.4: Effect of the projection angle on the estimated hit positions for glued-Dets.

	Parameter	Misalignment		Aligned vs. True	
		Mean [μm]	RMS [μm]	Mean [μm]	RMS [μm]
Dets	u	-3	64	-	-
	v	-210	1343	-	-
		Mean [mrad]	RMS [mrad]	Mean [mrad]	RMS [mrad]
	γ	0.01	0.50	-	-
		Mean [μm]	RMS [μm]	Mean [μm]	RMS [μm]
Rods	u	570	280	-11	42
	v	906	720	637	673
	w	635	375	73	43
		Mean [mrad]	RMS [mrad]	Mean [mrad]	RMS [mrad]
	α	-0.53	0.58	-0.14	0.18
	β	-7.40	4.64	-0.30	1.35
	γ	0.29	0.26	-0.10	0.03

TABLE 10.5: *Alignment with simulated tracks, misalignment scenario "Rods and Dets": The initial misalignment and the difference to the true positions after the first pass of the alignment are shown.*

by the direction of the particle. A misalignment in " β " leads to a wrong estimate of the track angle, introducing a bias in the calculated hit position in "u" and in "v" (the shift in "v" is large due to the small stereo angle). The effect is sketched in Figure 10.4. In the first pass, the determination of "u" and "v" is partially spoiled by the rotation β . In the second pass, the initial value of β is close to the "true" value, and the determination of "u" and "v" becomes more accurate.

After the second pass the alignment parameters are determined with high accuracy: $\approx 10 \mu\text{m}$ for "u", $\approx 40 \mu\text{m}$ for "v" and $\approx 30 \mu\text{m}$ for "w", with comparable precision for the rotations. In order to put the accuracy of rotations into perspective, one can estimate the corresponding translations for the extreme points, considering that the active area of Rods extends in "u" over about 100 mm, in "v" over approximately 1100 mm and the upper modules and the lower modules, respectively are located approximately ± 5 mm from the Rod middle plane in "w".

10.4.2 Misalignment of Rods and Dets

For the test described in this section, the shifts applied to the alignment parameters of Rods and Dets correspond to the precision of the real system as measured from cosmic particle tracking, and are described later in section 10.5. As described in section 10.3.2 the alignment is carried out in two passes. In the first pass only the Rods are aligned and in the second pass both Rods and Dets.

The initial misalignment and the alignment parameters obtained in the first pass are listed in Table 10.5. The corresponding plots are shown in Figure 10.5 for the translations and in Figure 10.6 for the rotations. The results after the second pass, where starting from the position obtained by the first pass Rods are aligned in "u", "v" and the detectors in "u", "v" and " γ " are listed in Table 10.6. The corresponding plots are shown in Figure 10.7 for the Rods, and Figure 10.8 for the Dets. One observes also in this scenario a relatively large error in the determination of "v" for the Rods in the first pass, that is corrected in the second. This is due to the effect of the hidden correlation between "v" and " β " discussed above, and is possibly also due to non-uniform illumination of the Dets of a given Rod. In order to illustrate the effect of non-uniform illumination one can imagine a Rod with just two modules: one displaced by Δv and the other by $-\Delta v$. As the displacement of the Dets is symmetric one would consider the Rod to be already optimally aligned in the "v" coordinate. If however the Dets are not aligned

	Parameter	Relative Shifts		Aligned vs. True	
		Mean [μm]	RMS [μm]	Mean [μm]	RMS [μm]
Rods	u	1	45	-10	9
	v	688	701	-50	44
		Mean [μm]	RMS [μm]	Mean [μm]	RMS [μm]
Dets	u	1	71	3	24
	v	184	1340	-25	35
		Mean [mrad]	RMS [mrad]	Mean [mrad]	RMS [mrad]
	γ	0.01	0.50	0.01	0.14

TABLE 10.6: *Alignment with simulated tracks, misalignment scenario "Rods and Dets": The relative shifts and the remaining misalignment after the second pass of the alignment are shown.*

individually but just the entire Rod is aligned as a single object (as in the first pass), different illumination of the two Dets will result in a shift of the Rod.

Concluding from Table 10.5 and Table 10.6, the remaining misalignment is low and all alignment parameters are determined with good precision, validating the choice of parameters for track selection and outlier rejection.

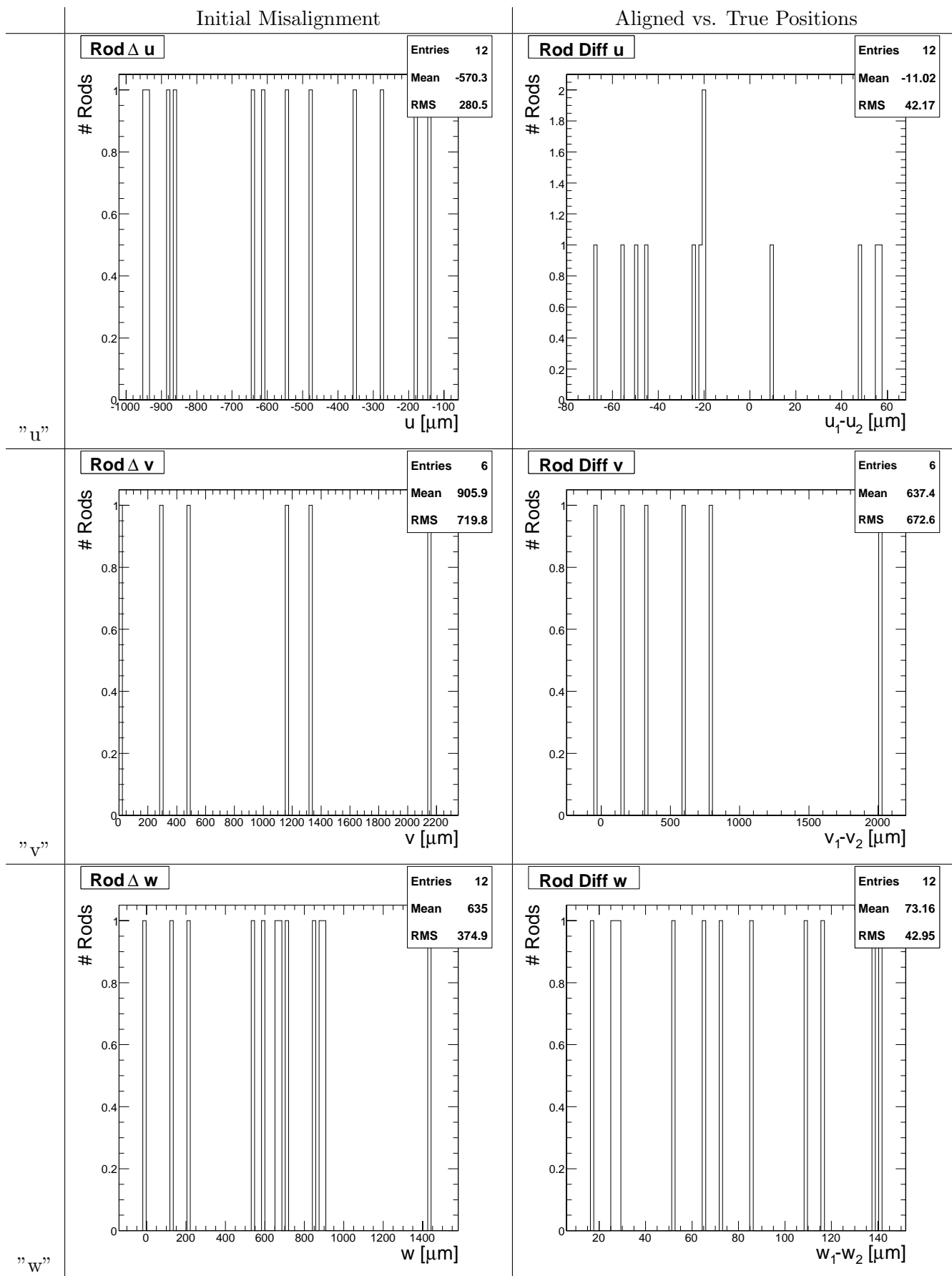


FIGURE 10.5: Alignment with simulated tracks; An artificial misalignment has been applied to Rods and Dets. Results from first pass of alignment. Here shown for the translations of Rods. The initial misalignment is shown (left), and the remaining misalignment (right).

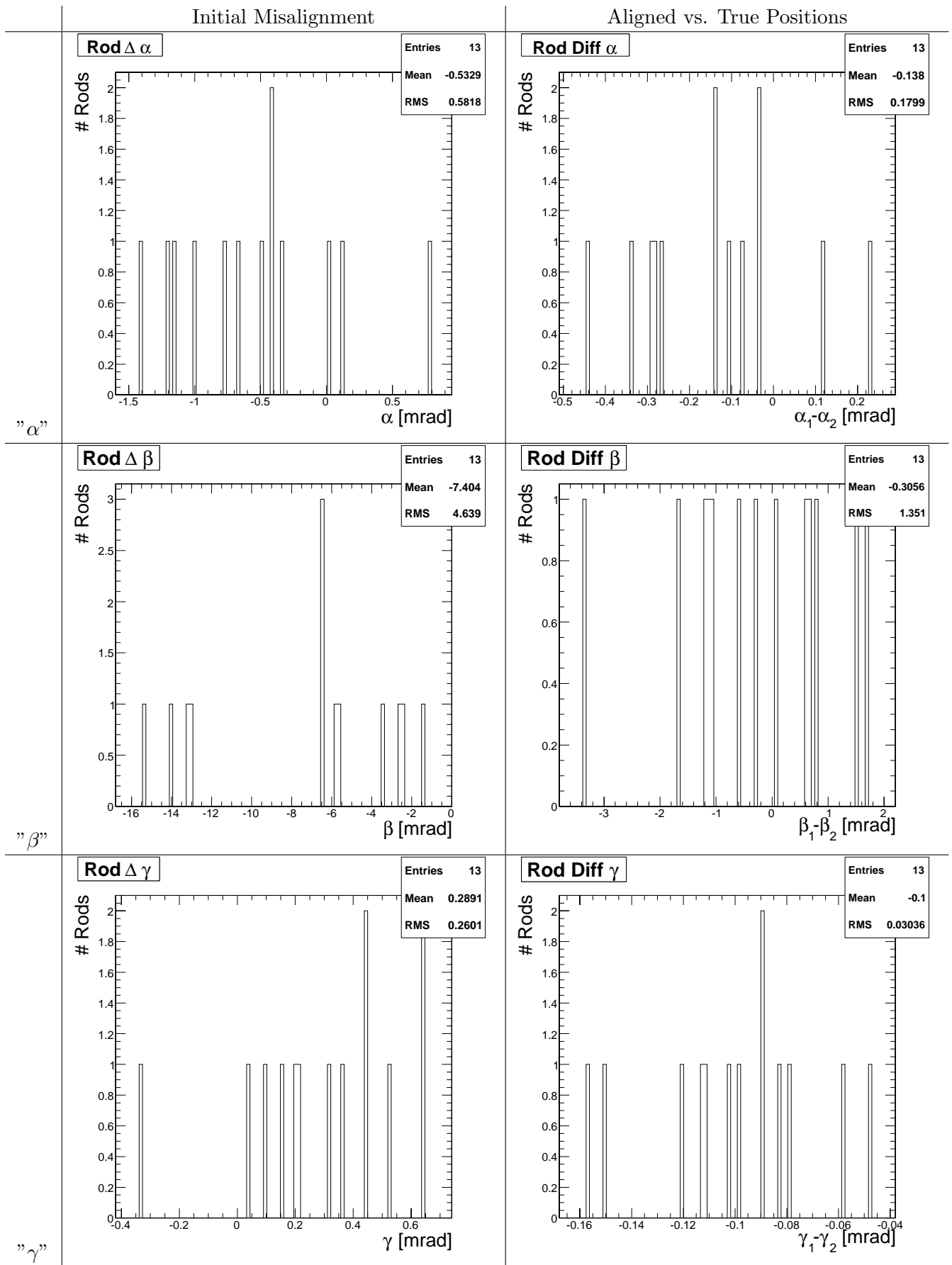


FIGURE 10.6: Alignment with simulated tracks; An artificial misalignment has been applied to Rods and Dets. Results from first pass of alignment. Here shown for the rotations of Rods. The initial misalignment is shown (left), and the remaining misalignment (right).

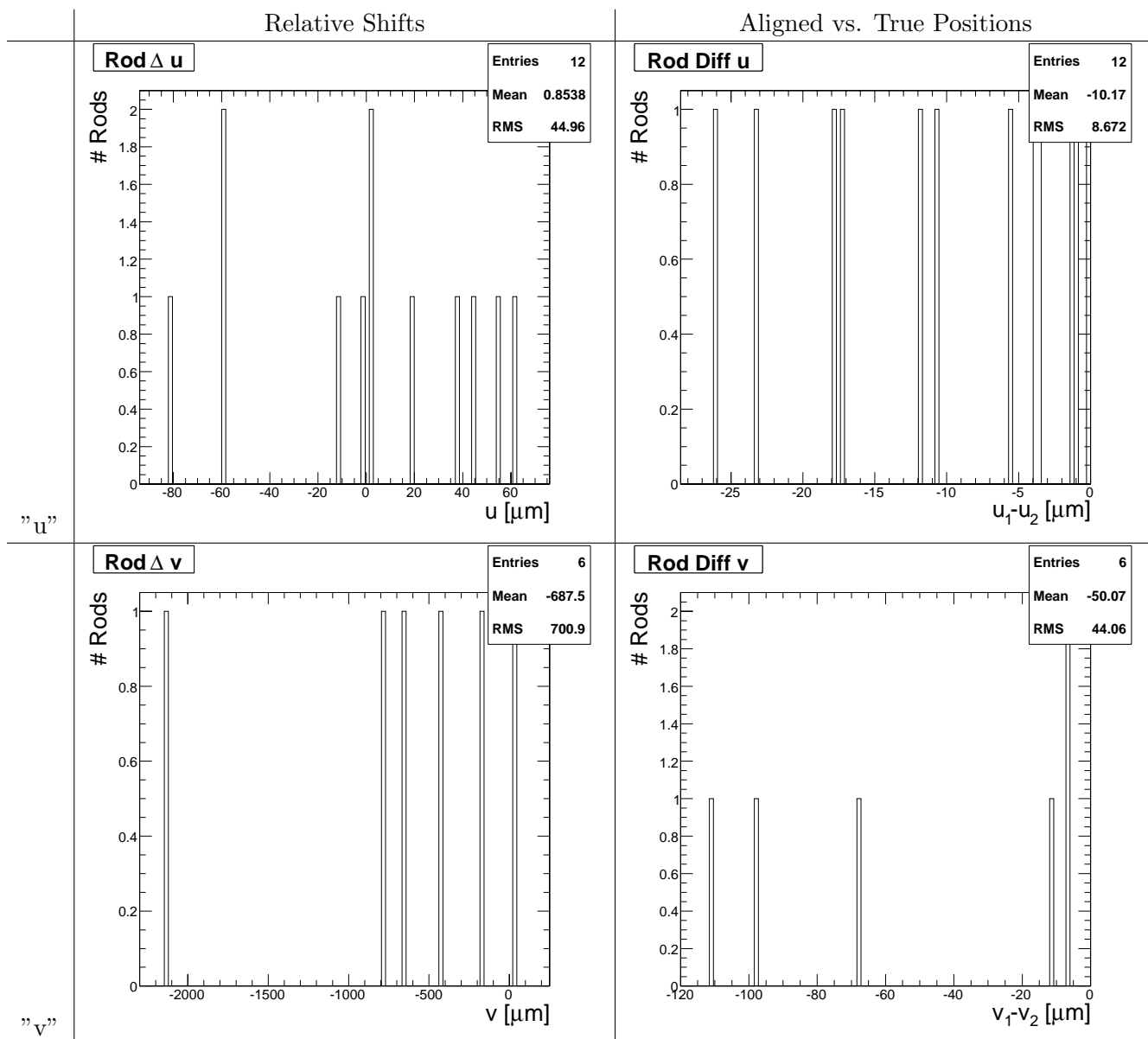


FIGURE 10.7: Alignment with simulated tracks; An artificial misalignment has been applied to Rods and Dets. Results after second pass of alignment. Here shown for the Rods. The relative shifts (left), and the remaining misalignment (right) are shown.

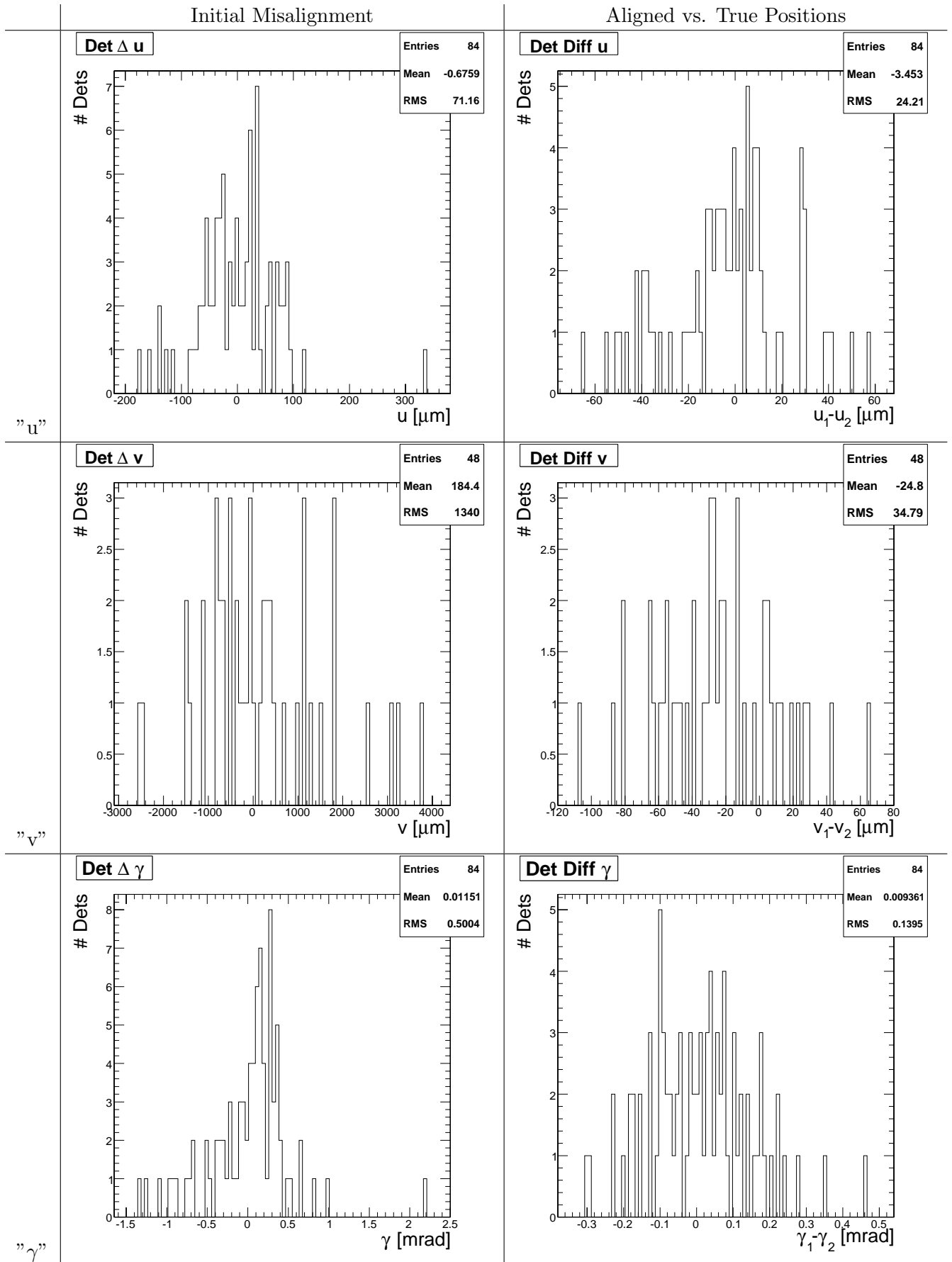


FIGURE 10.8: Alignment with simulated tracks; An artificial misalignment has been applied to Rods and Dets. Results from second pass of alignment. Here shown for the Dets. The initial misalignment is shown (left), and the remaining misalignment (right).

Run	Apv-Mode	Temperature [$^{\circ}C$]	#Events	#Tracks
200379	Decv	20	65 000	47 000
200397	Decv	20	51 000	37 000
200401	Decv	20	86 000	62 000
200881	Peak	-10	107 000	74 000
200921	Decv	-10	41 000	28 000

TABLE 10.7: *List of runs used for the alignment studies.*

10.5 Alignment of the Cosmic Rack

Applying the same procedure, that has been tested and validated with the simulation, the detectors of the Cosmic Rack are aligned using real data: tracks from cosmic particles.

10.5.1 Data Samples

For the alignment of the Cosmic Rack data have been collected in different conditions; the list of runs used for the alignment studies is given in Table 10.7.

10.5.2 Results from Alignment with Real Data

The results presented in the following have been obtained using a sample of 50000 events from run 200401, which corresponds to about 20000 tracks fulfilling the selection cuts. For an estimation of the accuracy achieved, the results are compared with those obtained from data recorded in run 200397.

The results from the alignment of the Rods in the first pass are listed in Table 10.8. The corresponding plots are given in Figure 10.9 for the translations and Figure 10.10 for the rotations. The results from the alignment after the second pass are shown in Table 10.9, Figure 10.11, Figures 10.12, respectively.

The absolute values of the alignment parameters for the Rods are a measurement of the precision of the Cosmic Rack support structure: the setup precision is in the order of a few 100 μm remarkable, especially considering that the Rods are housed in "drawers", that can slide out to facilitate assembly and connection. The alignment parameters for the Dets with respect to the Rod frame, presented later, describe the displacements of the modules within the Rod, providing a quantitative measurement of the geometrical precision of fully populated Rods. A detailed study on the precision of the Rods is given in section 10.6.

An estimate on the statistical precision of the alignment method is given by comparing the alignment parameters obtained from independent data sets: the RMS of the differences corresponds to $\sqrt{2}$ of the resolution. The estimated precision from the data is perfectly consistent with the expectation from the simulation as can be seen by comparing Table 10.8 with Table 10.5 and Table 10.9 with Table 10.6, respectively.

	Parameter	Absolute Shifts		Difference Samples A vs. B	
		Mean [μm]	RMS [μm]	Mean [μm]	RMS [μm]
Rods	u	-483	235	9	15
	v	582	326	-27	148.5
	w	546	339	57	43
		Mean [mrad]	RMS [mrad]	Mean [mrad]	RMS [mrad]
	α	-0.27	0.54	-0.02	0.21
	β	-7.51	4.43	0.22	1.07
	γ	0.36	0.27	0.02	0.02

TABLE 10.8: Alignment with "real" tracks: Alignment parameters obtained in the first pass, and comparison with parameters obtained from independent data sample.

	Parameter	Relative Shifts		Difference Samples A vs. B	
		Mean [μm]	RMS [μm]	Mean [μm]	RMS [μm]
Rods	u	-10	48	14	15
	v	348	292	53	71
Dets		Mean [mrad]	RMS [mrad]	Mean [mrad]	RMS [μm]
	u	-9	64	-7	23
	v	-25	1331	-55	123
		Mean [mrad]	RMS [mrad]	Mean [mrad]	RMS [mrad]
	γ	0.07	0.53	0.00	0.24

TABLE 10.9: Alignment with "real" tracks: Alignment parameters obtained in the second pass, and comparison with parameters obtained from independent data sample.

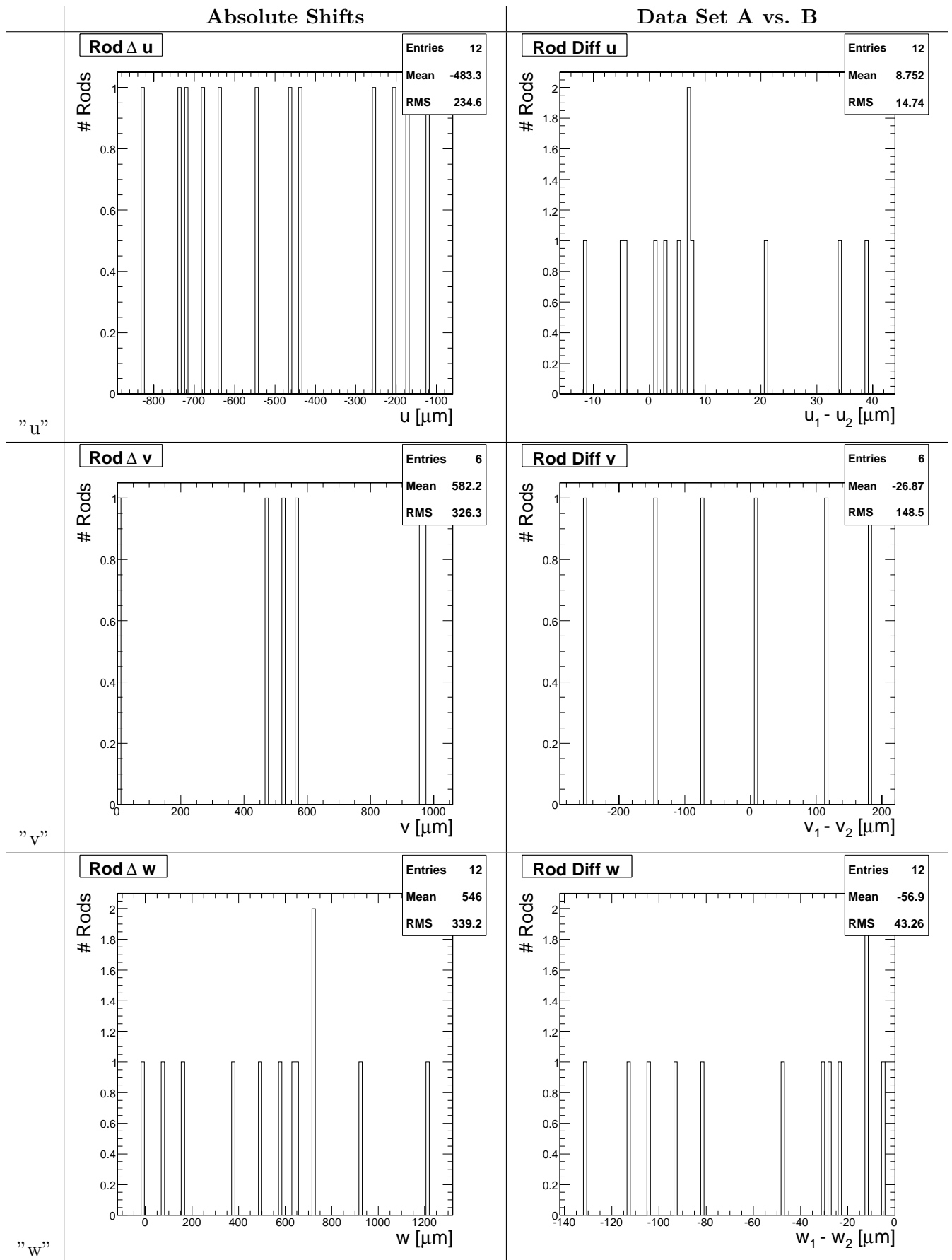


FIGURE 10.9: Alignment of the real system; Results from first pass of alignment for "Rods". The absolute shifts are shown (left), and the comparison with an independent data set (right).

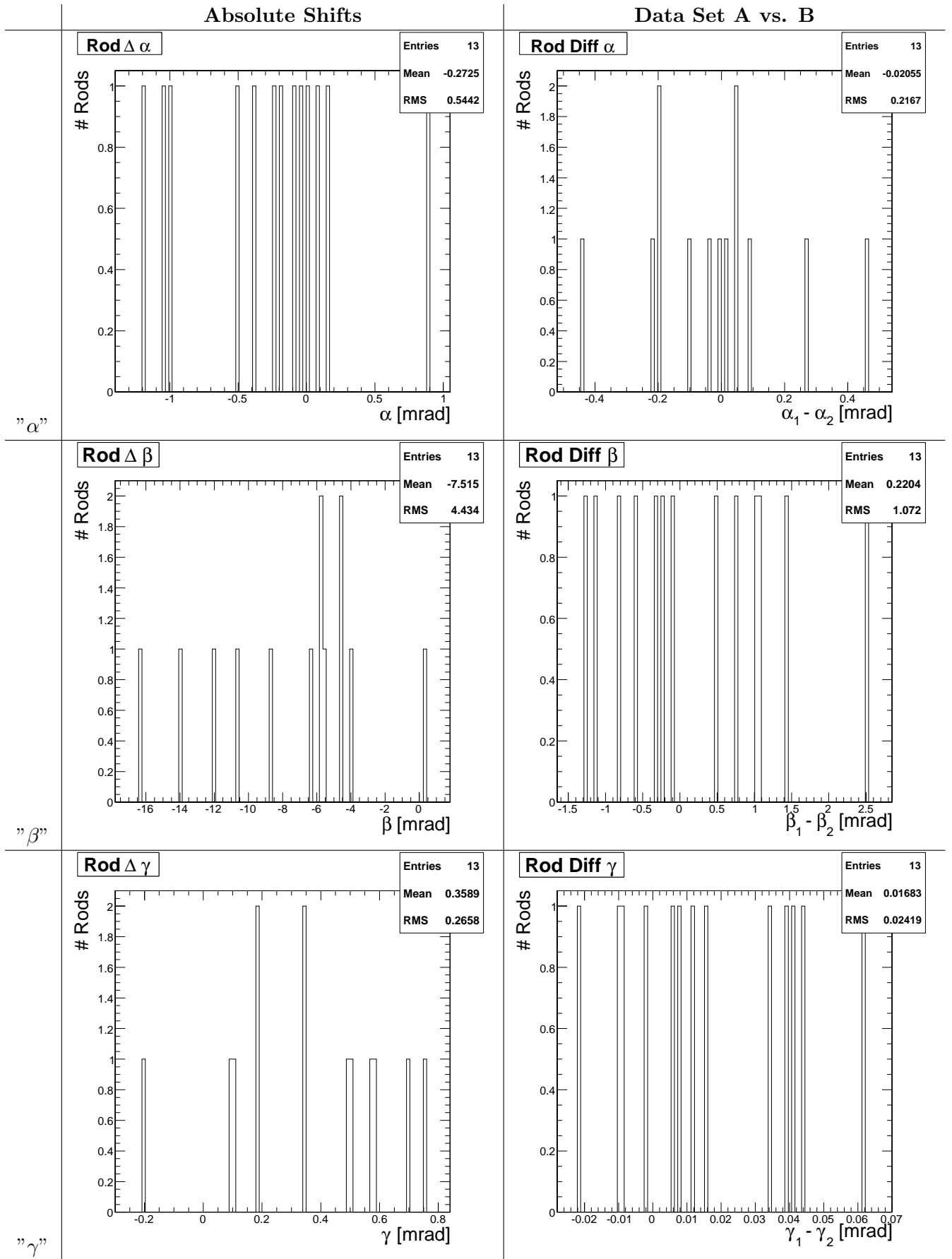


FIGURE 10.10: Alignment of the real system; Results from first pass of alignment. Here shown for the rotations of Rods. The absolute shifts are shown (left), and the comparison with an independent data set (right).

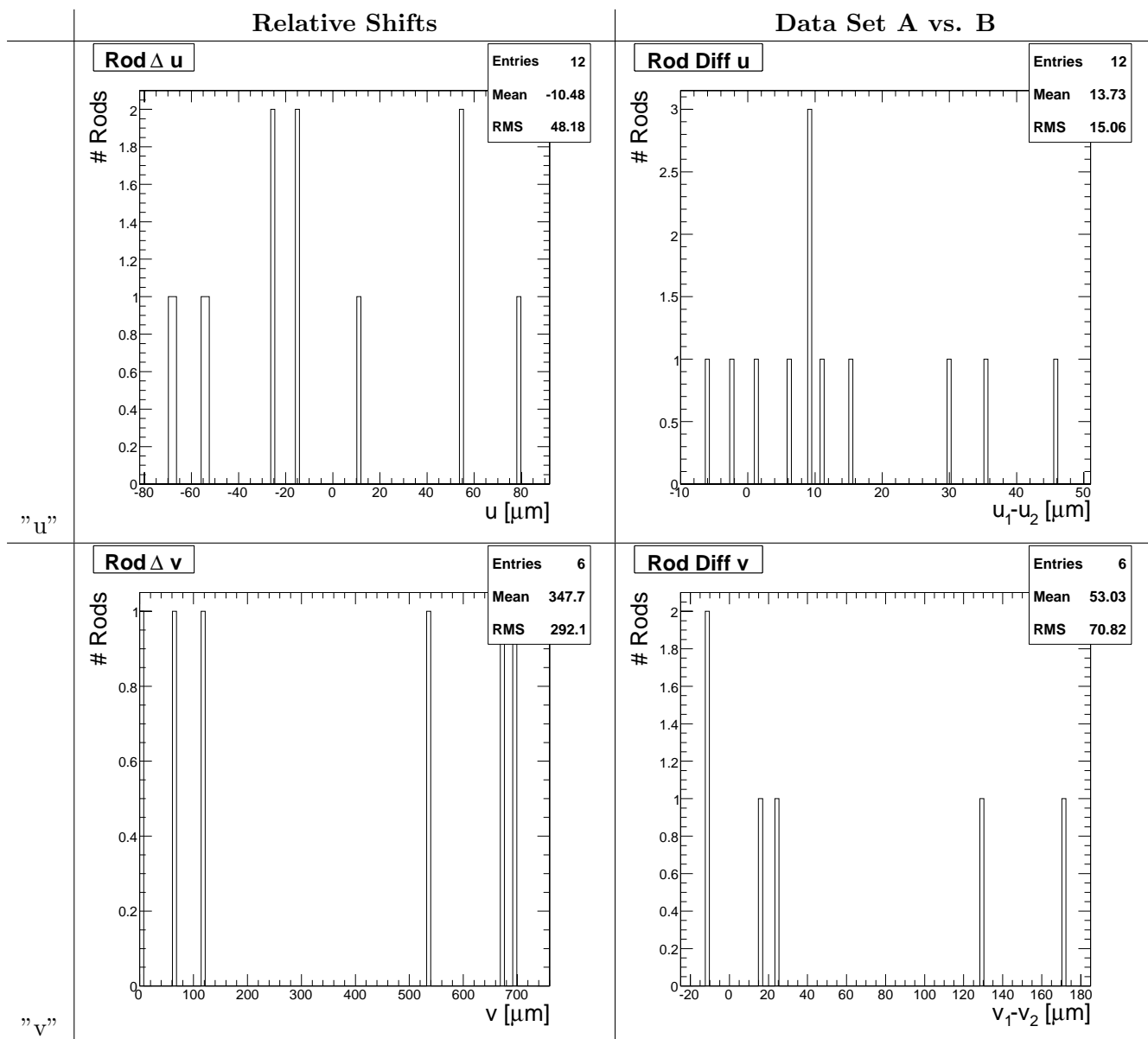


FIGURE 10.11: Alignment of the real system; Results from second pass of alignment. Here shown for the Rods. The relative shifts are shown (left), and the comparison with an independent data set (right).

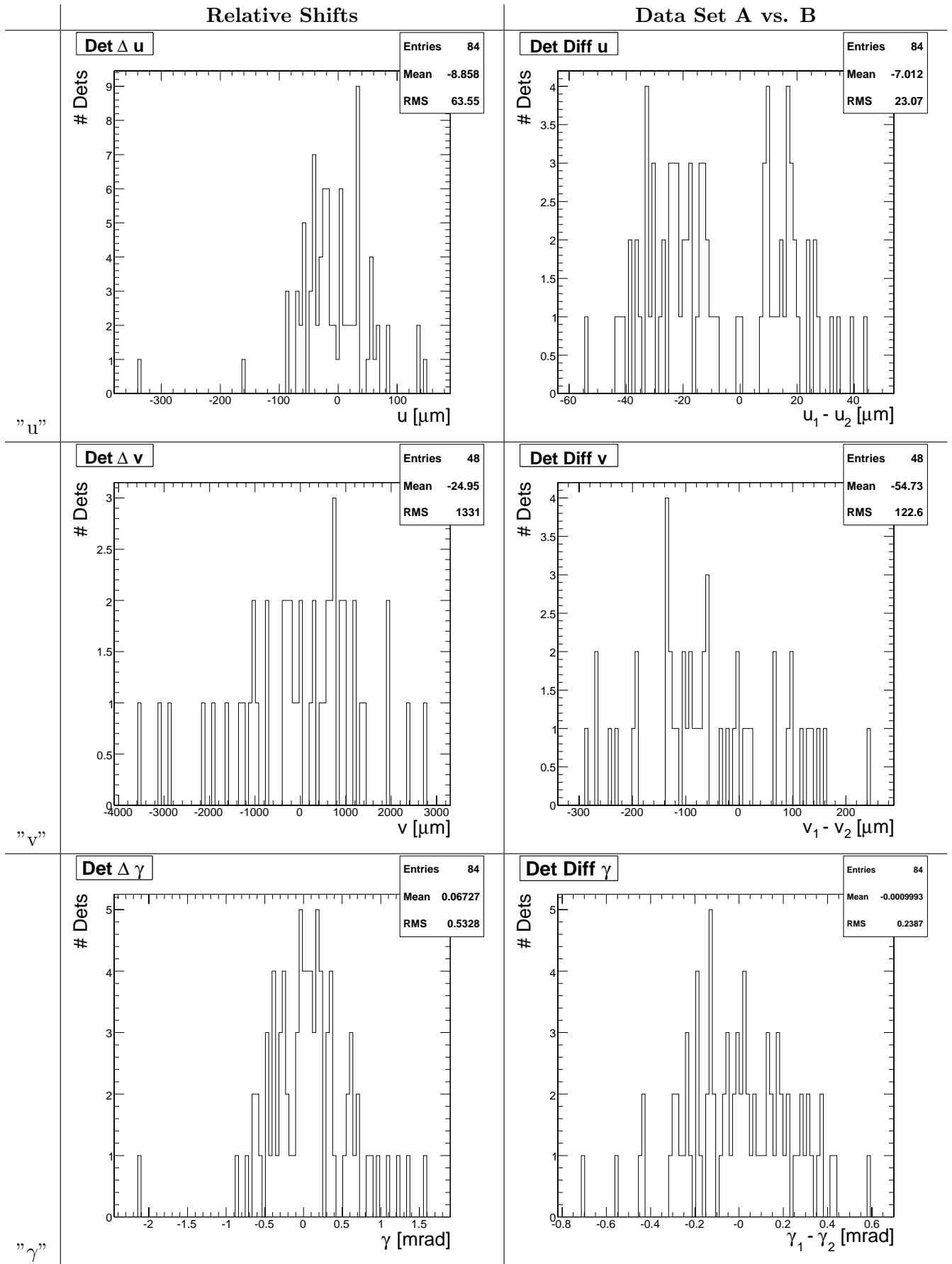


FIGURE 10.12: Alignment of the real system; Results from second pass of alignment for "Dets". The relative shifts are shown (left), and the comparison with an independent data sample (right).

10.5.3 Study of Residuals

To confirm the validity of the alignment parameters obtained, the hit-to-track residuals of individual Dets are studied. The distributions of the residuals for a single module before and after alignment are shown in Figure 10.13.

The mean of the distribution is related to the misalignment of the specific detector, while the width is given by multiple scattering and misalignment of the full system. The distribution after alignment is narrower and centered close to zero, indicating a successful alignment of the system. In this study, that makes use of relatively soft tracks, the width of the distribution of the residuals is dominated by multiple scattering. Therefore to quantify and visualize the effect of the alignment on the full system, we fit the mean of the residuals for each Det as in Figure 10.13 and we consider the distribution of the values for all the detectors in the system. Such distribution is shown in Figure 10.14 before alignment, after alignment and in the simulation with the ideal geometry. The mean values after alignment are centered close to zero with an RMS of only $6 \mu m$ in "u" and $115 \mu m$ in "v", such values are similar to those obtained from the simulation with ideal geometry ($5 \mu m$ in "u" and $82 \mu m$ in "v").

The width of the residuals are shown in Figure 10.15: the entries correspond to detectors grouped by layers; the three distributions show the values obtained from data before and after alignment, and from the simulation with ideal geometry. Layer 7 corresponds to the uppermost layer in the Cosmic Rack and layer 1 to the lowest. The width is reduced after alignment and the agreement between the simulation and the data after alignment indicates a good modelling of the muon spectrum and multiple scattering.

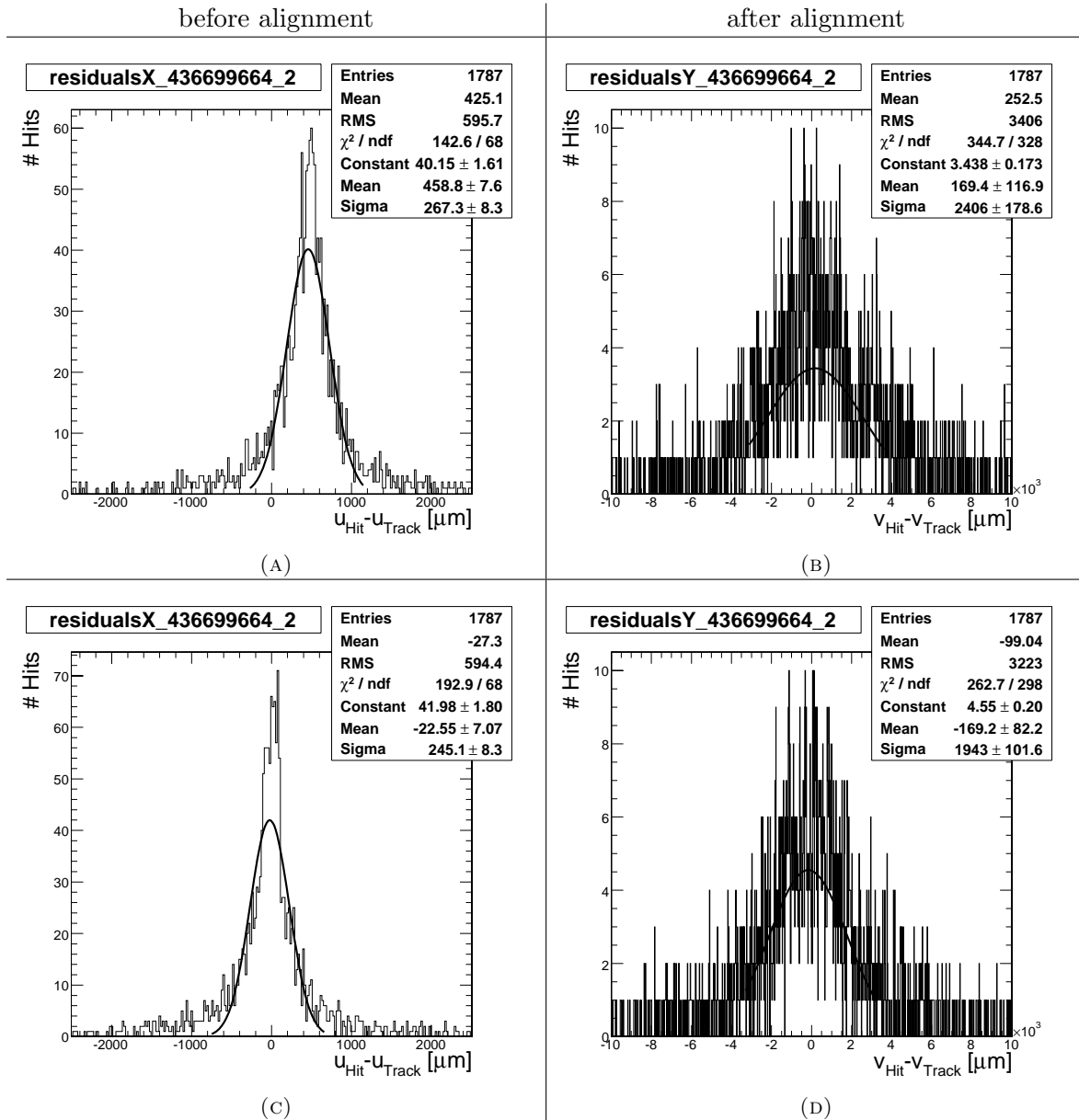


FIGURE 10.13: (a,b) hit-to-track residuals of a double-sided module before alignment. The residuals for the coordinate "u" are shown in the left and for "v" on the right. The core of the distribution is fitted with a gaussian function, to derive values for the Mean and RMS that do not depend too strongly on the presence of outliers. (c,d) residuals of the same module after alignment.

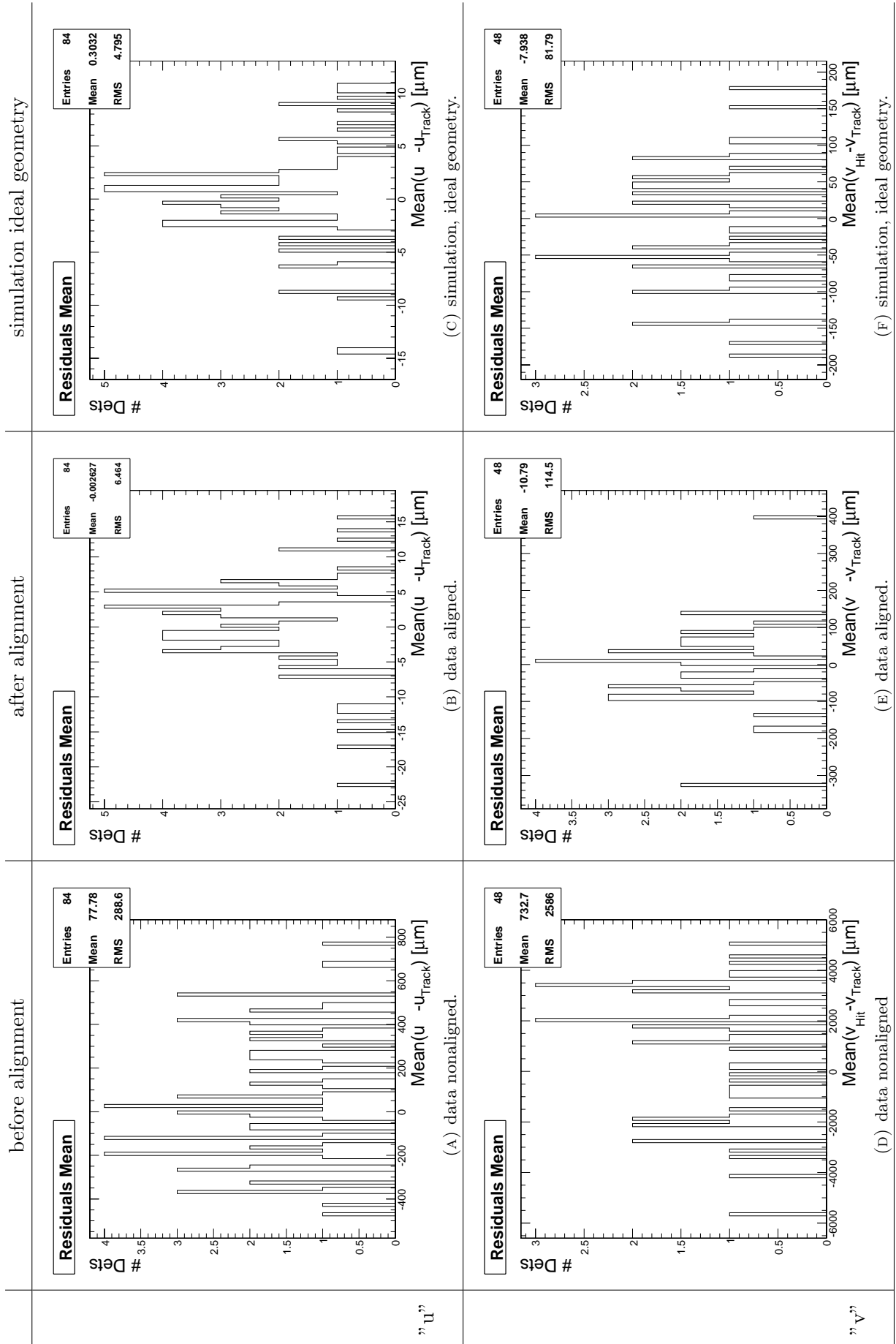


FIGURE 10.14: Mean of the residuals for the individual Modules.

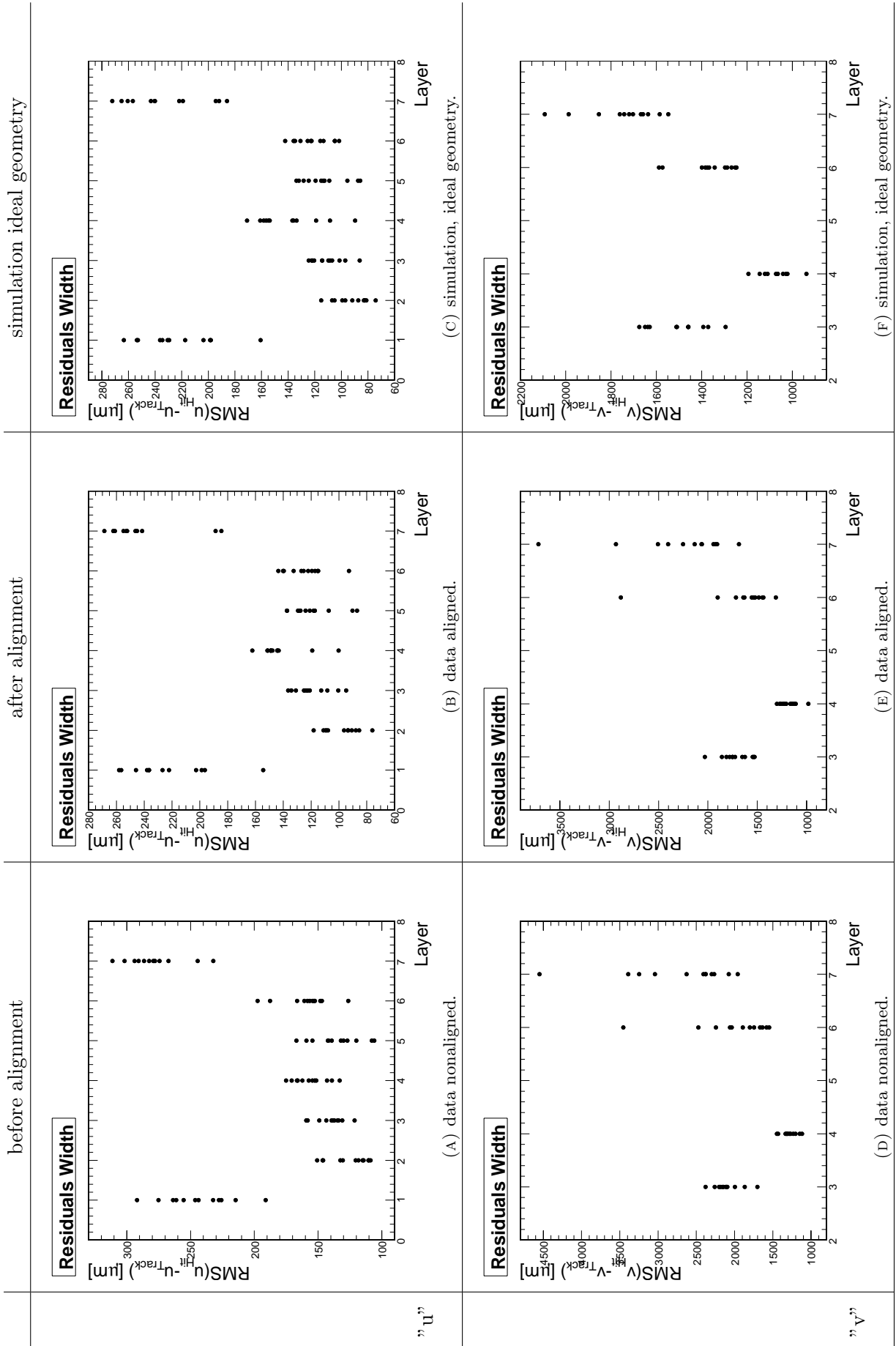


FIGURE 10.15: Width of the residuals for the individual modules as a function of the layer.

10.5.4 Precision versus Statistics

The precision of the alignment parameters depends on the number of tracks N used for the alignment. The precision is expected to scale with $\sqrt{1/N}$, until a systematic limit is reached. In Figure 10.16 the RMS of the differences of the alignment parameters obtained from two independent data samples is shown as a function of the number of tracks in the samples.

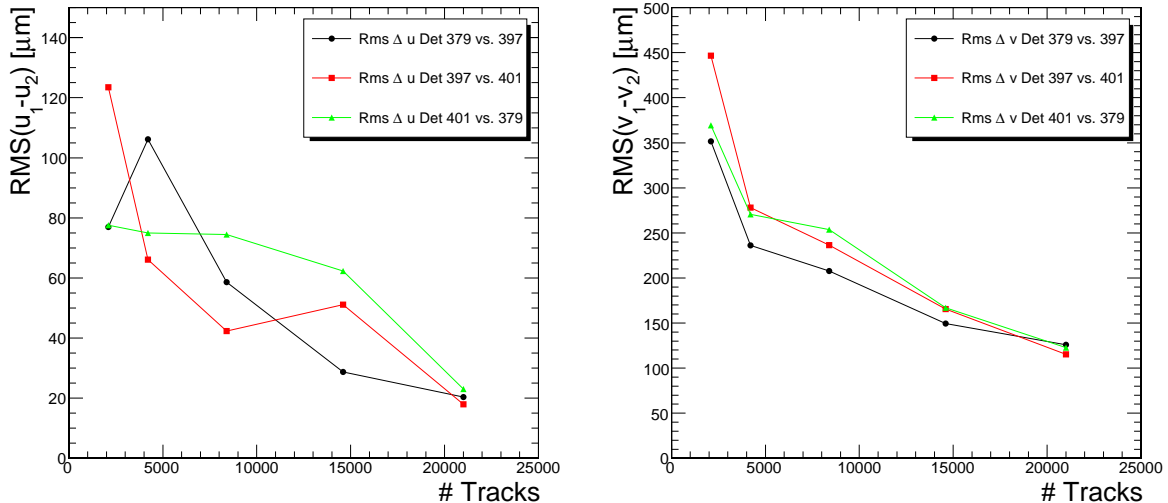


FIGURE 10.16: RMS of the difference between single Det alignment parameters (“ u ” on the left and “ v ” on the right), obtained from two independent data samples, displayed as a function of the number of tracks in the samples. The three graphs in the plots correspond to comparisons in all the combinations of the three datasets 200379, 200397 and 200401.

With 20000 tracks the precision does not appear to be saturated yet. These numbers can be useful to derive an indication of the statistics needed for a precision alignment of the Tracker: in this study 50000 events correspond to about 20000 tracks fulfilling the track selection criteria and a mean number of 1800 hits per detector. In the last iteration of the Millepede about 60% of the tracks are excluded due to the outlier rejection, leaving about 700 hits per detector.

10.6 Geometrical Precision of TOB Rods

Rods inside the Cosmic Rack (and also in the TOB) are held from four supporting spheres. The module position on the Rod is determined by two precision pins. All Rod frames have been measured on a Coordinate Measuring Machine (*CMM*) (see Figure 10.17), to qualify the assembly and measure the position and orientation of the module mounting pins with respect to the reference frame determined by the Rod supporting spheres.

These measurements can be translated to expected positions of the sensors in the Rod reference frame. Such data however do not account for the intrinsic precision of the module assembly (i.e. displacements of the sensors with respect to the spring clips, that are mounted on the Rod pins) and possible deformations of the Rod frame and pins occurring during Rod integration. Track-based alignment of the Cosmic Rack provides the first quantitative evaluation of the geometrical precision of fully integrated Rods.

10.6.1 Measurements

For the measurements presented in the following, the alignment was carried out following the procedure discussed above, but in order to increase the precision of the results, data from the

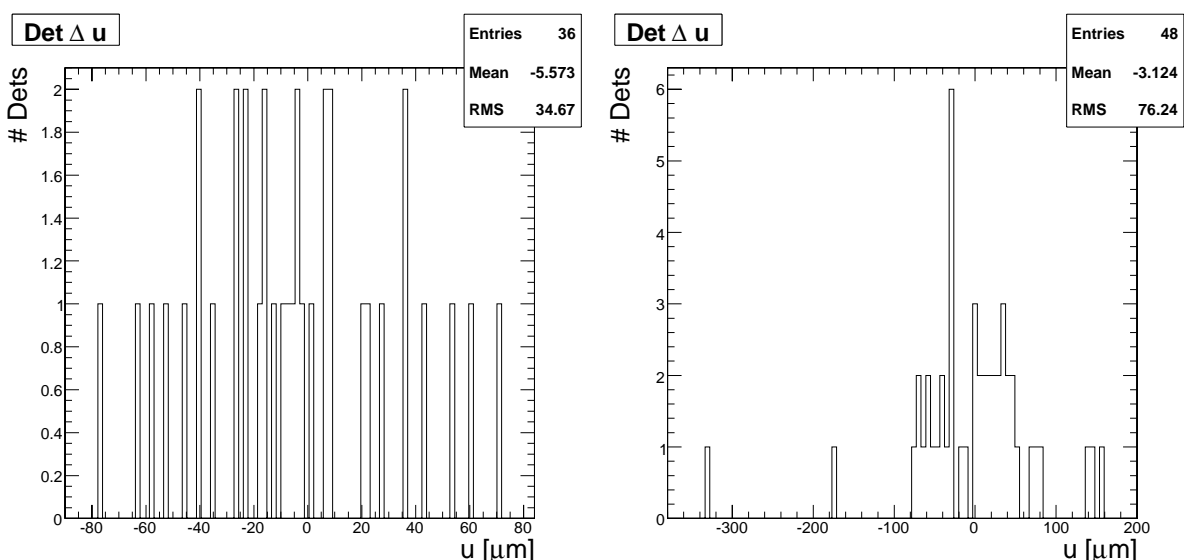


FIGURE 10.17: Rod frame measured by a CMM.

three runs taken at room temperature were combined into a large sample with a total of about 200000 events, corresponding roughly to 80000 tracks fulfilling the track selection criteria.

Due to the simultaneous alignment of Dets and Rods, the precision of the Cosmic Rack mechanics is automatically disentangled from the intrinsic precision of the Rods: the alignment parameters for the Rods reflect the precision of the support mechanics, while the alignment parameters of the Dets measure the displacement of the sensors with respect to their nominal position in the Rod frame, and therefore give directly the geometric precision of the Rod.

The results of these measurements are split into two groups, quantifying the precision of SS-Rods and DS-Rods separately. The intrinsic Rod precision in "u", i.e. the displacements of the modules in the direction across the strips are shown in Figure 10.18, and the precision in " γ " in Figure 10.19. For DS-Rods the displacement of the modules in the direction along the strips is shown in Figure 10.20.

FIGURE 10.18: Intrinsic Rod precision in "u", for SS₄ Rods (left) and DS Rods (right).

According to these plots SS-Rods have a precision of about $40\mu\text{m}$ in "u" and 0.3 mrad in " γ ". The precision for DS Rods appears to be worse: about $80\mu\text{m}$ in "u" and 0.6 mrad in " γ ". The interpretation of these results is discussed in the next section.

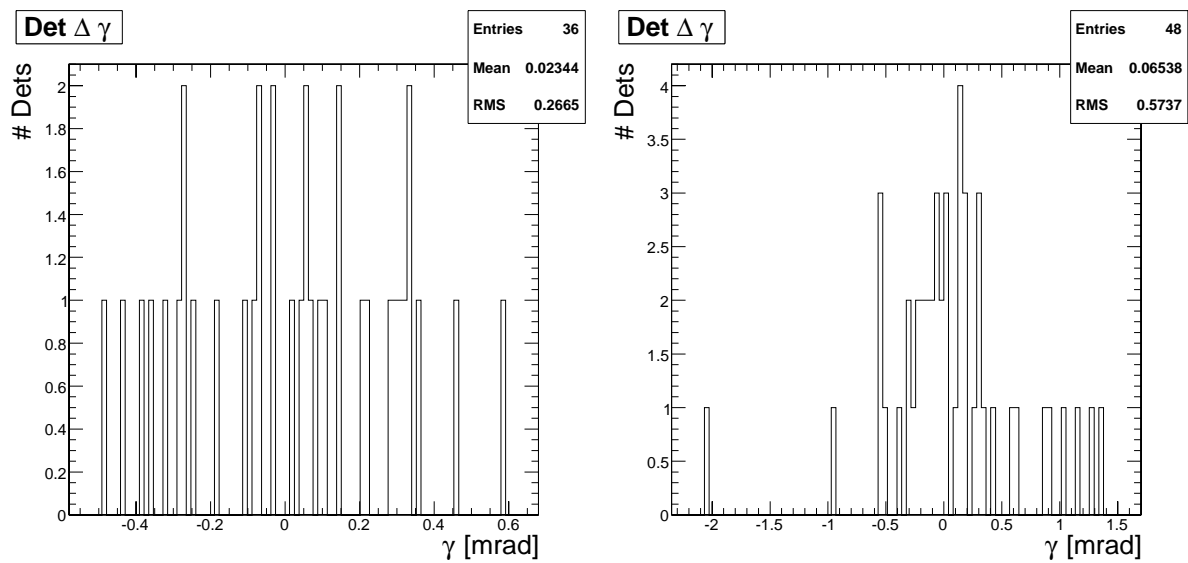


FIGURE 10.19: *Intrinsic Rod-precision in " γ " for SS₄ Rods (left) and DS Rods (right).*

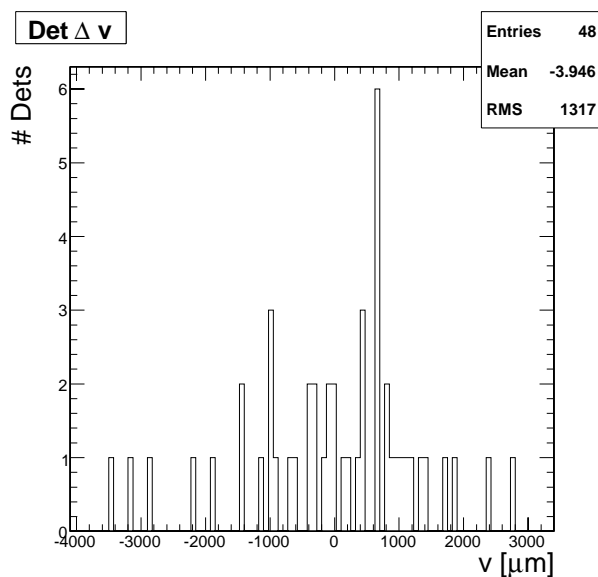


FIGURE 10.20: *Intrinsic Rod-precision in " v " for DS-Rods.*

10.6.2 Analysis and Interpretation of the Results

Despite the fact, that the alignment parameters are reproduced in statistically independent samples and correspond to a real improvement in the hit-to-track residuals (as discussed above), it is rather evident, that the alignment parameters for DS Rods cannot be directly interpreted in terms of the Rod geometry. The Rod mechanics is designed in such a way that the it necessarily yields comparable module positioning precision in the "u" and "v" coordinates; furthermore measured values of Δv as large as 2-3 mm (Figure 10.20) cannot correspond to a real shift of the detectors, as they exceed the clearance between the detectors and other elements in the Rod assembly.

In the current implementation of the alignment framework, pairs of r-phi and stereo detectors ("glued-Dets") are aligned together, with no provision for relative displacement and misalignment of the two detectors in the pair. In reality, while the position of the pins affects the two detectors in the same way, their orientation has a different effect, as mounting springs are clamped on the pins at different distance of about 4 mm; in addition the displacement of the sensors with respect to the spring clips is independent for the two detectors. Therefore a non-negligible displacement (and misalignment) between the two detectors of a pair is indeed expected. As demonstrated in Figure 10.21, due to the small stereo angle of 100 mrad, a relative displacement in "u" translates to a 10 times larger shift in "v" of the measured coordinate. It should be noted that, while a relative displacement of the two detectors in "u" is perfectly compensated by a 10 times larger shift of the pair in "v", a relative misalignment in the rotations between the two detectors (i.e. a deviation of the stereo angle from the nominal value) cannot be perfectly compensated: such effect could contribute to explain the apparently worse precision of the DS Rods also in the "u" coordinate. A confirmation of the effect discussed above can be obtained by studying the correlation between the measured displacements in the "u" and "v" coordinate: since some specific derivations from the nominal geometry are compensated by correlated shifts in Δu and Δv , one expects to find a certain degree of correlation between the measured displacements in the two views. The data are shown in Figure 10.24, and in fact a significant correlation of 0.55 is measured; the average scaling factor between the two quantities is about 10, consistent with the nominal stereo angle of 100 mrad.

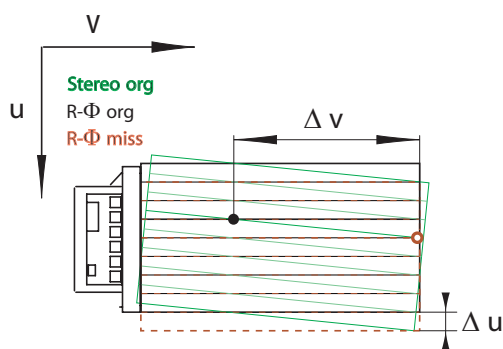


FIGURE 10.21: In the "glued-Dets" the 2D hit positions are estimated, by the projected intersection of the strips in the r-phi and stereo detectors. A relative displacement " Δu " of the two detectors translates via the stereo angle into a large apparent the shift of the pair in the direction "v".

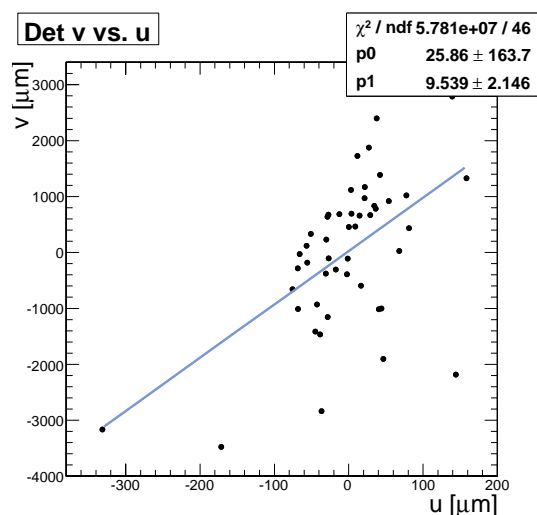


FIGURE 10.22: Correlation between the measured alignment parameters "u" and "v".

Finally the correlations between "u" and " γ " is studied. In the alignment framework, rotations are defined with respect to the center of an "alignable"; in a real Rod, a rotation is caused

by a relative displacement of the module mounting pins, and therefore the pivoting point is on average expected to be the middle of the two pins, as shown in Figure 10.23. For this reason one expects to find in the data a certain degree of anti-correlation between " γ " and " u " (defined with respect to the module center), and a scaling factor between the two quantities comparable between the distance from the center of the module and the pivoting point, that is 134 mm, as illustrated in Figure 10.23. The results are displayed in Figure 10.24; the measured correlation is -0.55, and the average scaling factor corresponds to a lever arm of 70 mm.

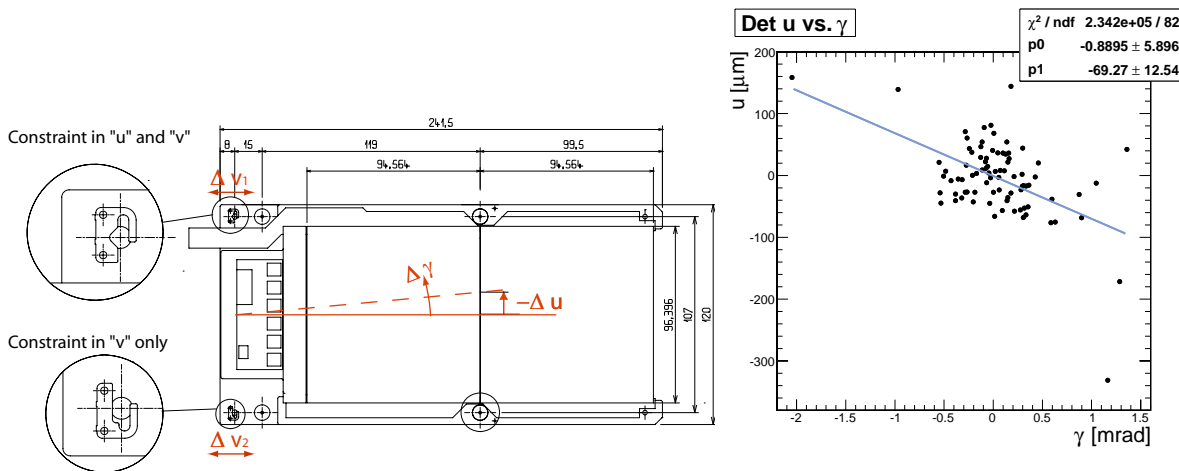


FIGURE 10.23: Mounting of a TOB module.

FIGURE 10.24: Correlation between measurements of " γ " and " u ".

10.6.3 Comparison with CMM Measurements

For a comparison with the expected module positions from the CMM measurements, only the 6 single-sided Rods are used. As shown in Figure 10.25, the alignment parameters have a significant correlation with the CMM measurements for the rotations (measured correlation of 0.6), but not in the translations (measured correlation of 0.1).

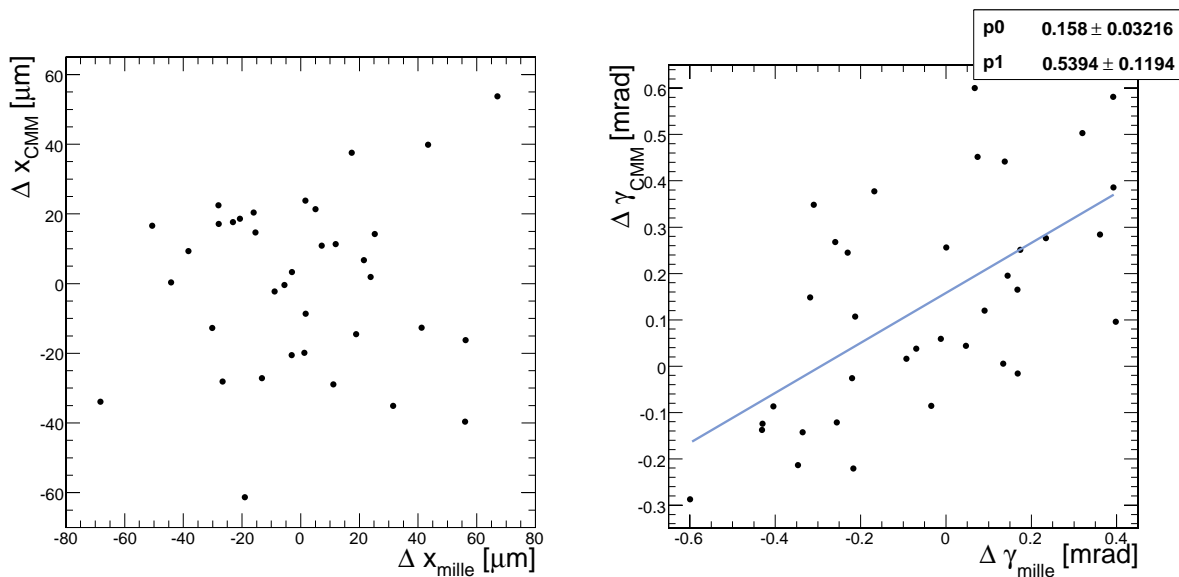


FIGURE 10.25: Correlation of the CMM measurements with the alignment parameters obtained from cosmic muon tracking. For the Translations (left) no significant correlation is observed (0.1), whereas the rotations are correlated with a factor of 0.6.

The analysis could be repeated in future on a larger sample of Rods now integrated in the Tracker. This study however suggests, that track-based alignment can be performed successfully without requiring corrections of the initial positions derived from the CMM measurements³.

10.6.4 Rod Geometry versus Operating Temperature

The Rod mechanics is mostly made of carbon fiber, that has a negligible coefficient of thermal expansion (CTE), however other Rod components (notably cooling pipes, made of Cu-Ni alloy, and the module supports, made of aluminum) have a significant CTE , and therefore a certain mechanical stress is induced on the Rod assembly when it is operated at -10°C . The Rod design has been optimized to minimize the risk, that such mechanical stress causes geometrical deformations to the structure. In order to check for such effects the alignment parameters from the data collected 20°C and at -10°C and compared.

The results of the parameters "u" and " γ " are shown in Figure 10.26 for all Rods, the results for "v" are shown in Figure 10.27 for DS Rods only.

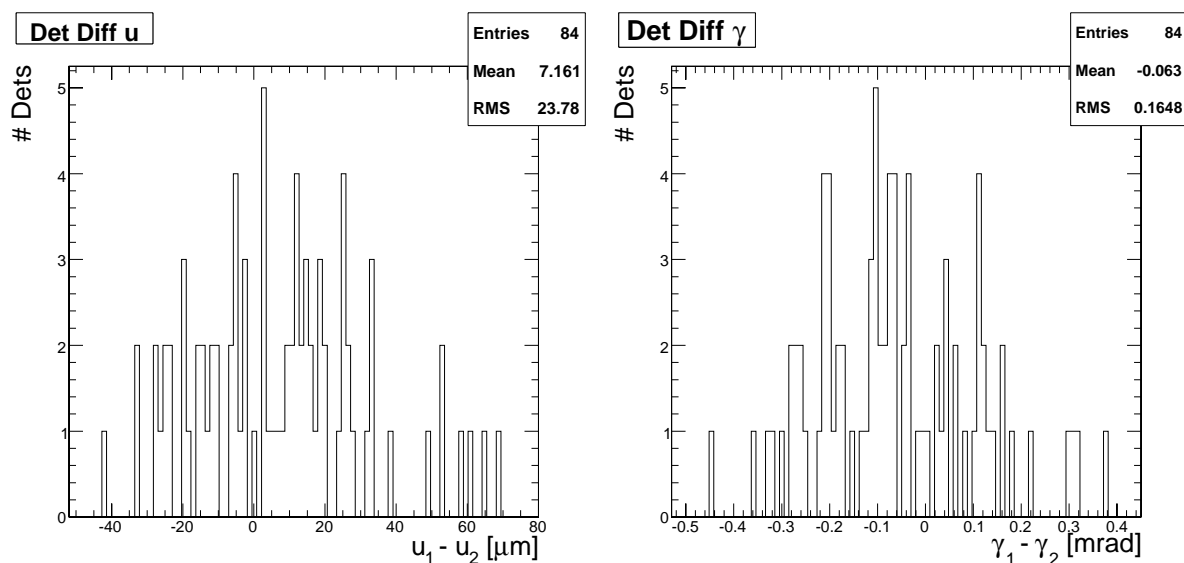


FIGURE 10.26: Comparison of the alignment parameters obtained from data collected in warm and cold for "u" and " γ ". The difference is compatible with the estimated measurement precision.

No significant displacement is observed: the measured differences are compatible with the estimated measurement precision. The Cosmic Rack mechanical structure is made of aluminum; therefore a contraction is expected when the temperature is lowered from 20°C to -10°C . The nominal distance between two Rods is 92 mm (see Figure 10.28); such distance is expected to shrink by about $65\ \mu\text{m}$ at -10°C (using the CTE of $2.3 \cdot 10^{-6}\text{K}^{-1}$), which is compatible with the measured difference of $-88\ \mu\text{m}$ as shown in Figure 10.29.

³The positions of Rods in the TOB mechanics are expected to be more precise than the positions of Rods in the Cosmic Rack mechanics

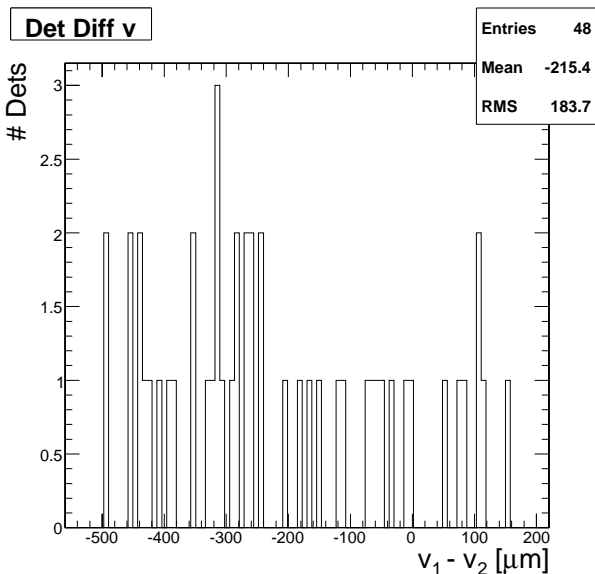


FIGURE 10.27: Comparison of the alignment parameters obtained from data collected in warm and cold for "v" (only for DS-Rods).

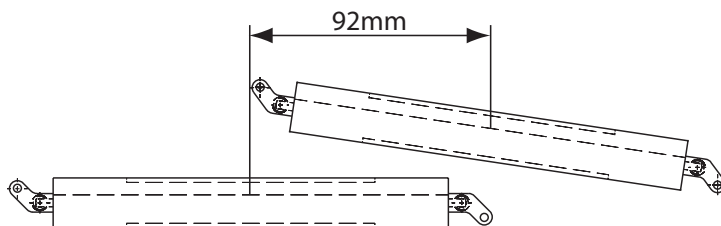


FIGURE 10.28: Placement of two Rods within a layer; the nominal distance between the centers of the active areas of the Rods is 92 mm.

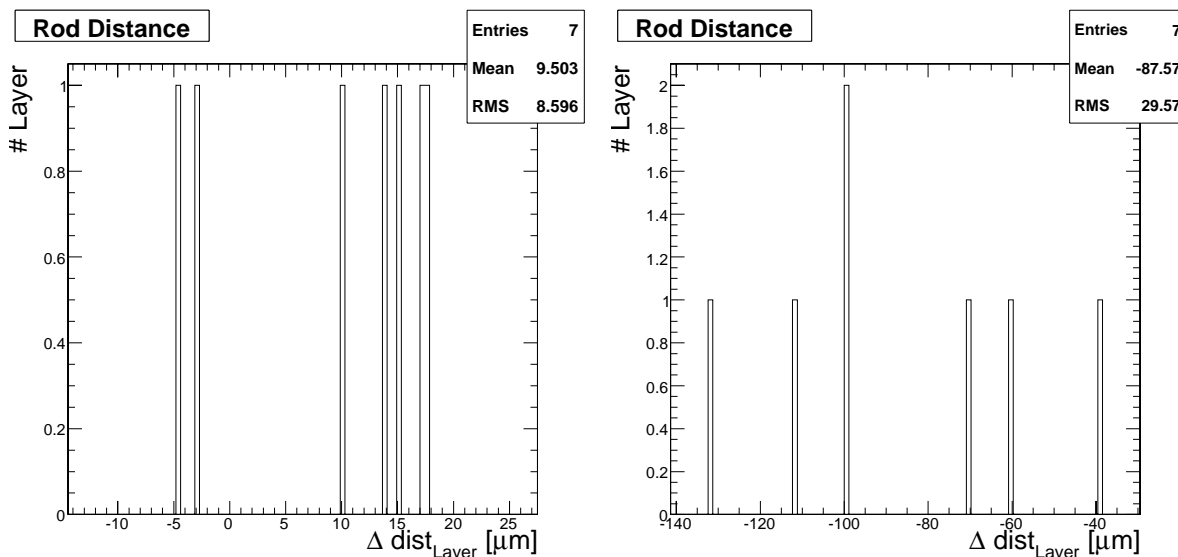


FIGURE 10.29: Comparison of the distance between the Rods in a layer: difference between two data sets recorded at room temperature (left), and difference between data taken at room temperature and in cold (-10°C) (right). The observed contraction of 88 μm is perfectly compatible with the expectation (65 μm).

10.7 Summary

The detectors in the Cosmic Rack have been successfully aligned using cosmic muons and the Millepede algorithm. The precision at the module level is better than $20 \mu m$ in "u" (the coordinate across the strips) and about $100 \mu m$ in "v" (the direction along the strips). Rotations of the modules around the axis normal to the sensor plane " γ " have been determined with a precision of about $0.2 mrad$.

The alignment has been validated comparing independent data sets and it has been shown that the residuals of the modules are centered close to zero.

The intrinsic precision of the Rods, i.e. the displacement of the modules with respect to their nominal positions in the Rod frame has been measured. Single-sided Rods have a precision in "u" better than $40 \mu m$ and $0.3 mrad$ in " γ ".

The corrections for double sided modules are larger (approximately $75 \mu m$ in "u" and $0.6 mrad$ in " γ "). However the analysis of the results has shown, that the current implementation of the alignment framework, which treats a pair of r-phi and stereo detectors as a single object is not adequate to achieve the ultimate alignment precision for DS modules. The framework needs to be extended to allow for independent alignment of the two detectors of a pair.

Chapter 11

Conclusions

The work presented in this thesis is focused on the qualification of the performance of the CMS Tracker Outer Barrel (TOB), that has been studied with a large scale test setup, the Cosmic Rack, using tracks from cosmic particles as physics signals. Experience in operating and commissioning the Tracker has been gained, during several months of operation, during which more than two million physics events were recorded.

The Cosmic Rack was successfully used to study the noise performance, perform precise measurements of the detector response, test the reconstruction software and qualify the geometrical precision of the TOB subassemblies.

11.1 Results

In a comprehensive noise analysis, different configurations for the TOB grounding were studied, to define and validate the final scheme. The analysis of the noise also revealed a large common mode noise introduced by the power supplies. Based on these results, the design of the Tracker power modules was reviewed and modified to remove the effect. A method for the calibration of the readout chain with the APV synchronisation pulse was implemented, to derive absolute measurements of the noise in "Equivalent Noise Charge". The measured values ($\approx 1400 e^-$ in peak mode and $\approx 2100 e^-$ in deconvolution mode) are in good agreement with the expectations. A study was dedicated to the measurement of the correlation between the noise fluctuations of neighboring strips. Significant values of about -25% in peak mode and -16% in deconvolution mode were found; such values are compatible with the expectations from capacitive couplings of neighboring strips.

The track reconstruction algorithms available in the CMS software framework were successfully adapted to the geometry of the Cosmic Rack. The measurement of the deposited charge corrected for the travelled path length gave Most Probable Values for the signal-to-noise ratio of 30 in peak mode and 20 in deconvolution mode. The dependence of the cluster size on the track angle was studied, to disentangle contributions from charge sharing and capacitive coupling. These measurements have shown, that in the absence of a magnetic field charge sharing is only relevant for inclined tracks and negligible for tracks perpendicular to the sensor surface. The coupling of the signal to the neighboring strips shows a strong dependence on the sampling time, and was determined to be 12% in deconvolution mode and 4% in peak mode at the optimal sampling point. A SPICE simulation was set up describing the silicon sensors as an R-C network and including a detailed simulation of the readout electronics to investigate the origin of the coupling. The values derived, and their dependence on the sampling point were compatible with the experimental measurements for peak mode and deconvolution mode.

The detectors of the Cosmic Rack were successfully aligned using tracks from cosmic muons and the Millepede algorithm. The precision at the module level is better than $20 \mu m$ in "u" (the coordinate across the strips) and about $100 \mu m$ in "v" (the coordinate along the strips). Rota-

tions of the modules around the axis normal to the sensor plane " γ " have been determined with a precision of about 0.2 mrad . The alignment results were validated by comparing independent data sets and by studying the hit-to-track residuals. The high precision achieved allowed for the first time to derive a measurement of the geometrical precision of the TOB subassemblies "Rods": the average displacement of the modules with respect to their nominal positions in the Rod frame was measured to be smaller than $40 \mu\text{m}$ in "u" and smaller than 0.3 mrad in " γ ". The corrections for Double Sided (DS) modules are larger (approximately $75 \mu\text{m}$ in "u" and 0.6 mrad in " γ "). However the analysis of the results showed that the current implementation of the alignment framework, which treats a pair of r-phi and stereo detectors as a single object, is not adequate to achieve the ultimate alignment precision for DS modules; the framework needs to be upgraded to allow for independent alignment of the two detectors of a pair. The comparison of the measurements carried out at room temperature (20°C) and at the projected Tracker operating temperature (-10°C) did not reveal any change in the Rod geometry. This study yielded the first experimental data on the geometrical precision and stability of the assembled rods, and provided important feedback for the development of the alignment software in CMS.

The studies carried out confirmed that the Outer Barrel meets the performance required to be operated in CMS.

11.2 Outlook and open Issues

The study of the detector response has shown a significant amount of capacitive coupling between neighboring strips. The method currently used to estimate the particle impact point and its precision, could be re-optimized to take such effect into account, possibly improving the tracking precision.

An upgrade of the CMS alignment framework has been planned, to address the problems related to the alignment of pairs of r-phi and stereo detectors, in order to achieve the ultimate precision in the determination of the detector positions. For a final qualification of the geometrical precision of DS-Rods, the alignment studies have to be repeated, making use of the updated framework.

Appendix A

Charge Sensitive Amplifier

A.1 Charge Amplification

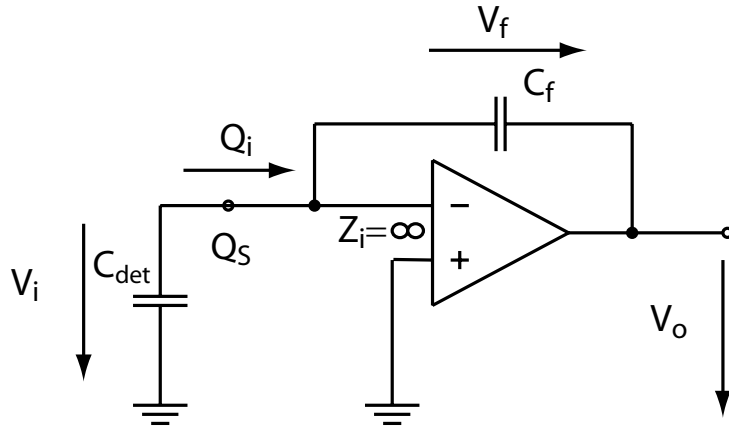


FIGURE A.1: Schematics of an ideal charge sensitive amplifier. C_{det} is the detector capacitance, C_f the feedback capacitance, Q_s the generated charge and Q_i the fraction of the charge flowing to the amplifier [73].

A charge sensitive amplifier is a voltage gain inverting amplifier with capacitive feedback. It acts as an integrator with low input impedance. In the block diagram of Figure A.1 the schematics of a charge sensitive amplifier are sketched; the detector is represented by a capacitance C_{det} .

With A being the open loop voltage gain of the amplifier, it can be written:

$$V_o = -A V_i \quad (\text{A.1})$$

$$V_i = V_o + V_f = V_o + Q_f/C_f \quad (\text{A.2})$$

The amplifier has ideally infinite input impedance ($Z_i = \infty$), therefore no current is flowing into the amplifier and $Q_i = Q_f$. It follows from the above equations:

$$V_i \cdot (A + 1) = Q_i/C_f \quad (\text{A.3})$$

For an input signal, the charge sensitive amplifier appears as an effective capacitance C_{in} , that is given by:

$$C_{in} = \frac{Q_i}{V_i} = (A + 1) \cdot C_f \quad (\text{A.4})$$

From the charge deposited on the detector Q_s , most is flowing to the amplifier, while a part remains on the detector capacitance C_{det} . The fraction of charge that is flowing to the amplifier Q_i is given by:

$$V_i = \frac{Q_s}{C_{in} + C_{det}} = \frac{Q_i}{C_{in}} \quad (\text{A.5})$$

$$Q_i = Q_s \frac{C_{in}}{C_{in} + C_{det}} \quad (\text{A.6})$$

Finally it follows for the output voltage:

$$V_o = -AV_i = -A \frac{Q_i}{C_{in}} \quad (\text{A.7})$$

$$V_o = -Q_s \frac{A}{C_f(A+1) + C_{det}} \quad (\text{A.8})$$

And the charge amplification A_Q is given by:

$$A_Q = V_o/Q_s = -\frac{A}{C_f(A+1) + C_{det}} \quad (\text{A.9})$$

In general the voltage gain of the amplifier is large ($A \gg 1$) and $C_f \cdot A \gg C_{det}$, therefore the equations shown above can be simplified to:

$$C_{in} = A \cdot C_f \quad (\text{A.10})$$

$$V_o = -\frac{Q_s}{C_f} \quad (\text{A.11})$$

$$A_Q = -\frac{1}{C_f} \quad (\text{A.12})$$

A.2 Equivalent Noise Charge

It is a common practice to summarize all the noise sources of a circuit, and represent them by a noise voltage v_{ni} appearing on the input of the amplifier. Even if the origin of the noise is inside the amplifier this is possible due to feedback. The schematics are illustrated in Figure A.2 where in addition to Figure.A.1 also the input capacitance of the amplifier C_i is taken into account.

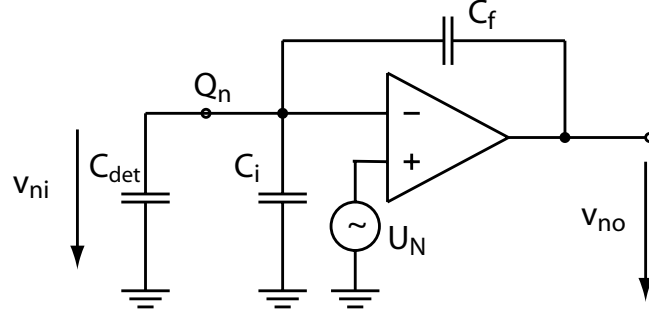


FIGURE A.2: Schematics of a charge sensitive amplifier, with a noise source U_N at its input. C_i is the "cold" input capacitance of the amplifier, i.e. without considering the feedback.

Assuming that - due to noise - a voltage v_{no} is present on the output, the relation to the corresponding noise voltage on the input v_{ni} is given by (voltage divider):

$$v_{no} = v_{ni} \frac{(\omega C_{det} + \omega C_i)^{-1} + (\omega C_f)^{-1}}{(\omega C_{det} + \omega C_i)^{-1}} \quad (\text{A.13})$$

$$v_{no} = v_{ni} \cdot \left(1 + \frac{C_i + C_{det}}{C_f} \right) \quad (\text{A.14})$$

The equivalent noise charge Q_n , is defined as the charge that - if applied at the input (of a noise-free) system - gives the same output voltage, as when the noise voltage v_{ni} is present. The ratio between an input charge, and the output voltage is given by the charge amplification A_Q (eqn.A.9). With eqn.A.12 it follows for the equivalent noise charge Q_n :

$$Q_n = \frac{v_{no}}{A_Q} = -v_{no} \cdot C_f \quad (\text{A.15})$$

$$Q_n = -v_{ni} \cdot (C_f + C_i + C_{det}) \quad (\text{A.16})$$

$$\tilde{Q}_n = -v_{ni} \cdot C_i + C_{det} = Q_n \cdot \frac{C_i + C_{det}}{C_f + C_i + C_{det}} \quad (\text{A.17})$$

To stress the dependence on the input capacitance eqn.A.17 is often written in the form:

$$Q_N^{RMS} = a + C_{det} \cdot b \quad (\text{A.18})$$

Where $a = v_{ni}^{RMS} \cdot (C_f + C_i)$ and $b = v_{ni}^{RMS}$.

Appendix B

Noise in Deconvolution Mode

The noise of the front-end electronics in deconvolution mode is derived in detail in [97]. Here a summary is given. The signal in deconvolution is the weighted sum of three samples v_i , that are taken from the output of CR-RC pulse shaper at a fixed sampling interval Δt . The signal in deconvolution mode at the time n s_n is given by:

$$s_n = \sum_{i=1}^3 w_i v_{n-i+1} \quad (\text{B.1})$$

$$s_n = w_1 v_n + w_2 v_{n-1} + w_3 v_{n-2} \quad (\text{B.2})$$

where w_i are the weights.

Assuming that only noise is present at the output of the CR-RC pulse shaper the expectation value of v_i and s_n are 0:

$$\langle s_n \rangle = \langle v_i \rangle = 0 \quad (\text{B.3})$$

The the variance of s_n is thus given by:

$$\sigma^2(s_n) = \left\langle \sum_{i,j=1}^3 w_i v_{n-i+1} \cdot w_j v_{n-j+1} \right\rangle \quad (\text{B.4})$$

The noise signal v_i can be split into two groups: contributions from parallel noise $\sigma_p^2(s_n)$ and serial noise $\sigma_s^2(s_n)$:

$$\sigma_{tot}^2 = \sigma_p^2 + \sigma_s^2 \quad (\text{B.5})$$

As serial and parallel noise are uncorrelated they can be treated separately and for each of them it can be written:

$$\langle s_n^2 \rangle = w_1^2 \langle v_n^2 \rangle + w_2^2 \langle v_{n-1}^2 \rangle + w_3^2 \langle v_{n-2}^2 \rangle \quad (\text{B.6})$$

$$w_1 w_2 \langle v_n v_{n-1} \rangle + w_2 w_3 \langle v_{n-1} v_{n-2} \rangle \quad (\text{B.7})$$

$$+ w_1 w_3 \langle v_n v_{n-2} \rangle \quad (\text{B.8})$$

Or equivalently:

$$\sigma^2(s) = (w_1^2 + w_2^2 + w_3^2) \sigma^2 + 2w_1 w_2 C(\Delta t) \quad (\text{B.9})$$

$$+ 2w_2 w_3 C(\Delta t) + 2w_1 w_3 C(2\Delta t) \quad (\text{B.10})$$

where $C(\Delta T)$ is the average correlation between a measurement at time t and another one at $t + \Delta T$.

For a CR-RC pulse shaper with a time constant τ the correlations for parallel noise $C_p(y)$ and for the serial noise $C_s(y)$ are given by:

$$C_p(y) = \sigma_p^2 (1 + y) e^{-y} \quad (\text{B.11})$$

$$C_s(y) = \sigma_s^2 (1 - y) e^{-y} \quad (\text{B.12})$$

with $y = \Delta T/\tau$.

The weights of the deconvolution algorithm as a function of $x = \Delta t/\tau$ are:

$$w_1 = 1/x \cdot e^{x-1} \quad (\text{B.13})$$

$$w_2 = -2/x \cdot e^{-1} \quad (\text{B.14})$$

$$w_3 = 1/x \cdot e^{-x-1} \quad (\text{B.15})$$

The contributions from serial and parallel noise after deconvolution (eqn.B.10) can be expressed by:

$$\sigma_p^2(s) = (\sigma_p^2 \cdot e^{-2}/x^2) [e^{2x} - 4x - e^{-2x}] \quad (\text{B.16})$$

$$\sigma_s^2(s) = (\sigma_s^2 \cdot e^{-2}/x^2) [e^{2x} + 4x - e^{-2x}] \quad (\text{B.17})$$

For the APV25 with $\Delta t = 25 \text{ ns}$, $\tau = 50 \text{ ns}$ and $x = 1/2$. One obtains for the noise after deconvolution:

$$\sigma_p(s) = \sigma_p \cdot 0.436 \quad (\text{B.18})$$

$$\sigma_s(s) = \sigma_s \cdot 1.534 \quad (\text{B.19})$$

In deconvolution mode the parallel noise decreases, while the serial noise increases. This can be qualitatively understood, as the effective shaping time after deconvolution is shorter, and parallel noise is $\propto \sqrt{\tau}$, whereas serial noise ($\propto 1/\sqrt{\tau}$) decreases with increasing shaping time.

The analysis presented is however only strictly complete in the absence of 1/f noise, which is fulfilled in good approximation for the APV25.

Bibliography

- [1] Particle Data Group Lawrence Berkeley National Laboratories. The Particle Adventure. <http://particleadventure.org/>. Fundamentals of Particles and more.
- [2] Peter W. Higgs. BROKEN SYMMETRIES AND THE MASSES OF GAUGE BOSONS. *Phys. Rev. Lett.*, 13:508–509, 1964.
- [3] CERN. Overall view of the LHC experiments. <http://livefromcern.web.cern.ch/livefromcern/antimatter/history/historypictures/LHC-drawing-half.jpg>.
- [4] LHC Design Report Volume I. <http://ab-div.web.cern.ch/ab-div/Publications/LHC-DesignReport.html>.
- [5] D. Denegri. Standard model physics at the LHC. Presented at the ECFA Large Hadron Collider Workshop, Aachen, Germany, Oct 4-9, 1990.
- [6] ATLAS: Detector and physics performance technical design report. Volume 1. CERN-LHCC-99-14.
- [7] CMS, Detector Performance and Software. CERN-LHCC-2006-001.
- [8] G. L. Bayatian et al. CMS technical design report, volume II: Physics performance. *J. Phys.*, G34:995–1579, 2007.
- [9] (ed.) Carminati, F. et al. ALICE: Physics performance report, volume I. *J. Phys.*, G30:1517–1763, 2004.
- [10] S. Amato et al. LHCb technical proposal. CERN-LHCC-98-04.
- [11] V. Berardi et al. TOTEM: Technical design report. Total cross section, elastic scattering and diffraction dissociation at the Large Hadron Collider at CERN. CERN-LHCC-2004-002.
- [12] William J. Marciano. Precision electroweak measurements and the Higgs mass. 2004.
- [13] CERN. CMS Outreach. <http://cmsinfo.cern.ch/outreach/>.
- [14] Dave Barney. Introduction to CMS for CERN guides. <http://cmsinfo.cern.ch/outreach/CMSdocuments/ForGuides/CMSforCERNguides.ppt>.
- [15] Alexander Oh. The CMS Data Acquisition and Trigger System. <http://berners-lee.physik.uni-dortmund.de/~behrendt/dpg2005/oh.ppt>.
- [16] T. Muller. The CMS tracker and its performance. *Nucl. Instrum. Meth.*, A408:119–127, 1998.
- [17] CMS Collaboration. Compact Muon Solenoid Experiment. <http://cmsinfo.cern.ch/outreach/CMSdocuments/CMSbrochure/CMS-Brochure03.pdf>.

- [18] M. Diemoz. The electromagnetic calorimeter of the CMS experiment. *Nucl. Phys. Proc. Suppl.*, 125:100–106, 2003.
- [19] CMS: The hadron calorimeter technical design report. CERN-LHCC-97-31.
- [20] CMS, the Compact Muon Solenoid. Muon technical design report. CERN-LHCC-97-32.
- [21] W. R. Leo. *Techniques for Nuclear and Particle Physics Experiments: A How to Approach*. Berlin, Germany: Springer (1994) 368 p.
- [22] G. Lutz. *Semiconductor Radiation Detectors*. Springer 1999, ISBN 3-540-64859-3.
- [23] M. Krammer. Halbleiter Detektoren, Vorlesungs Unterlagen. <http://wwwhephy.oeaw.ac.at/p3w/halbleiter/V0skriptum/V0-4-Halbleiterdetektoren.pdf>.
- [24] R. Bates. Semiconductor detectors. http://ppewww.physics.gla.ac.uk/~batesr/post_grad_lectures/PG_lectures_Semiconductor_detectors.pdf.
- [25] NSM. Semiconductors on NSM. <http://www.ioffe.rssi.ru/SVA/NSM/Semicond/Si/bandstr.htm>.
- [26] Alexander Furgeri. Quality assurance and irradiation studies on CMS silicon strip sensors. IEKP-KA-2005-1.
- [27] M. Stoye. *Calibration and Alignment of the CMS Silicon Tracking Detector*. PhD thesis, Desy Hamburg, 2006.
- [28] M. Friedl. *The CMS silicon strip tracker and its electronic readout*. PhD thesis, Vienna University of Technology, 2001.
- [29] W. Shockley. Currents to conductors induced by a moving point charge. *J. Appl. Phys.*, 9:635, 1938.
- [30] Simon Ramo. Currents induced by electron motion. *Proc. Ire*, 27:584–585, 1939.
- [31] H. Spieler. Introduction to radiation detectors and electronics, ix.1 semiconductor detectors ii the signal. http://www-physics.lbl.gov/~spieler/physics_198_notes_1999/PDF/IX-1-Signal.pdf.
- [32] G. Cavalleri, E. Gatti, G. Fabri, and V. Svelto. Extension of Ramo’s theorem as applied to induced charge in semiconductor detectors. *Nuclear Instruments and Methods*, 92:137–+, 1971.
- [33] I. V. Kotov. Currents Induced by Charges Moving in Semiconductor. *ArXiv Physics e-prints*, November 2003.
- [34] Ansoft. Maxwell SV finite element Analysis. <http://www.ansoft.com/maxwellsv/>.
- [35] V. Eremin, W. Chen, and Z. Li. Analytical solutions of minimum ionization particle induced current shapes of silicon detectors and simulation of charge collection properties. In *Nuclear Science Symposium and Medical Imaging Conference, 1993., 1993 IEEE Conference Record.*, pages 292–296, October/November 1993.
- [36] T. Bowcock. Notes on Semiconductor Devices for Particle Physics. http://hep.ph.liv.ac.uk/~tjvb/html/teaching_.html.
- [37] D. Kotlinski. The CMS pixel detector. Prepared for 8th International Conference on Advanced Technology and Particle Physics (ICATPP 2003): Astroparticle, Particle, Space Physics, Detectors and Medical Physics Applications, Como, Italy, 6-10 Oct 2003.

- [38] Derek Tournear. The silicon tracker for the GLAST large area space telescope. *Nucl. Instrum. Meth.*, A473:61–66, 2001.
- [39] D. Abbaneo. Layout and performance of the CMS silicon strip tracker. *Nucl. Instrum. Meth.*, A518:331–335, 2004.
- [40] HEPHY. Picture gallery of the CMS tracker. http://wwwhephy.oeaw.ac.at/p3w/cms_tracker/gallery/index.html.
- [41] J. L. Agram et al. The silicon sensors for the Compact Muon Solenoid tracker: Design and qualification procedure. *Nucl. Instrum. Meth.*, A517:77–93, 2004.
- [42] M. Krammer. Design, production and quality of the sensors for the silicon strip tracker of cms. Prepared for 9th ICATPP Conference on Astroparticle, Particle, Space Physics, Detectors and Medical Physics Applications, Villa Erba, Como, Italy, 17-21 Oct 2005.
- [43] S. Braibant et al. Investigation of design parameters for radiation hard silicon microstrip detectors. *Nucl. Instrum. Meth.*, A485:343–361, 2002.
- [44] O. Pooth. The CMS silicon tracker. *Nucl. Instrum. Meth.*, A569:21–24, 2006.
- [45] N. Demaria et al. New results on silicon microstrip detectors of CMS tracker. *Nucl. Instrum. Meth.*, A447:142–150, 2000.
- [46] S. Braibant et al. Investigation of design parameters and choice of substrate resistivity and crystal orientation for the CMS silicon microstrip detector. CMS Note 011/2000.
- [47] L. Feld. The CMS Silicon Tracker. http://web.physik.rwth-aachen.de/~feld/talks/CMS_Tracker_GSI.pdf.
- [48] R. L. Gluckstern. Uncertainties in track momentum and direction, due to multiple scattering and measurement errors. *Nucl. Instrum. Meth.*, 24:381–389, 1963.
- [49] M. Weber. The CMS tracker. *Nucl. Phys. Proc. Suppl.*, 142:430–433, 2005.
- [50] W. Adam, B. Mangano, T. Speer, and T. Todorov. Track reconstruction in the CMS tracker. CERN-CMS-NOTE-2006-041.
- [51] CMS, tracker technical design report. CERN-LHCC-98-06.
- [52] G. Hall. CMS Microstrip Tracker Electronics. http://cmstrackercontrol.web.cern.ch/CMSTrackerControl/documents/Geoff/Readout_summary.pdf.
- [53] M. Campbell et al. An introduction to deep submicron CMOS for vertex applications. *Nucl. Instrum. Meth.*, A473:140–145, 2001.
- [54] I2C Bus. <http://www.i2c-bus.org/>.
- [55] L. L. Jones et al. The APV25 deep submicron readout chip for CMS detectors. Prepared for 5th Workshop on Electronics for the LHC Experiments (LEB 99), Snowmass, Colorado, 20-24 Sep 1999.
- [56] G. Hall. Radiation hard fast electronics for LHC experiments. <http://indico.cern.ch/materialDisplay.py?materialId=6&confId=a042939>. Academic Training.
- [57] M. J. French et al. Design and results from the APV25, a deep sub-micron CMOS front-end chip for the CMS tracker. *Nucl. Instrum. Meth.*, A466:359–365, 2001.

- [58] A. Neviani. Apv25s0 - calibration circuit. http://www.e18.physik.tu-muenchen.de/research/compass/silicon/apv25/protected/APV25_Calibration_Circuit.pdf. Version 1.1.
- [59] J. Troska et al. Optical readout and control systems for the CMS tracker. *IEEE Trans. Nucl. Sci.*, 50:1067–1072, 2003.
- [60] Stefanos Dris. Performance of the CMS tracker optical links and future upgrade using bandwidth efficient digital modulation. CERN-THESIS-2007-015.
- [61] J. Troska. Optical Readout and Control Systems for the CMS Tracker. http://cms-tk-opto.web.cern.ch/cms-tk-opto/tk/presentations/nss2002_poster.pdf.
- [62] M. Friedl. Analog optohybrids for the readout of the CMS silicon tracker. *Nucl. Instrum. Meth.*, A518:515–518, 2004.
- [63] F. Drouhin et al. The CERN CMS silicon strip tracker control system. CMS-CR-2004-032.
- [64] Network Introduction and Planning Guide, Reference Manual. GA27-3677-05.
- [65] B. Gannon. Compact Muon Solenoid (CMS) Front End Driver (FED) Front-End FPGA. <http://www.m76.org/fed/fe.pdf>. Technical Description Version 1.3.
- [66] P. Sphicas. CMS: The TriDAS project. Technical design report, Vol. 2: Data acquisition and high-level trigger. CERN-LHCC-2002-026.
- [67] M. Eppard A.-S. Giolo-Nicollerat D. Abbaneo, A. Dierlamm. Validation of simulation with 2004 beam test data using the TOB Cosmic Rack. CMS AN 2005/045.
- [68] M. Weber. Der CMS Tracker: Tests mit dem "TOB Cosmic Rack". *High Energy Physics Seminar*, 2004.
- [69] E. Antilla. Cosmic rack mechanics. http://cms-ul-tmb.web.cern.ch/CMS_TMB/personal/anttila/crack/drawings.htm.
- [70] E. Antilla. "DESIGN AND CONSTRUCTION OF THE MECHANICS OF A COSMIC RAY TRACKING DEVICE". Master's thesis, TAMPERE UNIVERSITY OF TECHNOLOGY, 2005.
- [71] C. Bloch. Commissioning of the CMS tracker outer barrel. Prepared for 9th ICATPP Conference on Astroparticle, Particle, Space Physics, Detectors and Medical Physics Applications, Villa Erba, Como, Italy, 17-21 Oct 2005.
- [72] W.-M. Yao, C. Amsler, D. Asner, R.M. Barnett, J. Beringer, P.R. Burchat, C.D. Carone, C. Caso, O. Dahl, G. D'Ambrosio, A. DeGouvea, M. Doser, S. Eidelman, J.L. Feng, T. Gherghetta, M. Goodman, C. Grab, D.E. Groom, A. Gurtu, K. Hagiwara, K.G. Hayes, J.J. Hernández-Rey, K. Hikasa, H. Jawahery, C. Kolda, Kwon Y., M.L. Mangano, A.V. Manohar, A. Masoni, R. Miquel, K. Mönig, H. Murayama, K. Nakamura, S. Navas, K.A. Olive, L. Pape, C. Patrignani, A. Piepke, G. Punzi, G. Raffelt, J.G. Smith, M. Tanabashi, J. Terning, N.A. Törnqvist, T.G. Trippe, P. Vogel, T. Watari, C.G. Wohl, R.L. Workman, P.A. Zyla, B. Armstrong, G. Harper, V.S. Lugovsky, P. Schaffner, M. Artuso, K.S. Babu, H.R. Band, E. Barberio, M. Battaglia, H. Bichsel, O. Biebel, P. Bloch, E. Blucher, R.N. Cahn, D. Casper, A. Cattai, A. Ceccucci, D. Chakraborty, R.S. Chivukula, G. Cowan, T. Damour, T. DeGrand, K. Desler, M.A. Dobbs, M. Drees, A. Edwards, D.A. Edwards, V.D. Elvira, J. Erler, V.V. Ezhela, W. Fetscher, B.D. Fields, B. Foster, D. Froidevaux, T.K. Gaisser, L. Garren, H.-J. Gerber, G. Gerbier, L. Gibbons, F.J. Gilman, G.F. Giudice,

- A.V. Gritsan, M. Grünewald, H.E. Haber, C. Hagmann, I. Hinchliffe, A. Höcker, P. Igo-Kemenes, J.D. Jackson, K.F. Johnson, D. Karlen, B. Kayser, D. Kirkby, S.R. Klein, K. Kleinknecht, I.G. Knowles, R.V. Kowalewski, P. Kreitz, B. Krusche, Yu.V. Kuyanov, O. Lahav, P. Langacker, A. Liddle, Z. Ligeti, T.M. Liss, L. Littenberg, L. Liu, K.S. Lugovsky, S.B. Lugovsky, T. Mannel, D.M. Manley, W.J. Marciano, A.D. Martin, D. Milstead, M. Narain, P. Nason, Y. Nir, J.A. Peacock, S.A. Prell, A. Quadt, S. Raby, B.N. Ratcliff, E.A. Razuvaev, B. Renk, P. Richardson, S. Roesler, G. Rolandi, M.T. Ronan, L.J. Rosenberg, C.T. Sachrajda, S. Sarkar, M. Schmitt, O. Schneider, D. Scott, T. Sjöstrand, G.F. Smoot, P. Sokolsky, S. Spanier, H. Spieler, A. Stahl, T. Stanev, R.E. Streitmatter, T. Sumiyoshi, N.P. Tkachenko, G.H. Trilling, G. Valencia, K. van Bibber, M.G. Vincter, D.R. Ward, B.R. Webber, J.D. Wells, M. Whalley, L. Wolfenstein, J. Womersley, C.L. Woody, A. Yamamoto, O.V. Zenin, J. Zhang, and R.-Y. Zhu. Review of Particle Physics. *Journal of Physics G*, 33:1+, 2006.
- [73] H. Spieler. Pulse processing and analysis. http://www-physics.lbl.gov/~spieler/NSS_short-course/NSS02_Pulse_Processing.pdf.
- [74] A. Dierlamm. *Untersuchungen zur Strahlenharte von Siliziumsensoren*. PhD thesis, Universität Karlsruhe, 2003.
- [75] Karl Gill Robert Grabit Raquel Marquis Etam Noah Jan Troska Stefanos Dris, Markus Axer and Francois Vasey. Predicting the In-System Performances of the CMS Tracker Analog Readout Optical Links. CERN-CMS-NOTE-2006-008.
- [76] S. Paoletti E. Focardi. Comparison of the Electrical Performances of the Low Impedance Cable and the Copper Multi Service Cable for the CMS SST Tracker. CMS IN-2004/057.
- [77] M. Johnson. Oscillations in the CAEN tracker power supply, May 2006. Private communication.
- [78] G. Magazzu. CAEN power supply oscillations, May 2006. Private communication.
- [79] G. Lutz. CORRELATED NOISE IN SILICON STRIP DETECTOR READOUT. *Nucl. Instrum. Meth.*, A309:545–551, 1991.
- [80] Richard Brauer. CMS Tracker offline analysis software. <http://brauer.web.cern.ch/brauer/Ana/index.html>.
- [81] T. K. Gaisser. *Cosmic Rays and Particle Physics*. Cambridge University Press, 1991.
- [82] S. Kliewer. The Compact Cosmic Ray Telescope aboard the Kuiper Airborne Observatory. <http://www.lbl.gov/abc/cosmic/SKliewer/Index.htm>.
- [83] M. Boezio et al. Measurement of the flux of atmospheric muons with the CAPRICE94 apparatus. *Phys. Rev.*, D62:032007, 2000.
- [84] Giovanni Fiorentini, Vadim A. Naumov, and Francesco L. Villante. Atmospheric neutrino flux supported by recent muon experiments. *Phys. Lett.*, B510:173–188, 2001.
- [85] Anne Sylvie Giolo-Nicollerat. Spectrum of cosmic muons at sea-level. Private communication.
- [86] Thomas Hebbeker and Charles Timmermans. A compilation of high energy atmospheric muon data at sea level. *Astropart. Phys.*, 18:107–127, 2002.
- [87] J. Kremer et al. Measurements of ground-level muons at two geomagnetic locations. *Phys. Rev. Lett.*, 83:4241–4244, 1999.

- [88] P. Lecultre. Le petite telescope. Private communication.
- [89] M. Case. CMS Detector Description Home Page. <http://cmsdoc.cern.ch/cms/software/ddd/www/index.html>.
- [90] M. Case. Geant4: A toolkit for the simulation of the passage of particles thorough matter. <http://geant4.web.cern.ch/geant4/>.
- [91] CMS Collaboration. Cmssw. <http://cmslrx.fnal.gov/lxr/source>.
- [92] V. Brigljevic et al. Using XDAQ in application scenarios of the CMS experiment. 2003.
- [93] T. Speer et al. Track reconstruction in the CMS tracker. *Nucl. Instrum. Meth.*, A559:143–147, 2006.
- [94] F. Hartmann. The CMS tracker construction issues for large detector systems with industry involvement. *Nucl. Instrum. Meth.*, A549:171–177, 2005.
- [95] S.M. Sze. *Physics of Semiconductor Devices*. John Wiley and Sons, 1981.
- [96] G. Marseguerra. The APV25 readout chip. http://sirad.pd.infn.it/CMS/APV_25/giorgio/laurea18072k.ppt.
- [97] T. Hogg P. Jalocha E. Nygard S. Gadomski, G. Hall and P. Weilhammer. The Deconvolution Method of Fast Pulse Shaping at Hardron Colliders. Cern PPE/92-24.
- [98] M. Wingham M. Raymond. I2C settings for APV operation at cold temperatures measurements on a TOB module. http://www.hep.ph.ic.ac.uk/~dmray/pdf/TOB_cold_APV_params.pdf.
- [99] R. Turchetta. Spatial resolution of silicon microstrip detectors. *Nucl. Instrum. Meth.*, A335:44–58, 1993.
- [100] C. Delaere. Fit-functions for the APV25 pulseshaper. Private communication.
- [101] R. Bates. Semiconductor Detectors. http://ppewww.physics.gla.ac.uk/~batesr/post_grad_lectures/PG_lectures_Semiconductor_detectors.pdf.
- [102] Linear technology. LT-SPICE. <http://www.linear.com/designtools/software/>.
- [103] A. Candelori, A. Paccagnella, M. Spada, M. Vanzi, N. Bacchetta, and D. Bisello. SPICE analysis of Signal Propagation in Si Microstrip Detectors. *IEEE Trans. Nucl. Sci.*, 42:459–466, 1995.
- [104] N. Bacchetta et al. HSPICE simulations of Si microstrip detectors. *Nucl. Instrum. Meth.*, A409:142–147, 1998.
- [105] E. Barberis et al. Capacitances in silicon microstrip detectors. *Nucl. Instrum. Meth.*, A342:90–95, 1994.
- [106] T. Bergauer. Process Quality Control of Silicon Strip Detectors for the CMS Tracker. http://wwwhephy.oeaw.ac.at/u3w/b/bergi/www/papers/diploma_thesis_bergauer.pdf.
- [107] M. Raymond. APV25 preamplifier and pulse shaping circuit. Private communication.
- [108] A. Honma. M200 pitch adapter report. http://w3.iihe.ac.be/cms/1%20Detector%20Construction/3%20Pitch%20Adapters/4%20Collaboration%20Talks/data/pa_rep_Alan_011204.pdf.

- [109] I. Belotelov et al. Simulation of misalignment scenarios for CMS tracking devices. CERN-CMS-NOTE-2006-008.
- [110] M. Weber. The CMS Tracker Alignment Strategy. CERN-CMS-CR 2007/002.
- [111] B. Wittmer. *The Laser Alignment System for the CMS Silicon Microstrip Tracker*. PhD thesis, Rheinisch-Westfälische Technische Hochschule Aachen, Fakultät für Mathematik, Informatik und Naturwissenschaften, 2002.
- [112] M. Weber. CMS Tracker Alignment. <http://mweber.home.cern.ch/mweber/Talks.html#alignment>.
- [113] Tapio Lampen. *Detector Alignment Studies for the CMS Experiment*. PhD thesis, Helsinki Institute of Physics, 2007.
- [114] V. Karimaki, A. Heikkinen, T. Lampen, and T. Linden. Sensor alignment by tracks. *ECNF*, C0303241:TULT008, 2003.
- [115] Volker Blobel and Claus Kleinwort. A new method for the high-precision alignment of track detectors. 2002. hep-ex/0208021.
- [116] R. Fruhwirth, T. Todorov, and M. Winkler. Estimation of detector alignment parameters using the Kalman filter with annealing. *J. Phys.*, G29:561–574, 2003.
- [117] E. Widl, R. Fruhwirth, and W. Adam. A Kalman filter for track-based alignment. CERN-CMS-NOTE-2006-022.
- [118] V. Blobel. Millepede II, Linear Least Squares Fits with a Large Number of Parameters. <http://www.desy.de/~blobel/Mptwo.pdf>. Draft.
- [119] CMS Colaboration. trackerrecomaterial.xml. http://cmslxr.fnal.gov/lxr/source/Geometry/TrackerRecoData/data/trackerRecoMaterial.xml?v=CMSSW_1_3_3. Material budget for track reconstruction.
- [120] G. Flucke. Discussion on Alignment Parameters. Private communication.

